Internal Gravity Waves in Massive Stars

Rathish Previn Ratnasingam

Thesis submitted for the degree of
Doctor of Philosophy

School of Mathematics, Statistics & Physics
Newcastle University
Newcastle upon Tyne
United Kingdom

October 2020

I dedicate this thesis to my late brother, who left me and my family too soon. Wherever he is right now, I hope that he is in pure bliss..

Acknowledgements

I would like to thank two very important people that I could not have done this without – Professor Tamara Rogers and Dr Philipp Edelmann – who have provided me with the best supervision team one could ask for. For all the times I was not only given the right amount of academic support, but also the mental help required to make it through my PhD, I thank them whole-heartedly. Next, I would like to thank the two new members of the supervision team – Dr Riccardo Varnon and Ashlin Varghese – who have provided valuable input in the work I have been doing recently. I would also like to thank and congratulate another member of the team and a good friend who was awarded his PhD title very recently, Dr Alex Hindle.

With the continuous input from our collaboration team of observers, the work done for this thesis was always steered in the direction that allowed us to understand observational results better. Thus, I would like to thank Professor Conny Aerts, Dr May Gade Pedersen and Dr Dominic Bowman for their support.

In addition, I have been fortunate to have shared offices with a wonderful group of friends. I thank my office mates, Jack Walton, Dr Hadi Alshammari, and Laura Wadkin. Other graduate students and postdoctoral research associate who have made memorable contributions to my PhD studies are Dr Andrew Groszek, Dr Tom Bland, Dr Sophie Harbisher, Dr Francesca Fedele, Devika Tharakkal, Holly Middleton-Spencer, Aura Cristiana Radu and Clarissa Jade Barratt.

I wish to thank the computing support officers Dr Michael Beaty, John Nicholson, Dr George Stagg, and Dr Chris Graham, administrative staff Jackie Martin, Jackie Williams, Helen Green, Adele Fleck, Carol Andrew, Maria Adair, Georgina Kay-Black, Lauren Daley, Lauren Thompson and Michael McNally. Additionally, I wish to thank Gail de-Blaquiere of the SAgE Faculty Office. I also thank Professor Anvar Shukurov, Dr Graeme Sarson, Dr Paul Bushby and Dr Toby Wood for their general assistance during my research. I acknowledge the support of the staff and resources from the Topsy and Rocket HPC clusters at Newcastle University, Pleiades at NASA Ames, and the DiRAC@Durham facility managed by the Institute for Computational Cosmology on behalf of the STFC DiRAC HPC Facility (www.dirac.ac.uk), which is funded by BEIS capital funding via STFC capital grants ST/P002293/1 and ST/R002371/1, Durham University and STFC operations grant ST/R000832/1. I also acknowledge the support of the Royal Astronomical Society (RAS), for providing a travel grant for my summer school in fluid mechanics in Italy.

Finally, I would like to thank my parents, Ratnasingam S. Vellain and M. Loogasvary, and my brother, Sathesh Previn, for their support throughout this journey.

Abstract

Intermediate-mass stars in the main-sequence have radiative envelopes and convective cores. This configuration allows internal gravity waves (IGWs), generated stochastically at the convective-radiative boundary, to propagate through the radiation zone and produce signatures, which can be observed through space-based photometry and ground-based spectroscopy. In this thesis, we present results from the investigation of IGWs in intermediate-mass stars through theoretical and numerical studies.

The study of IGWs in intermediate-mass stars can be broken down into IGW propagation and IGW generation. In our work, we start with the study of IGW propagation in the linear regime. In this regime, IGW amplitudes are affected by three main features: radiative diffusion, density stratification and geometric effects. We study the implications of these three features on waves travelling within the radiative zones of non-rotating stars. As a simple measure of induced wave dynamics, we define a criterion to see if waves can become nonlinear and if so, under what conditions. We find that the IGW generation spectrum, convective velocities and the strength of density stratification all play major roles in whether waves become nonlinear. With increasing stellar mass, there is an increasing trend in nonlinear wave energies. The trends with different metallicities and ages depend on the generation spectrum.

Next, we move onto the study of non-linear IGW propagation using two-dimensional fully non-linear hydrodynamical simulations with realistic stellar reference states up to the stellar surface. When a single wave is forced, we observe wave self-interaction. When a spectrum of waves is forced, we find that the surface IGW frequency spectrum follows a power law with a slope consistent with recent observations. This power law is similar to that predicted by linear theory for the wave propagation, with small deviations which can be an effect of nonlinearities. When the same generation spectrum is applied to 3 $M_\odot$ models at different stellar rotation and ages, the surface IGW spectrum slope is very similar to the generation spectrum slope.

Finally, we study the IGW generation frequency spectrum from non-linear simulations of core convection as functions of stellar mass and age for intermediate-mass stars. This is an ongoing project and the current results show that the generation frequency slopes lie between -0 and -1 at lower frequencies, and between -1.5 and -3 at higher frequencies for all the stellar models, with the high-frequency slope of the $3M_\odot$ ZAMS model being consistent with previous numerical work (Rogers *et al.*, 2013).

Contents

List of Figures

List of Tables

Chapter 1

Introduction

As the universe cooled down after the Big Bang, structure formation started to occur. Quarks coagulated to form subatomic particles prior to the formation of nuclei and atoms (significantly later), leading to larger and larger structures. About 100 million years after the Big Bang, the first stars, known as the primordial stars formed. These stars were made up of hydrogen and helium with almost no contamination of metallic substances[1]. As the universe evolved further, stellar processes, mainly the spectacular explosion towards the end of a stellar life cycle known as a supernova, led to the formation of heavier metals which enriched the interstellar medium. This allowed stars of higher metallicities to form and populate the universe while being gravitationally bound in massive structures called galaxies. A popular analogy to express the abundance of stars in the universe is that currently, there are more stars in the whole universe than there are grains of sand on our planet.

1.1 The Life and Death of Stars

To quote the well-known British writer C.S. Lewis, "a star is a huge ball of flaming gas". This simple yet accurate description is, however, not sufficient. To add more depth to this quote, a star is a ball of very hot ionised gas, also known as plasma, that is in hydrostatic equilibrium (see Fig. 1.1), the balance between thermal pressure pushing outwards and self-gravity. The source of thermal pressure, which is a mixture of gas and radiation pressure, is the nuclear fusion process that occurs at the stellar core. To a small degree, there is electron degeneracy pressure, resulting from the Pauli exclusion principle, which requires that no two fermions be in the same quantum state. However, this degeneracy pressure is often not taken into account due to its relatively small contribution to the total pressure when modelling stars in their hydrogen-burning lifetime, also known as main-sequence

[1] All elements excluding hydrogen and helium.

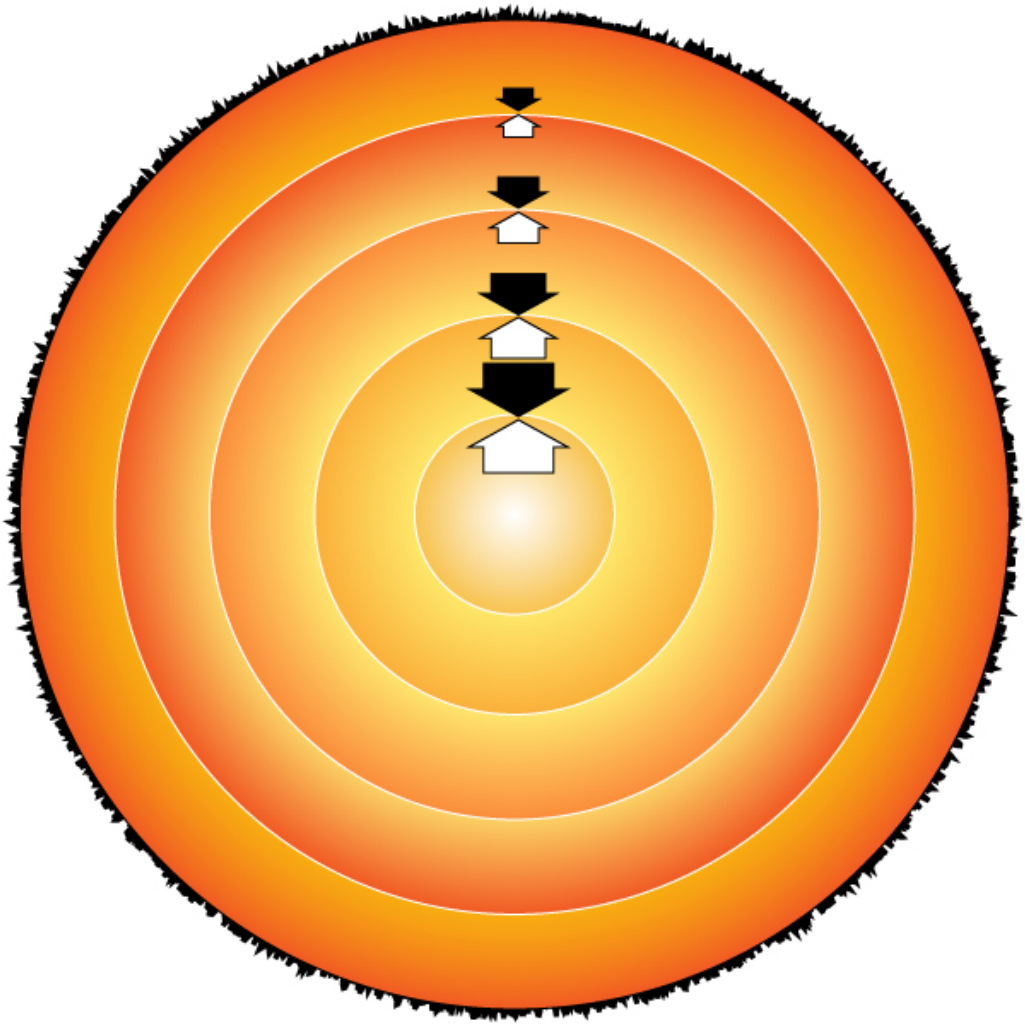

Figure 1.1: Hydrostatic equilibrium in stars. The black arrows represent self-gravity acting inwards and the white arrows represent thermal pressure pushing outwards. Note that hydrostatic equilibrium is and will always be satisfied at different radii for any main-sequence star. Photo Credit: `https://scienceatyourdoorstep.com/2019/04/29/what-keeps-a-star-stable/`

stars.

Before hydrogen-burning begins, a protostar undergoes gravitational contraction until the core becomes hot enough for hydrogen fusion to be ignited. In some cases, the core may never become hot enough for hydrogen ignition to begin, which results in "failed" stars, also known as brown dwarfs. Once the fusion process starts, the star stops contracting as thermal pressure provides an outward force that balances the gravitational collapse (hydrostatic balance). This point in time of a star's life is known as the Zero-Age-Main-Sequence or ZAMS. The star then spends most of its life burning hydrogen. When the mass fraction of hydrogen in the stellar core drops to half its initial value, this point in time is called the middle-of-the-Main-Sequence, or midMS, which is an uncommon acronym in

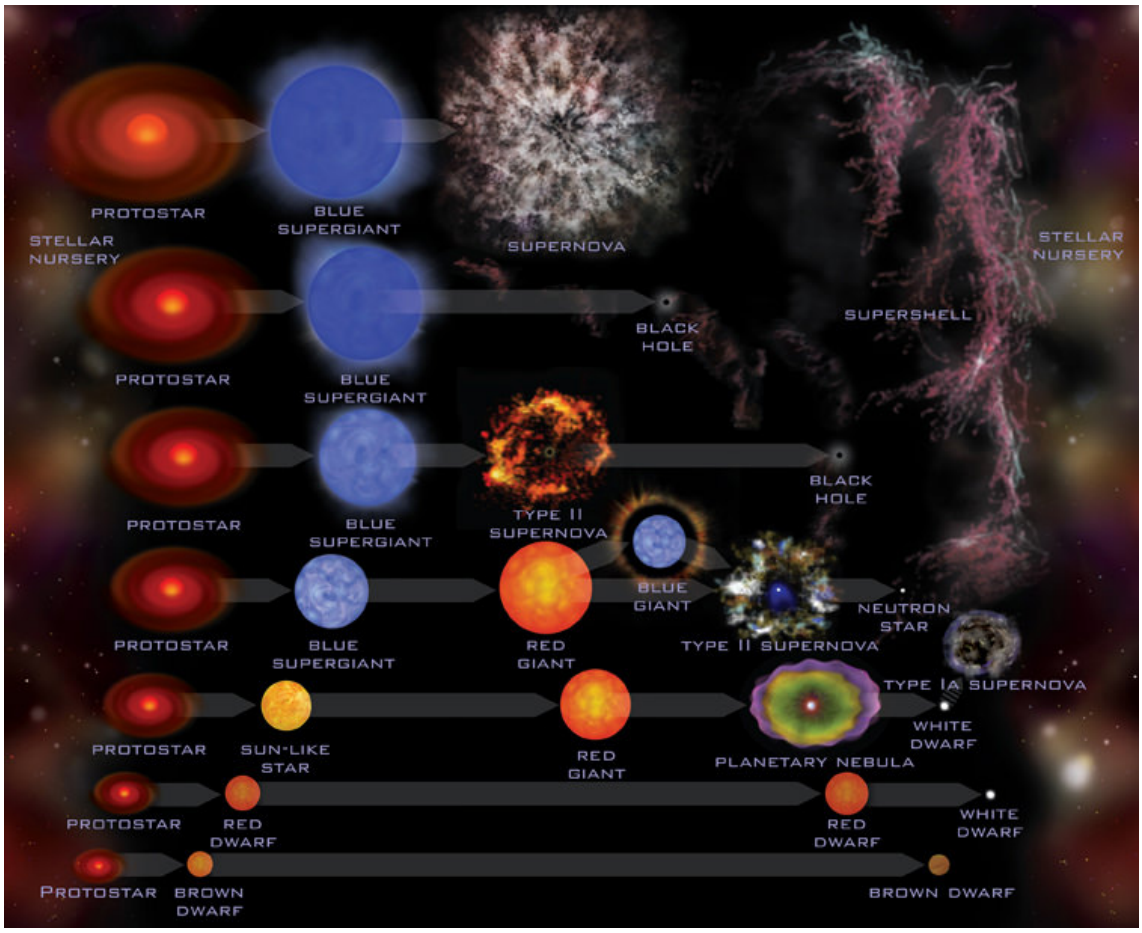

Figure 1.2: The life cycle of Stars. This picture shows all possible outcome of stars that start off with different masses, from very low mass protostars that do not ignite hydrogen fusion at all, to low mass stars that evolve into white dwarfs by shedding their outer envelope, to high mass stars that undergo supernovae and eventually evolve into neutron stars or black holes. Photo Credit: Universe Today (https://www.universetoday.com/24629/life-cycle-of-stars/)

the stellar community but one that I will be using frequently in this thesis. When all the core hydrogen fuel has been used up, the star has reached the Terminal-Age-Main-Sequence, or TAMS, and evolves into the post-main sequence stage, which eventually leads to the death of a star.

Figure 1.2 shows the possible evolutionary tracks of very low-mass to very high mass stars. This diagram shows how low mass stars (i.e. red dwarfs and sun-like stars), evolve through different tracks to eventually become white dwarfs and high mass stars, which eventually undergo a core-collapse/Type II supernova to become a neutron star or a black hole. In the field of observational astrophysics, the general evolution of a star can be traced on a very important plot known as the Hertzsprung–Russell (HR) diagram (see Fig. 1.3), a plot of stellar luminosity against the stellar surface temperature. The main-sequence stars mostly lie on the central diagonal, with more luminous and hotter/bluer stars on the top

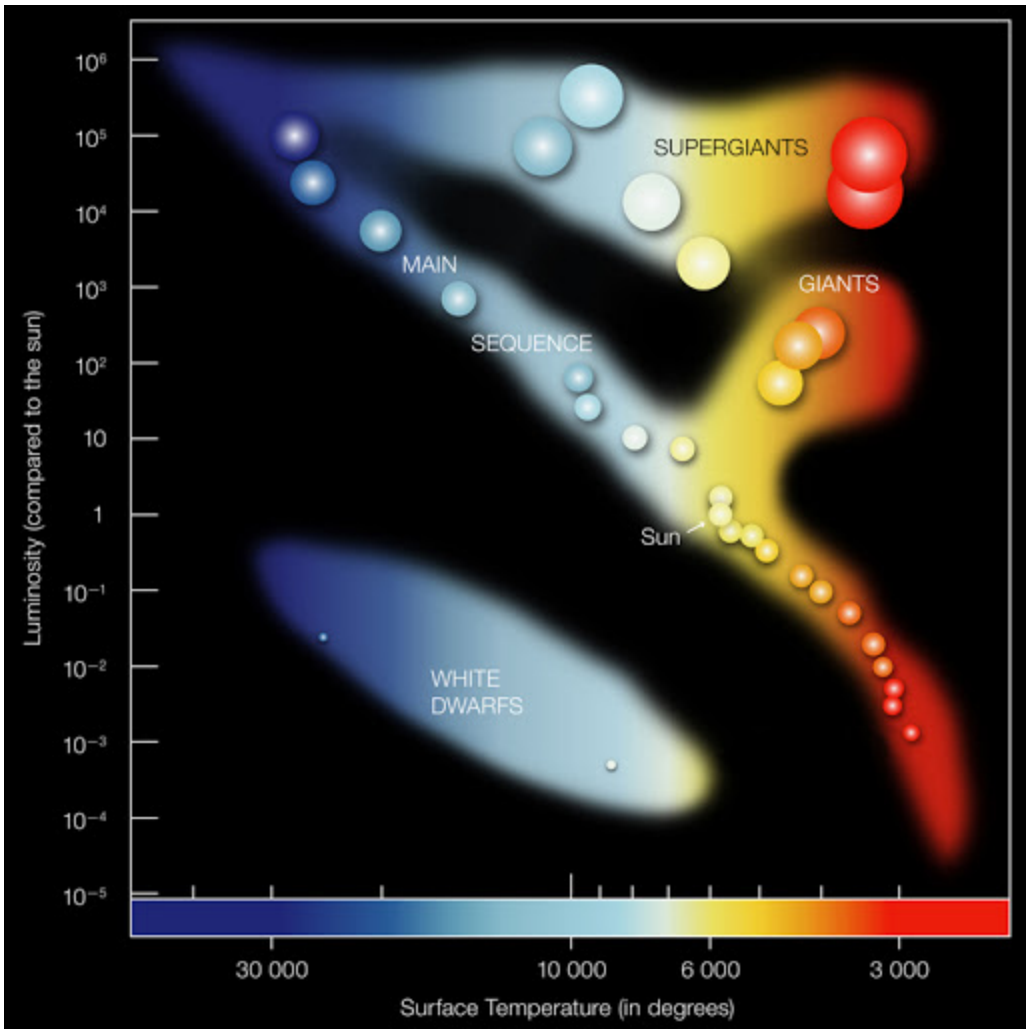

Figure 1.3: The Hertzsprung–Russell diagram. Note that the x-axis of this plot is sometimes replaced with colour index (B-V), which is a proxy for temperature. All the models used in this work are from the diagonal in the centre of the figure labeled as Main Sequence. Photo Credit: NASA/CXC/SAO

left corner, and less luminous and cooler/redder stars on the bottom right corner. The top right corner of the diagram shows the giants and supergiants, which are the most massive and luminous stars. The bottom left corner of the diagram shows the white dwarfs, which have low-luminosity and very high temperature. These astrophysical objects are the final stage of the evolution of a low-mass star and they are supported by electron degeneracy pressure against gravitational collapse.

To improve the efficiency of stellar studies, we turn to the commonly-used stellar classification system: the Morgan-Keenan system. In this system, stars are classified according to their spectral type and represented with certain letters, as shown in Table 1.1. Note that we will be using the subscript $\odot$ to denote solar parameters from here on. The

Class	Surface Temperature (K)	Mass ($M_\odot$)
O	$\geqslant 25000$	$\geqslant 16$
B	10000 – 25000	2.1 – 16
A	7500 – 10000	1.4 – 2.1
F	6000 – 7500	1.04 – 1.4
G	5000 – 6000	0.8 – 1.04
K	3500 – 5000	0.45 – 0.8
M	$\leqslant 3500$	0.08 – 0.45

Table 1.1: Stellar spectral classification scheme.

average surface temperature within the class and the mass range is also given in the table. Within each alphabet class, the stars are further divided into numbers ranging from 0–9 (hottest to coolest) and roman numerals, *I - VII* (most luminous to least luminous). Our closest star, the Sun, is a class G2 *V*, for example. Throughout this thesis, I will be using this classification system multiple times, referring only to the spectral class (the letters) of the star.

1.2 The Internal Structure of Stars

In the simplest case of studying stellar internal structures, there are three equations (Kippenhahn *et al.*, 2012) that are usually considered:

$$\frac{\partial P}{\partial r} = -\frac{GM_r\rho}{r^2} - \rho\frac{\partial^2 r}{\partial t^2}, \tag{1.1a}$$

$$\frac{\partial T}{\partial r} = -\frac{3\kappa\rho L_r}{16\pi acT^3r^2}, \tag{1.1b}$$

$$\frac{\partial L_r}{\partial r} = 4\pi r^2\rho\left(\epsilon - T\frac{\partial S}{\partial t}\right). \tag{1.1c}$$

The set of equations (1.1) describes the time evolution of a spherically symmetric star, provided the initial conditions and the boundary conditions are specified. In Eq. (1.1a), P is pressure, r is the radial coordinate, G is the gravitational constant, M_r is the mass coordinate[2], ρ is the stellar density and t is time. This equation describes the relationship between the pressure difference at two (radial) boundaries of a fluid element ($\partial P/\partial r$) and the gravitational force acting on that fluid element ($-GM_r\rho/r^2$), taking into account the changes in the geometry of said element ($\rho\left[\partial^2 r/\partial t^2\right]$). If the time derivative in Eq. 1.1a vanishes then, the star is in hydrostatic equilibrium. If the time derivative in Eq. 1.1c vanishes then the star is in thermal equilibrium. In the second equation, Eq. (1.1b), T is the stellar temperature, κ is the stellar opacity, L_r is the luminosity, a is the radiation con-

[2]The mass enclosed within a sphere at a particular radius.

stant and c is the speed of light. This equation is derived from the direct proportionality between the temperature gradient ($\partial T/\partial r$) at any given radius in a star and the heat flux ($-3\kappa\rho L_r/16\pi acT^3r^2$) at that radius. Finally, in Eq. (1.1c), ϵ represents the heat source in the star and S represents entropy. This equation is derived from the first law of thermodynamics which states that the change in the internal energy of a star ($1/4\pi r^2\partial L_r/\partial r$), is equal to the heat source, ϵ subtracted by the work done in the system ($T\partial S/\partial t$). If the time derivative in Eq. (1.1c) vanishes then, the star is in thermal equilibrium. In one-dimensional stellar modeling, it is common to work in the Lagrangian frame, or with mass coordinates. Thus, using stellar density, the set of equations (1.1), can be written with mass coordinates using the following conversion factor:

$$\frac{\partial r}{\partial M_r} = \frac{1}{4\pi r^2\rho} \tag{1.2}$$

Note that in most advanced stellar modeling, there are many more factors that will be taken into account. For example, in one dimension, stellar wind and element compositional effects, and in more than one dimension, stellar rotational and magnetic effects.

Without going into much detail on the additional effects mentioned above, there is one crucial mechanism within a star that is currently heavily studied: thermal energy transport. Equation (1.1b) describes only the radiative heat energy transport through the direct proportionality of the radiative heat flux and the temperature gradient but there are three forms of thermal energy transfer that can occur from the heat generated through the central hydrogen fusion process; conduction, convection and radiation. Stellar interiors are divided into convection and radiation zone as one of these two heat transfer mechanisms usually dominates. Conduction occurs throughout the whole star and does not significantly affect heat transfer (except in compact objects, such as white dwarf interior). Note that two (or all three) mechanisms can be active at the same point in a star. For example, radiative and conductive processes still do occur in the convection zone.

Figure 1.4 shows the internal structure of stars at different mass ranges. For stellar masses less than 0.5 $M_\odot$, most of the stellar interior will be convective, very similar to gas giant planets. According to the stellar classification scheme (See Table 1.1), such stars are labelled as class M with effective temperatures less than 3500 K. Although there is a small overlap of type K mass range with the mass range of fully convective stars, type K stars are not considered to be fully convective. In fact, a recent study (Baraffe, Isabelle & Chabrier, Gilles, 2018) found that the transition mass might be even smaller, close to 0.31 $M_\odot$.

For stellar masses from 0.5 $M_\odot$ to approximately 1.5 $M_\odot$ (Class F, G and A), the hydrogen-to-helium fusion process that occurs through the production of a deuterium nucleus, also known as the p-p chain, is dominant and does not establish a strong temperature

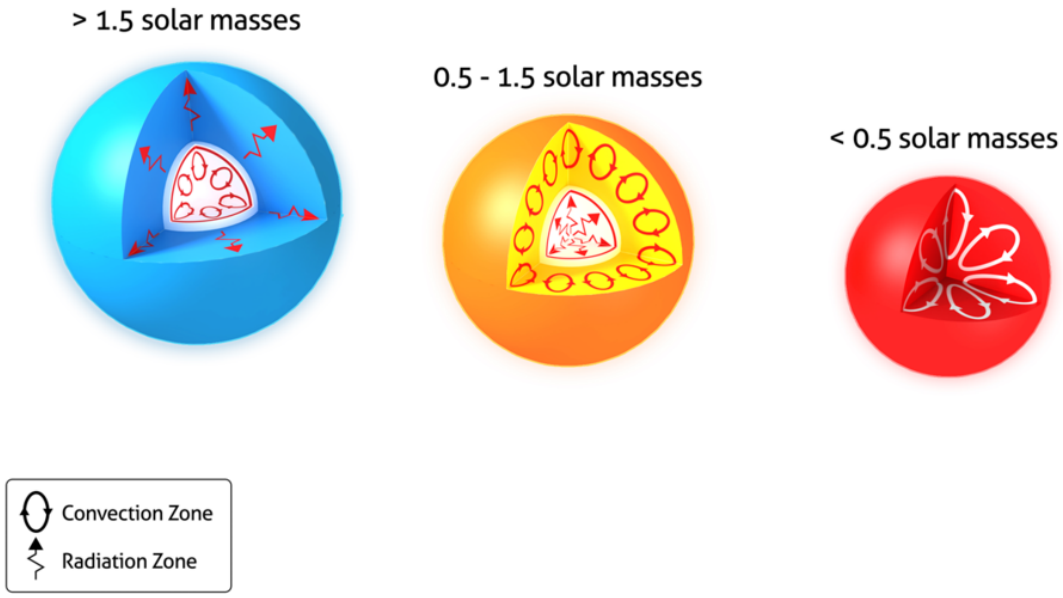

Figure 1.4: The location of convection and radiation zones in stars and their mass ranges. Photo Credit: Sun.org - www.sun.org, released under CC-BY-SA 3.0

gradient in the core leading to the core being radiative. Closer to the stellar surface, the cooler temperature means that fully-ionised particles can become partially-ionised, which are more opaque to photons. This causes the temperature gradient to steepen leading to the formation of a convection zone. Note that the exact details of this temperature gradient relation to heat transport mechanism will be addressed in the next section. Our closest star, the Sun (see Fig. (1.5)), is a good example, where approximately 70% of the total solar interior is a radiation zone whilst the remaining 30% is a convection zone. l

For stellar masses above 1.5 $M_{\odot}$ (Class B and O), hydrogen fusion process occurs through the use of intermediate Carbon, Nitrogen and Oxygen nuclei as catalysts (also known as the CNO cycle), and this process is more dominant than the p-p fusion process. The CNO cycle establishes a temperature gradient steep enough for convection to set in, causing the core to be convective and the surrounding envelope, where the temperature gradient is less steep, to be radiative. In some cases, a thin surface convection zone may develop, which is normally associated with an opacity bump (due to the presence of metals) close to the stellar surface. Figure 1.6 shows the location of the convection zones (marked in blue), for the stellar models used in this work, generated using a one-dimensional stellar evolution software (see Chapter 2, Section 2.2), with the top panel showing radius as a function of solar units and the bottom panel showing radius as a function of the total stellar radius of that particular model. Generally, the surface convection zone is bigger for

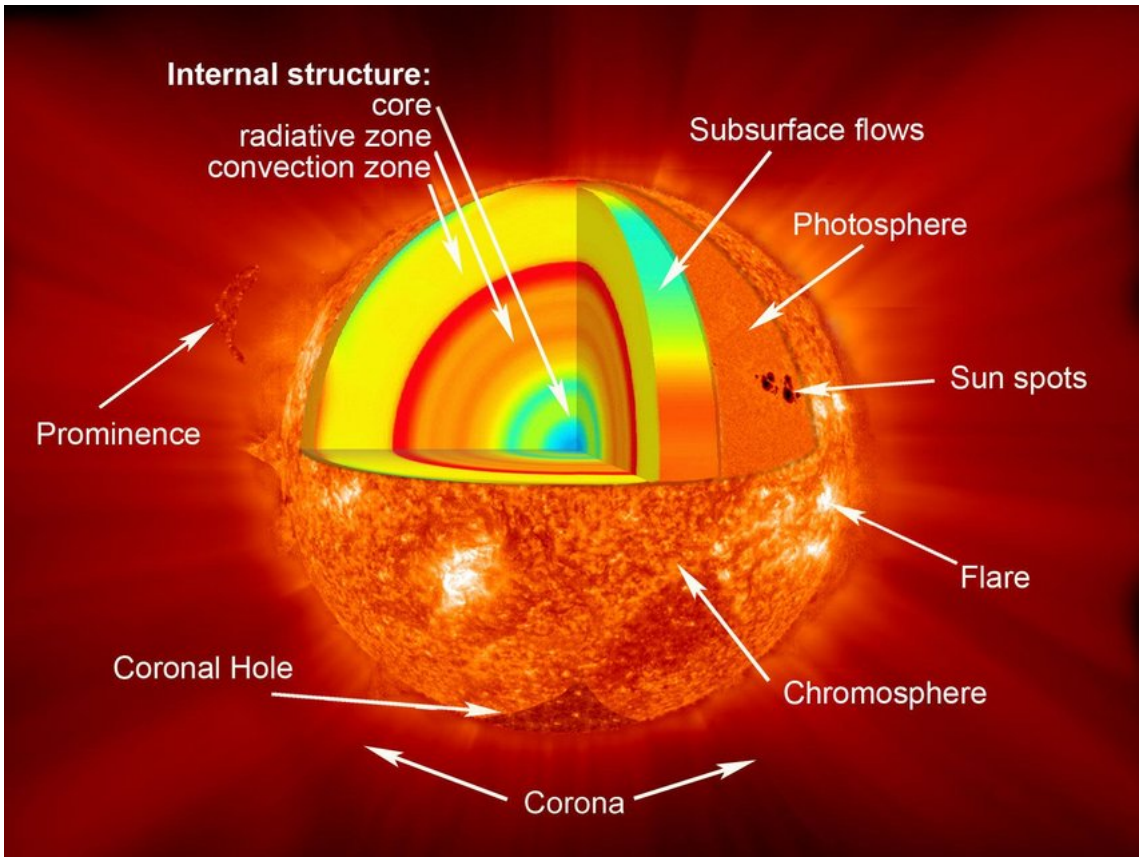

Figure 1.5: The Solar Structure. The internal structure can be seen to be divided into the convection zone (yellow) and the radiation zone (from the red region to the core). It is usually assumed in solar modeling that the radiation zone extends from the centre of the star to 70% of the total radius, whilst the convection zone covers the remaining 30%. Photo Credit: NASA

older and more massive stars and the convective core decreases in size with age.

1.2.1 The Convection and Radiation Zones

An adiabatic process occurs without the loss or gain of thermal energy from a system. In such a system, there will be a specific temperature, pressure and density profile that corresponds to adiabats, where energy transfer will be purely mechanical. In stars, the profiles of the quantities mentioned above can fall under two categories; subadiabatic or superadiabatic.

In a superadiabatic region, the temperature profile of the surrounding atmosphere is steeper than that of any adiabatic perturbations arising in the system (Fig. 1.7(a)). On the other hand, the density profile of the surrounding atmosphere is shallower than that of the same adiabatic perturbation (Fig. 1.7(b)). As a result, a radially displaced (in either the positive or negative direction) fluid element will continue to move in that direction as the density of the perturbation decreases more rapidly than the density of the surrounding

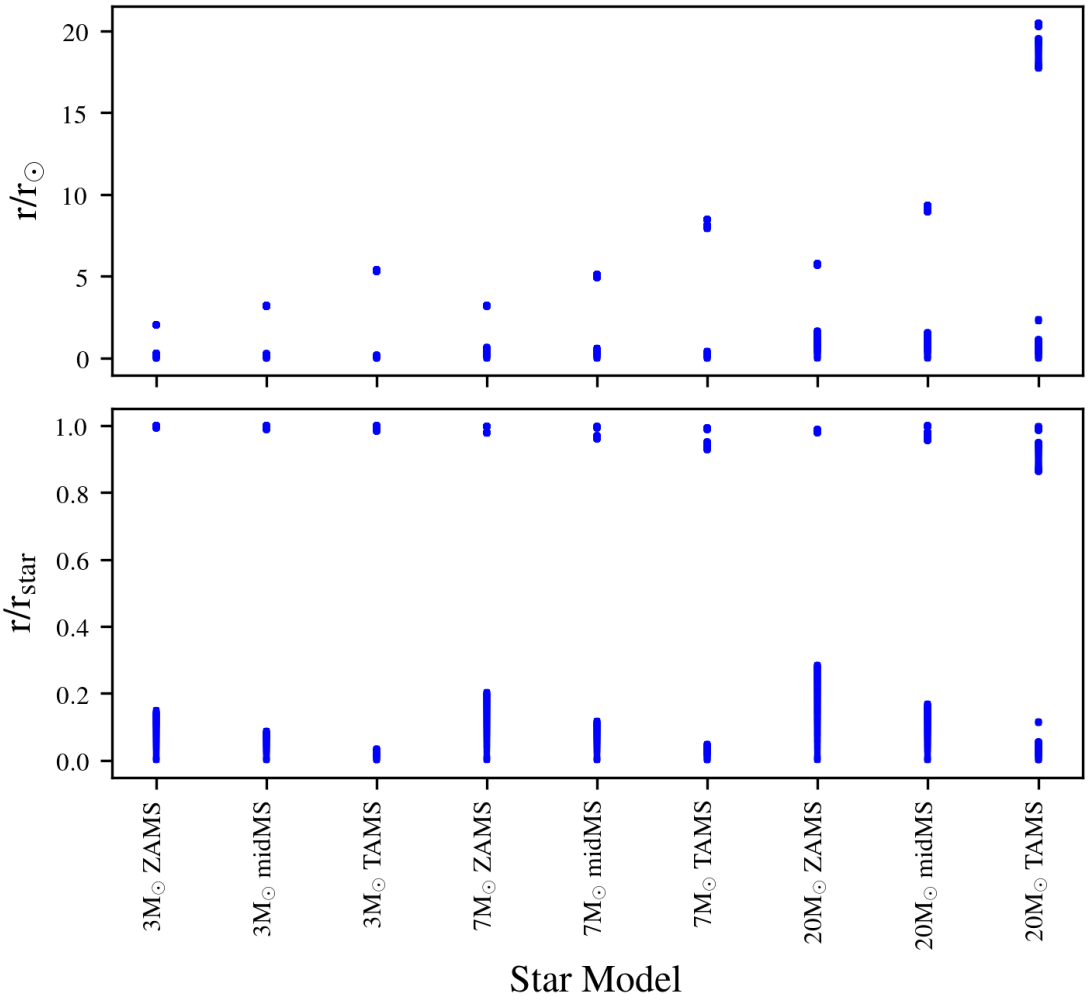

Figure 1.6: The location of the convection zone (marked in blue) as a function of stellar mass/age (x-axis) and stellar radius in units of total solar radius (top panel) and in units of total stellar radius (bottom panel). Note that from the bottom panel, the surface convection zones are always located very close to the total stellar radii for all the models shown. Thus, the total stellar radii for the models in the top panel are indicated by the location of the surface convection zone.

atmosphere, while the pressure stays equal to its surroundings (Fig. 1.7(c)). Buoyancy drives the motion of the perturbation, until it encounters a cooler region, allowing heat exchange. The fluid element then becomes anti-buoyant and sinks until it encounters and warmer region where it can gain heat through conduction and rises again. This is how convective motion operates and thus, superadiabatic temperature and density profiles can give rise to convection zones. This region is said to be convectively unstable, where the following inequality is valid:

$$\frac{dP}{d\rho} > \left(\frac{dP}{d\rho}\right)_{adiabatic}, \tag{1.3}$$

which describes a steeper decrease in the density of the perturbation compared to the surrounding atmosphere with the pressure of the two being equal. Considering an ideal gas system (which will be the assumption made in the majority of my work), this inequality can be written as

$$\frac{P}{T}\frac{dT}{dP} > \left(\frac{P}{T}\frac{dT}{dP}\right)_{adiabatic}. \tag{1.4}$$

It is common in the field of stellar astrophysics to represent the right-hand-side of Eq. (1.4) with ∇_{ad} so we can re-write this equation as

$$\frac{P}{T}\frac{dT}{dP} > \nabla_{ad}, \tag{1.5}$$

which is also known as the Schwarzschild criterion. In stars, there are regions where this equality is not sufficient to describe convection as this criterion is for a purely thermal system. In these regions (e.g. convective-radiative boundaries), convection can also influenced by compositional gradients. The Ledoux criterion allows a better representation of convection zones in these circumstances as follows:

$$\frac{P}{T}\frac{dT}{dP} > \nabla_{ad} + B, \tag{1.6}$$

where B, which is also written as ∇_{μ} in literature, is the Ledoux term (e.e Unno *et al.* (1989); Brassard *et al.* (1991)). This term can be expressed as

$$B = -\frac{1}{\chi_T}\sum_{i=1}^{N-1}, \left(\frac{\partial \ln P}{\partial \ln X_i}\right)_{\rho,T,X_{j\neq i}} \frac{d\ln X_i}{d\ln P} \tag{1.7}$$

where, χ_T is defined as $(\partial \ln P/\partial \ln T)_{\rho}$ at constant density and X is the mass fraction of different components in the fluid with the index i representing each component.

In a subadiabatic region, the temperature profile of the surrounding atmosphere is less steep than that of any adiabatic perturbations arising in the system (Fig. 1.8(a)). The density profile of the surrounding atmosphere is shallower than that of the same adiabatic perturbation (Fig. 1.8(b)). Thus, when an adiabatic fluid element is displaced radially outwards, the density of said element will be higher than the density of the surrounding atmosphere (Fig. 1.8(c)). This causes the element to become anti-buoyant and sink until it propagates beyond its starting point. After this point, the density of the surrounding atmosphere will be higher than that of the fluid element and thus, the fluid element decelerates and starts rising, due to buoyancy. The same scenario occurs when the fluid element is displaced radially inwards. Any adiabatic perturbation will oscillate around a mean position instead of travelling continuously in the radial direction, and this type of fluid motion leads to internal gravity waves or IGWs (see next section). The radiation zones of stars have subadiabatic temperature and density profiles and this region is said

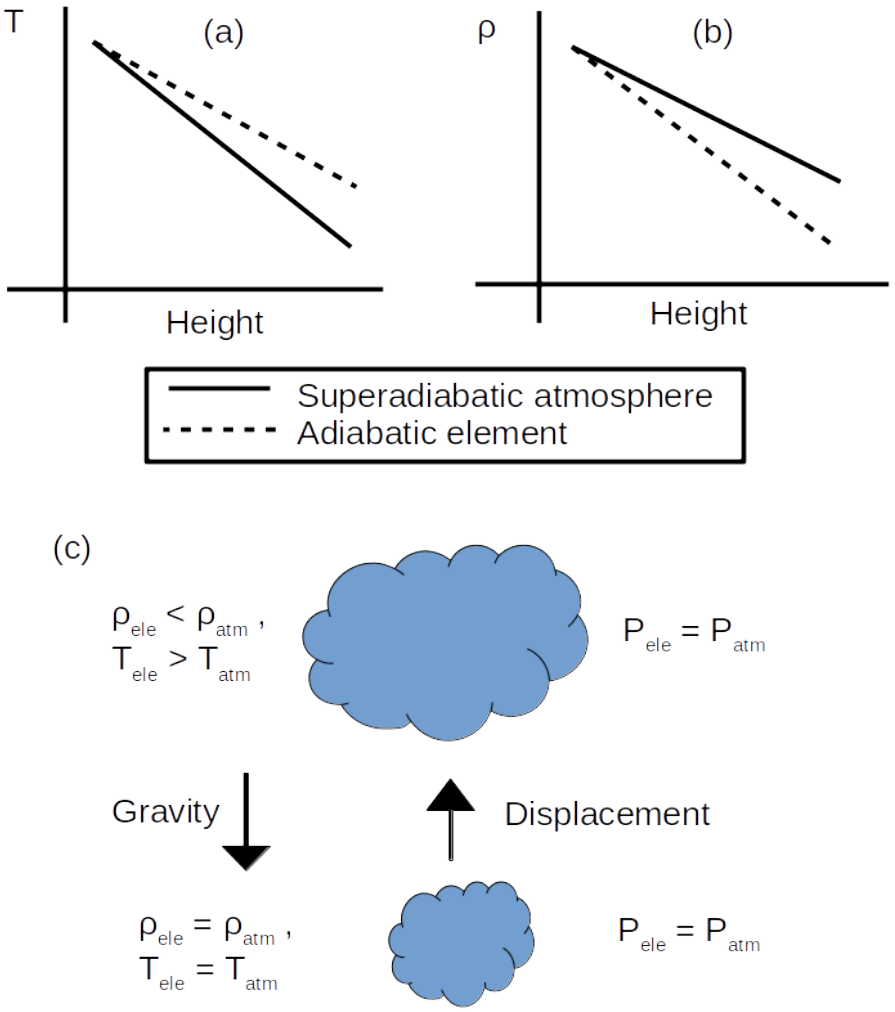

Figure 1.7: The behaviour of an adiabatic fluid element in a superadiabatic atmosphere. This system is convectively-unstable.

to be convectively stable. The Schwarzschild criterion for the radiation zone is thus,

$$\frac{P}{T}\frac{dT}{dP} < \nabla_{ad}, \tag{1.8}$$

and the Ledoux criterion is

$$\frac{P}{T}\frac{dT}{dP} < \nabla_{ad} + B. \tag{1.9}$$

Using either the Schwarzschild or the Ledoux criteria, we can write the maximum frequency that IGWs can possess in the radiation zone as

$$N^2 = \frac{g^2\rho}{P}\frac{\chi_T}{\chi_\rho}\left(\nabla_{ad} - \frac{P}{T}\frac{dT}{dP} + B\right). \tag{1.10}$$

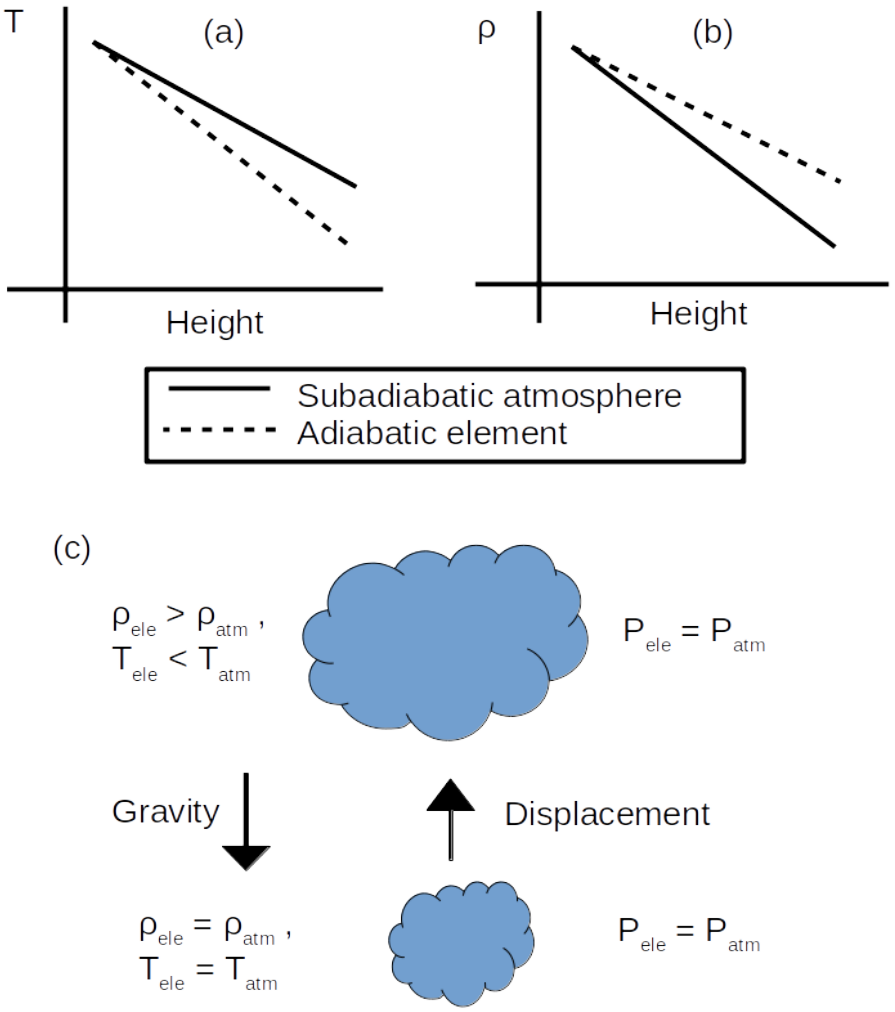

Figure 1.8: The behaviour of an adiabatic fluid element in a subadiabatic atmosphere. This system is convectively stable.

where N is known as the Brunt–Väisälä frequency and χ_ρ is defined as $(d\ln P/d\ln\rho)_T$ at constant temperature.

Convection and radiation zones in stars are always adjacent to each other, whether it is a larger star with a convective core and a radiative envelope or a smaller star with a radiative core and a convective envelope. However, as mentioned in the previous section, some stars (especially ones with higher masses) develop surface convection zones and some even develop intermediate convection zones.

The neighbouring location of the radiation and convection zones means that they will interact and become the source of many mechanical processes in a star. There are many uncertainties about how the boundary layer is defined and the transition profile[3] between

[3]The change from superadiabaticity to subadiabaticity and vice versa.

a convection zone and a radiative zone is currently unknown but likely to be spatially and time-dependent. However, the one-dimensional temperature, density and pressure profiles are thought to be smooth[4]. Within the boundary layer, overshooting (or undershooting for convection zones above radiation zones) of fluid from the convection layer causes chemical and angular momentum mixing, and can influence the generation of IGWs to a certain degree. For example, the work done in Pedersen *et al.* (2018) showed that the gravity mode, which is an IGW stationary mode, period spacings in slowly pulsating B–type stars, changes with the use of either a step function or an exponential function, applied to the $\partial P/\partial\rho$ (see Eq. (1.3)) of a star. The change in gravity-mode spacings was found to be noticeably clearer for younger stars. Thus, studying IGWs in stars is clearly paramount as it provides a way to understand stellar interiors.

1.3 Internal Gravity Waves (IGWs)

The effect of gravity waves in large fluid bodies has been observed in many dynamical systems within our own atmosphere. For example, when a uniform layer of air encounters an obstacle such as a mountain, atmospheric gravity waves are formed, provided the atmospheric region is stably-stratified[5]. These waves carry energy and angular momentum towards the ionosphere, causing the formation of wave clouds (see Fig. 1.9). Surface gravity waves, that form at the interface between the air and the ocean, can be clearly observed breaking on shorelines. Internal gravity waves forming in the air above oceans impose themselves on ocean surfaces leading to the formation of periodic calm and rough patches which are visible in satellite images.

Internal gravity waves or IGWs are fluid waves which propagate within stably stratified regions for which the restoring force is gravity. Since IGWs are fluid waves, the dispersion relation for IGWs can be derived analytically from the linearisation of the Navier-Stokes equation with an appropriate choice of energy equation. Generally, the dispersion relation is written as

$$\omega = N\sqrt{\frac{k_h^2}{k_v^2 + k_h^2}}, \tag{1.11}$$

where k_v is the vertical wavenumber, k_h is the horizontal wavenumber and ω is the wave angular frequency. Depending on the number of dimensions considered, k_h can be either m/r, where m is the index number in a Fourier basis (two-dimensional analysis) or $\ell(\ell - 1)/r$, where ℓ is the spherical harmonic degree (three-dimensional, spherical analysis). All quantities, except the wave frequency, in this dispersion relation vary with stellar radius,

[4] At least, in the case of horizontally-averaged profiles.

[5] The term stably stratified or stable stratification will be repeatedly used in this thesis, which means density varying in the radial direction.

Figure 1.9: An example of wave clouds formed from atmospheric gravity waves. Photo Credit: Chris Wilson (http://www.antarctica.gov.au/magazine/2011-2015/issue-28-june-2015/science/refining-gravity-waves-in-climate-models)

r. The phase velocity of IGWs is then

$$\mathbf{v_p} = \frac{\omega}{|\mathbf{k}|}\hat{\mathbf{k}} \tag{1.12}$$

$$= \frac{N}{|\mathbf{k}|}\sqrt{\frac{k_h^2}{k_v^2 + k_h^2}}\hat{\mathbf{k}} \tag{1.13}$$

$$= \frac{Nk_h}{|\mathbf{k}|^3}\left(k_v\hat{\mathbf{v}} + k_h\hat{\mathbf{h}}\right), \tag{1.14}$$

where $|\mathbf{k}|$ is the magnitude of the total wavenumber, $k = \sqrt{k_h^2 + k_v^2}$ and $\hat{\mathbf{k}}$ is the unit vector of the total wavenumber, $\mathbf{k}/|\mathbf{k}|$. The unit vectors, $\hat{\mathbf{v}}$ and $\hat{\mathbf{h}}$, represent the vertical and horizontal direction respectively. Unconventional representations of these unit vectors were chosen here because this derivation can be done using Cartesian, cylindrical or spherical coordinates, with clear definition of the vertical and horizontal directions. In 3 dimensions, the horizontal direction is defined using the remaining two directions, provided a vertical representation has been chosen (e.g. in Cartesian coordinates, choosing the z-direction as the vertical means the unit vector of $\sqrt{x^2 + y^2}$ represents the horizontal direction). The

group velocity is

$$\mathbf{v_g} = \frac{\partial \omega}{\partial k_v}\hat{\mathbf{v}} + \frac{\partial \omega}{\partial k_h}\hat{\mathbf{h}} \tag{1.15}$$

$$= -\frac{N k_v k_h}{\left(k_h^2 + k_v^2\right)^{3/2}}\hat{\mathbf{v}} + \frac{N k_v^2}{\left(k_h^2 + k_v^2\right)^{3/2}}\hat{\mathbf{h}} \tag{1.16}$$

$$= \frac{N k_v}{|\mathbf{k}|^3}\left(-k_h\hat{\mathbf{v}} + k_v\hat{\mathbf{h}}\right) \tag{1.17}$$

From the group velocity and phase velocity, we can see an important property of IGWs: the group velocity is perpendicular to the phase velocity, which indicates that IGWs are transverse waves.

Internal gravity waves also have the property that the vertical and horizontal velocities are spatially $\pi/2$ rad out of phase with each other in the horizontal direction. This can be seen in Fig. 1.10, which shows a time snapshot of vertical and horizontal velocity profiles for a monochromatic gravity wave forced at the bottom boundary of an annulus. This can be understood from the continuity equation, given as

$$\frac{\partial \rho}{\partial t} + \nabla.(\rho\mathbf{u}) = 0 \tag{1.18}$$

which states that the rate of mass change has to be equal to the accumulation of mass within the system. Expanding out the second term in Eq. (1.18), gives $\rho(\nabla.\mathbf{u}) + \mathbf{u}.\nabla\rho$, and since $\nabla.\mathbf{u}$ is the only term that contains a horizontal derivative, the use of Fourier basis to represent the vertical velocity and horizontal velocity allows us to derive the relationship between these quantities as $u_v \propto imu_h$. Tracking the changes in these parameters (i.e. temperature, horizontal and vertical velocities) with time at a single point in the domain would show that the vertical velocity and temperature are out of phase by $\pi/2$ rad whilst the vertical and horizontal velocities are in phase.

Another important property of IGWs is that they generally have lower frequencies compared to sound waves. They become more important in systems with low Mach numbers[6](e.g. stellar interiors) and are limited by the Brunt–Väisälä frequency in the system. In stars, the boundary conditions imposed on these waves (the Brunt–Väisälä frequency going to zero at the point of generation and the stellar surface or core, depending on the direction of IGW propagation) means that stationary modes can form, which are called gravity modes or g-modes. These g-modes are extremely important in the observational study of asteroseismology as they provide the means to probe stellar interiors. This will be discussed in further detail in the final section of this chapter.

In stellar interiors, IGWs have recently gained attention as they can possibly be the reason behind a few unexplained phenomena. For example, Rogers *et al.* (2012) showed

[6]The ratio between the local flow velocity and the speed of sound in the medium.

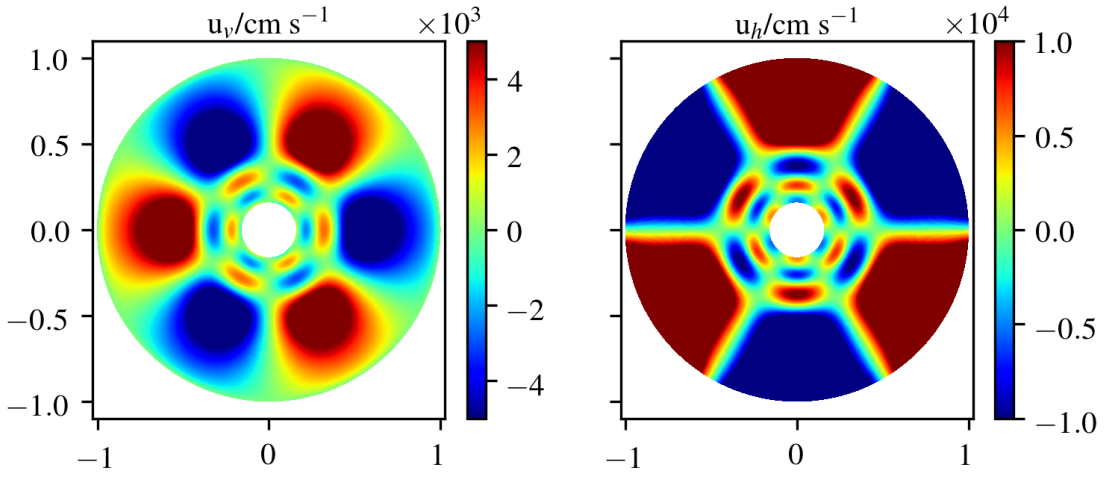

Figure 1.10: The radial (left) and horizontal (right) velocity perturbations due to monochromatic internal gravity waves forced at the bottom boundary of a stably stratified circular disc. The x and y axes represent the Cartesian x and y coordinates in units of stellar radius. Looking along a horizontal line at any given radius, the vertical and horizontal velocities are expected to be spatially out of phase by 90 degrees, which can be observed in the figure.

that in cases where an extra-solar planet has a retrograde orbit, this misalignment can be caused by angular momentum transport, mediated by breaking IGWs, within the host star instead of planetary interactions as commonly thought. The transfer of angular momentum to the surface can result in the surface rotating in the opposing direction of the bulk of the star. Fuller *et al.* (2014) showed that IGWs reduce differential rotation in evolved stars through dissipation of angular momentum during propagation. Edelmann *et al.* (2019) and Bowman *et al.* (2019) showed that IGWs can be used to explain stellar brightness variabilities from both a numerical and observational point of view. Thus, it is indeed the right time to study the mechanism behind the generation and propagation of these waves in stars.

1.3.1 IGW Generation

Previous studies show that investigating IGWs in stars can be broken down into two parts: generation and propagation/dissipation. Starting with IGW generation, the most widely studied generation mechanisms are turbulent convection, κ-mechanism and tidal interaction. We focus mainly on stochastic IGW generation through turbulent convection here as this is the mechanism we primarily study.

κ-mechanism

The κ-mechanism is defined as a process where opacity drives the pulsation in variable stars. The κ-mechanism described schematically in 1.11. Any compressed layer in a star will become denser and thus more opaque and as a result, heat flow from the core will be stopped and allowed to build-up (1). This causes an increase in outward pressure, which causes the layer to expand outward and cool down (2), thus becoming more transparent to radiation. As the heat flow through the layer is restored, the outward pressure decreases causing the layer to compress again, repeating the cycle (3).

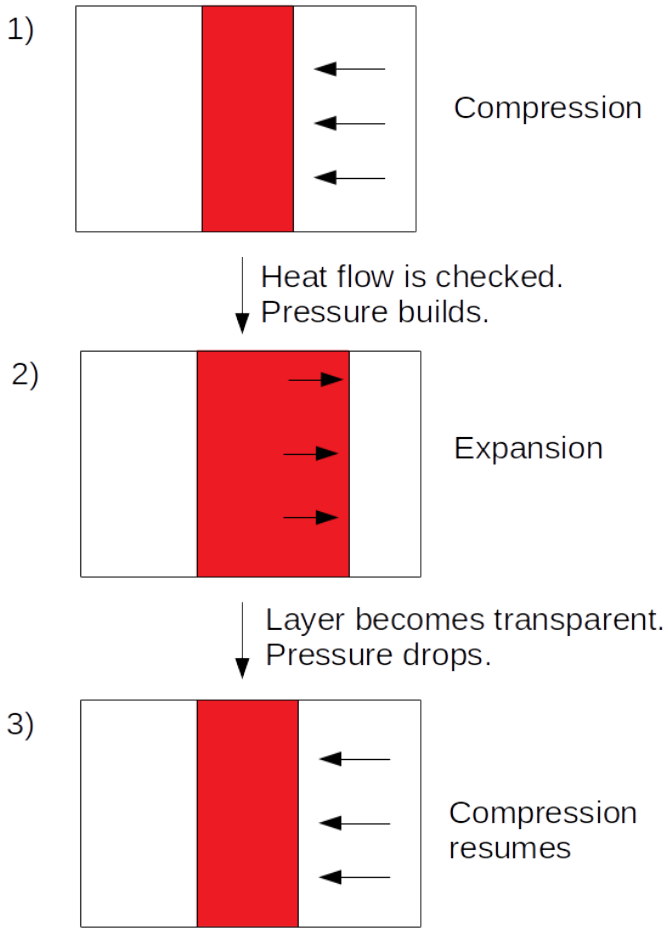

Figure 1.11: The κ-mechanism.

Generally, the opacity in stars are represented with Kramers opacity, which is the opacity due to bound-free and free-free electrons(Kippenhahn *et al.*, 2012) and is proportional to density but inversely proportional to $T^{3.5}$. This means that when a layer is compressed, the increasing density and temperature of the layer causes the layer to become less opaque

due to the higher temperature sensitivity. However, certain types of stars (i.e. Cepheid and RR Lyrae variables) possess regions containing partially ionised hydrogen and helium, close to the surface. Thus, when such a region is compressed, energy is spent in ionisation and the temperature of the layer increases more slowly. This allows the κ-mechanism to occur and drive very periodic radial modes. These well-defined stable period and amplitude of pulsations allow these stars to be cosmic standard candles.

Tidal Interaction

In cases where stars exist in a binary system (two-star system) or in a planetary system with a large planet, the two bodies will impose tidal forces on each other. The general idea behind tidally generated IGWs is that a stellar companion creates a perturbation at the convective-radiative boundary layer, which causes the generation of IGWs propagating away from the perturbation. Note that this can occur both for stars with convective envelopes and stars with radiative envelopes. It was found that the IGWs generated through tidal interactions tend to have frequencies equal to the forcing frequency and small wavenumbers/large scale. One of the first discussions on tidal forcing was done in Zahn (1975), which noted that in a close binary system, there are two important observable results due to the radiative dissipation of these waves: first, both stars experience a torque that can accelerate spin-orbit synchronisation and second, the brightness variation from both stars will be different than expected. More recently, Su *et al.* (2020) performed 2D simulations of tidally-generated IGWs and showed that the breaking of these waves at stellar surfaces can lead to the formation of critical layers[7] in early-type[8] stars and white dwarfs.

Turbulent Convection

Convection is a heat transfer process that involves movement of fluid through a thermal or compositional gradient. In stellar interiors (and quite often, planetary interiors), convection is mostly thermal where the superadiabatic temperature profile allows transport of heat within the convection zone. Additionally, the convection is also turbulent[9], characterised by the low viscosities and large length-scales of the fluid in the convection zone. Taking this into consideration, one of the first studies done on IGW generation from turbulent convection is Press (1981), who studied the nonlinearity of gravity waves

[7] A critical layer is where the mean horizontal flow velocity is equal to the IGW horizontal phase velocity.

[8] Defined as hot, luminous stars of spectral type O, B, A, and F0 to F5.

[9] Turbulence (in the context of convection) is defined by a sufficiently high dimensionless quantity called the Rayleigh number, or Ra, which describes the relative magnitude of thermal driving to dissipative forces in the fluid motion. In such systems, the higher the Ra, the more chaotic the convective fluid motion becomes.

generated through large-scale eddies in the stellar convection zone of a solar-like star[10]. Indeed, this work focused more on the properties of the waves themselves, rather than the generation process but it was one of the first studies on internal gravity waves in stars. Garcia Lopez & Spruit (1991) extended this work to study the mixing induced by IGWs to explain lithium depletion in F-type stars. Both studies derive an expression for the generated IGW flux by starting with an assumption: the size, λ and velocity, v_e of the convective eddies are connected through the Kolmogorov's spectrum for turbulence,

$$\lambda \propto v_e^3. \tag{1.19}$$

These eddies deform the interface to generate IGWs with a convective timescale of

$$\omega_e = \frac{\pi v_e}{\lambda} \sim \lambda^{-2/3}, \tag{1.20}$$

where ω_e is the convective turnover frequency. Continuity of pressure and density fluctuations across the interface means that the amplitudes of the wave $u(\lambda) = v_e(\lambda)$. However, through incoherent eddy superposition, waves of larger wavelengths are expected to be produced as well. Taking this into account, the expression for wave amplitudes becomes

$$u(\omega, \lambda_h) = \left(\frac{\lambda}{\lambda_h}\right) \frac{\omega\lambda}{\pi} \tag{1.21}$$

where λ_h is the horizontal wavelength of an IGW. The factor λ/λ_h arises from considering that statistically, the amplitude of an IGW at one wavelength will be set by the square root of the number of eddies, n_e, at the interface:

$$u(\omega, \lambda_h) = \frac{1}{n_e^{1/2}} v_e. \tag{1.22}$$

This equation states that the IGW amplitude at one wavelength is determined by the contribution of realistic, incoherent eddies that are out of phase (Garcia Lopez & Spruit, 1991). In the case where all the eddies are exactly in phase, we expect $u = v_e$. The quantity, n_e, can be estimated by taking the product of the IGW wavelengths, λ_x (x-direction) and λ_y (y- direction) and dividing it by the eddy size, λ:

$$n_e = \frac{\lambda_x \lambda_y}{\lambda^2}, \tag{1.23}$$

and $\lambda_x = \lambda_y = \lambda_h$ minimises n_e for a fixed horizontal wavenumber, $k_h^2 = k_x^2 + k_y^2$. Contributions from $k_x \neq k_y$ are ignored as they are weaker. From the work done in Lighthill

[10]Stars with radiative cores and convective envelopes.

(1978) and Phillips (1980), the IGW generation flux was then expressed as

$$F(\omega, \lambda_h) = \frac{\rho}{2\pi^3} \frac{\left(N^2 - \omega^2\right)^{1/2}}{N^2} \frac{\lambda^4 \omega^4}{\lambda_h} \tag{1.24}$$

where $\lambda_h > \lambda$. This expression is one of the first to provide a relation between generated wave flux and IGW properties (i.e. IGW wavelength and frequency) through the study of convective eddies in stars.

Later on, Kumar *et al.* (1999) showed that in the Sun, the energy flux per unit frequency in waves at generation can be calculated using the following expression:

$$F = \frac{\omega^2}{4\pi} \int dr \frac{\rho^2}{r^2} \left[\left(\frac{\partial \xi_r}{\partial r} \right)^2 + \ell(\ell+1) \left(\frac{\partial \xi_h}{\partial r} \right)^2 \right] \exp\left[\frac{-\ell(\ell+1) h_\omega^2}{2r^2} \right] \frac{v^3 L^4}{1 + (\omega \tau_L)^{15/2}}, \tag{1.25}$$

where r is the radial coordinate, ρ is density as a function of r, ξ_r is the IGW radial displacement, ℓ is the spherical harmonic mode, v is the convective velocity, L is the radial size of a turbulent eddy, τ_L is the characteristic convective time and h_ω is the radial size of the largest eddy at r with characteristic frequency of ω or greater. By considering the continuity of the radial velocity at the interface of the radiation zone and the convection zone, an expression for the normalised radial displacement, ξ_r, can be obtained. When this expression is substituted into Eq. (1.25), L is approximated with pressure scale heights[11] and ρv^3 is approximated with $F_\odot$, Kumar *et al.* (1999) obtains the following expression:

$$F \sim \frac{F_\odot k_h^3 H_c^5 \exp\left[-\left(H_c (N_c/\omega)^{3/(n+3)} \right)^2 k_h^2 \right]}{r_c^2 N_t} \left(\frac{\omega}{N_c} \right)^{-15/(n+3)} \tag{1.26}$$

where n is the polytropic index, H_c is the pressure scale height at the bottom of the convection zone, r_c is the radius at the bottom of the convection zone and, N_c and N_t are the Brunt–Väisälä frequencies at the bottom of the convection zone and the top of the radiation zone. Note that at the transition region between the convection zone and the radiation zone, the Brunt–Väisälä frequency is expected to go to zero. Thus, we expect $N_c = N_t = 0$. However, the transition region is one where convective overshooting occurs, which results in IGWs forming at different places within this region. This leads to the general assumption that $N_c = N_t$, which are both the highest frequency of IGW in the system, usually limited by observational results or the resolution of simulations. A more recent work, Lecoanet & Quataert (2013), revisited the work done in Kumar *et al.* (1999) and calculated the IGW eigenfunctions analytically at generation in a local, Boussinesq[12] and Cartesian domain. The similarity to Kumar *et al.* (1999) relates to the assumption that

[11] The length-scale at which pressure decreases by e^{-1}.

[12] An approximation where density variation with height is ignored in all parts of the fluid hydrodynamical equations except when multiplying with the gravity term.

IGWs are excited by Reynolds' stress, associated with convective eddies in a Kolmogorov turbulent cascade.

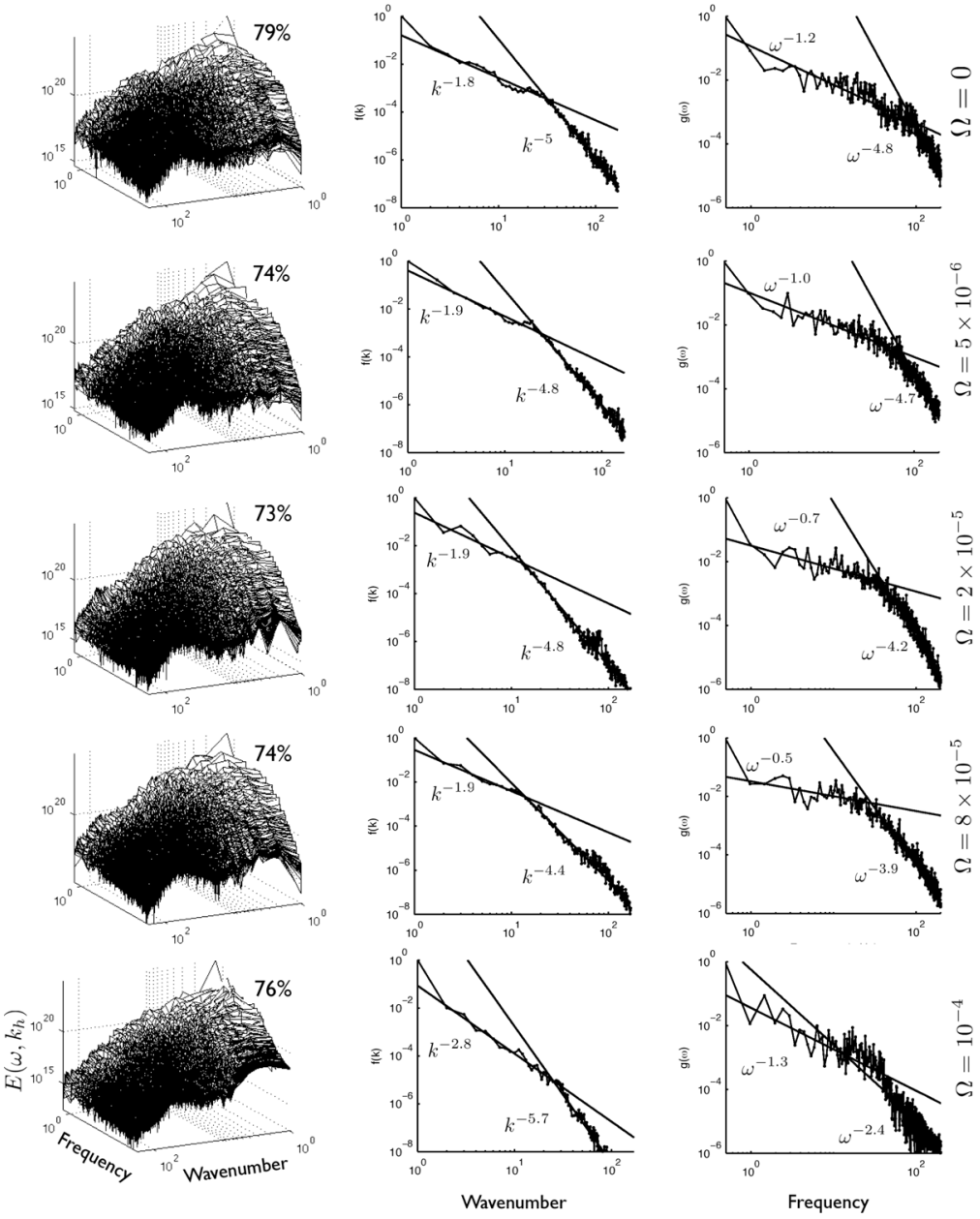

Figure 1.12: The left column shows wave energy as a function of frequency and horizontal wavenumber at half the the pressure scale height, H_p outside the convection zone from Rogers *et al.* (2013). The middle column shows normalized fits in wavenumber while the right column shows normalized fits in frequency to the singular value decomposition of wave energy.

Like the work in Press (1981); Garcia Lopez & Spruit (1991), the works in Kumar *et al.* (1999) and Lecoanet & Quataert (2013) provide a crucial piece of information for IGW

generation study: the IGW generation amplitudes as functions of wave frequency and horizontal wavenumber. Although they are all similar in terms of the use of Kolmogorov's turbulence spectrum to derive convective eddy timescales, they have critical differences. The most important difference is the work in Press (1981) and Garcia Lopez & Spruit (1991) derive convective-radiative interface IGW generation while Kumar *et al.* (1999) and Lecoanet & Quataert (2013) derive IGW generation through bulk forcing. In particular, bulk forcing means that waves are generated inside the convection zone from the interaction between the fluctuating fluid velocities and move through an evanescent region until they reach the radiation zone where they show oscillatory behaviour again.

We have looked at different theoretical work that predicted the IGW generation flux in stars from convective eddies. However, eddies are not the only type of structures found in a turbulent convection zone. It is well-known from experiments (Ansong & Sutherland, 2010) and simulations(Rogers *et al.*, 2013; Edelmann *et al.*, 2019) that overshooting convective plumes (Rieutord & Zahn, 1995) are present and possibly dominant in generating IGWs. In terms of theoretical work, this was first studied by Townsend (1966) in a terrestrial context. Montalbán & Schatzman (2000) used a plume model developed by Rieutord & Zahn (1995) to derive the IGW spectrum generated at the bottom of the convection zone of a solar-type star. Later, Pinçon *et al.* (2016) developed a semi-analytical model for the same situation to be used in 1D stellar evolution codes. A common result of all these models is an exponential frequency spectrum, proportional to $\exp\left(-\omega^2 t_{\mathrm{b}}^2\right)$ with a characteristic plume incursion timescale t_{b} and ω being the generated wave frequency. Wavenumber dependence is similarly exponential. Then, the total spectrum results from a combination of plumes of different sizes and timescales.

In Rogers *et al.* (2013), the first prediction on the convection-induced IGW generation spectrum based on numerical simulations of stellar interior was done. Unlike the theoretical spectra discussed previously, this work focused specifically on stars with convective cores and radiative envelopes. As mentioned before, these stars have masses above 1.5 $\mathrm{M}_{\odot}$, and for this particular work, the focus was on a 3 $\mathrm{M}_{\odot}$ star. The simulations were done using an infinite cylinder geometry, corresponding to an equatorial slice through the star. Variations along the z-axis were set to 0, effectively limiting the number of dimensions to two. The most relevant results from Rogers *et al.* (2013) are shown in Fig. 1.12, which shows the frequency and wavenumber generation spectra for 3 $\mathrm{M}_{\odot}$ models with different stellar rotations[13]. One thing to note here is that this work assumes that the energy from waves, $E(\omega, k_h)$, can be represented by a separable function, $f(k_h)$ and $g(\omega)$. Another important note here is this work simulated IGW generation through both plumes and eddies and favours IGW generation through convective plume penetration while not completely discrediting the theoretical work done previously which assumes IGW generation through

[13]Solid body rotation.

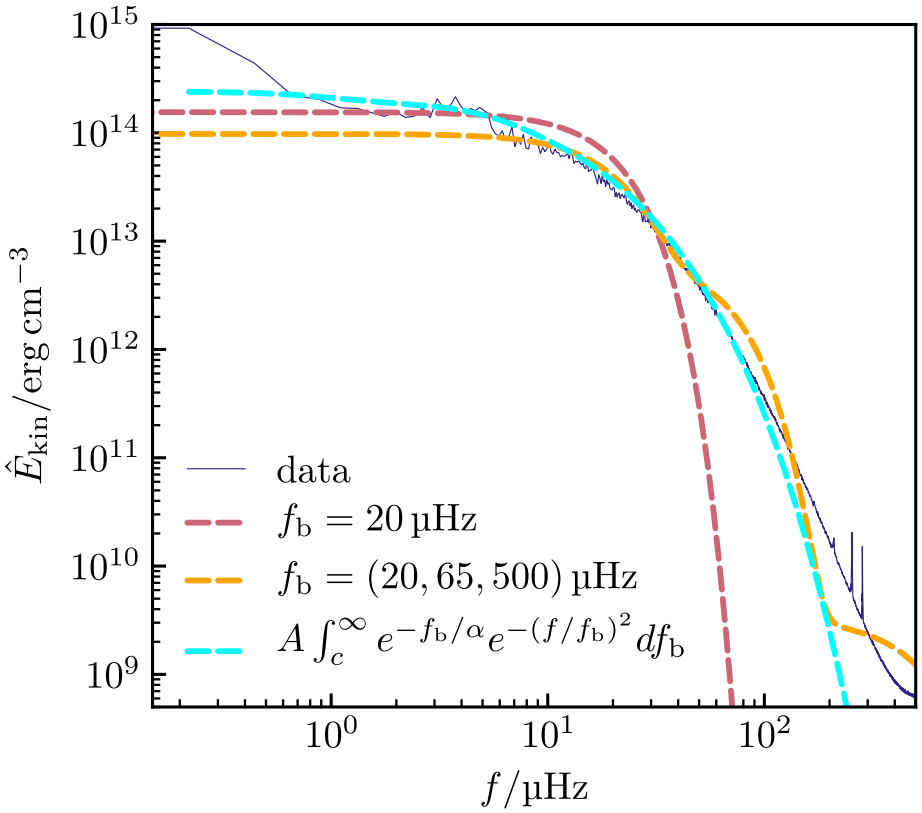

Figure 1.13: Kinetic energy spectrum on top of the convection zone for 3 $M_\odot$ model from Edelmann *et al.* (2019). The dashed lines show the theoretical spectrum for plume excitation from Pinçon *et al.* (2016). The red line is the case of a single plume frequency, f_b . The orange line is a combination of three different frequencies. The cyan line is using a plume frequency distribution following the equation shown in the legend.

Reynolds' stresses. The work done in Edelmann *et al.* (2019), further supports this with 3D simulations of a 3 $M_\odot$ star. One extra step in the work done in Edelmann *et al.* (2019) is to compare the frequency spectra from 3D simulations with the theoretical work done in Pinçon *et al.* (2016). Figure 1.13 shows the data from the 3D simulations in Edelmann *et al.* (2019) compared with the theoretical spectrum from Pinçon *et al.* (2016).

1.3.2 IGW Propagation

IGWs with frequencies less than the Brunt–Väisälä frequency propagate in stably stratified regions. As they propagate, they can experience several effects: internal reflection, thermal diffusion, critical layer encounter and/or other non-linear processes. One of the basic properties of any wave is reflection. IGWs undergo this process when they encounter a hard boundary, which in the case of stars, occurs when the Brunt–Väisälä frequency is equal to the wave frequency. As a result, some percentage of the waves approaching the

boundary is reflected while some percentage is transmitted across the boundary into an evanescent region where the wave-like behaviour is lost. As an example, in massive stars (stars with convective cores and radiative envelopes), IGWs generated at the convective-radiative interface travels until it encounters a surface convection zone. Close to the radiative-convective interface, the Brunt–Väisälä frequency goes to 0 and the waves are internally reflected setting up stationary modes (Alvan *et al.*, 2015), also known as g-modes. Another example of internal reflection occurs in older massive stars, which have a spike in their Brunt–Väisälä profiles (see Fig. 2.10 in Section 2.5.5), spanning a length of less than 10% of the size of the radiation zone. This spike is located close to the bottom of the radiation zone and forms due to a compositional gradient left behind by a shrinking core. Waves with frequencies between the peak of the spike and the average Brunt–Väisälä frequency in the radiation zone are internally reflected within this spike and form trapped modes.

As IGWs propagate through the radiation zone, they are subject to radiative and thermal diffusion. One of the earliest works done to investigate this process in stars is Press (1981), which shows that the wave's amplitude changes proportional to

$$u_v \propto r^{-3/2}\rho^{-1/2}\left(\frac{N^2}{\omega^2}-1\right)^{-1/4} e^{-\tau} \tag{1.27}$$

where the damping opacity, $\tau \propto \omega^{-4}k_h^3$. This proportionality implies that the IGW vertical amplitude, which is $\xi_v = u_v/\omega$, can increase with the decreasing density, decrease with increasing stellar radius or decrease with increasing damping opacity from the stellar core to the stellar radius. The Brunt–Väisälä frequency varies significantly throughout the radiation zone ($\sim$ 4–5 times), it still plays a smaller role in changing the wave amplitude than the density and damping opacity. From this linear analysis, we can see that the combination of all these effects determines which waves reach the stellar surface with sufficient amplitudes to be detected by observers (Ratnasingam *et al.*, 2019). Besides linear radiative damping, waves are expected to undergo linear viscous damping. However, this mechanism is often ignored as radiative damping is a much more dominant process in stars. This is due to the Prandtl number, Pr, which is the ratio of kinematic viscosity to the thermal diffusivity, being much less than 1 in stars. In fact, the work done in Garaud *et al.* (2015) shows that the Prandtl number is less than 10^{-4} in the stellar interiors of stars of masses up to 30 $M_\odot$.

IGWs generated at the convective-radiative boundary can transfer angular momentum throughout the radiation zone and are anti-diffusive, which means that the deposition of angular momentum throughout different parts of the radiation zone drives shear flow. Based on the work done in Zahn *et al.* (1997), the transport of angular momentum by

waves can be written as

$$\rho\frac{\partial}{\partial t}\left(r^2\overline{\Omega}\right) = -\frac{1}{r^2}\frac{\partial}{\partial r}\left(r^2\rho r\overline{\sin\theta v_r v_\theta}\right) + \frac{1}{r^2}\frac{\partial}{\partial r}\left(\rho\nu r^4\frac{\partial\overline{\Omega}}{\partial r}\right) \tag{1.28}$$

by taking the horizontal average of the azimuthal component of the momentum equation, where the overline denotes horizontal averages with $\overline{\Omega} = \int_0^\pi \Omega\sin^3\theta d\theta / \int_0^\pi \sin^3\theta d\theta$. The kinematic viscosity is represented by ν. This equation shows that mean zonal flow (the term on the left) is modified by the divergence of the horizontally-averaged Reynolds stress (first term on the right), which can also be expressed with wave flux, and damped by viscous dissipation (second term on the right). Using this expression and some further approximations, Alvan *et al.* (2013) studied the interaction between gravity waves and critical layers, where the wave frequency becomes equal to the rotating flow frequency, and found that waves are over-damped in these layers on top of radiative and viscous damping. Other studies such as Winters & D'Asaro (1989, 1994) have shown that some wave energy is transmitted through the critical layer and some are reflected, but approximately one-third of the wave energy causes the acceleration of the background mean flow.

IGWs also undergo strong non-linear interactions when their amplitudes exceed a certain threshold. An example of strong non-linear interaction is wave breaking, which causes the energy in waves to be converted to turbulent kinetic energy. In solar-type stars with convective envelopes and radiative cores,Barker & Ogilvie (2010) showed that inward-travelling IGWs from the surface convection zone grow in amplitude due to smaller stellar radius (Eq. (1.27)) and can break close to the stellar core, when the non-linearity parameter exceeds the value of 1. Rogers *et al.* (2012), on the other hand, showed that the IGWs generated at the top of the convection zones of massive stars can grow in amplitude as they propagate towards the stellar surface due to decreasing stellar density and break. This can result in angular momentum deposition on the stellar surface.

1.4 Observational Results

We have made much progress in theoretical and numerical investigations of stellar interiors based on early observations of the Sun alone. With the recent launch of NASA's Parker Solar Probe, we are about to study our closest star in very high detail. This mission focuses on investigating the solar corona, the outermost layer of the Sun with a temperature of a few million degrees Kelvin. Located below the corona is the photosphere, the visible surface of the Sun. So far, direct observational data (photometric and spectroscopic) on the inner workings of the Sun has been limited to this region, so the question to ask here is what is going on below this layer in the Sun or even, any star?

The study of stellar or planetary interiors through observations of surface variations

only is known as seismology. The study of stellar interiors, other than the Sun[14], through the interpretation of observed non-radial oscillation modes is known as asteroseismology (Aerts *et al.*, 2010). Non-radial oscillation modes here refer to horizontal fluid waves that set up stationary modes, in the form of pressure waves (p-modes) or gravity waves (g-modes). Gravity modes allow the probing of radiative regions while pressure modes probe the outer envelope of stars.

The study of g-modes in high-mass stars came along much later than the study of p-modes, mainly due to one factor: The low frequencies of gravity waves means that the observing time required to collect data for one wave period is longer compared to that of pressure waves. Generally, pressure waves have higher frequencies and possess a lower frequency limit known as the Lamb frequency, S_ℓ:

$$S_\ell^2 = \frac{\ell(\ell+1)c_s^2}{r^2}, \tag{1.29}$$

where c_s is the speed of sound in the stellar interior. On the other hand, gravity waves have lower frequencies and possess an upper frequency limit, the Brunt–Väisälä frequency. Note that the generally p-modes do not always have frequencies higher than g-modes. There can be overlaps between g-modes and p-modes frequencies and when this occurs, the modes are called mixed modes.

It was not until the COnvection ROtation and planetary Transits (CoRoT) mission when the first detection of g-modes in main-sequence stars came along through the work in Degroote, P. *et al.* (2010). Long, uninterrupted and high-precision photometric data allowed the study of period spacing[15] and the identification of g-modes in O- and B-type stars. Later missions such as Kepler, modified Kepler (K2), BRIght-star Target Explorer (BRITE) and Transiting Exoplanet Survey Satellite (TESS) kept providing more photometric data, mainly from O- and B-type stars due to these stars being brighter and thus providing better observational data of surface brightness variations. However, there was a setback. These observations were limited to the study of single modes such as g-modes forming due to the κ-mechanism and tidal interactions, which produces waves with one specific frequency and wavenumber. Thus, when it comes to detection of IGWs, which involves investigating a stochastically generated spectrum of waves, additional methods, such as the use of ground-based spectroscopy data to complement the photometric data from missions, have to be deployed (see Chapter 6, Aerts *et al.* (2010)).

Aerts & Rogers (2015) is the first study to compare the numerical simulation results of the surface variations caused by stochastically-generated IGWs by core convection to data from asteroseismology. Figure 1.14 shows the comparison done between the spectra

[14]The seismological study of the Sun is known as helioseismology

[15]The difference between the periods of modes of the same degree and consecutive radial orders.

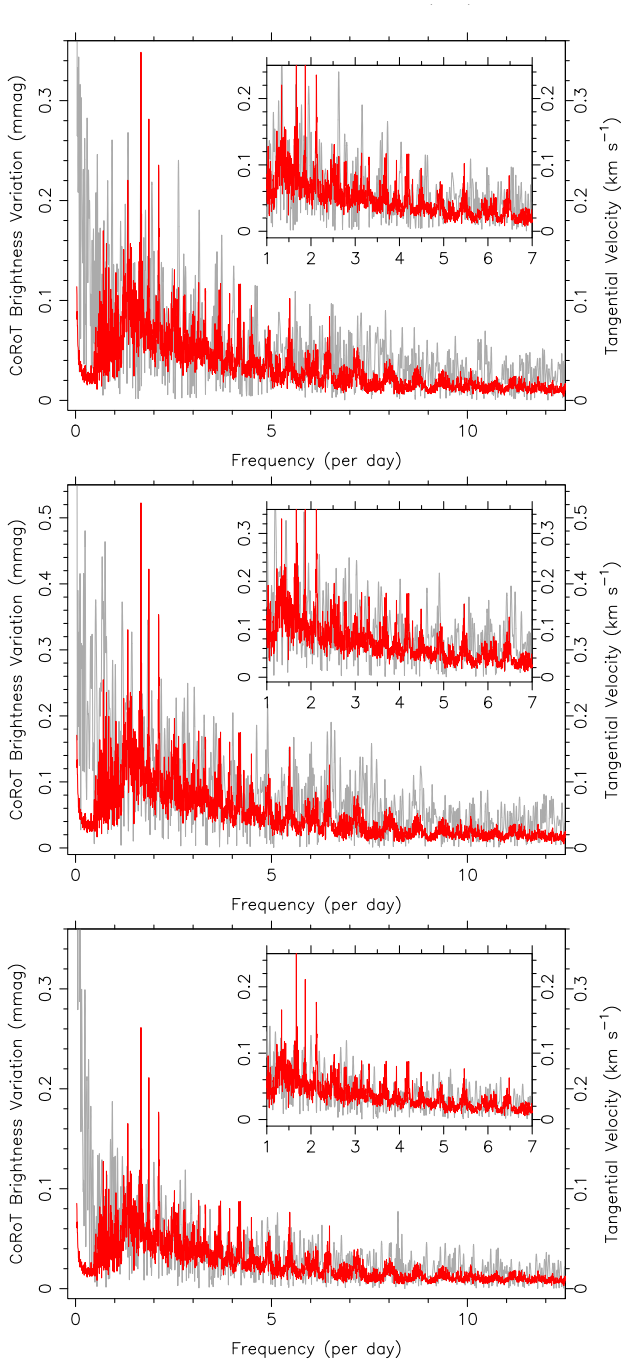

Figure 1.14: Measured amplitude spectra (gray) over-plotted with the predictions of IGWs for case D11 (red) for HD 46150 (top), HD 46223 (middle), and HD46966 (bottom) from Aerts & Rogers (2015). The ratios between brightness and tangential velocity variations used are 2, 3, and 1.5, from top to bottom.

of tangential velocities from numerical simulations (red lines) and brightness variation of three different stars observed (from the top panel to bottom: HD 46150, HD 46223,

and HD 46966) through the CoRoT space mission. All three models are those of mid-O-type stars, which are not expected to show period spacings of g-modes from the kappa mechanism. This work was done with the assumption that the numerical stellar surface tangential velocity spectrum could be converted to brightness variations through a simple multiplication factor. The work done in Shiode *et al.* (2013) provided an exhaustive table of values for this conversion factor. The remarkable matching between the observed spectrum and numerical spectrum paved the way to more intense studies of stars to determine if this variability is indeed due to IGWs.

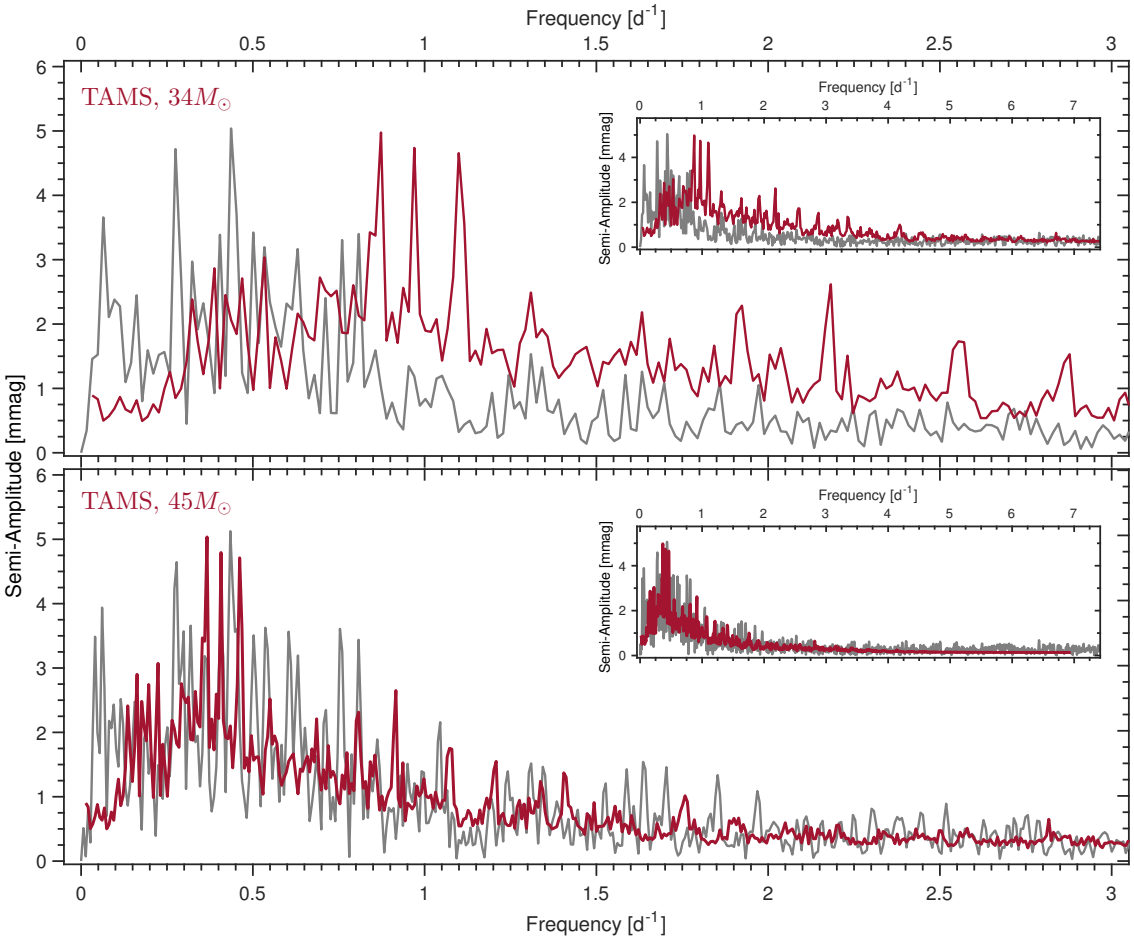

Figure 1.15: The observed amplitude spectrum of the light curve of V973 Sco (gray) compared to the amplitude spectrum from a two-dimensional annulus simulation from Ramiaramanantsoa *et al.* (2018). The simulations is that of a 3 $M_\odot$ star with a convective core and radiative envelope, scaled in frequency using the work done in Shiode *et al.* (2013) to account for the status of V973 Sco as a supergiant and two possibilities for its current mass ($\sim$ 34 $M_\odot$ according to Martins *et al.* (2005); $\sim$ 35 – 45 $M_\odot$ according to Crowther & Evans (2009)). The observed amplitude spectra had to be re-calculated with a higher resolution for the bottom plot to provide a fair comparison.

Another work that compared surface brightness spectra from numerical simulations

and observations is Ramiaramanantsoa *et al.* (2018). This work investigates the BRITE nanosatellite observations of Blue Supergiants (BSGs), up to 45 $M_{\odot}$, and using the respective conversion factors given in Shiode *et al.* (2013), found a good matching with the numerical surface velocity spectrum given in Rogers *et al.* (2013). Figure. 1.15 shows the comparison done between the brightness variation from BSG (V973 Sco) and the simulation results from Rogers *et al.* (2013) and it was found that the 45 $M_{\odot}$, TAMS model showed a better matching. Finally, more recently, the work done in Bowman *et al.* (2019, 2020) shows that using more than 50 observed stellar (mainly O- and B-type stars) data from the K2 and TESS space missions, combined with high-resolution ground-based spectroscopy, the tangential velocity frequency slopes were found to match those from numerical simulations in Rogers *et al.* (2013), Edelmann *et al.* (2019) and Horst *et al.* (2020). The work done in Bowman *et al.* (2019, 2020) has been crucial to my work and will be addressed in more detail in Chapter 3.

With such promising data provided by asteroseismology, a few crucial weakness of directly comparing numerical simulation results and observational data have to be addressed. First, most observational data are of O- and B-type stars, which are massive and sometimes, more evolved. The equation of state for the interior of massive stars tend to be more complex (as opposed less massive stars which can be approximated by the simpler ideal gas equation). Second, these high-mass stars will most certainly have surface convection zones. The effect of a surface convection zone on the stellar surface spectrum is not well-known, which unfortunately further reduces the comparability of data. Third, the chemical composition, size and rotational speed of these stars are realistically expected to be different from the models used in hydrodynamical simulations. Thus, comparing numerical and observational data means that a high number of approximations are being made, which puts a constraint on either set of data. However, it is still worth investigating whether stars abide by the rules and regulations set by numerical simulations.

1.5 Summary

With the subject of IGWs in intermediate to massive stars being the centre of investigation by both observational and theoretical research groups, there is a large motivation to study them. My work at Newcastle University involved the investigation of IGWs in various ways such as studying them through analytical and numerical methods and investigating their properties in the linear and non-linear regimes. I present my work in this thesis, which is divided into four chapters: Introduction, Linear IGW Propagation, Non-linear IGW Propagation, Core Convection & Waves and Conclusion & Outlook. Chapter 2 will be based on the work done in Ratnasingam *et al.* (2019), where we will be presenting the changes in wave nonlinearity due to linear effects in the stellar radiation zone. Chapter 3

will be based on the work done in Ratnasingam *et al.* (2020), where we will be discussing the non-linear characteristics shown by IGWs such as weak interactions. Chapter 4 will be on a very recent project that studies the effect of stellar age and mass on core convection and thus, IGW generation. The final chapter will conclude this thesis and discuss future outlook.

Chapter 2

Linear Wave Propagation

Linear wave theory has been integrated into the curriculum in many university courses, especially in physics and mathematics-related courses. Studying the linearisation of a set of differential equations and using a wave ansatz to solve these equations is one of the standard procedures when one needs to solve problems analytically. An example of this method is solving the linearised vorticity equation with rotational terms using the wave ansatz, allows one to develop the dispersion relation for Rossby waves, also known as planetary waves. These waves are observed in the Earth's atmosphere and can lead to the formation of cold-air cyclones. Another example is the development of Alfven waves, which is a solution of the linearised Magneto-HydroDynamics (MHD) equations. The study of these waves is extensive, ranging from their effects in gas giant planets and stars to interstellar/intergalactic medium.

To study internal gravity waves (IGWs), we introduce two important approximations: the anelastic approximation and the Boussinesq approximation. The anelastic approximation filters out acoustic waves without assuming hydrostatic balance and the Boussinesq approximation is a subset of the anelastic approximation, which ignores all density variations in a fluid system except one that varies with gravity. These approximations allow the continuity equation to be written as

$$\nabla \cdot \overline{\rho}\vec{v} = 0, \tag{2.1}$$

in the anelastic approximation and

$$\nabla \cdot \vec{v} = 0, \tag{2.2}$$

in the Boussinesq approximation. The approximations have been crucial in studying linear (and non-linear) IGWs and have been investigated extensively in many systems, such as the Earth's oceans (Boussinesq-like system due to ocean density being approximated as a constant) and stellar interiors (where both the Boussinesq and anelastic approximations

have been applied). In this study, we investigate these linear waves in the stellar radiation zones of intermediate-mass stars with convective cores and radiative envelopes. More specifically, this chapter will be describing the work done on linear IGW propagation in the radiation zone. Note that the graphs, data and results presented in this chapter follow closely the work done in Ratnasingam *et al.* (2019).

2.1 IGW Generation Spectrum (in more detail)

In this section, we revisit the introduction to wave generation by turbulent convection described in Section 1.3.1. To start off, we look at the expression from Kumar *et al.* (1999), given in Eq. (1.25). This expression for generated wave flux was originally developed for pressure waves in Goldreich & Kumar (1990). Kumar *et al.* (1999) then extended this prescription to gravity waves. The original prescription treats wave generation by bulk convection due to three sources: changes in entropy at fixed pressure (monopole terms), buoyancy variations (dipole terms) and internal stresses (quadrupole terms). It was argued in Goldreich & Kumar (1990) that while the monopole and dipole terms generate more acoustic radiation, they very nearly cancel each other and therefore, the only term considered was the quadrupole term or the term due to internal Reynolds stresses. This assumption was carried forward in Kumar *et al.* (1999), yet it is unclear that this approximation is valid for IGW. Using flux equations calculated for p-modes from previous work (Goldreich & Kumar, 1990; Goldreich *et al.*, 1994), Kumar *et al.* (1999) assumed continuity of radial velocities across the convective-radiative interface and derived a flux equation for IGW generated by Reynolds stresses as shown in Eq. (1.25) in Chapter 1. Substituting $n = 1.5$ for the convection zone and $H_c = u_c/\omega_c$ (with the assumption that the largest convective eddies are of comparable sizes to the size of the convection zone) gives

$$F \sim u_c^3 \, \frac{\rho_c k_h^3}{r_c^2 N_c} \left(\frac{u_c}{\omega_c}\right)^5 \left(\frac{\omega}{\omega_c}\right)^{-10/3} \exp\left[-k_h^2 \left(\frac{u_c}{\omega_c}\right)^2 \left(\frac{\omega}{\omega_c}\right)^{-4/3}\right], \tag{2.3}$$

where u_c, ω_c, and ρ_c are the bulk convective velocity, convective turnover frequency and density at the convective-radiative boundary, respectively. The term, N_c is the Brunt–Väisälä frequency at the bottom of the radiation zone while r_c is the thickness of the convection zone. Note that exactly at the convective-radiative boundary, N_c is 0. However, for our case, we make an assumption that all waves are generated where the Brunt–Väisälä frequency is equal to the highest wave frequency that we test. One reason why this assumption is acceptable is that the effect of convective processes (i.e. overshoot) from the core does not end abruptly at $N = 0$, waves of a particular frequencies are expected to be generated at multiple radial points after the radius where $N = 0$. This makes our

assumption a conservative one. The horizontal wavenumber, k_h is defined as

$$k_h = \frac{\sqrt{\ell\ (\ell+1)}}{r}, \tag{2.4}$$

where ℓ is the spherical harmonic degree (we will be referring to ℓ as wavenumber in this chapter, unless stated otherwise). Note that in spherical harmonics, there is also the order, m, but that quantity cancels out in the derivation of the IGW dispersion relation (Press, 1981). Eq. (2.3) is converted into a wave displacement equation by equating it to a wave flux equation, $\rho_c \left(\omega \xi_h \sqrt{\ell(\ell+1)}\right)^2 v_g$ as given in Kumar *et al.* (1999), where v_g is the vertical IGW group velocity (see Eq. (2.12)), ξ_h is the horizontal wave displacement and we have assumed that $\xi_h \gg \xi_v$. Using $u_h = \xi_h \omega$ gives the following relation,

$$\begin{aligned} u_{h,K} \sim u_c \frac{k_h^2}{r_c \sqrt{\ell(\ell+1)}} \left(\frac{u_c}{\omega_c}\right)^3 \left(\frac{\omega}{\omega_c}\right)^{-13/6} \\ \exp\left[-\frac{k_h^2}{2}\left(\frac{u_c}{\omega_c}\right)^2 \left(\frac{\omega}{\omega_c}\right)^{-4/3}\right], \end{aligned} \tag{2.5}$$

where u_h is the horizontal fluid velocity and the subscript K refers to "Kumar". The work by Kumar *et al.* (1999) was revisited by Lecoanet & Quataert (2013), who also produced theoretical predictions for the IGW generation flux, but for three different Brunt–Väisälä frequency profiles at the convective-radiative transition, where they used either a discontinuous function, a smooth tanh function or a continuous piecewise linear function. All three profiles have various power laws on k_h and ω. We chose to work exclusively with the discontinuous case here, as this scenario is currently considered the most probable in stars (Lecoanet, private communication). Thus, we convert Eq. (50)[1] from Lecoanet & Quataert (2013), which expresses the vertical IGW generation displacement as a function of horizontal wavenumber and frequency to a horizontal velocity perturbation expression given as

$$u_{h,LD} \sim u_c \left(\frac{k_h u_c}{\omega_c}\right)^{5/2} \left(\frac{\omega}{\omega_c}\right)^{-17/4}, \tag{2.6}$$

where the subscript LD refers to "Lecoanet Discontinuous".

In addition to theoretical work, there has been significant numerical work done to investigate the transition between convective and radiative regions and convective overshoot (Hurlburt *et al.*, 1986; Brummell *et al.*, 2002) with a few having focused on IGW generation (Rogers & Glatzmaier, 2005; Brun *et al.*, 2011; Rogers *et al.*, 2013; Alvan *et al.*, 2014, 2015). For instance, Rogers *et al.* (2013) predicts that for a star with zero rotation, the energy

[1]The conversion from vertical displacement to horizontal displacement is done using the IGW amplitude relation given in Eq. (2.18), with the assumption that $N \gg \omega$, and the conversion to velocity perturbation is $u = \xi/\omega$. The pressure scale height, H, from Eq. (50) is expressed as u_c/ω_c.

Spectra	a	b
Flat[F]	0	0
Kumar *et al.* (1999)[K]	-2.17	1
Lecoanet & Quataert (2013)[LD]	-4.25	2.5
Rogers *et al.* (2013)[R]	-0.6	-0.9

Table 2.1: The table shows how a and b in Eq. (2.7), are defined for different works. The flat spectrum represents one with no dependence on ω or ℓ. The letters shown in square brackets will be used to represent its respective spectrum.

carried[2] by IGW scales as $E \propto \omega^{-1.2}\left(\sqrt{\ell(\ell+1)}\right)^{-1.8}$ in the low wave number ($\ell \lesssim 10$) and low frequency ($\omega \lesssim 10$ µrad s^{-1}) regime, just outside the convection zone. While it is possible that the negative exponent associated with the wavenumber dependence is due to the reduced dimensionality of those simulations, more recent three-dimensional simulations also show reduced efficiency for shorter wavelengths/larger wavenumbers (Edelmann *et al.* (2019), Alvan *et al.* (2014)). Furthermore, these simulations show a similar frequency dependence, so we take the 2D simulations to be representative. Taking the kinetic energy as $E \propto (\omega\xi_h)^2 \propto u_{h,R}^2$ where ξ is the fluid displacement amplitude and the subscript R refers to "Rogers", $u_{h,R}$ is found to be proportional to $\omega^{-0.6}\left(\sqrt{\ell(\ell+1)}\right)^{-0.9}$.

The IGW generation spectrum, which represents the collection of waves generated at the convective-radiative interface can be summarised as power laws in both wavenumber and frequency and described by:

$$u_0(\omega, \ell) \propto \omega^a \left(\sqrt{\ell(\ell+1)}\right)^b \tag{2.7}$$

where the values of a and b for different prescriptions are shown in Table 2.1. An additional IGW generation spectrum, the flat spectrum, has been introduced in Table 2.1, which represents a spectrum with no dependence on ℓ and ω. This spectrum will act as a test case and will be referred to as spectrum F from now on. This spectrum is likely to not be a physical generation spectrum and is not derived from any theoretical or numerical work. Also, the table does not show the extra dependencies of spectrum K on k_h and ω in the exponential term as shown in Eq. (2.5). However, we do consider the effect of this exponential term in our analysis.

2.2 Modules for Stellar Astrophysics (MESA)

Currently, several different 1D stellar evolution codes are being utilised by multiple research groups across the globe. For example, the Geneva code (GENEC) has been used

[2]Approximately 79% of the energy in IGWs were fit by a separable function, where E$(\omega, l) \propto$ g(ω)*f(ℓ).

to do studies on population synthesis (Georgy *et al.*, 2014) and it is widely used in the pre-supernovae/supernovae research community. There is also KEPLER Weaver *et al.* (2017), a general-purpose stellar evolution/explosion code that incorporates implicit hydrodynamics and a detailed treatment of nuclear burning processes. It has been used to study the complete evolution of massive and supermassive stars, all major classes of supernovae, hydrostatic and explosive nucleosynthesis, and x- and gamma-ray bursts on neutron stars and white dwarfs.

Another stellar evolution code, which is the one used for this project is the Modules for Stellar Astrophysics or MESA(Paxton *et al.*, 2011, 2013; Paxton *et al.*, 2015; Paxton *et al.*, 2018, 2019), which was developed by Bill Paxton and his team at the Kavli Institute of Theoretical Physics in Santa Barbara. This one-dimensional, Lagrangian stellar evolution code is open-source and is used widely in the stellar community. In my work, this code has been used to produce stellar parameter values (i.e. stellar density, temperature, gravity etc) which are required to study IGW generation and propagation. The input parameters for MESA are set using "inlists" (available publicly on zenodo) and in Section 2.4, I have stated the basic parameters set in MESA to produce the models I needed for this work.

2.3 Linear IGW propagation

IGWs undergo two main processes in the linear regime; amplitude damping due to radiative diffusion and amplification due to density stratification. In stellar radiation zones, radiative diffusion is an attenuation mechanism, where wave amplitudes are damped as they propagate vertically. The dissipation of energy and angular momentum from these waves leads to a non-zero divergence of the Reynolds stress, hence causing to an acceleration of the mean flow, which is a positive or negative average horizontal motion of fluid at any radius within stellar interiors. In other words, the horizontal fluid velocity at any radius can be described as

$$u_h(r) = \langle u'_h \rangle + u'_h \tag{2.8}$$

where $\langle u'_h \rangle$ is the mean flow and u'_h is the perturbation velocity, which can be related to IGW amplitudes in the radiation zone.

To quantitatively understand the effect of radiative damping on IGWs, we follow the work of Press (1981) and Kumar *et al.* (1999), where the radiative damping opacity, which is a function of IGW angular frequency, ω, spherical harmonic degree, ℓ, and radius, r, is defined as

$$\tau(\omega, \ell, r) = \int_{r_{\rm interface}}^{r} \frac{\gamma[\omega, \ell, r']}{|v_g[\omega, \ell, r']|} dr' \tag{2.9}$$

where γ is the damping rate, given by

$$\gamma(\omega, \ell, r) = K k_v^2 \tag{2.10}$$

and k_v, the vertical wavenumber, is defined as

$$k_v^2 = k_h^2 \frac{N^2 - \omega^2}{\omega^2}, \tag{2.11}$$

where N is the Brunt–Väisälä frequency. The expression for the vertical wavenumber is a different form from that given in Eq. (1.11), which has been rearranged as the IGW horizontal wavenumber and frequency are free parameters that we manipulate. Thus, it follows that the vertical group velocity, v_g is defined as

$$v_g(r) = \frac{\partial \omega}{\partial k_v} = -\frac{(N^2 - \omega^2)^{1/2} \omega^2}{k_h N^2}. \tag{2.12}$$

The thermal diffusivity, K, is given by

$$K(r) = \frac{16 \sigma T^3}{3 \rho^2 \kappa c_p}, \tag{2.13}$$

where σ is the Stefan-Boltzmann constant while T, ρ, κ and c_p are stellar temperature, density, opacity and specific heat capacity, respectively, which are all functions of stellar radius. The full expression of terms inside the integral of Eq. (2.9) then, becomes

$$\frac{\gamma}{v_g} = \frac{16 \sigma T^3}{3 \rho^2 \kappa c_p} \left(\frac{(\ell(\ell+1))^{3/2} N^3}{r^3 \omega^4} \right) \left(1 - \frac{\omega^2}{N^2} \right)^{1/2}. \tag{2.14}$$

The integral in Eq.(2.9) is done from $r_{\text{interface}}$, which the radius at which the convective-radiative interface is located, to a chosen radius, r. The interface location is chosen using the sign of Brunt–Väisälä frequency from MESA. In MESA, N is defined using the Ledoux criterion, which is given in Eq. (1.10). In the case of ideal gas, $\chi_T / \chi_\rho = 1$ in Eq. (1.10). Note that it is common to work in the asymptotic regime and assume $N \gg \omega$. However, we keep the $\sqrt{N^2/\omega^2 - 1}$ term in our propagation equation, mainly because, although the asymptotic assumption applies in most of the radiation zone, it fails to do so close to the convective-radiative boundaries as N approaches 0.

Using a locally Boussinesq, plane wave approximation with thermal diffusion and globally anelastic approximation with adiabatic perturbations (where the lengthscale is less than one IGW wavelength), the following differential equation can be derived from the

linearised continuity, momentum and energy equations (Press, 1981):

$$\frac{\partial^2 \Psi}{\partial r^2} + \left[\left(\frac{N^2}{\omega^2} - 1 \right) k_h^2 + \frac{iK}{\omega} \left(\frac{\partial^2}{\partial r^2} - k_h^2 \right)^2 \right] \Psi = 0 \tag{2.15}$$

where

$$\Psi = \rho^{1/2} k_h^{-2} u_v. \tag{2.16}$$

Without the last term in the square brackets, this differential equation in Cartesian coordinates is known as the Taylor, Goldstein and Synge equation (TGS). Solving Eq. (2.15) with a well-established tool in theoretical physics called Wentzel–Kramer–Brillouin or WKB approximation with the assumption of a potential that varies slowly with radius (terms in the square bracket of Eq. 2.15), the following proportionality can be derived:

$$\begin{aligned} u_v \propto k_h^{3/2} \rho_c^{-1/2} \left(\frac{N^2}{\omega^2} - 1 \right)^{-1/4} \exp \left[i \int k_v dr - i\omega t \right] \\ \exp \left[-\frac{1}{2} \int \left(\frac{K k_h^2}{N} \right) \left(\frac{N}{\omega} \right)^4 \left(\frac{N^2}{N^2 - \omega^2} \right)^{1/2} \right], \end{aligned} \tag{2.17}$$

which is the full version of Eq. (1.27). We can see that the last term, is the radiative damping term. In the Boussinesq approximation which applies locally, the divergence of the velocity perturbations is zero and the following relation is true:

$$k_v u_v = -k_h u_h \tag{2.18}$$

As a result, we can write the horizontal velocity component as

$$\begin{aligned} u_h \propto k_h^{3/2} \rho_c^{-1/2} \left(\frac{N^2}{\omega^2} - 1 \right)^{1/4} \exp \left[i \int k_v dr - i\omega t \right] \\ \exp \left[-\frac{1}{2} \int \left(\frac{K k_h^2}{N} \right) \left(\frac{N}{\omega} \right)^4 \left(\frac{N^2}{N^2 - \omega^2} \right)^{1/2} \right], \end{aligned} \tag{2.19}$$

Due to the relation in Eq.(2.18), the analysis in this work could be done with either the horizontal amplitude or the vertical amplitude. We choose to work with the horizontal amplitude. The main objective of this work was to study the evolution of IGW amplitudes with radius, which are generated at the convective-radiative boundary. So, the proportionality sign in Eq. (2.19) allows us to write the following equation:

$$u_h(\omega, \ell, r) = u_0(\omega, \ell) \left(\frac{r_0}{r} \right)^{3/2} \left(\frac{\rho_c}{\rho(r)} \right)^{1/2} \left(\frac{N^2 - \omega^2}{N_c^2 - \omega^2} \right)^{1/4} e^{-\tau/2}, \tag{2.20}$$

where u_0 is the velocity perturbation amplitude (which takes the magnitude of convective

velocities, u_c, into account) from different generation spectra and r_0 is the radius at which the waves are generated. From hereon, I will refer to the $(r_0/r)^{3/2}$ term as the geometric term (GEO) and the $(\rho_c/\rho(r))^{1/2}\left((N^2-\omega^2)/(N_c^2-\omega^2)\right)^{1/4}$ term as the density stratification term (DS). Note that the geometric term results from the spreading out of IGWs over the surface of a sphere.

Using stellar parameters and Brunt–Väisälä frequencies obtained directly from MESA, $\gamma(r)/v_g(r)$ was calculated and integrated using the cumulative trapezoidal method for different final radii. Thus, the IGW amplitudes at the stellar surface, defined in MESA using the photosphere tables option (see Jieun *et al.* (2016), Section 3.3 for details on boundary conditions), in the linear regime were calculated.

2.3.1 Nonlinearity Parameter

Phillips (1966), Press (1981) and Barker & Ogilvie (2010) have shown that the nonlinearity of waves can be represented by the ratio of wave displacement to wavelength in either horizontal or vertical directions. This leads to the definition of the nonlinearity parameter, ϵ, as follows:

$$\epsilon = \xi_h k_h = \frac{u_h}{\omega} k_h, \tag{2.21}$$

where we have replaced the horizontal displacement with horizontal perturbation velocity over frequency. An IGW is said to be non-linear, when its displacement becomes comparable to or larger than its wavelength, which is equivalent to the strong condition, $\epsilon \geqslant 1$. However, one also expects as ϵ approaches 1, non-linear effects can become important.

To consider only the horizontal components, we can first show that

$$\frac{k_h}{k_v} = \sqrt{\frac{\omega^2}{N^2-\omega^2}}, \tag{2.22}$$

from rearranging Eq. (2.11). By substituting this equation into Eq. (2.18) and using $u = \xi\omega$, the following relation is expected to be satisfied in the radiation zone:

$$k_h\xi_h \sim \left(\sqrt{\frac{\omega^2}{N^2-\omega^2}}\right) k_v \left(\sqrt{\frac{N^2-\omega^2}{\omega^2}}\right) \xi_v \sim k_v\xi_v, \tag{2.23}$$

which shows that considering wave nonlinearity in the horizontal and vertical directions leads to the same result.

2.4 Model Setup

Models of stars with masses, 3 $M_\odot$, 7 $M_\odot$ and 20 $M_\odot$ were constructed using the MESA stellar evolution code from ZAMS, when the core hydrogen mass fraction (X_c) is approx-

imately 0.7 to middle of main sequence (midMS), when $X_c \approx 0.35$, followed by terminal age main sequence (TAMS), when $X_c \approx 0.01$. Mass loss was implemented through the Van Loon stellar wind scheme (van Loon, J. Th. *et al.*, 2005; Renzo, M. *et al.*, 2017). Stellar metallicity, Z, was set to be equal to the solar value of $Z = 0.02$. The sign of the Brunt–Väisälä frequency was used to determine the extent of the radiation zone which means

$$N(r)^2 > 0 \tag{2.24}$$

refers to a radiation zone and

$$N(r)^2 < 0 \tag{2.25}$$

refers to a convection zone. However, to account for the fact that the IGW frequencies must be less than the Brunt–Väisälä frequency for linear calculations, the extent of the radiation zone was further limited to regions where the Brunt–Väisälä frequency exceeds 100 µrad s^{-1}, which was the highest IGW wave frequency we tested. It was found that in all our stellar models, the Brunt–Väisälä frequency increases rapidly from zero at the core convective-radiative interface and decreases rapidly back to zero at the surface (or sometimes, intermediate) radiative-convective interface, if one exists. Therefore, at both the top and bottom convective-radiative boundaries, the regions of the radiative zone cut out by imposing the above condition were small, being less than 0.5% of the star's total radius (see Table 2.2) and less than 0.43% of the star's radiation zone radial size.

As an example of data from models produced by MESA, Fig. 2.1 shows thermal diffusivities (see Eq. (2.13)) of 8 stellar models, within the boundary described above. The radial extent of the convection zone is indicated by the dots at the beginning of each line plot. The 20 $M_\odot$ TAMS model has not been included as it was found to develop an intermediate convection zone at $r/r_{star} = 0.11$, with the convective core extending from the centre up to $r/r_{star} = 0.055$. It can be seen that for any particular stellar mass, the convection zone shrinks as the star evolves while the radiation zone expands. This is an important factor in IGW propagation which will be addressed further in later sections.

Figure 2.2 is an example of how wave amplitudes are affected by density stratification, geometry and radiative diffusion for a 3 $M_\odot$ ZAMS star. The top panel shows how the amplitude for a $\omega = 10$ µrad s^{-1} wave changes due to density stratification and geometric effects alone within the radiation zone of the chosen stellar model. The middle panel shows the effect of radiative diffusion on IGWs of different frequencies with an initial wave amplitude of 1 and wavenumber of 1 whilst the bottom panel shows how IGW amplitudes changes due to all three effects. In Fig. 2.2a, DS and GEO (see Eq. (2.20)) are coupled together because they do not depend significantly on ω as the Brunt–Väisälä frequency in DS varies very little across the radiation zone (see Fig. 2.10). Across the radiation zone, density decreases by almost eight orders of magnitude while radius increases

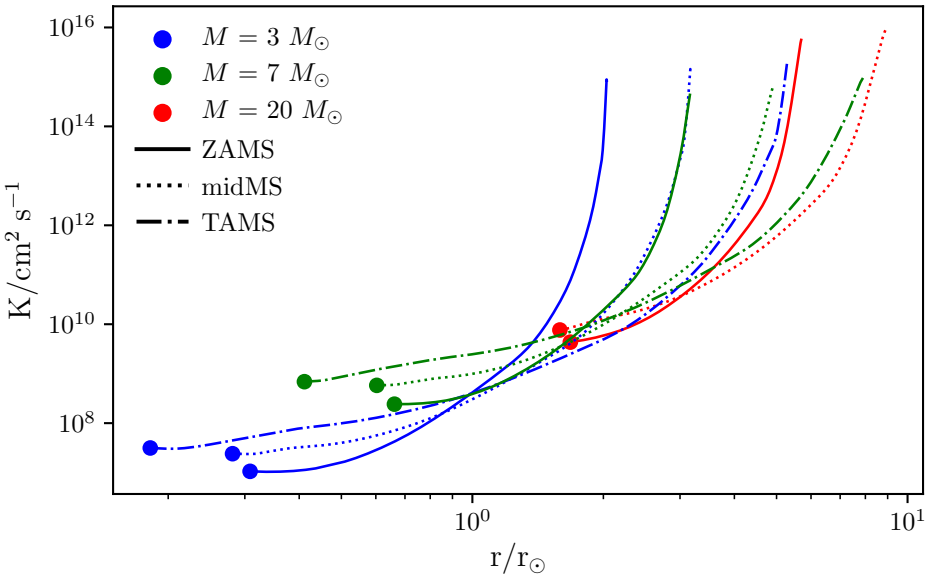

(a) Thermal diffusivity as a function of radius, in units of solar radius.

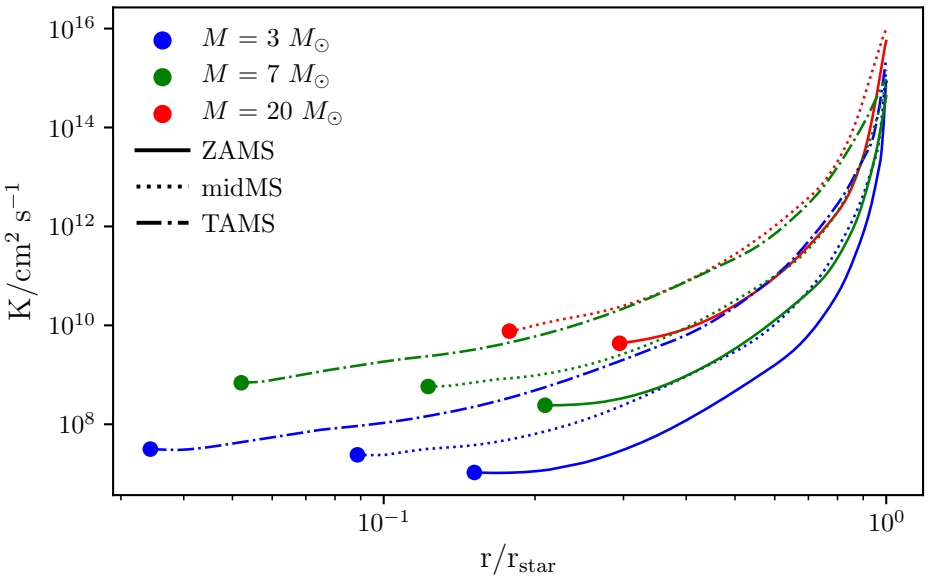

(b) Thermal diffusivity as a function of radius, in units of stellar radius.

Figure 2.1: Thermal diffusivity as a function of radius, in units of (a) solar radius and (b) stellar radius, for different stellar masses generated using MESA. The value, M in the legend represents the mass of the stellar models used in solar mass units, $M_\odot$. The circular markers at the beginning of each plot indicate the locations of the convective-radiative interface. The large variation in magnitude seen in the thermal diffusivity profiles is mainly due to the large variation in density profiles of stars.

Stellar Mass	Stellar Age	Inner Cut-out	Outer Cut-out
3	ZAMS	0.048	0.0
	midMS	0.020	0.001
	TAMS	0.0	0.016
7	ZAMS	0.103	0.007
	midMS	0.059	0.031
	TAMS	0.011	0.311
20	ZAMS	0.394	0.004
	midMS	0.117	0.035

Table 2.2: The table shows percentages of the radiative zone (in terms of the total stellar radius) that were cut out close to the inner convective zone (Inner Cut-out) and close to the surface convection zone (Outer Cut-out) for the different stellar models we used.

by approximately one order of magnitude. This generally leads to the growth of wave amplitudes as the density stratification term dominates over the geometric term. The trend also shows a sharp increase close to the convective core and a sharp decrease close to the surface convection zone caused by the Brunt–Väisälä frequency changing rapidly (by more than three orders of the magnitude). In Fig. 2.2(b), waves of higher frequencies are damped less than waves of lower frequencies due to the damping opacity being proportional to ω^{-4} (see Eq. (2.14)). Physically, this can be understood by comparing timescales. When the period of a wave is much smaller than the damping timescale (i.e. high-frequency waves), the waves effectively do not "see" the effect of damping. As the wave frequency decreases, the wave period increases causing this value to approach the damping timescale. This means that lower frequency waves are attenuated more. In stellar interiors, IGWs are affected by radiative damping, density stratification and geometry simultaneously, which is shown in Fig. 2.2(c). Waves that do not succumb to damping rapidly (i.e. higher frequency waves) undergo an increase in amplitude due to density stratification as they propagate through the radiation zone of a star towards the surface. Close to the surface convection zone, both increasing thermal diffusivity and rapidly decreasing Brunt–Väisälä frequency cause IGW amplitudes to decrease rapidly as seen for the case when $\omega = 5.0$ µrad s^{-1} (red line). As the Brunt–Väisälä frequency decreases towards the surface, more waves are likely to be internally reflected at radii where their frequencies are equal to the Brunt–Väisälä frequency and possibly set up standing modes. Our analysis does not consider this scenario. Instead, the main aim of this work has been to study the range of frequencies and wavenumbers at which these waves become non-linear.

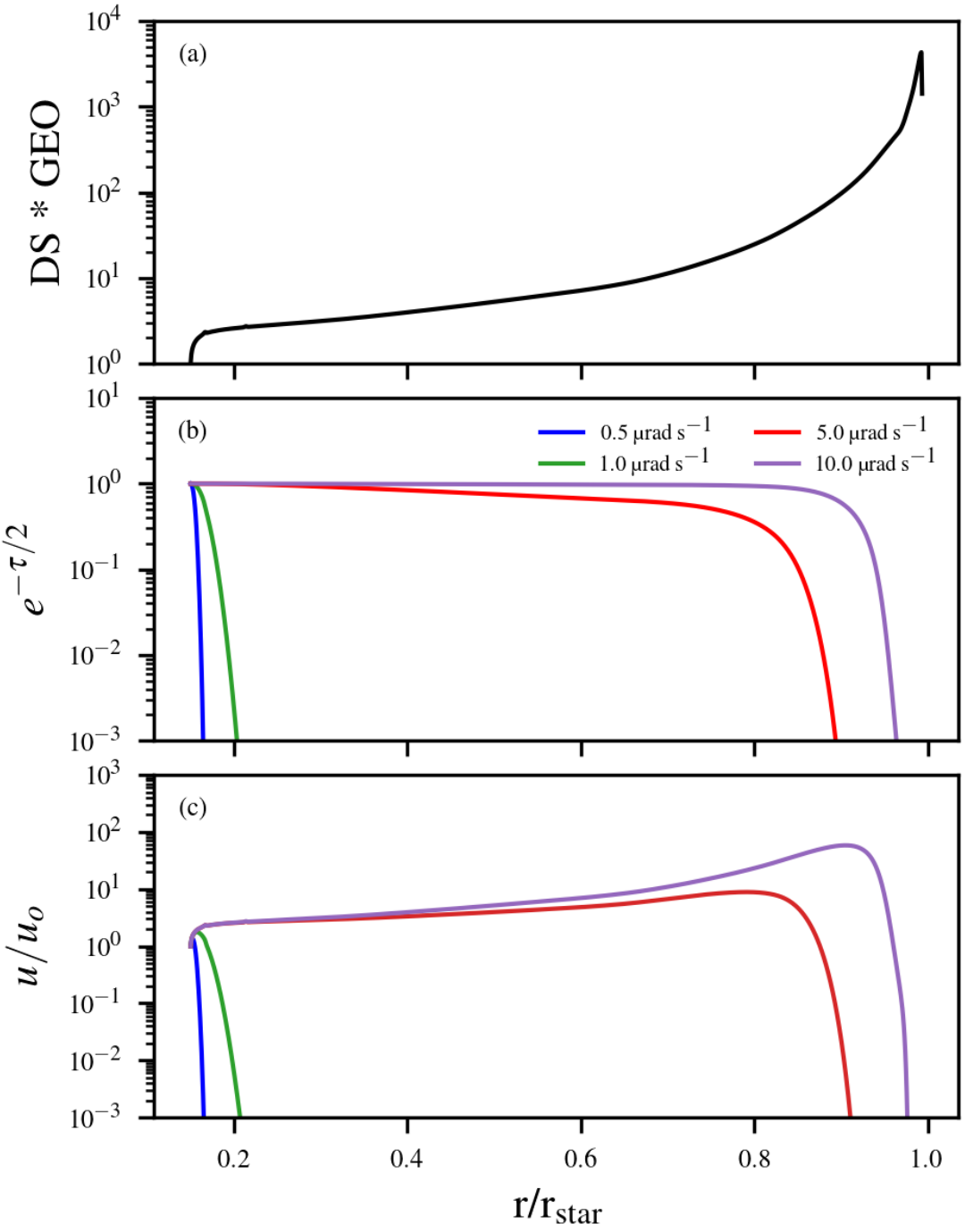

Figure 2.2: (a) The density stratification term (DS) $\omega = 10$ μrad s^{-1} , and the geometric term (GEO), (b) radiative damping and the (c) normalised amplitude profiles as functions of radii, in units of total stellar radius. The different coloured lines in the middle and bottom plots represent different IGW frequencies as given in the legend. The wavenumber, ℓ, is set to 1.

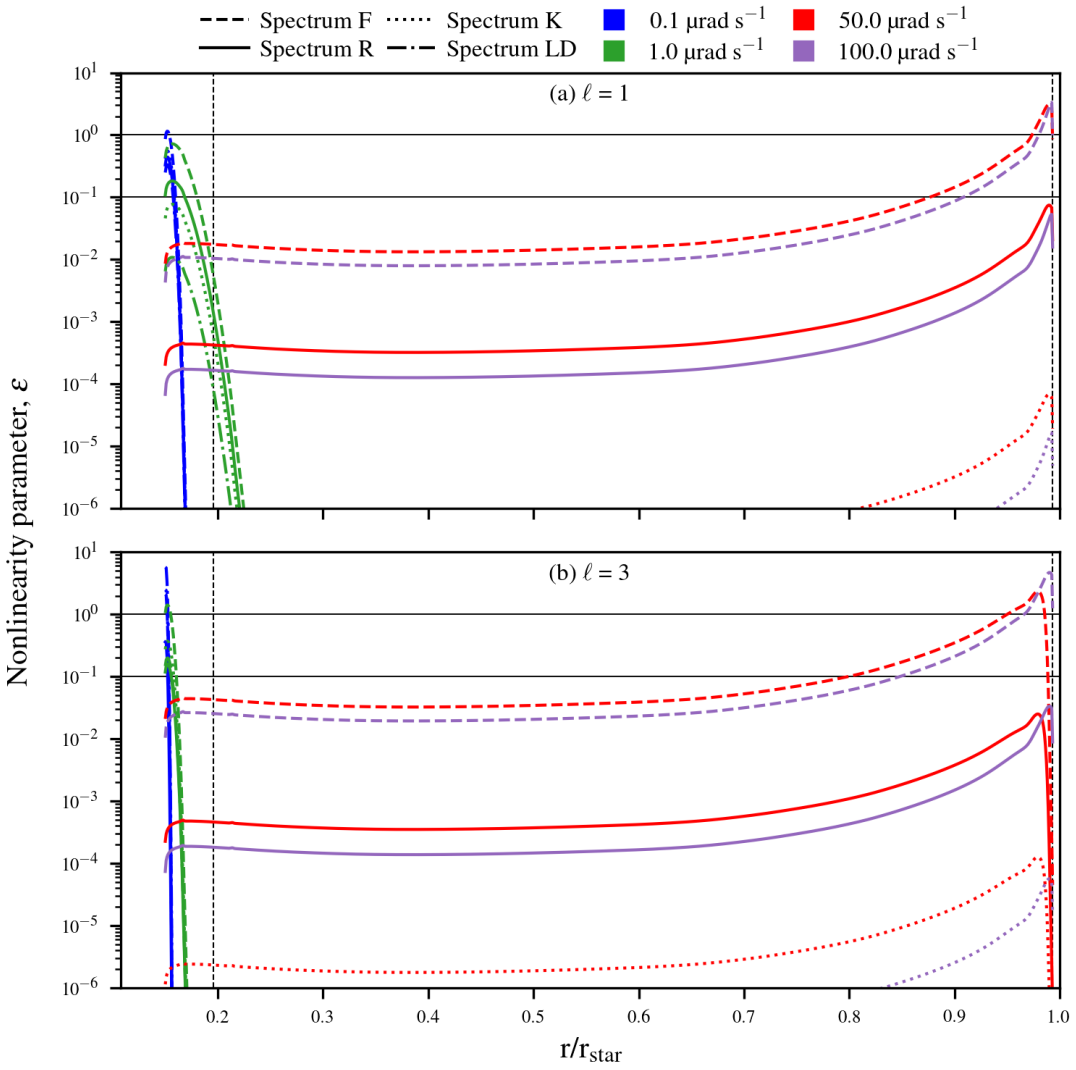

Figure 2.3: Nonlinearity parameter, ϵ, versus radii for a 3 $M_\odot$ star at ZAMS for (a) $l = 1$ and (b) $l = 3$. The two dotted vertical lines show the location of $r_{\mathrm{min,break}}$ and the surface convection zone. while the two straight horizontal lines mark $\epsilon = 1.0$ (top) and $\epsilon = 0.1$ (bottom). The colours blue, green, red and indigo have been used to represent IGW frequencies of 0.1 μrad s^{-}1, 1 μrad s^{-}1, 10 μrad s^{-}1 and 100 μrad s^{-}1 respectively while different linestyles represent different initial spectrum as shown in the legend.

2.5 Project Results

Using Eq. (2.20) and Eq. (2.21), we calculate the nonlinearity parameters for a chosen set of frequencies and wave numbers dictated by the generation spectra listed in Table 2.1 and present in Fig. 2.3. The convective velocity (u_c), which is required to compute IGW generation wave amplitudes (see Section 2.1), was calculated by taking the average of

all MESA-generated convective velocities[3] in the grid points between the first and third quartile (in radius) of the convection zone, as shown below:

$$u_c = u_{\rm MLT} = \frac{1}{{\rm N}_g/2} \sum_{{\rm N}_g/4}^{3{\rm N}_g/4} u_i \tag{2.26}$$

where i is grid space index inside the convection zone and N_g is the last grid index within the convection zone. The term u_i refers to the convective velocity at the grid with index i. We label u_c as $u_{\rm MLT}$, since the convective velocities in the convection zone are computed using mixing length theory (MLT). The convective turnover frequency, ω_c, was set as

$$\omega_c = \frac{u_c}{r_c}. \tag{2.27}$$

In Fig. 2.3, solid black horizontal lines in both plots represent $\epsilon = 1$ (strong nonlinearity condition) and $\epsilon = 0.1$ (weak nonlinearity condition). We chose these two separate conditions here because Press (1981) showed that waves with $\epsilon > 1$ will most certainly become non-linear and (Barker & Ogilvie, 2010) showed that non-linear effects may also become important at ϵ lower than one. Note that from here on, my analysis of non-linear waves (by either the strong or weak condition) will be only on those that become non-linear beyond 0.5 H_P from the convective-radiative interface, which is the nominal convective overshoot depth (Rogers *et al.*, 2013). I will refer to this as $r_{\rm min,break}$.

Since the damping opacity is proportional to ω^{-4} and ℓ^3 (see Eq. (2.14)), higher-frequency and lower-ℓ waves are expected to be damped less, without consideration of generation spectra. Thus, they are more likely to become non-linear close to the stellar surface from amplitude growth alone. When all the generation spectra are considered as shown in Fig. 2.3, we see that not only do the waves need to have higher frequencies and lower wavenumbers to become non-linear close to the surface, they must also be generated with sufficient amplitudes. Non-linear waves from spectrum F satisfy both these criteria for our example. On the other hand, low-frequency waves that are generated with high amplitudes have a higher chance of becoming non-linear close to the convective core. Figure 2.3 shows that as frequency decreases, the initial ϵ for all generation spectra increases. This means that before the effect of damping starts to dominate, these low-frequency waves can become non-linear near the core.

2.5.1 IGW Generation Spectra Dependence

The different line styles in Fig. 2.3 represent different IGW generation spectra introduced in Section 2.1. It can be seen that when $\ell = 1$ (top panel) and $\ell = 3$ (bottom panel), only

[3]The represent bulk convective forcing.

1 out of the 16 waves shown become non-linear under the strong condition, which is the 100 µrad s^{-1} wave generated from spectrum F. This is because the flat spectrum allows high-frequency waves to be generated with high enough amplitudes. This, coupled with the fact that high-frequency waves experience lower damping, allows the 100 µrad s^{-1} wave to become strongly non-linear close to the stellar surface. Note that zero dependence on IGW frequency or wavenumber means that all waves generated from spectrum F start with the same initial amplitude. However, since the nonlinearity parameter is $k_h u_h/\omega$, the initial ϵ will be different for different frequencies and horizontal wavenumbers. We show the frequency and wavenumber dependence of each generation spectrum in Table 2.3. Waves from the other three generation spectra do not become strongly non-linear, either because they are not generated with a large enough amplitude or because they experience large damping.

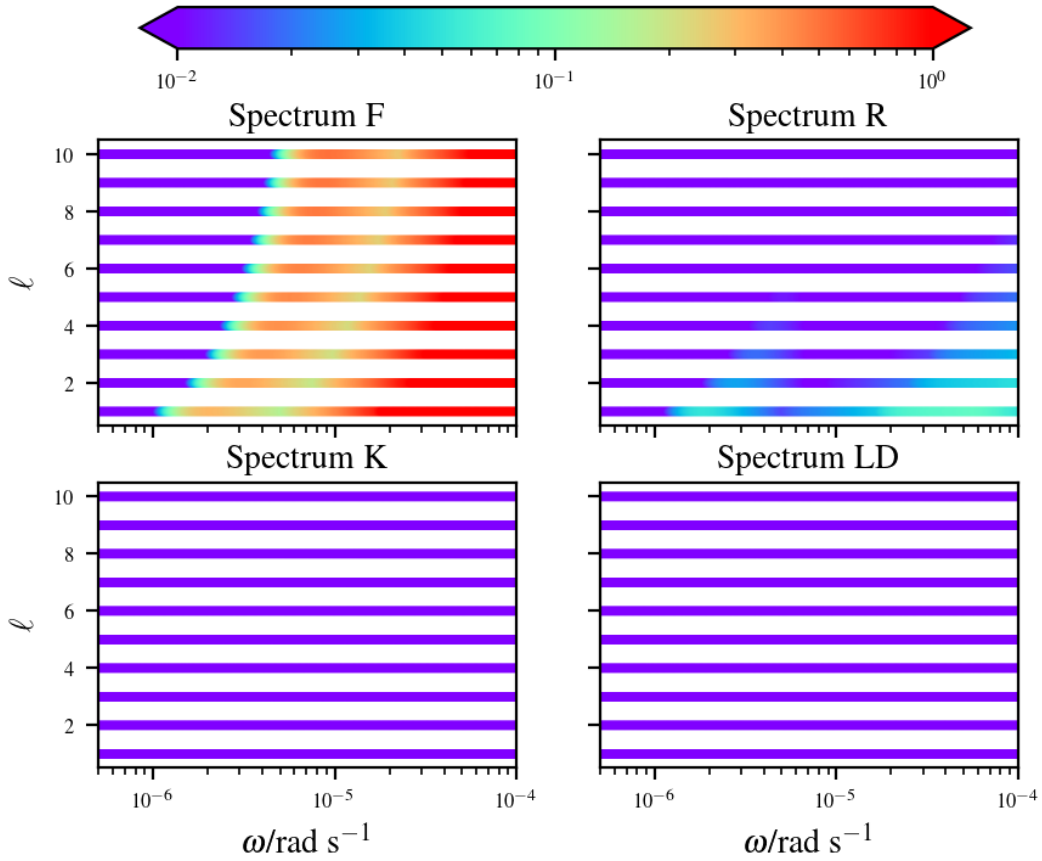

Figure 2.4: Colour maps of the nonlinearity parameter, ϵ, for different spectra (as described in Table 2.1). The y-axes represent wave number, ℓ and the x-axes represent ω in rad s^{-1}. The colours represent the maximum ϵ reached by an IGW of a given wave number and frequency at radii more than 0.5 H_P from the convective-radiative interface (see Eq. (2.21)).

Looking at waves with $\epsilon > 0.1$ at $r > r_{\rm min,break}$, we can see one additional wave gener-

Spectra		
Flat[F]	ω^{-1}	ℓ^{1}
Rogers *et al.* (2013)[R]	$\omega^{-1.6}$	$\ell^{0.1}$
Kumar *et al.* (1999)[K]	$\omega^{-3.17}$	ℓ^{2}
Lecoanet & Quataert (2013)[LD]	$\omega^{-5.25}$	ℓ^{3}

Table 2.3: The table shows how the nonlinearity parameter depends on the wave frequency and wavenumber at generation.

ated with spectrum F satisfying the weak condition. At lower frequencies, gravity waves are more likely to become non-linear closer to the convective-radiative interface because of higher generation amplitudes and the rapid increase of the Brunt–Väisälä frequency. However, for waves generated from any of the more realistic generation spectra (Spectrum R, K and LD), their amplitudes do not increase sufficiently to become non-linear.

At $\ell = 3$ (bottom panel of Fig. 2.3), a few differences can be noted in the ϵ behaviour compared to that for $\ell = 1$. First, for waves of the same frequency, small-scale waves are generated with higher ϵ. Waves from Spectrum LD have the largest change in ϵ, followed by spectrum K and spectrum R (see Table 2.3). Second, increasing ℓ results in increased damping which causes the peaks of ϵ to occur at lower radii in the $l = 3$ case compared to the $l = 1$ case. This can lead to higher ℓ waves not achieving sufficient ϵ to become non-linear. Thus, for a fixed frequency, the wavenumber determines which of the two effects mentioned above dominate.

Figure 2.4 shows the nonlinearity parameter with a broader range of IGW horizontal wavenumbers ($\ell = 1$ – 10) and frequencies ($\omega = 0.5$ µrad s^{-1} to 100 µrad s^{-1}), where the spacing between wave frequencies was chosen to be equal in the logarithmic scale, $d\log_{10}(\omega) =$ constant. The colour scheme represents the maximum ϵ reached by an IGW of a given wavenumber and frequency at any $r > r_{\mathrm{min,break}}$ and any nonlinearity parameter above 1.0 or below 0.01 will be red or blue respectively. The lower limit of ϵ has been set to 0.01 to provide a clear view of how ϵ varies across the weak condition ($\epsilon = 0.1$). It was found that spectrum F has the highest fraction of non-linear waves (for both strong and weak nonlinearity conditions), while spectrum K and spectrum LD show no non-linear waves. Spectrum R shows that non-linear waves are potentially concentrated in the lower-ℓ regime. However, there is an irregular trend with increasing frequencies. At the lowest frequencies (0.5 µrad s^{-1} - 1.0 µrad s^{-1}), damping is at its highest causing most waves to be damped rapidly. Across all other tested frequencies at low-ℓ, we see two peaks in ϵ. The peak at low frequency is due to waves becoming non-linear close to the convective core. The second peak at a higher frequency is due to waves becoming non-linear close to the surface. In between, waves are of high enough frequencies to not be generated with sufficient amplitude to break near the core but of low enough frequency to still be damped before reaching the surface. This damping is, of course, wavelength-dependent, hence the

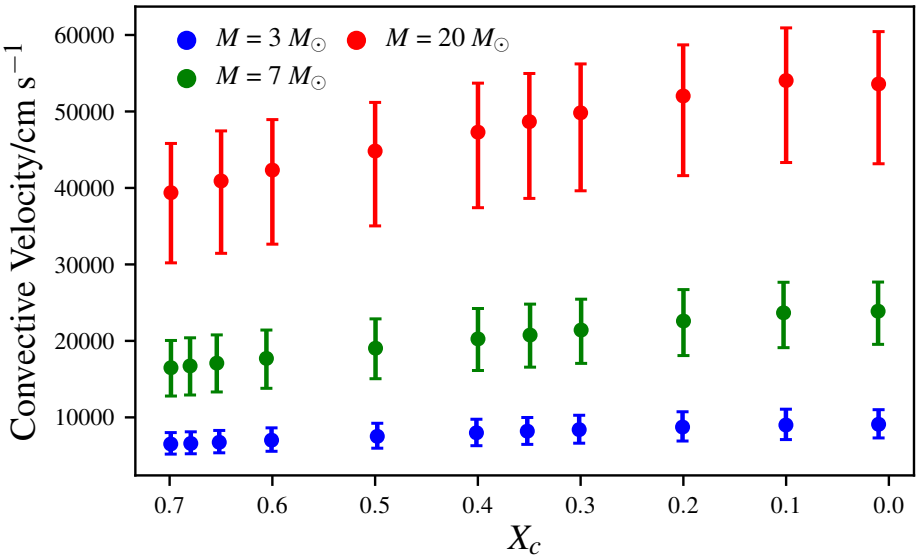

Figure 2.5: The bulk convective velocities, $u_{\rm MLT}$ as a function of central hydrogen mass fraction, X_c. The error bars indicate the variation of convective velocities across the convection zone. The upper limit of the error bar is the maximum convective velocity within the chosen radial range, where we calculate the bulk convective velocity (see Eq. (2.26)), whilst the lower limit represents the minimum velocity. Even though we do not test models older than midMS for 20M$_\odot$, we include the convective velocities from core convection here for references from other chapters.

structure seen in ℓ.

In conclusion, one can see that with MLT velocities, only waves from spectrum R and spectrum F can become non-linear.

2.5.2 Convective Velocity Dependence

The bulk convective velocities, u_c, were obtained from the formulation of mixing length theory (Biermann, 1951; Böhm-Vitense, 1958) in MESA. While being widely adopted, it is also well known that this prescription is likely not an accurate representation of the three-dimensional nature of turbulent convection. In particular, simulations of turbulent convection in intermediate-mass stars (Rogers *et al.*, 2013; Edelmann *et al.*, 2019) generally show significantly more intermittency than this prescription allows for. In addition to the uncertainty related to MLT, the MLT velocity itself, $u_{\rm MLT}$, can vary significantly within the convection zone. Generally, within the convection zone of a MESA stellar model, the MLT velocity varied by approximately one order of magnitude for all the masses and ages investigated (see Fig. 2.5). Furthermore, a recent work (Couston *et al.*, 2018), which looked at 3D simulations of IGW generated by turbulent convection, has shown that at the point of generation, the steep fall-off in frequency dependence as in spectrum K and LD occurs well away from the traditional convective turnover frequency relation. This

introduces further uncertainties to a factor of 2 – 5 in the value of ω_c, which in turn affects u_c. Thus, we investigated the effect of varying convective velocities by varying u_c from one-third to three times the u_{MLT} used in previous sections.

Fig. 2.6a and Fig. 2.6b show how the nonlinearity parameter changes with higher and lower convective velocities. In Fig. 2.6a, where u_c was set to one-third of the initial u_{MLT}, only waves from spectrum F show strong nonlinearity. Spectrum F is only a test case, so this means realistically, virtually no waves become non-linear. On the other hand, when u_c was set to 3 u_{MLT}, waves from all spectra, except spectrum LD, exhibit strong/weak nonlinearity.

For a larger u_c, spectrum K can be seen to exhibit less non-linear waves at high frequencies compared to spectrum F and R as these waves are generated with lower amplitudes. At low frequencies and larger ℓ, generation amplitudes are larger but damping is also larger. This causes only a small range of waves with specific frequencies and ℓ to become non-linear. Whether waves become non-linear depends sensitively on the amplitudes of convective velocity which may very well be time-dependent. Hence, it is entirely possible that the occurrence of non-linear waves is also time-dependent.

2.5.3 IGW Energies

The plots in Fig. 2.4 to Fig. 2.6 show how non-linear waves are distributed over the range of chosen wavenumbers and frequencies but it does not capture the dynamics of these non-linear waves in the radiation zone. To better understand the impact breaking waves would have in stellar processes like mixing and angular momentum transfer, we look at the kinetic energy in waves that become non-linear, which can be represented by the following relation:

$$E \propto u_h^2.$$

Note that we are referring to the kinetic energy here, which is calculated from the total velocity, $v_t = \sqrt{u_v^2 + u_h^2}$. However, due to the our choice of frequencies, the Brunt–Väisälä frequencies are always larger than the wave frequencies, which means that the vertical wavenumbers will always be larger than horizontal wavenumbers (see Eq. (2.22)). At any given radius, the relation in Eq. (2.21) holds true for IGWs, so $u_h > u_v$. For the flat spectrum, the wave energies are distributed equally for all wave numbers and frequencies. For spectrum R,

$$E \propto \left(\sqrt{\ell(\ell+1)}\right)^{-1.8} \omega^{-1.2},$$

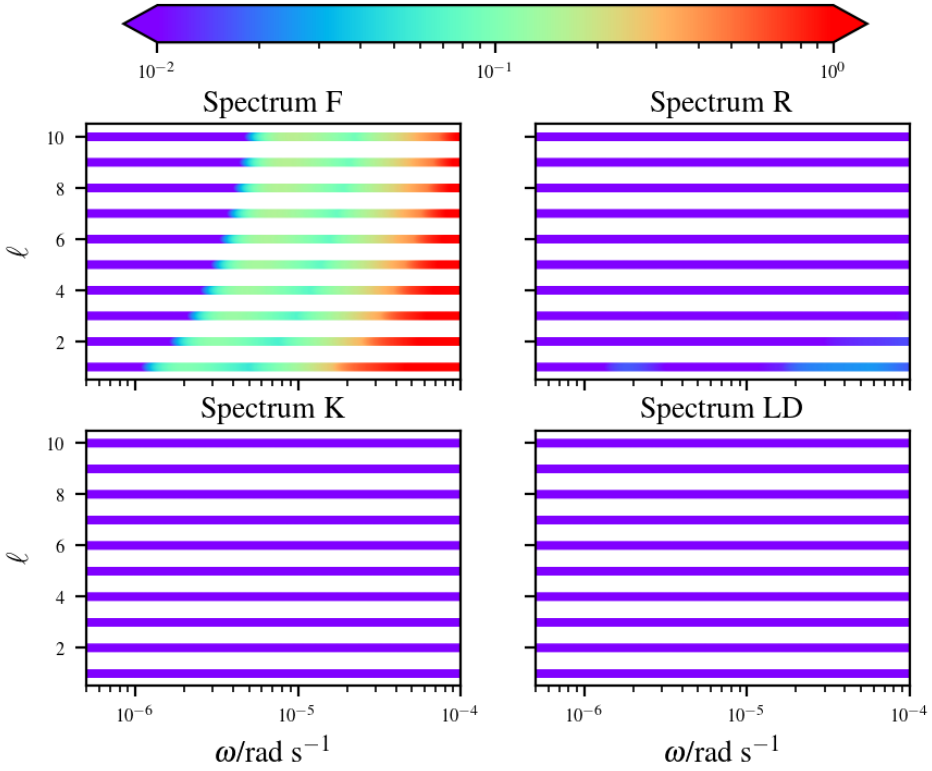

(a) Similar to Fig. 2.4 but with $u_c = u_{\mathrm{MLT}}/3$.

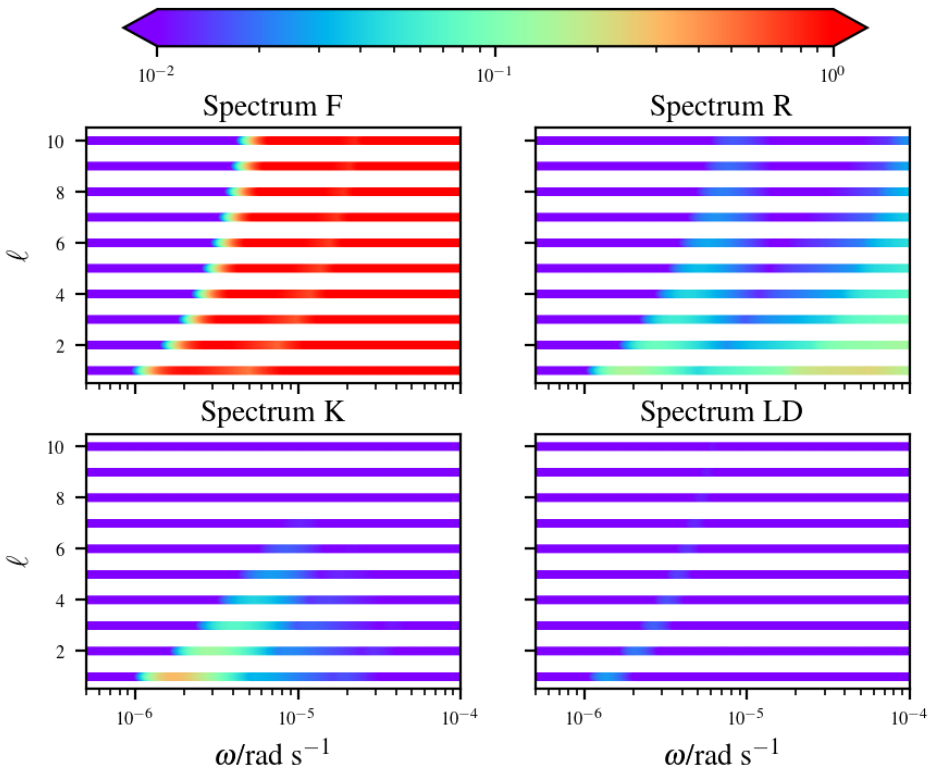

(b) Similar to Fig. 2.4 but with $u_c = 3u_{\mathrm{MLT}}$.

Figure 2.6: Colour maps of non-linear waves for different convective velocities.

which means that waves with the lowest wave numbers and lowest frequencies possess the highest energies. On the other hand, for spectrum LD,

$$E \propto \left(\sqrt{\ell(\ell+1)}\right)^4 \omega^{-8.50}.$$

Therefore, the waves that carry the most energy are the high-wave number, low-frequency waves. Finally, for spectrum K,

$$E \propto \left(\sqrt{\ell(\ell+1)}\right)^2 \omega^{-4.34} \exp\left[-k_h^2 \left(\frac{u_c}{\omega_c}\right)^2 \left(\frac{\omega}{\omega_c}\right)^{-4/3}\right].$$

The distribution of wave energies for spectrum K is not as direct as for the other spectra due to the exponential term. In Figure 2.7, which shows the non-linear wave energy trend for all generation spectra, we can see that for spectrum K and $u_c = u_{\rm MLT}$, the non-linear wave energies are highest for low-ℓ and low-ω waves.

The ratio of energy in waves that satisfy $\epsilon \geqslant 0.1$ to the total energy of all waves within the frequency ($\omega = 0.5$ µrad s^{-1} to 100 µrad s^{-1}) and wave number ($\ell = 1$ – 10) ranges considered, is

$$\frac{E_{\epsilon \geqslant 0.1}}{E_{\rm Total}} = \frac{\left(\sum_{l,\omega} u_h^2 \, \Delta\omega\right)_{\epsilon \geqslant 0.1}}{\sum_{l,\omega} u_h^2 \, \Delta\omega}, \tag{2.28}$$

where the numerator on the right-hand side represents the sum over IGW amplitudes that satisfy $\epsilon \geqslant 0.1$, at radii larger than $r_{\rm min,break}$, while the denominator is the total energy input in waves. The spacing between frequencies is represented by $\Delta\omega$. The spacing between ℓ is 1. Both energy terms in the numerator and the denominator are energies supplied by convective processes, so this ratio was calculated at the point of wave generation.

Applying Eq. (2.28) to the same stellar model for cases of $u_c = u_{\rm MLT}$ and $u_c = 3\ u_{\rm MLT}$ gives the values shown in Table 2.4 at $Z = 0.02$. Energy ratios for spectrum F are always close to one as most waves generated from spectrum F become non-linear as shown in Fig. 2.4 and Fig. 2.6. For $u_c = u_{\rm MLT}$, only spectrum F shows any appreciable energy in non-linear waves (see Fig. 2.4). When u_c is increased to 3 $u_{\rm MLT}$, all the generation spectra, except spectrum LD, produce non-linear waves. Non-linear waves from spectrum R and spectrum K have moderately higher energy ratios (see Table 2.4). This is due to the significant overlaps between the nonlinearity parameter trend (see Fig. 2.6b) and the wave energy trend (Fig. 2.7), for both spectrum R and spectrum K. In fact, due to the larger overlap for spectrum K, non-linear waves from spectrum K have a higher energy ratio compared to spectrum R.

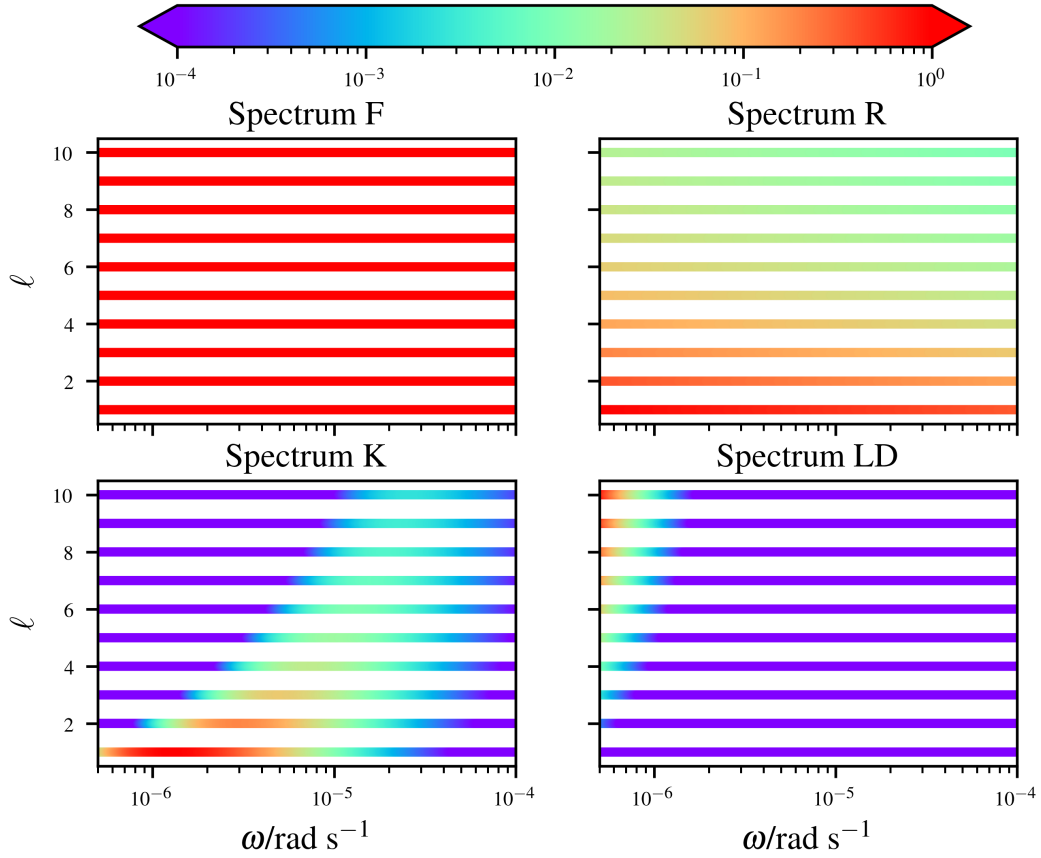

Figure 2.7: Colour maps of the non-linear wave energies normalised to the maximum wave energy for different spectra at $u_c = 3\ u_{\rm MLT}$. At $u_c = \ u_{\rm MLT}$, the plots show similar trends to the case of $u_c = 3\ u_{\rm MLT}$, with the exception of spectrum K, a smaller spread of high wave energies over frequency for higher ℓ and lower ω waves.

2.5.4 Metallicity Dependence

In the results discussed above, we have used a stellar model generated with an initial metallicity of 0.02, equal to the solar metallicity. To investigate the effect of different initial metallicities on the production of non-linear waves, we generated stellar models at ZAMS with initial metallicities of 0.006 and 0.06, and tested these models with different wave generation spectra at $u_c = u_{\rm MLT}$ and $u_c = 3\ u_{\rm MLT}$. As in the previous section, we have chosen a fixed nonlinearity condition of $\epsilon \geqslant 0.1$. We calculate energy ratios based on Eq. (2.28) and show them in Table 2.4.

The trend with spectrum F shows a slight decrease with decreasing metallicities due to increasing damping as lower metallicties lead to lower opacities (see Fig 2.8a). Other than spectrum F, virtually no other spectrum shows non-linear waves for any metallicity at $u_c = u_{\rm MLT}$. The exception is spectrum R which shows a slight increase in non-linear wave energy at $Z = 0.006$ because the product of the density stratification term and

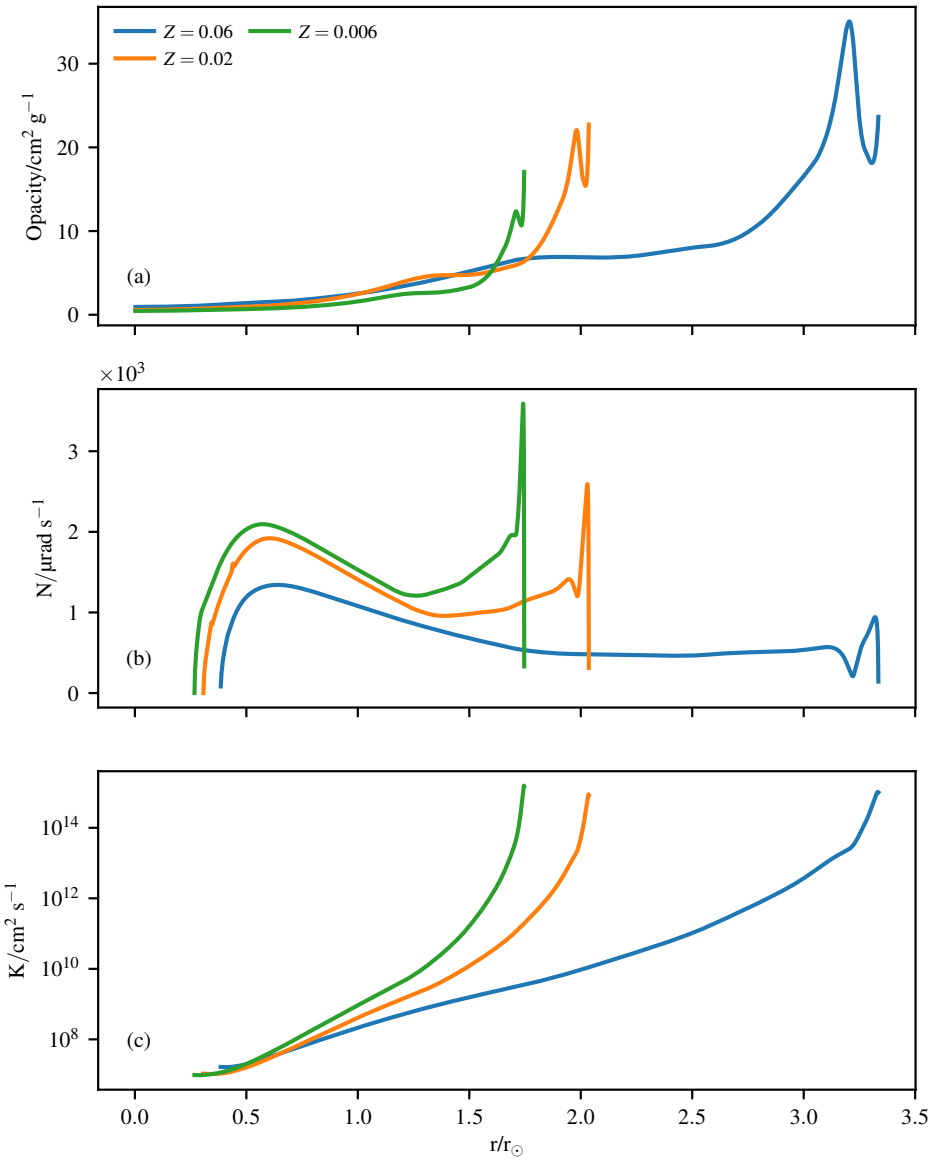

Figure 2.8: (a) Opacity, (b) Brunt–Väisälä frequency and the (c) thermal diffusivity profiles as a function of radius, in units of solar radius. Colour representations for all three plots are stated in the legend of the top panel. The opacity profiles (top panel) for all three metallicities show bumps occurring at radii where $\log_{10} T = 5.3$, which is known as the iron opacity bump. This bump, together with temperature and pressure profiles are responsible for the bump seen in the Brunt–Väisälä frequency squared profile (middle panel). Note that higher metallicities lead to shallower thermal diffusivity slopes but the surface thermal diffusivity values are approximately equal (bottom panel).

Spectra	$u_c/u_{\rm MLT}$	$Z = 0.06$	$Z = 0.02$	$Z = 0.006$
F	1	0.968	0.968	0.959
	3	0.971	0.9705	0.9635
R	1	0.0	0.0	5.54×10^{-2}
	3	0.234	0.223	0.182
K	1	0.0	0.0	0.0
	3	0.481	0.480	0.606
LD	1	0.0	0.0	0.0
	3	0.0	0.0	0.0

Table 2.4: The table shows the energy ratios of non-linear waves for different stellar metallicities at ZAMS.

geometric term (see Fig. 2.2) becomes larger due to decreasing total stellar radius (as shown in Fig. 2.8) and increasing Brunt–Väisälä frequency spike (see Fig. 2.8b) causing wave amplification close to the stellar surface.

Moving to $u_c = 3\ u_{\rm MLT}$, we see that spectrum R and spectrum K have opposite trends in non-linear energy ratios for decreasing metallicity. Spectrum R shows a decreasing trend because of the same reason spectrum F shows a decreasing trend. Spectrum K shows an increasing trend as convective velocities are found to be higher when stellar metallicity is lower. Spectrum LD shows no non-linear waves in any of the cases.

2.5.5 Age and Mass Dependences

To investigate whether there are any trends of waves becoming non-linear with varying stellar mass and age, we extended our analysis to include stellar masses up to 20 $M_\odot$ and X_c down to 0.01, where we have used the central hydrogen mass fraction, X_c, as a proxy for stellar age. A fixed nonlinearity condition of $\epsilon \geqslant 0.1$ was chosen. The stellar metallicities were fixed at 0.02.

Figure 2.9 shows how these energy ratios change as a function of X_c, with $u_c = 3$ $u_{\rm MLT}$, for 3 $M_\odot$, 7 $M_\odot$ and 20 $M_\odot$ main-sequence stars. From midMS onwards, no data is plotted for 20 $M_\odot$ (bottom panel of Fig. 2.9), as the star develops a convection zone in the radiation zone between the convective core and the surface convection zone. A quick analysis of waves generated from the intermediate convection zone showed that no waves become non-linear for all spectra except spectrum F. This was due to the very small convective velocities generated in this narrow convection zone. Waves generated with such small amplitude never reach sufficient amplitudes to become non-linear. This intermediate zone can also significantly attenuate waves from the core.

In general, we see a decreasing trend of non-linear wave energies with increasing age for spectrum F, R and initially for K. In fact, for spectrum K, this decrease leads to no waves becoming non-linear with the effect being more prominent at lower stellar masses.

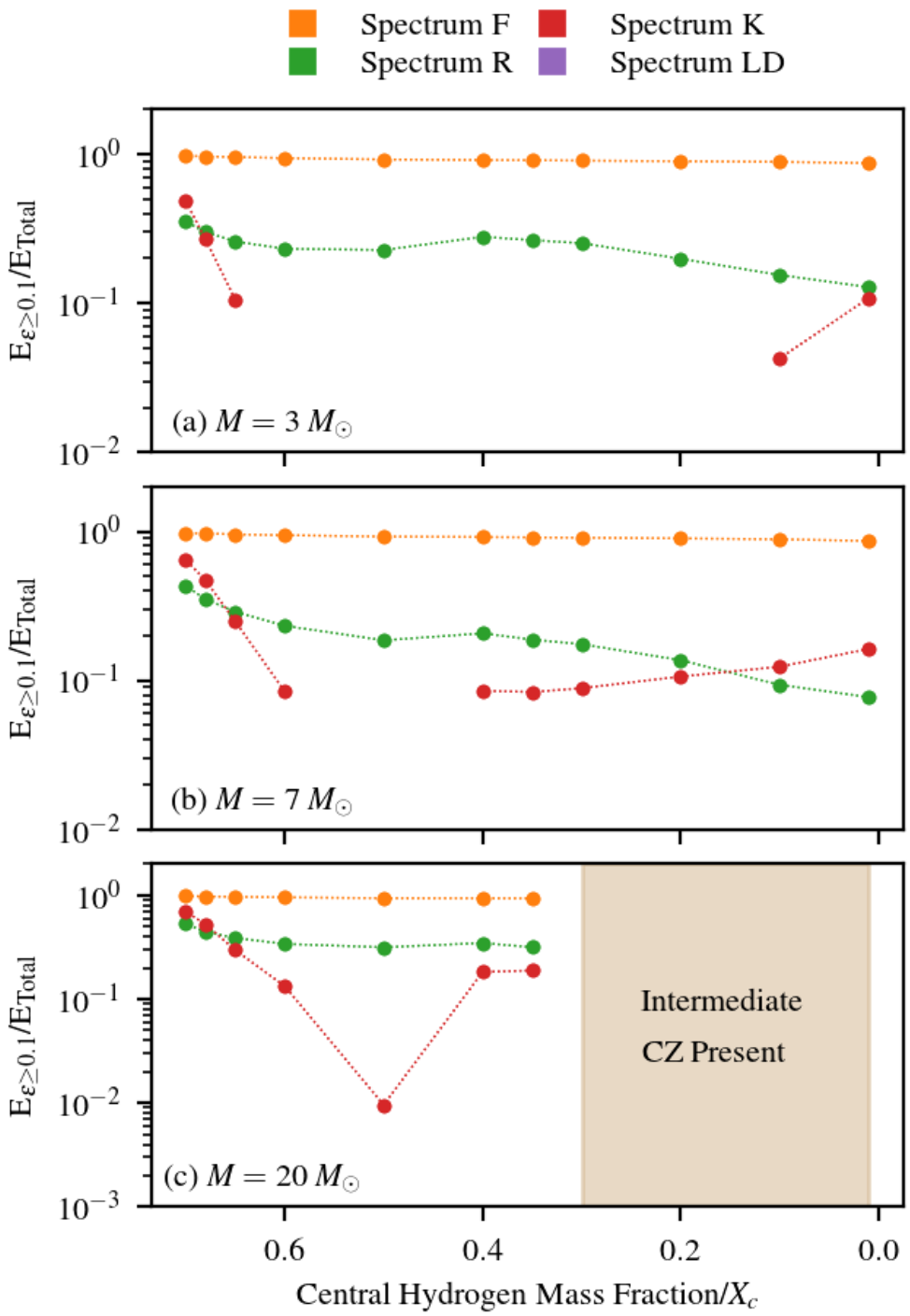

Figure 2.9: Energy ratios of waves with $\epsilon \geqslant 0.1$ to total energy from all waves against central hydrogen mass fractions for stars with masses (a) 3 $M_\odot$, (b) 7 $M_\odot$ and (c) 20 $M_\odot$. The dotted lines with circular markers represent waves with $u_c = 3\ u_{\text{MLT}}$. The highlighted region in the plot for 20 $M_\odot$ shows where the intermediate convection zone (CZ) starts to develop. The missing data points for spectrum K is due to no waves becoming non-linear with our chosen nonlinearity parameter limit. The missing data points for spectrum LD is because no waves from this generation spectrum become non-linear.

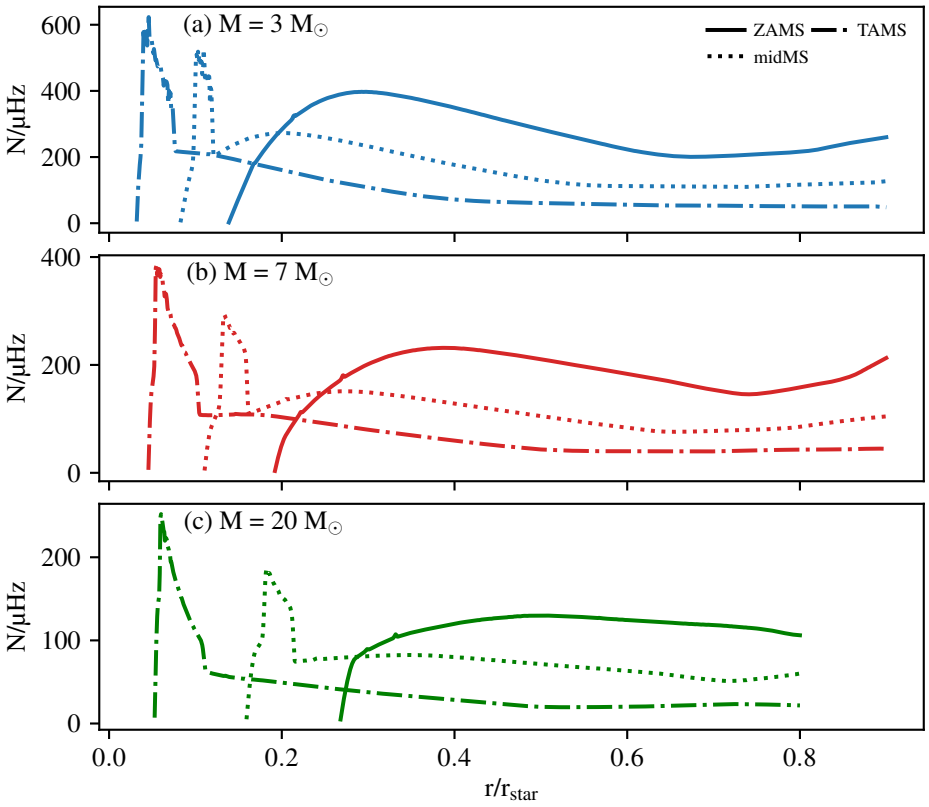

Figure 2.10: The Brunt–Väisälä frequency profile in the radiation zone for 8 stellar models. The top panel represents the profiles for a (a) 3 $M_\odot$ star, the middle panel for a (b) 7 $M_\odot$ star and the bottom panel for a (c) 20 $M_\odot$ star. The x-axis represents stellar radius in units of total stellar radius.

To understand this, we look at various factors that affect the wave amplitude. First, the Brunt–Väisälä frequency profiles in Fig. 2.10, from the different stellar models that we have used, show that when a star starts to undergo hydrogen burning and evolve from ZAMS, its core contracts slowly leaving behind a steep hydrogen abundance gradient (Dziembowski *et al.*, 1991). This leads to the formation of a sharp "spike" in the Brunt–Väisälä frequency profile near the edge of the convective core, which broadens and moves inwards with the convective core surface. This spike effectively traps low-frequency, high-wave number waves causing fewer waves to become non-linear close to the stellar surface. Moreover, the Brunt–Väisälä frequencies are lower for older stars which means the density stratification term (from Eq. (2.20)) will be smaller too. Furthermore, as the star ages, stellar density varies over the same magnitude across the radiation zone but the star grows in size. This causes the density gradient to decrease and simultaneously, the geometric term to grow, leading to their product (as shown in Eq. (2.20)) being smaller in older stars.

Going back to Fig. 2.9, we see an increasing trend in non-linear wave energy ratios for

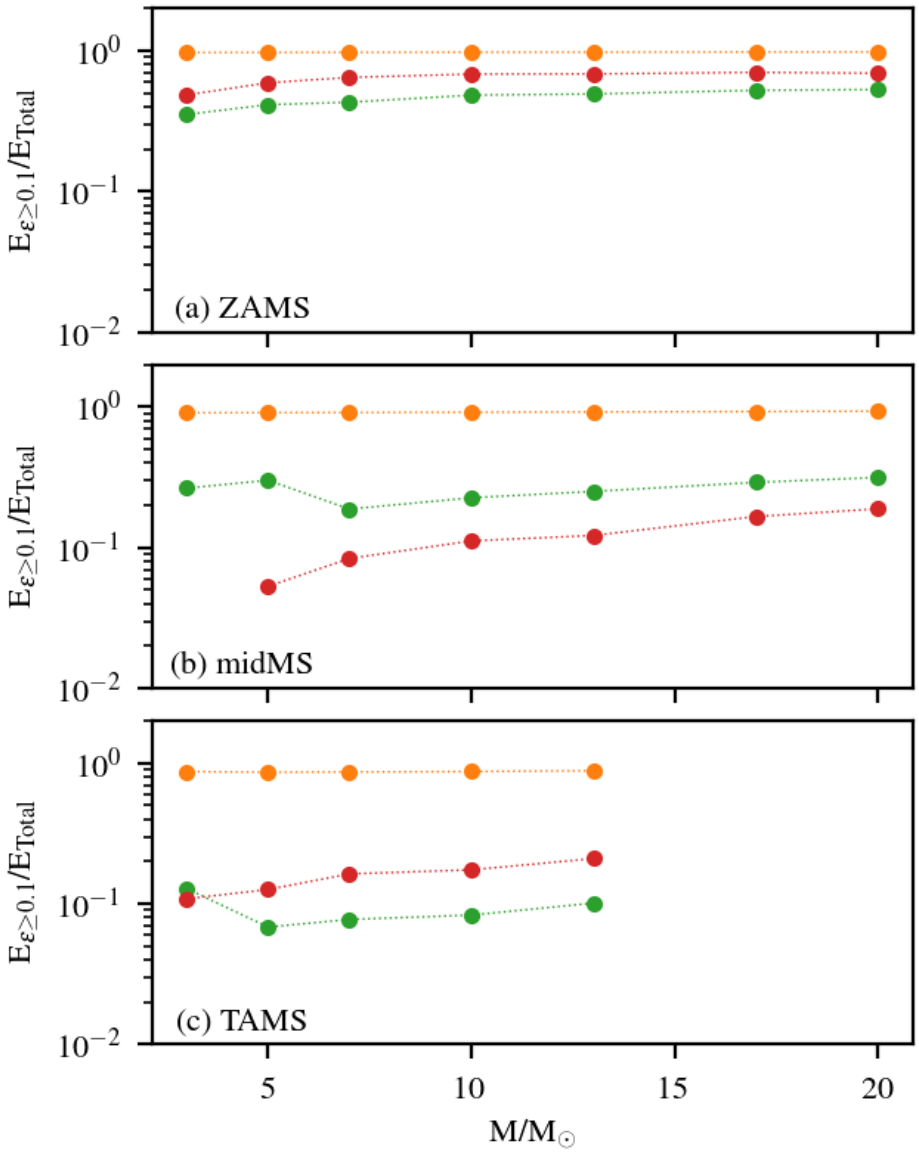

Figure 2.11: Energy ratios of waves against stellar masses at (a) ZAMS, (b) midMS and (c) TAMS. Refer to Fig. 2.9 for the colour representation. Note that we have omitted the 17 $M_\odot$ energy ratio here as the Brunt–Väisälä frequencies in most of the radiation zone were found to be close to or less than 100 µrad s^{-1}. Again, the missing data points for spectrum LD is because no waves from this generation spectrum become non-linear.

spectrum K at higher ages. To explain this, we look at Fig. 2.10, which shows that the peak Brunt–Väisälä frequency close to the stellar surface is smaller for older stars. This causes higher frequency waves to experience lower damping close to the surface which allows more waves to cross the $\epsilon > 0.1$ threshold.

Figure. 2.11 shows wave energy ratios as a function of mass with the top panel representing ZAMS models, the middle panel representing midMS models and the bottom

panel representing TAMS models. As in the case for age dependence, energy ratios of waves from spectrum R are higher than energy ratios of waves from spectrum K, when the initial metallicities of the models are set to the solar metallicity of 0.02. In general, the non-linear energy ratios for all spectra increase slightly with increasing mass. This can be explained by the increasing convective velocities with mass (see Fig. 2.5). Furthermore, Fig. 2.10 shows that for larger stellar masses, the Brunt–Väisälä frequencies are lower, which leads to lower damping.

2.6 Summary and Discussion

Through this project, we found that depending on the spectrum and amplitudes of waves generated by convection, some IGWs may become non-linear in the radiative regions of intermediate-mass stars. This can occur because the amplitudes of high(er) frequency/longer wavelength waves are amplified by density stratification. Therefore, if such waves are generated with sufficient amplitude, they can become non-linear along their journey towards the stellar surface. On the other hand, lower frequency waves, which are generated with larger amplitudes, can become non-linear close to the convective core. These waves that break near the convective core may lead to enhanced mixing beyond a nominal "overshoot depth".

One crucial element as to whether waves can become non-linear and break in stellar radiative regions is the wave generation spectrum. Compared to the theoretical generation spectra from Lecoanet & Quataert (2013) and Kumar *et al.* (1999), with their steep fall off at frequencies higher than the convective turnover frequency, the numerical generation spectra from Rogers *et al.* (2013) show that more waves may become non-linear and consequently, more energy is in these non-linear waves for MLT convective velocities.

The assumed convective velocity also plays an important role in the ability of waves to become non-linear, with even a factor of three increase causing significant differences in total non-linear wave energies. In this case, non-linear wave energy ratios from the theoretical generation spectrum of Kumar *et al.* (1999) became comparable to those from the numerical generation spectrum R. Given the likelihood of variation in convective velocities by at least this order, it is worth trying to understand the role that intermittency plays in determining the wave spectrum. This is important especially after the results from a recent numerical work from Couston *et al.* (2018) which shows that the steep fall-off in energy with frequency dependence occurs away from the classical theory for convective turnover frequency. Indeed, it may be possible that the wave generating process at the convective-radiative interface and wave breaking process at the surface may be time-dependent.

We found that age, mass and metallicity also affect the fraction of waves becoming non-linear, but to a lesser degree. Generally, as stars become older, the fraction of energy

that goes into non-linear waves decreases because the receding convective core leaves behind a compositional gradient and hence, the spike in the Brunt–Väisälä frequency which effectively filters waves from propagating outward. As the mass increases, the fraction of non-linear waves increases slightly due to increasing convective velocities. As the metallicity increases, the fraction of non-linear waves behaves differently, depending on generation spectra.

Clearly, wave breaking and the ensuing turbulence that is generated would lead to more efficient mixing and angular momentum transport than simple radiative dissipation. The strong observational evidence for enhanced coupling between convective and radiative regions (Beck *et al.*, 2012; Deheuvels *et al.*, 2012; Tayar & Pinsonneault, 2013) and the possible observational detections of IGW(Aerts & Rogers, 2015; Aerts *et al.*, 2017, 2018; Ramiaramanantsoa *et al.*, 2018) both point to breaking IGW, which in turn, points to a flatter frequency generation spectrum from convection than what theoretical models predict or higher convective velocities than those predicted by MLT. Thus, it seems natural to study the propagation of these waves in the radiation zone through numerical simulations, which I did for my second project (see next Chapter).

Chapter 3

Non-linear Wave Propagation

In Chapter 1, we introduced some effects that IGWs undergo when they are propagating through the stellar radiation zone such as radiative damping and non-linear interactions. In the previous chapter, we studied the linear propagation of IGWs in stellar radiation zones and looked at the effect of radiative diffusion on IGW amplitudes and their non-linearity as they propagate through the radiation zone. In this chapter, we try to understand these non-linearities for realistic cases of IGW generation amplitudes through non-linear simulations of the radiation zone. The final goal of this project was to investigate the surface IGW spectrum produced from a realistic IGW generation spectrum forced at the bottom boundary of a radiation zone. We do this for a 3 $M_\odot$ model at different rotation rates and ages. This work had the major advantages of using realistic, stellar thermal diffusivities and a simulation domain that covered almost the whole radiation zone. This chapter is based on the work done in Ratnasingam *et al.* (2020).

3.1 Non-linear Simulations

We ran non-linear simulations using a pseudo-spectral code written for solving the Navier-Stokes equations in the anelastic approximation (Eq. (3.1) – Eq. (3.3)), within the geometry of an equatorial slice (see Fig. 1.10) of the chosen stellar model (Rogers & Glatzmaier, 2005). We will refer to these equations as the RG equations, from here on. These equations differ from the general fully compressible Navier-Stokes equation used widely in the field and also differ from the some other forms of anelastic approximation. (Brown *et al.*, 2012) did an analysis of the different hydrodynamical equations with the anelastic approximation, including the RG equations. The main difference of the RG equations with the other equations and a reason why we choose these equations is the use of a temperature-based energy equation, instead of an entropy-based one. The equations are

$$\nabla \cdot \overline{\rho}\vec{v} = 0, \tag{3.1}$$

$$\frac{\partial \vec{v}}{\partial t} = -(\vec{v}\cdot\nabla)\vec{v} - \nabla\left(\frac{P}{\overline{\rho}}\right) - C\overline{g}\vec{\hat{r}} + 2(\vec{v}\times\vec{\hat{z}}\Omega) + \overline{\nu}\left(\nabla^2\vec{v} + \frac{1}{3}\nabla(\nabla\cdot\vec{v})\right), \tag{3.2}$$

$$\frac{\partial T}{\partial t} = -(\vec{v}\cdot\nabla)T + (\gamma-1)Th_\rho v_r - v_r\left(\frac{\partial \overline{T}}{\partial r} - (\gamma-1)\overline{T}h_\rho\right) + \frac{1}{c_v\overline{\rho}}\nabla\cdot(c_p\overline{K}\overline{\rho}\nabla T) + \frac{1}{c_v\overline{\rho}}\nabla\cdot(c_p\overline{K}\overline{\rho}\nabla\overline{T}). \tag{3.3}$$

where ρ, T and P are the perturbation density, temperature and pressure respectively. Any quantity with an over-line/bar represent the background state variables which vary only with radius. Radial velocity, v_r and the tangential velocity, v_θ, together form the velocity vector, $\vec{v}$. The negative inverse density scale height is represented by $h_\rho = (d\ln\rho/dr)$. The rotational angular velocity and viscosity are represented by Ω and $\overline{\nu}$. The adiabatic index, γ is set to be 5/3. The specific heat capacity at constant volume and specific heat capacity at constant pressure are represented by c_v and c_p respectively. The reference state gravity is represented by $\overline{g}$. The co-density, C, is

$$C = -\frac{1}{\overline{T}}\left(T + \frac{1}{\overline{g\rho}}\frac{\partial\overline{T}}{\partial r}P\right). \tag{3.4}$$

In the radial direction, the RG equations are solved using a uniform finite difference scheme, specifically the central difference method (Grossmann *et al.*, 2007). In the horizontal direction, the spectral solution method is applied where stellar variables are expanded in sines and cosines as shown below:

$$f(r,\theta,t) = \sum_{n=0}^{N_n}\left[f_{n,sin}(r,t)\sin(n\theta) + f_{n,cos}(r,t)\cos(n\theta)\right]. \tag{3.5}$$

The non-linear terms of the RG equations are integrated with time using the Adams-Bashforth method, of the following form:

$$f_{t+\Delta t} = f_t + \frac{\Delta t}{2}\left(3G_t - G_{t-\Delta t}\right), \tag{3.6}$$

where the subscript represents the time at which the quantity is considered and G is the time derivative of f. The linear terms are integrated with time using the Crank-Nicolson method, of the following form:

$$f_{t+\Delta t} - \alpha\Delta t G_{t+\Delta t} = f_t + (1-\alpha)\Delta t G_t \tag{3.7}$$

where α is variable chosen between 0.5 and 1, to balance out numerical accuracy and stability. This implicit method was chosen to timestep the linear terms as explicit methods require very small time interval to achieve stability when solving diffusion terms. The implicit method provides higher stability, but at the cost of computation time and a slight loss in accuracy which can be fine-tuned with the factor, α, in Eq. (3.7)

To simplify computations, the streamfunction, ψ, is introduced, which is defined as $\overline{\rho}\vec{v} = \nabla \times \psi$ and expanded through its relation with radial and horizontal velocities as

$$v_r = \frac{1}{\overline{\rho} r}\frac{\partial \psi}{\partial \theta};\ v_\theta = -\frac{1}{\overline{\rho}}\frac{\partial \psi}{\partial r}. \tag{3.8}$$

Equation (3.2) can then be written in terms of vorticity, defined as $\nabla \times \vec{v}$, which reduces the number of equations needed to be solved and ensures that the divergence-free mass flux criterion is fulfilled by construction because of the following identity, $\nabla \cdot \left(\nabla \times \vec{A}\right) = 0$, where $\vec{A}$ is a vector.

The temperature perturbation, T, boundary conditions are as follows: T was set to zero at both the bottom and top boundaries of the simulation domain. The radial velocity, v_r, was set to zero at the top boundary and forced (see Section 3.1.1 for the forcing functions) at the bottom boundary to mimic wave generation. For the horizontal velocities, v_θ at the top boundary, a stress-free boundary condition was imposed, which means

$$\frac{\partial v_\theta}{\partial r} = 0. \tag{3.9}$$

At the bottom boundary, the divergence-free mass-flux condition (see Eq. (3.1)) ensures that v_θ is forced because in these simulations, the radial velocity, v_r, is set through the streamfunction, ψ (see Eq. (3.13) in Section 3.1.1).

MESA (see Chapter 2, Section 2.2) was used to generate models of a 3 $M_\odot$ star at various ages, which are used as the reference state for these simulations. Stellar metallicity, Z, was set to be equal to the solar value of $Z = 0.02$. The mixing length parameter was set as 1.8 and the convective overshoot profile was set to exponential. The inlists used to produce these models are available publicly on zenodo.

To set the Brunt–Väisälä frequency in the radiation zone, we had two options: a modified Schwarzchild criterion or the Ledoux criterion. The modified Schwarzchild criterion, based on the work in Rogers *et al.* (2013), has the following form of Brunt–Väisälä frequency:

$$N^2 = \frac{\overline{g}}{\overline{T}}\left(\frac{d\overline{T}}{d\overline{r}} - (\gamma - 1)\,\overline{T} h_\rho\right). \tag{3.10}$$

As a comparison, Fig 3.1 shows the Brunt–Väisälä frequency calculated using the modified Schwarzschild criterion and the Ledoux criterion for a $3M_\odot$, ZAMS star model. The Brunt–Väisälä frequency calculated from the modified Schwarzschild criterion differ than

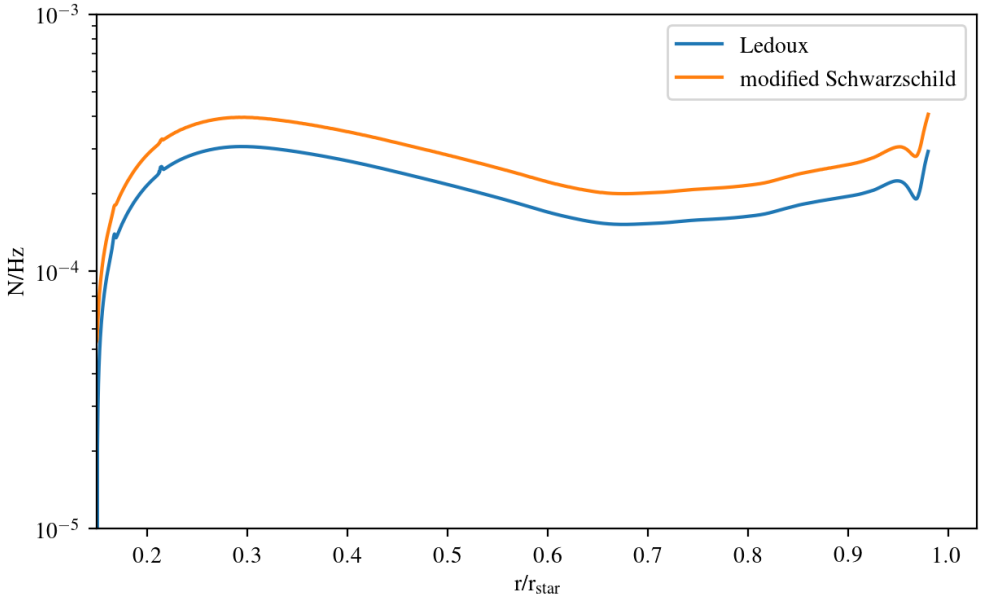

Figure 3.1: The Brunt–Väisälä frequency profile calculated from Eq. (3.10) (orange) and from MESA (blue) of a $3M_{\odot}$, ZAMS star model. The profile has been cut at $r/r_{star} = 0.99$, where the surface convection zone begins.

that from the Ledoux criterion by a factor of γ. A detailed analysis on why this is the case has been done in Brown *et al.* (2012). For our simulations, choosing the modified Schwarzschild criterion would require the calculation of the Brunt–Väisälä frequency from stellar temperature and density profiles, whilst choosing the Ledoux criterion would require the creating a new stellar temperature profile from the Brunt–Väisälä frequency given by MESA. We chose the modified Schwarzschild criterion for this work and we will refer to the Brunt–Väisälä frequencies in this thesis as N_{mod}.

The sign of the Brunt–Väisälä frequency was used to determine the extent of the radiation zone defined by

$$N_{mod}(r)^2 > 0. \tag{3.11}$$

This means that for all the models that we have used, the simulation domain starts at the top of the convective core and ends at the base of the surface convection zone. For 3 $M_{\odot}$ stellar models at ZAMS, midMS and TAMS, this covers between 16% to 99% of the total stellar radius. This whole region is then divided into 1500 grid cells in the radial direction and up to 680 spectral nodes in the horizontal direction in our simulations. Figure 3.1 shows the radial resolution and total stellar radius for all the models used in this work.

Model	RZ Resolution/10^8 cm	Radius of simulation domain/10^{11} cm
$3M_\odot$ ZAMS	1.19	1.42
$3M_\odot$ midMS	1.34	2.21
$3M_\odot$ TAMS	2.38	3.69

Table 3.1: The radial resolution used for all the models in this work. We also include the total radius of the simulation domain in centimetres.

3.1.1 Wave Forcing

In order to mimic the generation of IGWs by convection without the added computational cost, the waves are forced as perturbations to the radial velocity, which depend on the frequency and wavenumber in the following manner:

$$v_{r,0}(\omega, \ell) \propto \omega^a m^b \tag{3.12}$$

where the values of a and b for different prescriptions are shown in Table 2.1. The term, m, comes from the definition of the horizontal wavenumber in 2D, where $k_h = m/r$, where m is an integer starting from 1. Here, I introduce an additional spectrum $\mathrm{R_{break}}$, which has two values for "a", which are -0.6 and -2.4, as this spectrum is one with a broken power-law with a transition at 30 µHz. Note that from here on, we switch from using angular frequencies, with units of µrad s^{-1}, to frequencies, with units of µHz.

We follow the work done in Rogers *et al.* (2008) to force these spectra in our simulations using cosine functions, as shown below:

$$\psi = A_{gen} r_c \rho_c \sum_{m=1}^{N_m} m^{b-1} \cos(m\theta) \sum_{i=1}^{N_f} \left(\frac{\omega_i}{\omega_c}\right)^a \cos(\omega_i t), \tag{3.13}$$

where ψ is the same as in Eq. (3.8). The terms, N_m and N_f are the number of discrete wavenumbers and frequencies (constrained by the resolution of our simulations). The convective turnover frequency is defined using Eq.(2.27). For a $3M_\odot$ star at ZAMS, ω_c is approximately 0.05 µHz and varies insignificantly between the models I have used. The stellar density at the bottom of the radiation zone is defined as ρ_c respectively. To keep the energy input for the different generation spectra constant, we introduce the constant, A_{gen}. This value is calculated from matching the volume-averaged mixing-length velocity in the convection zone, provided by MESA, with the integrated $v_{r,gen}$ over all the tested wavenumbers and frequencies.

One of the concerns with using this type of forcing is whether the expected wave flux matches the convective flux. In previous theoretical (Lecoanet & Quataert, 2013) and numerical (Rogers *et al.*, 2013) models, the wave flux, F_w, was found to be roughly the Mach number multiplied by the convective flux, $F_{\mathrm{conv}} = \rho_c u_c^3$. Since the Mach number

Model	Integrated Flux (Units of $F_{\rm conv}$)
ZAMS (no rotation)	0.025
ZAMS ($\Omega = 0.796$µHz)	0.016
ZAMS ($\Omega = 12.73$µHz)	0.021
midMS	0.049
TAMS	0.094

Table 3.2: The integrated flux for all the models in this work calculated using Eq. (3.14). Both Ω in the table refer to the rotation rate of the models, whilst midMS and TAMS refer to middle-of-the-Main-Sequence and Terminal-Age-Main-Sequence models respectively.

for core convection is generally $\sim 10^{-2}$, $F_w \sim 10^{-2} F_{\rm conv}$. To check this, we used the work done in Zahn *et al.* (1997), Kiraga *et al.* (2003) and Alvan *et al.* (2014), where the total integrated wave flux is calculated as follows:

$$F_w = \int_{\omega}^{N} \int_{m} \rho \frac{v_r^2(k_h, \omega')}{k_h \omega'} V_g(k_h, \omega') \, \mathrm{d}m \, \mathrm{d}\omega' \tag{3.14}$$

$$= \int_{\omega}^{N} \int_{m} \frac{\rho r}{N^2} \frac{\omega' v_r^2 \sqrt{N_{mod}^2 - \omega'^2}}{m^2} \, \mathrm{d}m \, \mathrm{d}\omega', \tag{3.15}$$

where V_g is the group velocity. To account for how wave forcing is a smooth process which occurs over the convective-radiative interface, we calculated the integrated wave flux close to the bottom boundary of the simulation domain (and not at the exact boundary), for all the models used in this project, and present them in Table 3.2. The integrated wave flux was found to be consistent with the results seen in Rogers *et al.* (2013).

3.2 Resolving Internal Gravity Waves

To limit our conclusions and investigation to waves which can be both resolved numerically and do not dissipate completely due to thermal diffusion and viscosity, we begin with a discussion on the resolution limit. Low-frequency IGWs have short radial wavelengths, which can be difficult to resolve numerically. The resolving power of our simulations is estimated by using the dispersion relation of IGWs (Eq. (2.11)). The radial wavelength, λ_r, of an IGW is then $2\pi/k_r$. To find the grid spacing required to resolve an IGW in the vertical direction, we calculate the ratio of radial wavelength to grid spacing, dr, for a given horizontal wavenumber, m, and angular frequency, ω, using

$$\frac{\lambda_r}{dr} = \frac{1}{dr} \frac{2\pi r}{m} \sqrt{\frac{\omega^2}{N_{mod}^2 - \omega^2}}. \tag{3.16}$$

Figure 3.2 shows the maximum IGW wavenumber that can be resolved for a frequency

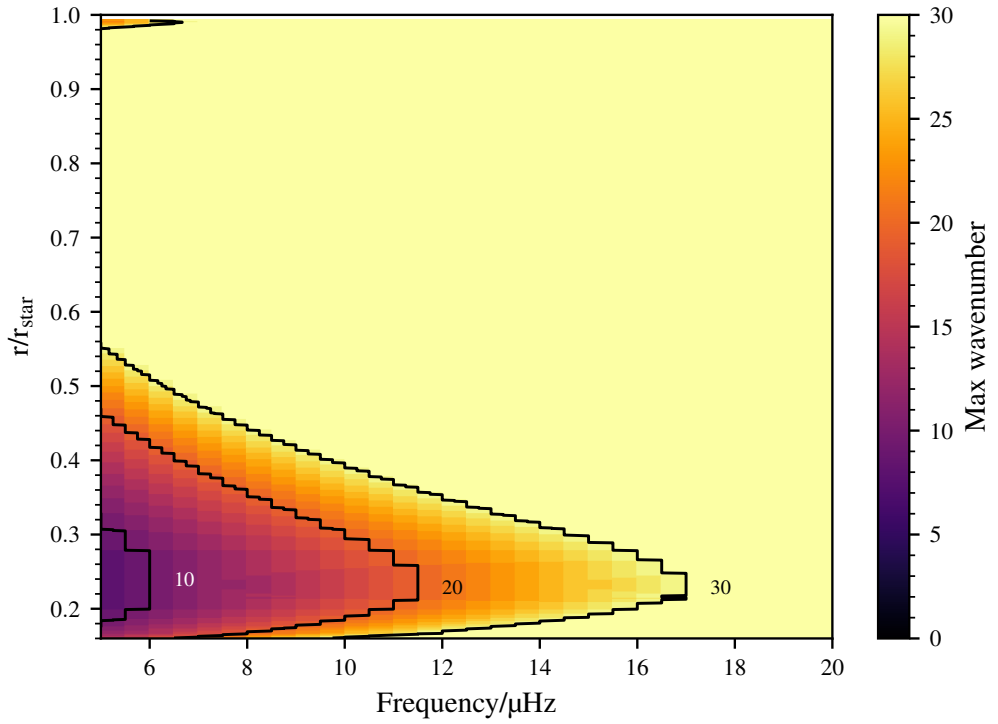

Figure 3.2: The smallest radial wavelengths that can be resolved with four grid points as a function of radius and wave frequency in μHz. The contour lines represent regions where the maximum wavenumber is equal to the value indicated next to the lines.

range of 5 μHz to 100 μHz inside the propagation cavity, using a minimum resolution requirement of four grid cells per vertical wavelength, $\lambda_r/dr = 4$. The smaller resolving power at lower frequencies is due to lower frequency waves having smaller vertical wavelengths. The increase in resolving power with increasing radius is due to increasing vertical wavelengths, caused by decreasing Brunt–Väisälä frequency (see Fig. 3.21). Very close to the surface, the Brunt–Väisälä frequency increases very rapidly before dropping to zero, causing the resolving power to decrease. From the plot, one can see that we cannot reliably resolve lower frequency and larger wavenumber waves, especially at small radii. In the horizontal direction, we use up to 680 spectral nodes and thus, m up to this value should be theoretically resolved. However, in most of our simulations, only wavenumbers up to 20 contribute to the results we expect to observe (i.e. surface IGW spectrum).

Another limit affecting IGWs is given by radiative diffusion and viscosity. Both quantities have to be increased beyond their stellar values to ensure numerical stability. IGWs with high wavenumbers and low frequencies are expected to be affected primarily and we use a dimensional analysis argument to roughly estimate the largest IGW wavenumber before an IGW is completely dissipated by viscous effects/radiative diffusion. This means to match the dimensions of viscosity/thermal diffusivity, we use the IGW wavelength and

frequency. We chose the total wavelength and the angular wave frequency, ω, respectively and under the assumption that $k_r \gg k_h$, we obtain

$$m_{max} = \left(\frac{2\pi}{\max(\nu, \kappa)} \frac{r^2 \omega^3}{N^2 - \omega^2} \right)^{1/2}, \tag{3.17}$$

where m_{max} is the maximum wavenumber at a given frequency and radius before waves are completely dissipated by thermal diffusion or viscosity and the max function selects the larger of the two arguments. Along the radial path of a 10 µHz wave, the minimum value of m_{max} is found to be 6. For all frequencies above 10 µHz, m_{max} was found to be higher and thus, taking into account the numerical resolution limit and the thermal diffusion/viscosity limit, we chose an optimal frequency range of 10 µHz to 500 µHz and a wavenumber range of 1 to 20 for all analysis in the following sections.

3.3 Monochromatic Wave Analysis

3.3.1 Linear RG Equations

To start off the investigation on IGWs in the radiation zone, we return to a concept introduced in Chapter 2, which is the linearising of the Navier-Stokes equations. The general idea is to assume that the linear terms are larger than the non-linear terms in the hydrodynamical equations and introduce a wave-like ansatz to solve the linearised equations. In this work, we follow similar steps and apply it to Eq. (3.1), (3.2) and (3.3) to obtain

$$\nabla \cdot \overline{\rho} \vec{v} = 0, \tag{3.18}$$

$$\frac{\partial \vec{v}}{\partial t} = -\nabla \left(\frac{P}{\overline{\rho}} \right) - C \overline{g} \vec{\hat{r}} \tag{3.19}$$

$$\frac{\partial T}{\partial t} = -v_r \left(\frac{\partial \overline{T}}{\partial r} - (\gamma - 1) \overline{T} h_\rho \right) \tag{3.20}$$

where the rotational, thermal diffusion or viscous effects are not considered. In cylindrical coordinates, the choice of limiting our analysis to two-dimensions allows the z-derivatives to be set to zero. The three equations shown above can then be reduced to a second-order differential equation with $\alpha(r)$ as the evolving term:

$$\begin{aligned} 0 = \partial_{rr}\alpha + \frac{m^2}{r^2} \left(\frac{N^2_{mod}}{\omega^2} - 1 \right) \alpha \\ + \left[\frac{1}{2} \left(\partial_r h_\rho \right) - \frac{1}{2} h_\rho^2 + \frac{1}{2r} h_\rho \right] \alpha \\ + \frac{1}{4r^2} \alpha. \end{aligned} \tag{3.21}$$

where $\alpha = v_r(r)\overline{\rho}(r)^{1/2}r^{3/2}$. The derivation of this equation is given in Appendix A. We have used a wave ansatz of the form $v_r(r,\theta,z) \propto v_r(r)e^{im\theta}e^{-i\omega t}$, where m is the horizontal wavenumber[1], ω is the angular frequency and θ is the angular coordinate in the equatorial plane. Generally, in the radiation zone, there will be regions where the oscillatory term (OT), $\left(N^2_{mod}/\omega^2 - 1\right) m^2/r^2$, dominates and regions where the density term (DT), $0.5\left[(\partial_r h_\rho) - h_\rho^2 + h_\rho/r\right]$, dominates. When the ratio of OT to DT is less than 1, an IGW loses its wavelike behaviour and the approximate radius where this ratio is exactly equal to 1 is called the turning point (Aerts *et al.*, 2010). As mentioned in earlier chapters, behaviour such as internal reflection and wave transmission occurs at this turning point and we shall explore this in the following sections.

With the assumption that IGW wavelength is much smaller than the density scale height which is equal to a locally Boussinesq approximation, DT can be neglected. The last term is always smaller than $\left(N^2_{mod}/\omega^2 - 1\right) m^2/r^2$ as ω is always smaller than N_{mod} and m is always bigger or equal than 1, as there are no purely radial IGWs. So, negelecting this term and DT in Eq (3.21) and applying the WKB approximation to the remaining form of the equation allows us to determine the dependence of the radial IGW amplitude (Please refer to Appendix A for the derivation of this expression) as follows:

$$v_r \propto m^{-1/2}\rho^{-1/2}\, r^{-1}\, (N^2_{mod} - \omega^2)^{-1/4}. \tag{3.22}$$

Applying the same procedure to the anelastic equations in three dimensions, using spherical harmonics (Schmitz, 1990), gives a similar dependence of v_r on ρ but slightly different dependence on r, as follows:

$$v_r \propto (\ell(\ell+1))^{-1/4}\rho^{-1/2}\, r^{-3/2}\, (N^2_{mod} - \omega^2)^{-1/4}. \tag{3.23}$$

Comparing the results in 2D and 3D, we obtain a simple conversion factor of $r^{1/2}$, when $m = (\ell(\ell+1))^{1/2}$, which causes waves in 2D to have slightly higher surface amplitudes. As an example, comparing a wave with $m = 1$ in 2D and a wave with $\ell = 1$ in 3D, both generated near the convection zone at $\mathrm{r/r_{star}} = 0.14$ with hypothetically the same amplitude, the surface IGW amplitude (at $\mathrm{r/r_{star}} = 0.99$) ratio will be

$$\frac{v_{r,2D}}{v_{r,3D}} = (0.99)^{-1-(-1.5)}(0.14)^{1-1.5} = 2.659. \tag{3.24}$$

3.3.2 Single wave validation

To start the investigation, we forced single monochromatic IGW at the bottom boundary of the simulation domain. The background viscosity was set to a constant value 1×10^{12}

[1]We use the term, wavenumber to represent m and k_h, which is m/r, interchangeably in this chapter and in all cases, we make it clear which one we are referring to.

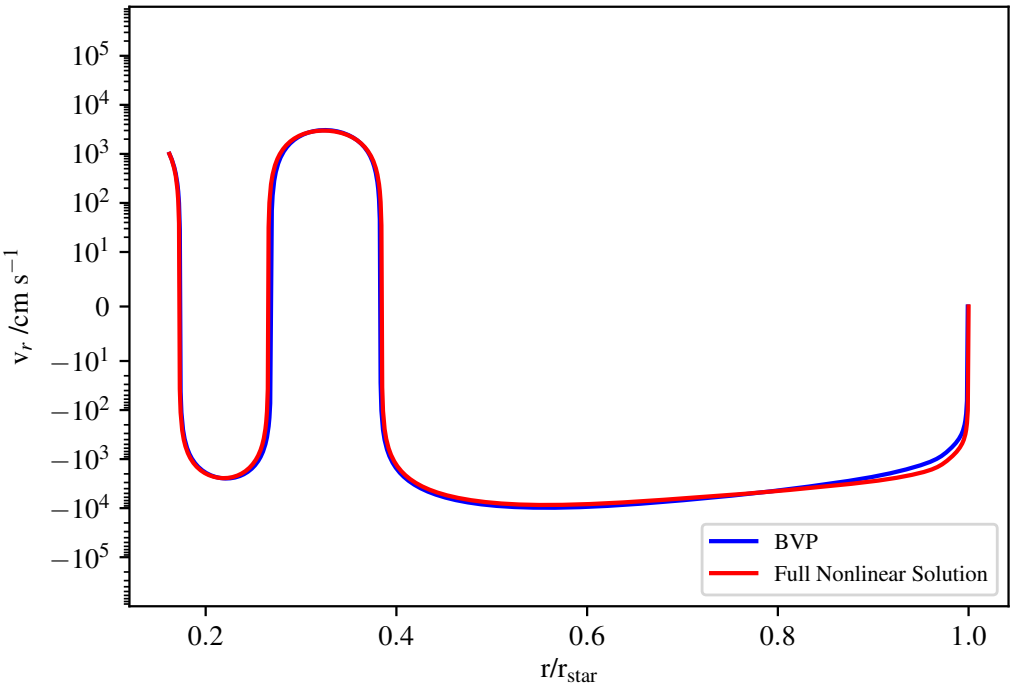

Figure 3.3: Radial velocities along a ray against the radius of the star in units of the total stellar radius. The red line represents solutions from the fully non-linear hydrodynamical simulation. The blue line represents solutions from solving Eq. (3.21) as a boundary value problem (BVP). The y-axis of the plot has a linear scale between -10 and 10, and uses log scaling outside this range.

cm^2 s^{-1}. The simulations were run for a time of 720 wave cycles for a forced wave with an amplitude of 1000 cm s^{-1}, frequency of 120 μHz and wavenumber of $m = 3$. Note that the magnitude of the amplitude was chosen based on the range for bulk velocities (10^2 cm s^{-1} – 10^4 cm s^{-1}) in the convection zone predicted by MLT for this stellar model.

Figure 3.3 shows the radial velocity profile for this wave as a function of radius. The red line represents results from the fully non-linear simulation while the blue line represents the solution from Eq. (3.21) solved using a tridiagonal matrix solver (Thomas, 1949) with the top and bottom boundary values set to match the boundary values of the hydrodynamical simulation. Although the simulation is fully non-linear, the good matching between the red line and the blue line here can be attributed to three factors. First, the forced wave experiences very little radiative damping due to its high frequency (see Chapter 2). Second, we varied the explicit viscosity, by one order of magnitude in both directions (larger and smaller) in the domain and saw no observable changes to the waveform, meaning it is not in the regime where viscous damping is relevant. Finally, the forced wave has a low non-linearity parameter (Eq. (2.21)) as defined in Section 2.3.1. We find that ϵ does

not exceed 0.00127 anywhere in the domain. Thus, the forced wave is not expected to experience strong non-linear effects ($\epsilon \geqslant 1$). However, these waves might still undergo weak non-linear interactions, as seen in later sections.

3.3.3 Non-linear simulations of monochromatic waves

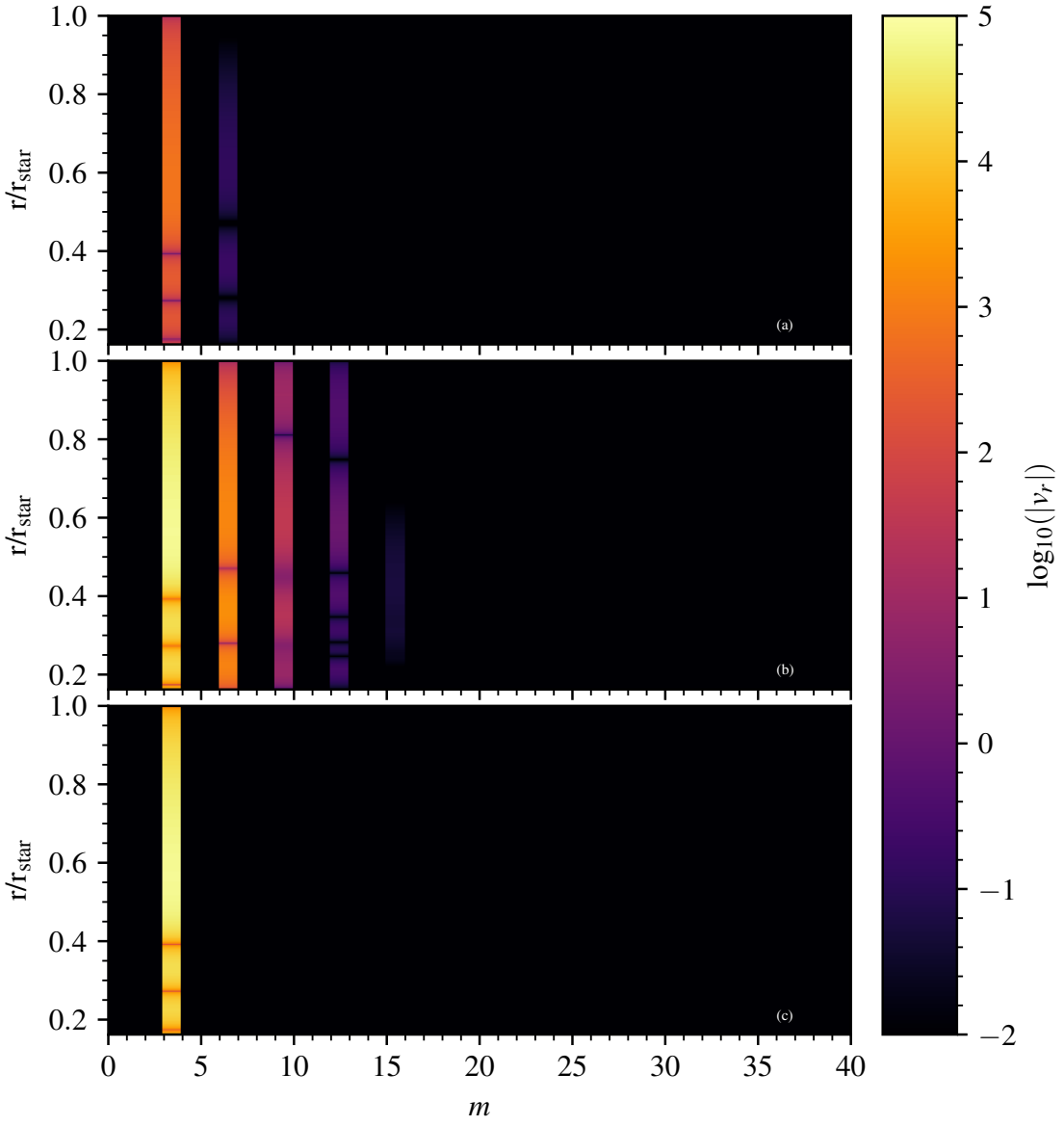

Figure 3.4: Spatial Fourier transform of the radial velocities at $t = 60$ wave cycles at different radii for a wave forced at 120 µHz and $m = 3$. The top panel (a) represents simulations results with a wave forced at an amplitude of 100 cm s^{-1} whilst the middle panel (b) represents simulation results with a wave forced at an amplitude of 1000 cm s^{-1}. The bottom panel (c) represents simulation results with no non-linear terms forced at an amplitude of 1000 cm s^{-1}.

In a non-linear system, we can expect forced monochromatic gravity waves to undergo self-interaction. To investigate this, we look at how energy is transferred between waves of different wavenumbers. Figure 3.4 shows wave amplitudes as functions of stellar radius and wavenumbers for a wave forced at 120 µHz and $m = 3$. The forced wave has an amplitude of 100 cm s^{-1} in panel (a) and 1000 cm s^{-1} in panel (b). In panel (c), we ran a simulation with a wave forced at an amplitude of 1000 cm s^{-1}, frequency 120 µHz and $m = 3$ but with the non-linear terms turned off in the code. In Fig. 3.4(a), we observe a wave at $m = 6$, which is an indication of energy transfer from larger scales to smaller scales. Despite having a very low non-linearity parameter ($\epsilon \leq 0.000126$), there is still energy transfer occurring. Increasing the amplitude to 1000 cm s^{-1} ($\epsilon \leq 0.00126$) causes more waves to be generated at larger m, as shown in Fig. 3.4(b), whilst switching off the non-linear terms completely removes waves at higher wavenumbers, as shown in Fig. 3.4(c). As expected, this shows that the non-linear wave self-interaction transfers energy from large to small scales and the energy transfer rate is dependent on the forced wave amplitude.

	Ratio of harmonic amplitudes		
Forcing Amplitude/cm s^{-1}	$m = 3$	$m = 6$	$m = 9$
100	1	1	1
1000	10	10^2	10^3
10000	100	10^4	10^6

Table 3.3: The table shows the approximate ratio of harmonic amplitudes between stated forcing amplitudes (left column) and the lowest forcing amplitude, which is 100 cm s^{-1}. These ratios are approximate averages over the whole simulation regime. The forced wavenumber is $m = 3$, whilst the first harmonic is $m = 6$ and the second harmonic is $m = 9$.

To quantify the rate of energy transfer as a function of wave amplitude, we compare the amplitudes of the higher harmonics for the two different forcing amplitudes. Table 3.3 shows the ratio of harmonic amplitudes from the simulations with the stated forcing amplitude (100 cm s^{-1}, 1000 cm s^{-1} and 10000 cm s^{-1}) to the harmonic amplitudes from the simulation with the lowest forcing amplitude (100 cm s^{-1}). At the zeroth harmonic ($m = 3$) order, the ratio of harmonic amplitudes increases by the same order of magnitude as the increase in the forcing amplitude, which means that increasing the forcing amplitude by 10 causes a linear increase in the $m = 3$ wave amplitudes. At the first harmonic order ($m = 6$), the ratio of amplitudes is 100 and at the second harmonic order ($m = 9$), it is 1000. Running another simulation with a forcing of 10000 cm s^{-1}, we find the ratios of harmonic amplitudes to be 10^4 at $m = 6$ and 10^6 at $m = 9$. This indicates that the energy transfer to higher wavenumbers is larger for higher forced wave amplitudes and it is proportional to $A_r^{2(h+1)}$, where A_r is the ratio of amplitudes between the forced waves and h is the harmonic order. The factor of 2 comes from the dimensional argument that

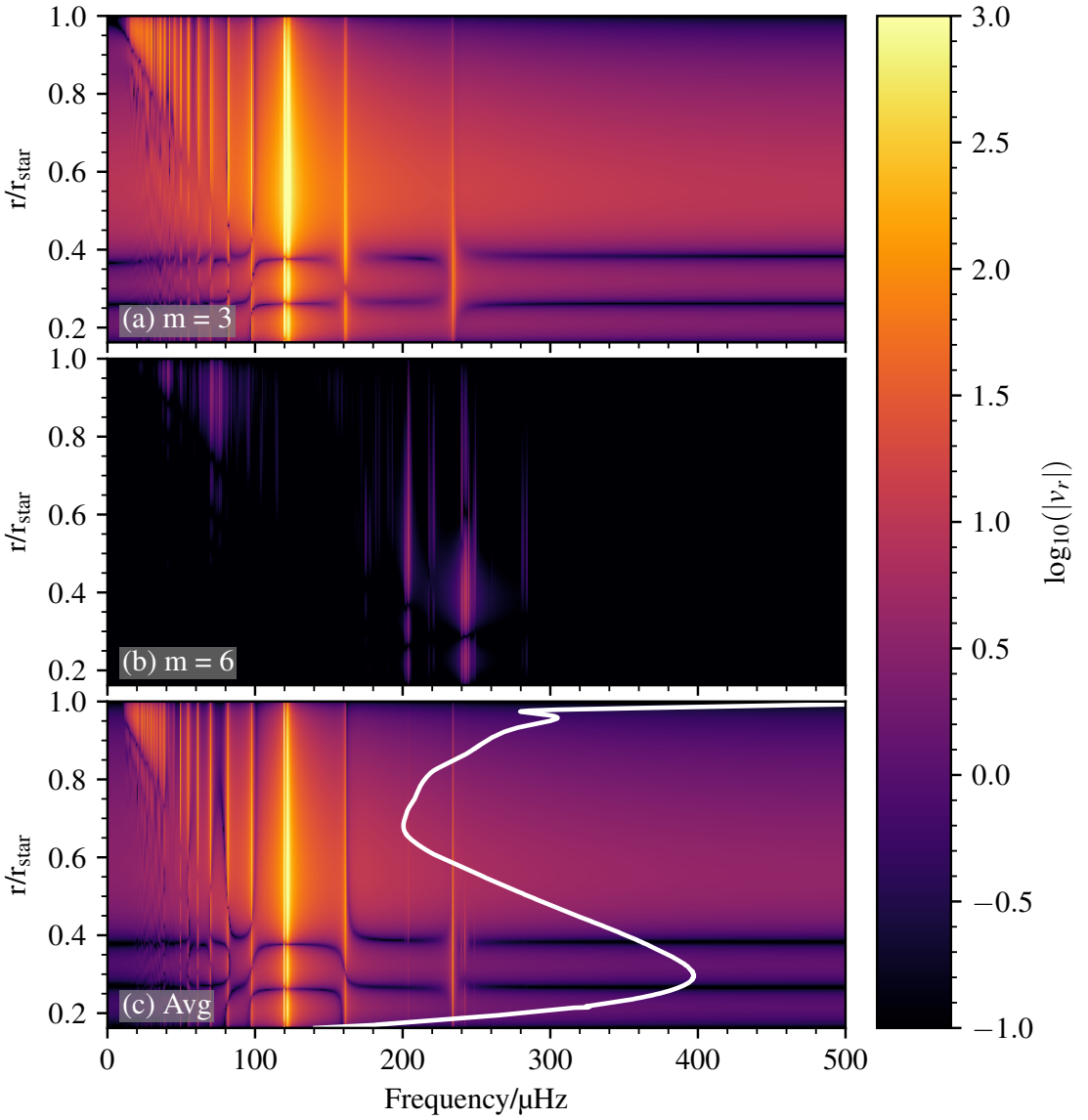

Figure 3.5: Radial velocities as functions of stellar radius and frequency for a wave forced at 120 μHz and $m = 3$. Panel (a) shows the radial velocities at a wavenumber $m = 3$, panel (b) is for $m = 6$ and panel (c) shows the wavenumber-averaged radial velocities. The white line in panel (c) indicates the Brunt–Väisälä frequency profile for this stellar model. We observe waves at frequencies lower than the forced wave frequency, which is likely related to the interaction between these waves and the varying Brunt–Väisälä frequency profile.

at least the kinetic wave energy is proportional to the square of velocity.

Moving to energy transfer between waves in frequency space, Fig. 3.5 shows vertical velocity amplitudes at different radii and frequencies for the $m = 3$ (Fig. 3.5(a)) and $m = 6$ (Fig. 3.5(b)) as well as amplitudes averaged over all wavelengths (Fig. 3.5(c)), for the simulation with a 120 μHz, $m = 3$ wave, forced with an amplitude of 1000 cm

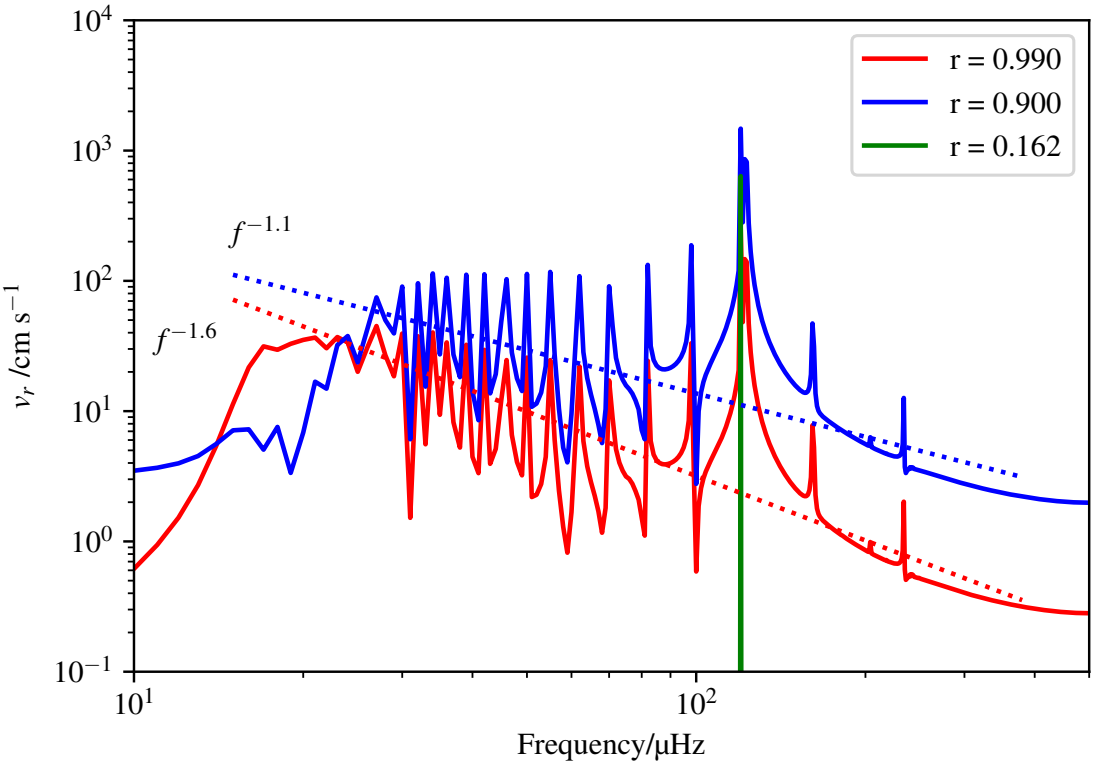

Figure 3.6: Temporal Fourier transforms of the radial velocities at three different radii for a wave forced at 120 μHz and $m = 3$. The radii given in the legend are in units of the total stellar radius. The dashed lines represent straight line fits to $\log_{10}(v_r)$ and $\log_{10}(\text{freq})$.

s^{-1}. The Brunt–Väisälä frequency profile has been plotted (white line) in the bottom panel. We find two main results from this analysis. First, forcing a wave close to a cavity mode frequency[2] produces more efficient energy transfer to different cavity mode frequencies. For example, from Fig. 3.5(a), we can see that at approximately 235 μHz, a fundamental mode (stationary wave with zero nodes) can be observed and at 160 μHz, the first harmonic cavity mode (stationary wave with 1 node). Second, weakly non-linear interactions between waves allow energy transfer to waves at frequencies that are integer multiples of the forced wave frequency. In Fig. 3.5(b), we observe a wave at 240 μHz, which is indicative of resonant triadic interactions, first discovered in the context of fluid dynamics in Phillips (1960, 1961). Detailed analysis of this form of weakly non-linear interaction can be found in Müller *et al.* (1986). To summarise, energy transfer between internal gravity waves can occur when the following conditions are met:

$$\vec{k}_1 \pm \vec{k}_2 = \pm\vec{k}_3 \tag{3.25}$$

[2]By cavity mode frequency, we mean the eigenfrequencies of the system. These frequencies result from the eigenmode solution of the linear Navier-Stokes equations in the anelastic approximation. These are stationary waves which are also referred to as g-modes in asteroseismology.

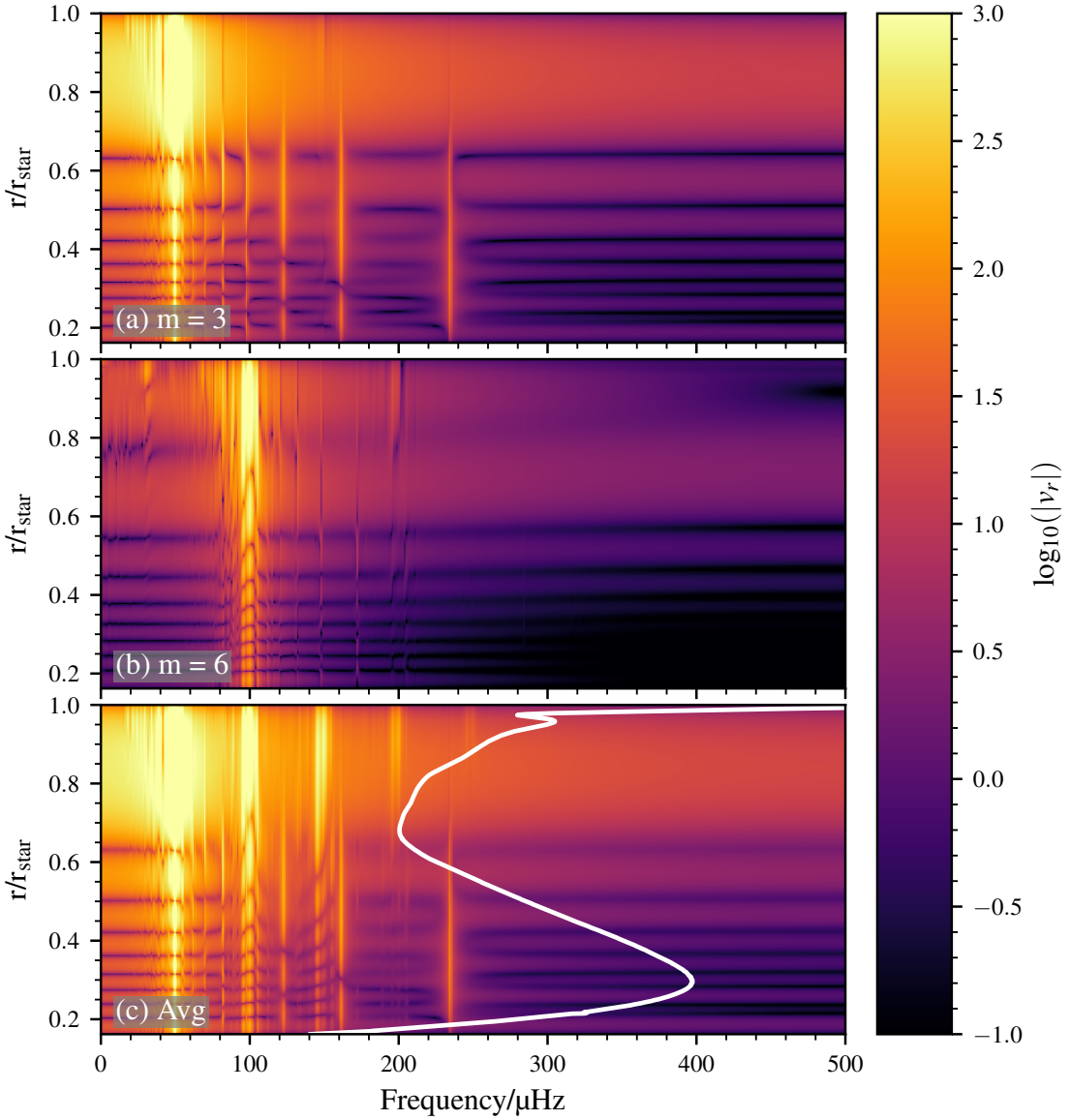

Figure 3.7: Radial velocities as functions of stellar radius and frequency for a wave forced at 50 μHz and $m = 3$. Panel (a) shows the radial velocities at a wavenumber $m = 3$, panel (b) is for $m = 6$ and panel (c) shows the wavenumber-averaged radial velocities. The white line in panel (c) indicates the Brunt–Väisälä frequency profile for this stellar model

$$\omega_1(\vec{k}_1) \pm \omega_2(\vec{k}_2) = \pm\omega_3(\vec{k}_3) \tag{3.26}$$

where the terms on the left side of the equations above are the wavenumbers and frequencies of the parent waves whilst the terms on the right are the wavenumber and frequency of the daughter wave.

Figure 3.6 shows line plots of the radial velocity spectrum at the top of the radiation

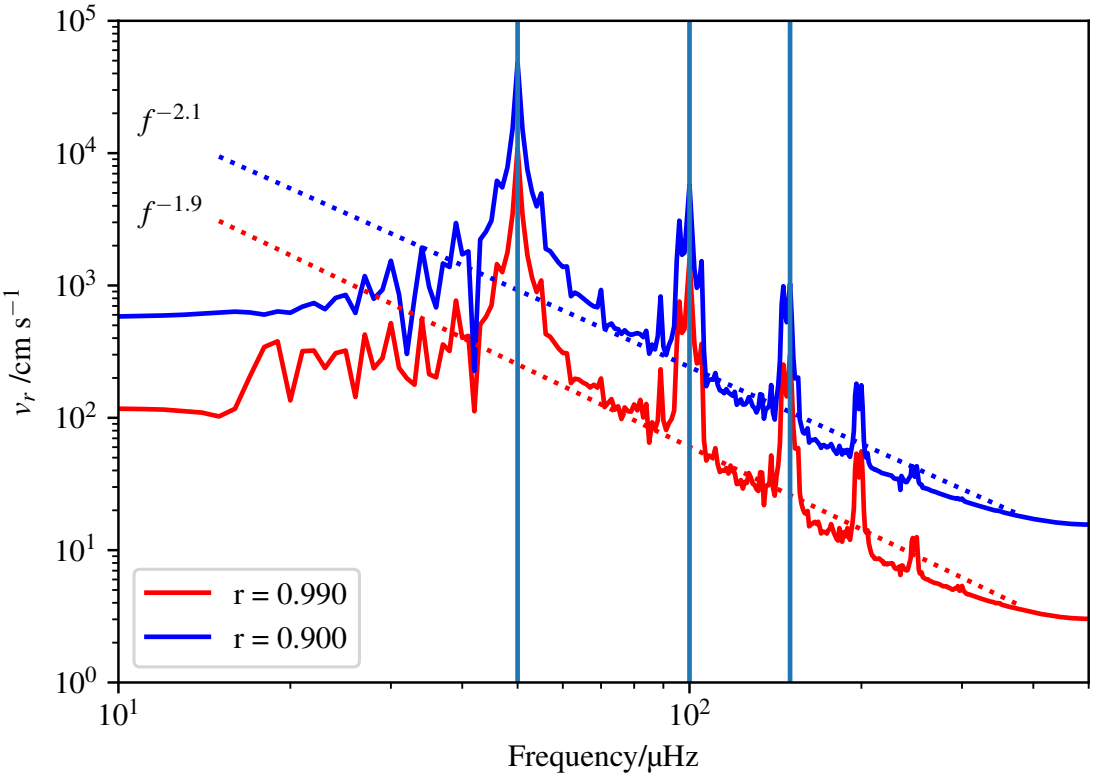

Figure 3.8: Temporal Fourier transforms of the radial velocities at three different radii for a wave forced at 50 μHz and $m = 3$. The radii given in the legend are in units of the total stellar radius. The dashed lines represent straight line fits to $\log_{10}(v_r)$ and $\log_{10}(\text{freq})$. The vertical straight lines represents frequencies 50 μHz, 100 μHz and 150 μHz.

zone ($r/r_{star} = 0.99$ and $r/r_{star} = 0.90$)[3]. Past numerical simulations of stellar interiors that included the convective core and resolved IGWs have been limited to r = 0.9 for numerical stability, which is why we include the spectrum at this radius for comparison purposes. The spike with the green line indicates the forcing frequency. The propagation of this wave to the surface causes similar peaks at r = 0.90 (blue line) and r = 0.99 (red line), as expected. The slope in logarithmic frequency space was found to be -1.1 at 90% the total radius and -1.6 at 99% the total radius. At lower frequencies, thermal diffusion dominates, leading to waves at generation being damped over a short distance. However, the presence of low-frequency wave structures at large radii show that the transfer of energy from high-frequency waves to low-frequency waves occurs locally, as seen in Fig. 3.5(a) and Fig. 3.6.

Fixing the wavenumber at $m = 3$, we investigated the evolution of the radiation zone with two other forced frequencies: one at 10 μHz and the other at 50 μHz. In both cases, the forced wave amplitude was set to 1000 cm s^{-1}. Figure 3.7 shows the frequency spectra

[3]We will refer to r/r_{star} as r from here on unless stated otherwise.

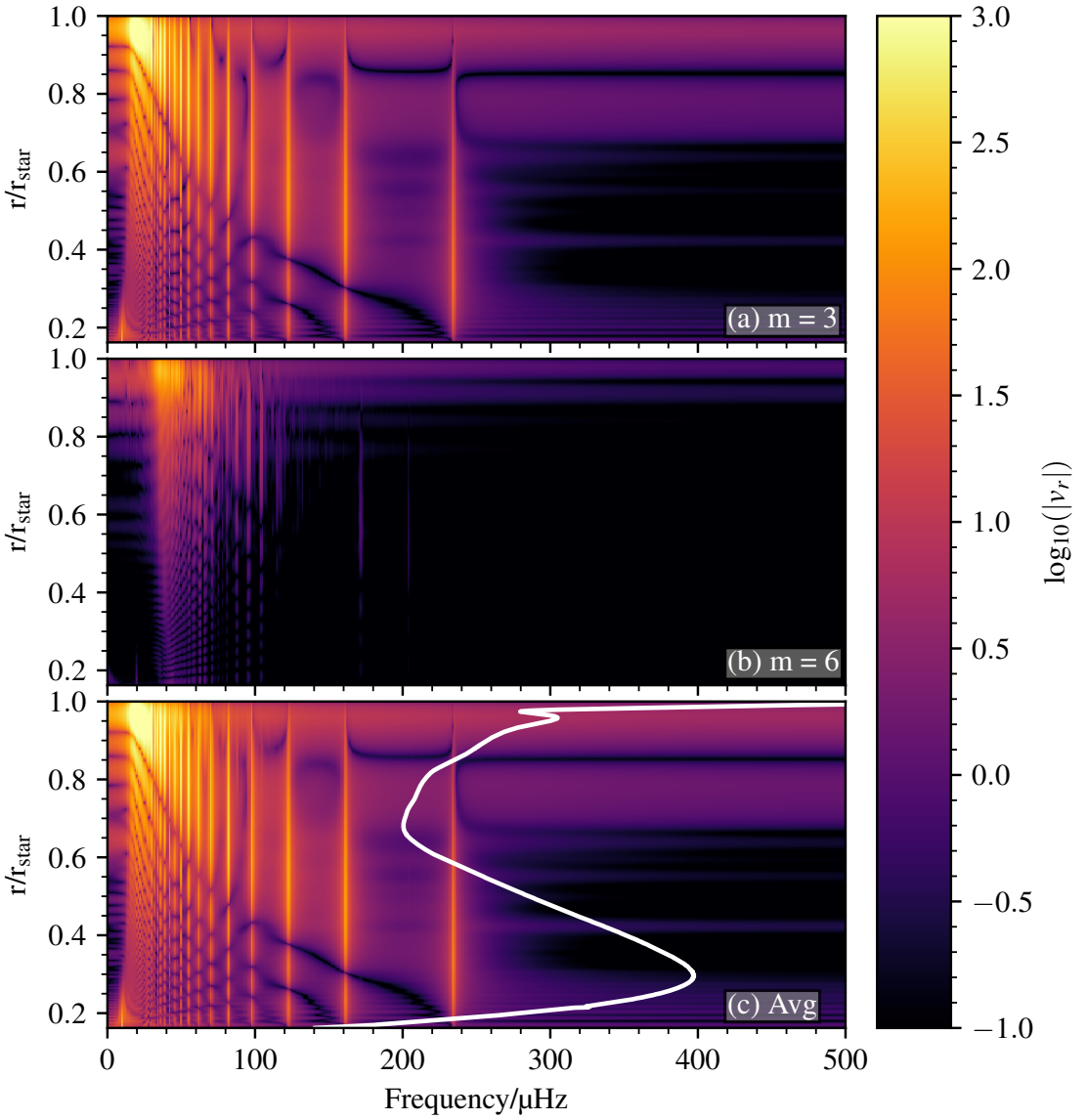

Figure 3.9: Radial velocities as functions of stellar radius and frequency for a wave forced at 10 μHz and $m = 3$. Panel (a) shows the radial velocities at a wavenumber $m = 3$, panel (b) is for $m = 6$ and panel (c) shows the wavenumber-averaged radial velocities. The white line in panel (c) indicates the Brunt–Väisälä frequency profile for this stellar model.

for a wave forced at 50 μHz, similar to Fig. 3.5 for a forced wave with a frequency of 120 μHz and $m = 3$. Looking at the frequency spectrum at $m = 3$ (top panel), we see the wave modes that resonate with the cavity, being generated. At $m = 6$ (middle panel), we see a wave at 100 μHz but no resonant cavity modes are generated. In the bottom panel, we observe peaks at integer multiples of 50 μHz. This is a clear feature of triadic interaction. To investigate the surface frequency spectrum, we take two slices of the plot in Fig. 3.7, which show that at 90% the total radius of the star, the frequency slope is -1.9, whilst at

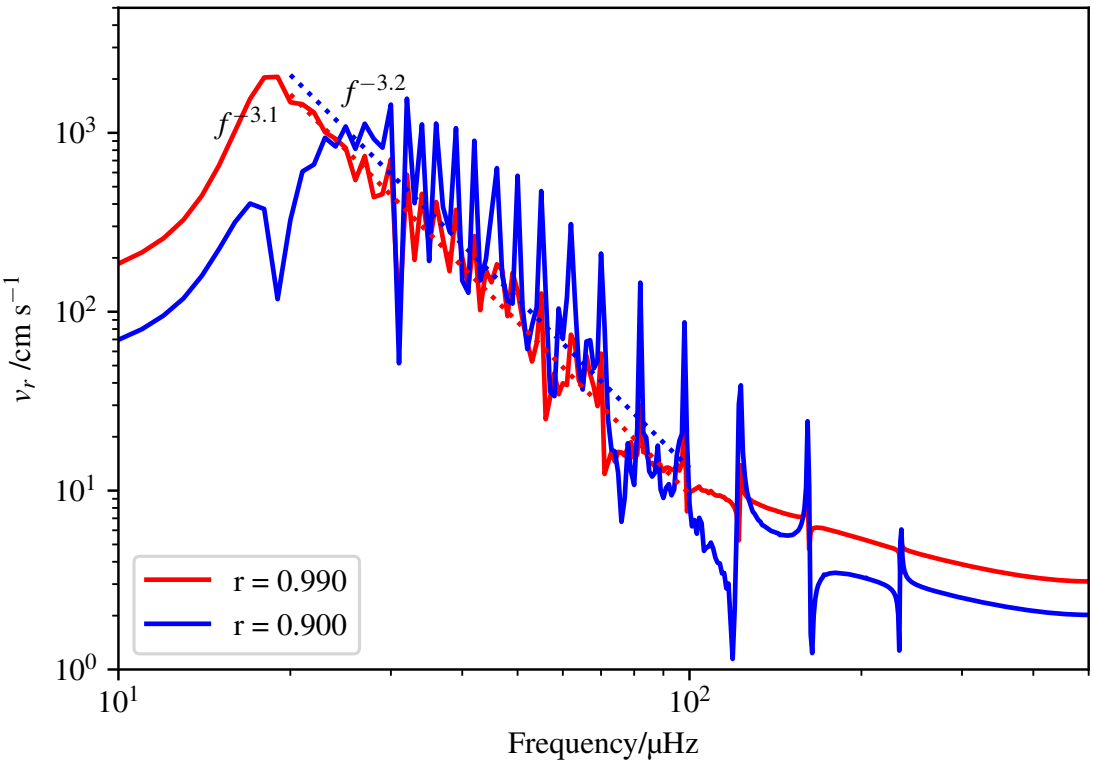

Figure 3.10: Temporal Fourier transforms of the radial velocities at three different radii for a wave forced at 10 μHz and $m = 3$. The radii given in the legend are in units of the total stellar radius. The dashed lines represent straight line fits to $\log_{10}(v_r)$ and $\log_{10}(\text{freq})$.

99%, the slope is -2.1 (see Fig. 3.8).

When a wave with a frequency of 10 μHz and $m = 3$ is forced at the bottom boundary, this wave can be seen to damp over a very short distance as shown in Fig. 3.9(a). However, at $m = 3$, almost all the cavity modes are forced. At $m = 6$ (panel (b)), triadic interactions close to the bottom boundary allow a wave of 20 μHz to be formed, which then excites cavity modes at higher frequencies and so on. Finally, in Fig. 3.10, we can see that the frequency slopes are -3.2 and -3.1 for the cases of $r = 0.9$ and $r = 0.99$ respectively. This slope is even steeper than that in the case of the 50 μHz wave.

To summarise, we found that when single waves are forced at the bottom of the radiation zone with very low non-linearity parameter, non-linear energy transfer occurs from the forced wave to higher harmonic. The two main energy transfer mechanisms are wave self-interaction and cavity mode interaction. Moreover, we found that the slope of the frequency spectrum becomes steeper with smaller forced wave frequency.

3.3.4 Further Wave Validation

From the analysis in this section so far, one may ask whether all the waves have reached steady states[4] or even whether they are actually IGWs (satisfy the IGW dispersion relation), apart from the forced waves. To check wave stability, we investigated the evolution with time of all three forced monochromatic (10 µHz, 50 µHz and 120 µHz) waves at an amplitude of 1000 cm s^{-1}, and one of their daughter waves. Figure 3.11 shows the evolution of amplitude of a 10 µHz, $m = 3$ wave and one of its daughter wave, a 20 µHz, $m = 3$ wave as a function of time, at radii r = 0.163 (blue dots), r = 0.581 (orange dots), r = 0.833 (green dots) and r = 0.99 (red dots), all in units of the total stellar radius. After an initial rapid increase, both of these waves appear to be in steady-state at all radii with some marginal fluctuations and a slight decrease in time.

We performed the same analysis on the 50 µHz, $m = 3$ and 120 µHz, $m = 3$ forced wave simulation data and the results are shown in Fig. 3.12 and Fig. 3.13. For the cases of the 50 µHz, $m = 3$ and 100 µHz, $m = 3$ waves (see Fig. 3.12), we see that both amplitudes are still increasing with time, with the 50 µHz, $m = 3$ wave amplitudes increasing with a shallower gradient compared to the 100 µHz, $m = 3$ wave amplitudes. This exponential increase is indicative of non-linear interaction, specifically triadic interaction between waves. It also shows that this wave has not reached a clear steady state and can be a reason why we don't observe cavity modes in this simulation (see Fig. 3.7). In stellar interiors, we expect the forcing amplitude to be 100 – 1000 times smaller than that used here, which means that the non-linearity parameter will be smaller. Thus, we found that when the same wave is forced with a lower amplitude (100 cm s^{-1}), the increase in amplitude is slower compared to that seen in all the waves in Fig. 3.12.

Fig. 3.13 shows the wave amplitude evolution for a 120 µHz, $m = 3$ forced wave and its daughter waves at 240 µHz, $m = 3$. These waves show steady-state evolution from the beginning of the simulation. We found that it takes at least 1.9×10^8 s, or 6 years for the 120 µHz, $m = 3$ wave amplitude at any radius to drop by 1 order of magnitude, provided the amplitudes do not stabilise before that. One might argue that the time it takes for any wave to reach a steady-state is the damping time, $t_{\rm damp}$, expressed as

$$t_{\rm damp} = \gamma^{-1} = K k_r^2, \tag{3.27}$$

based on the work done in Kumar *et al.* (1999). Figure 3.14 shows the damping time as a function of radius for all forced monochromatic waves and one of their daughter waves. It can be seen the damping time varies substantially (almost 6 orders of magnitude between the bottom and top of the radiation zone). We also plot the damping time as γ^{-1} (red dashed lines) at the stellar surface (r = 0.99) for all three forced wave simulations in

[4]Steady-state evolution refers to constant time-averaged IGW amplitudes.

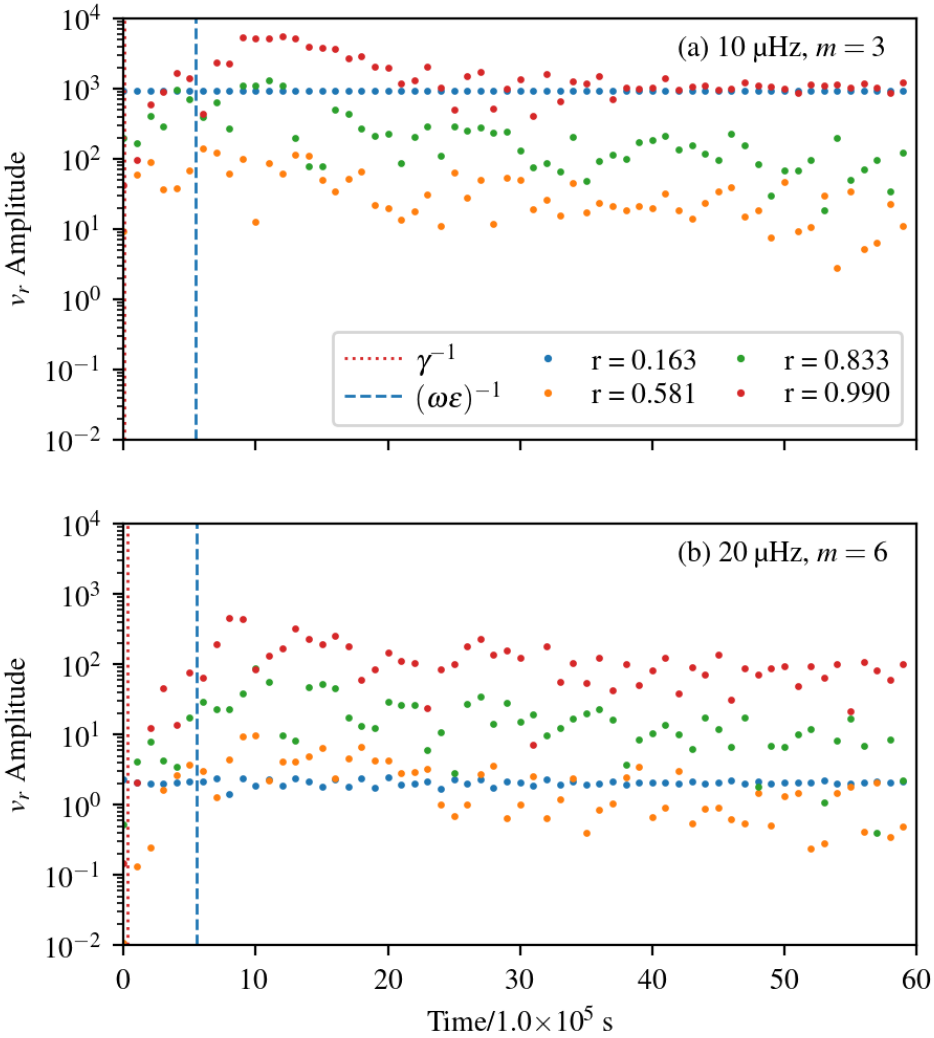

Figure 3.11: The amplitude evolution of a (a) 10 μHz, $m = 3$ wave and its daughter wave, (b) 20 μHz, $m = 3$ wave from a simulation where on 10 μHz, $m = 3$ wave was forced at the bottom boundary of the radiation zone of a 3 $M_\odot$ star. The colours represent different radii (given in units of the total stellar radius). The vertical dashed lines represent the non-linear timescale, $(\omega\epsilon)^{-1}$, at generation whilst the vertical dotted lines represent the damping timescale, γ^{-1} at the stellar surface.

Fig. 3.11, Fig. 3.12 and Fig. 3.13. We find that this damping time was not an acceptable indication of the time it takes for these IGWs to reach steady state. Unfortunately, without knowing the approximate time required for these waves to reach a steady-state, it will not possible to estimate the final, stable amplitudes of these waves. Note that it is also entirely possible that the decreasing amplitude is related to non-linear energy transfer, which is also another reason why the damping time is not a good estimate for the time taken for the waves to reach steady-state amplitudes.

To check whether the forced waves and their harmonics in our simulations are IGWs,

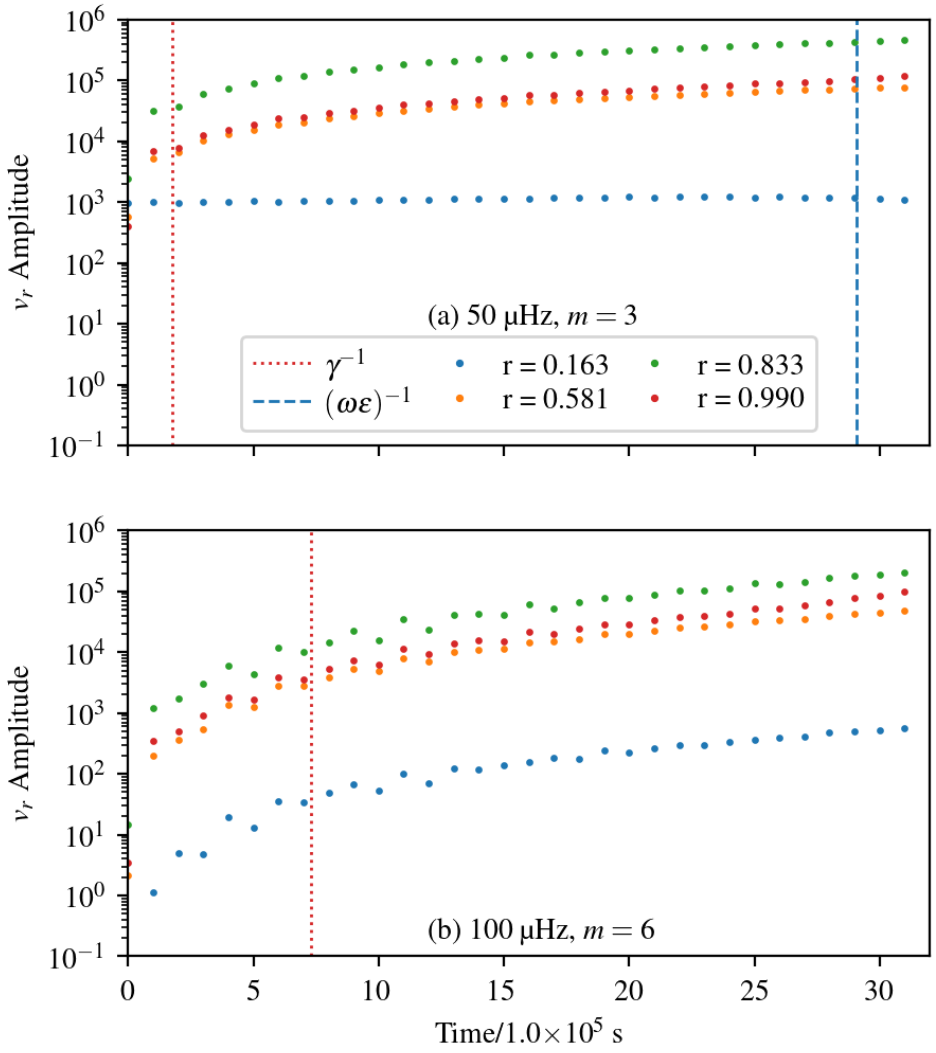

Figure 3.12: The amplitude evolution of a (a) 50 μHz, $m = 3$ wave and a (b) 100 μHz, $m = 3$ wave from a simulation where on 50 μHz, $m = 3$ wave with an amplitude of 1000 cm s^{-1} was forced at the bottom boundary of the radiation zone of a 3 $M_\odot$ star. The colours represent different radii (given in units of the total stellar radius). The vertical blue dashed line represents the non-linear timescale, $(\omega\epsilon)^{-1}$ at generation whilst the vertical red dotted lines represent the damping timescale, γ^{-1}, at the stellar surface.

we utilised a method described in Edelmann *et al.* (2019), where visible nodes are used to calculate the IGW radial wavenumber as a function of radius. The ratio of this radial wavenumber to the radial wavenumber calculated using the IGW dispersion relation is plotted in Fig. 3.15 for forced frequencies (a) 120 μHz, $m = 3$, (b) 50 μHz, $m = 3$, and (c) 10 μHz, $m = 3$. When this ratio is close to one (indicated by the colour white), the dispersion relation is satisfied. For all three forced waves discussed in Fig. 3.11, Fig. 3.12 and Fig. 3.13 and their daughter waves, which are expected to be produced from triadic

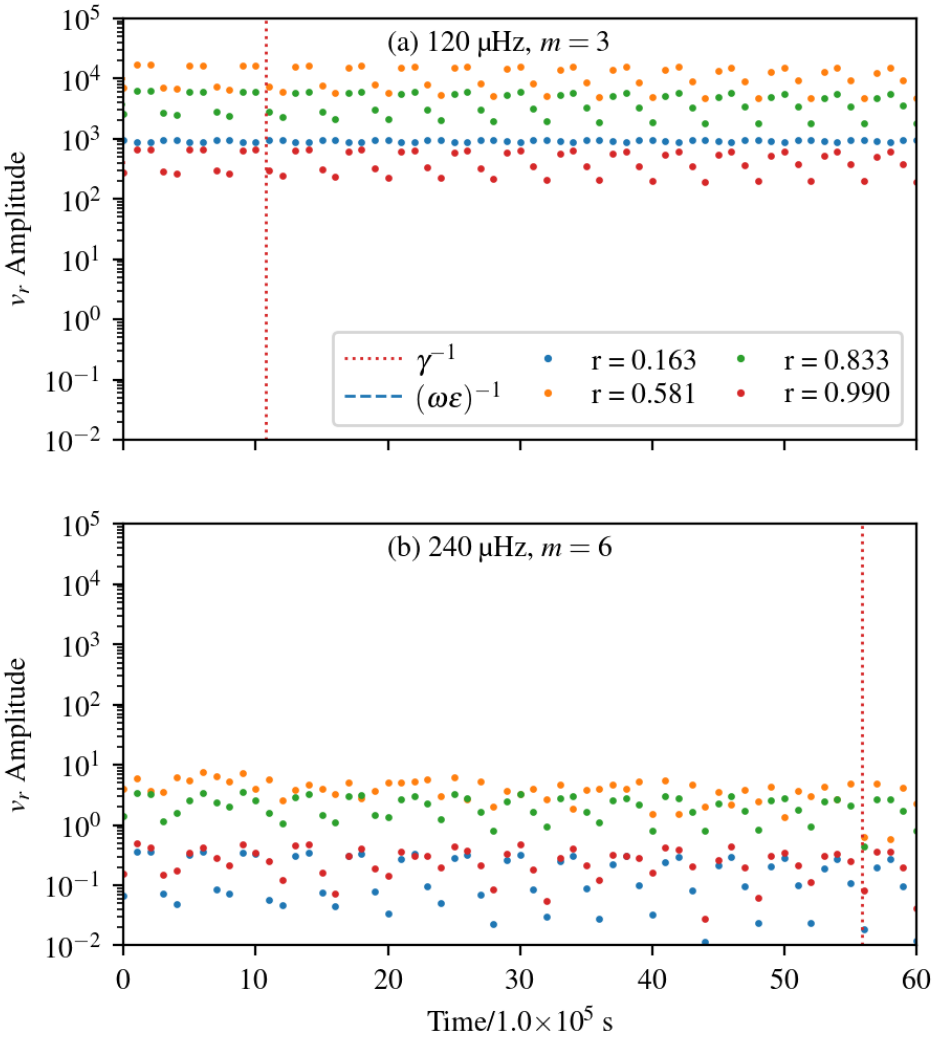

Figure 3.13: The amplitude evolution of a (a) 120 μHz, $m = 3$ wave and a (b) 240 μHz, $m = 3$ wave (right panel) from a simulation where on 120 μHz, $m = 3$ wave was forced at the bottom boundary of the radiation zone of a 3 $M_\odot$ star. The colours represent different radii (given in units of the total stellar radius). The vertical dashed lines represent the non-linear timescale ,$(\omega\epsilon)^{-1}$, at generation whilst the vertical dotted lines represent the damping timescale, γ^{-1} at the stellar surface.

interactions, we can see that the dispersion relation is at least partly satisfied in the radiation zone. This partial satisfaction of IGW dispersion relation can be explained by waves losing their wave properties at the turning point (see Aerts *et al.* (2010)), defined by the location where the wave term (second term) in Eq. (3.21) becomes smaller than the density terms (terms in the square bracket) and the last term, as discussed in Section 3.3.1.

Previously, we discussed cavity modes, which are eigenmode solutions to the linear wave equation. We found that they have higher amplitudes when the forced wave frequency is close to a cavity mode. To check whether the cavity modes we observe satisfy

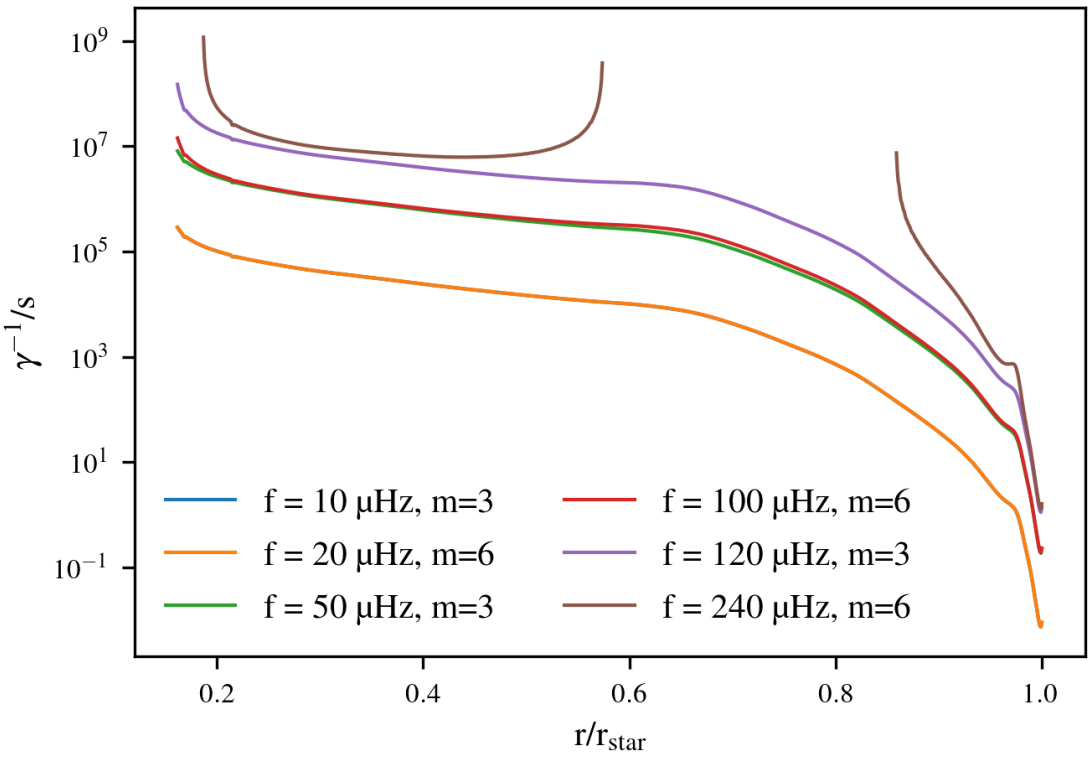

Figure 3.14: The damping time, defined as γ^{-1} against the stellar radius in units of the total stellar radius for waves of several frequencies and wavenumbers indicated in the legend. The lines for 10 μHz, $m = 3$ (blue) and 20 μHz, $m = 3$ (orange) almost overlap each other.

the dispersion relation, we return to Fig. 3.15. We observe thin, white lines at higher frequencies (indicating IGW dispersion relation being satisfied) in almost all the plots, except for the 100 μHz, $m = 6$ case as seen in Fig. 3.15b(ii). We will return to why this might be occurring but first, to check whether the dispersion relation is satisfied at lower frequencies, we use a root-finding method on the following expression, from Aerts *et al.* (2010) to extract the asymptotic cavity mode frequencies:

$$\int_{r_{\rm gen}}^{r_{\rm tp}} \frac{m}{r} \left(\frac{N^2_{mod}}{\omega^2} - 1 \right)^{1/2} dr = \left(n - \frac{1}{2} \right) \pi \tag{3.28}$$

where $r_{\rm gen}$ is the generation radius, $r_{\rm tp}$ is the turning point radius, and n is the number of nodes in a cavity mode. The plots in Fig. 3.16 show these eigenfrequencies (red vertical lines) overplotted on the simulation results for forced wave frequencies of (a)120 μHz, (b)50 μHz and (c)10 μHz at the stellar surface (r = r$_{\rm star}$). For 10 μHz and 120 μHz, the analytical cavity mode frequencies match the simulation results well as shown in Fig. 3.16c and Fig. 3.16a. At 50 μHz (see Fig. 3.16b), this does not seem to be the case as we observe the 50 μHz peak dominating the spectrum at $m = 3$ and the 100 μHz peak dominating

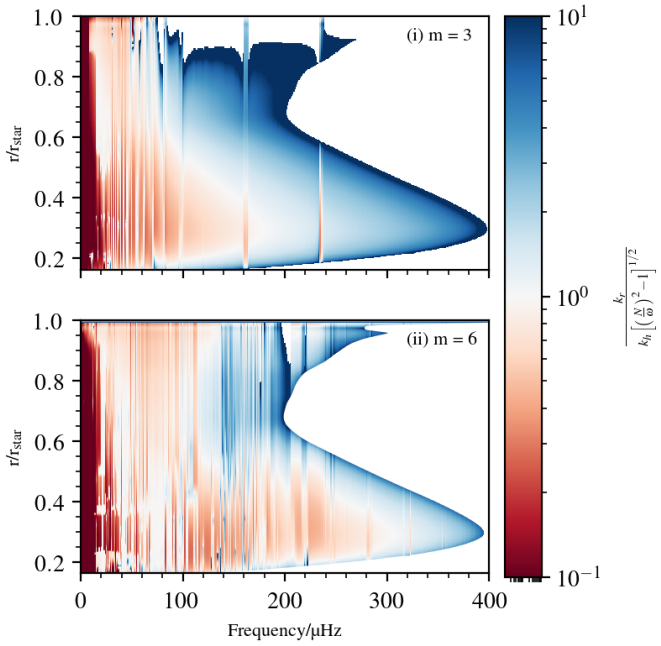

(a) 120 μHz

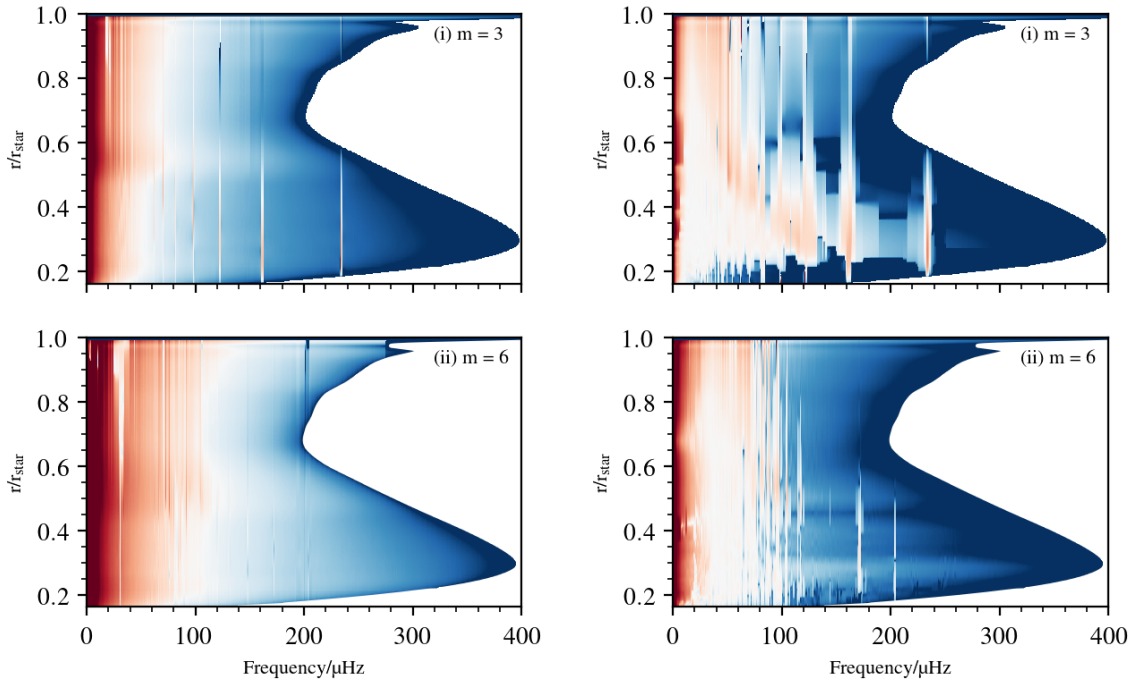

(b) 50 μHz

(c) 10 μHz

Figure 3.15: The ratio of visible radial wavenumber to theoretical radial wavenumber as functions of stellar radius, in units of total stellar radius, and frequency. The panels represent simulations with forced waves at (a)120 μHz, $m = 3$, (b)50 μHz, $m = 3$ and (c)10 μHz, $m = 3$. The top and bottom plots in each panel represent radial wavenumber ratios at (i) $m = 3$ and (ii) $m = 6$.

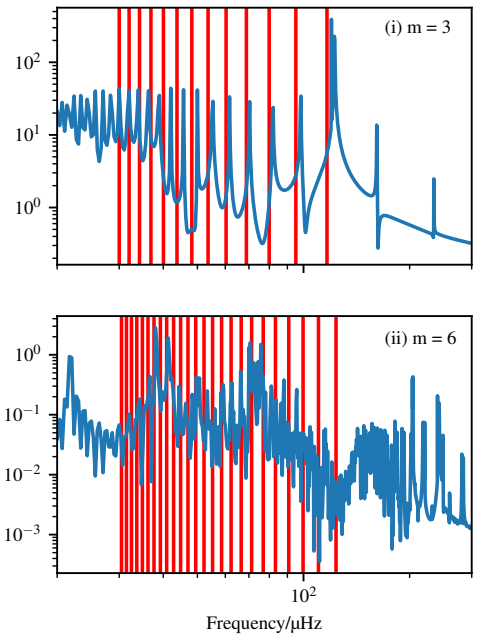

(a) 120 μHz

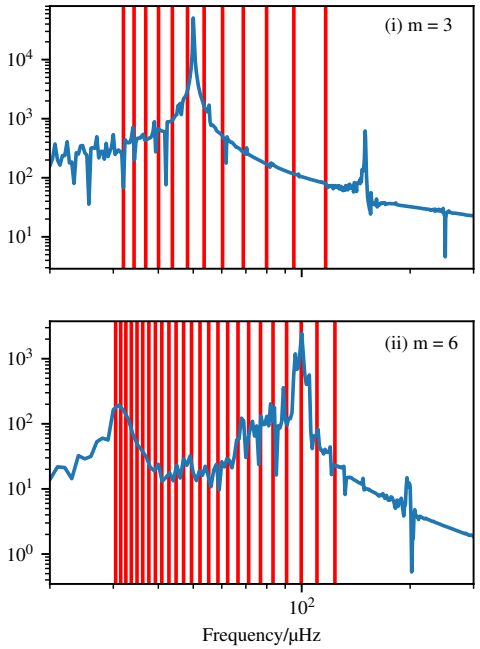

(b) 50 μHz

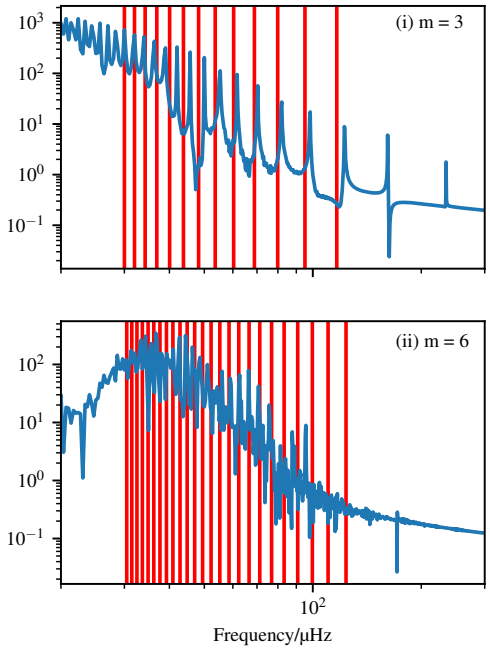

(c) 10 μHz

Figure 3.16: The wave amplitude as a function of frequency at the stellar surface. The red vertical lines represent eigenfrequencies calculated using the asymptotic analytical solution of the linear wave equation (see Eq. (3.21)). The three panels represent simulations with forced waves at (a)10 μHz, $m = 3$, (b)50 μHz, $m = 3$ and (c)120 μHz, $m = 3$. The top and bottom plots in each panel represent wave amplitudes at (i) $m = 3$ and (ii)$m = 6$.

at $m = 6$. Referring back to Fig. 3.15b, we see that the dispersion relation is satisfied for these two peaks close to the bottom boundary of the radiation zone indicating that these two peaks start as waves. Thus, it is unclear here as to why the cavity modes are not as visible as they are for the other two forced wave cases. A likely reason is a 50 µHz, $m = 3$ wave is not close to any cavity mode frequency, which leads to cavity modes not being excited with high energy.

3.4 Two-Wave Analysis

In a system with multiple forced waves, there will be interactions between different waves in addition to wave self-interactions, as discussed in the previous section. These non-linear interactions can lead to the generation of waves at different frequencies and wavelengths. We investigated this non-linear wave-wave interaction by forcing two different waves at the bottom of the radiation zone; one at 10 µHz, $m = 3$ and another at 50 µHz, $m = 5$. Both waves were forced with the same amplitude of $1000\,\mathrm{cm\,s^{-1}}$.

Figure 3.17 shows the frequency spectra of the wave amplitudes in the radiation zone for different wavenumbers. Looking at the top panel of the figure which shows the wavenumber-averaged wave amplitudes, we observe several distinct features. First, we see clear standing modes at frequencies which are integer multiples of 50 µHz up to the Brunt–Väisälä frequency limit in the domain. These are waves generated from the self-interaction of the forced 50 µHz wave, as discussed in the previous section. Figure 3.17(c) shows that the 50 µHz forced wave is generated at the correct frequency and additionally, grows in amplitude as it propagates through the radiation zone.

The second feature of panel (a) is we see the 10 µHz forced wave being damped over a very short radial distance. Looking at the frequency spectrum at $m = 3$ (Fig. 3.17(b)), we see that the damping of 10 µHz occurs rapidly in the radiation zone and the pattern of IGWs is similar to that seen in Fig. 3.9 for the single forced wave.

Finally, the interaction between the two forced waves produces waves at wavenumbers that are non-integer multiples of 3 and 5. Looking at Fig. 3.17(d), which shows the frequency spectrum at $m = 8$, we see waves near 40 µHz and 60 µHz spanning the whole simulation domain, which are expected from triadic interaction. We also observe waves at frequencies lower than 40 µHz and higher than 60 µHz. One possible explanation for the formation of these waves is cavity mode interaction, as discussed in the previous section. Another explanation is non-linear interaction between secondary waves. Waves formed from non-linear interactions between the forced waves can then interact to form new waves with a different wavenumber and frequency. Thus, we found that non-linear interaction between two different waves leads to the formation of a broad spectrum of waves.

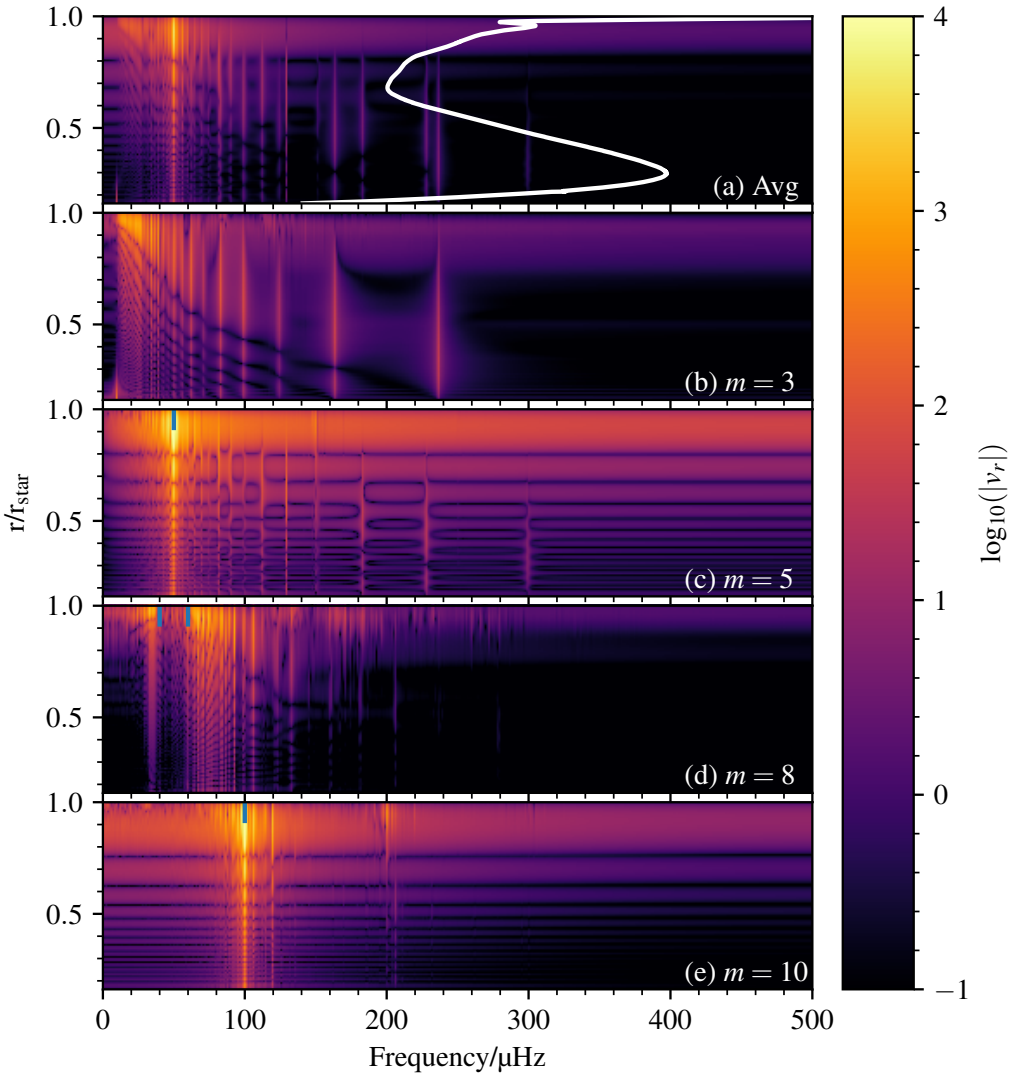

Figure 3.17: Wave amplitudes as a functions of stellar radius and wave frequency. Panel (a) shows the wave amplitudes averaged over wavelengths with the Brunt–Väisälä frequency profile overplotted in white. Panels (b) to (e) show the wave amplitudes at $m = 3$, $m = 5$, $m = 8$ and $m = 10$ respectively.

3.5 Multiple-Wave Analysis

The ultimate goal of this investigation is to study non-linear propagation of IGWs generated from core convection in realistic stellar conditions. The spectra described in Section 3.1.1 are a selection of prescriptions from different numerical simulations and theoretical studies on stellar convection. To study the effect of these different excitation spectra on the waves in the radiative zone, we forced a spectrum of waves at the bottom boundary

of the system with frequencies between 10 µHz and 500 µHz and $m = 1 - 20$ [5].

We found that for the cases of spectrum K and spectrum LD, the slope of the frequency spectrum was so steep that more than 50% of the energy in waves was in frequencies less than 10 µHz. Waves with such low frequencies are damped over very short distances, which means that they do not directly contribute to any surface spectrum. In addition to this, spectrum K and spectrum LD were derived for stars with convective envelopes, which makes the work done in Rogers *et al.* (2013) more relevant for this investigation. Thus, we work here with just one generation spectrum; $\mathrm{R_{break}}$.

Figure 3.18 shows frequency spectra at two different radii for the generation spectrum, $\mathrm{R_{break}}$, where panel (a) shows the radial velocity amplitudes (v_r), panel (b) shows the tangential velocity amplitudes (v_θ) and panel (c) shows the temperature perturbation amplitudes (T), at r = 0.98 (red line) and r = 0.90 (green line). Simulations were run for at least 100 wave cycles, for the wave with the smallest frequency and wavenumber (10 µHz, $m = 1$), which reached an amplitude that is constant up to 5% within 40 wave cycles. This particular wave is chosen as an example here as it takes the longest time to reach equilibrium. We will be using r to represent $\mathrm{r/r_{star}}$ from here on. Previous work using anelastic simulations (Rogers *et al.*, 2013; Edelmann *et al.*, 2019) of stellar interiors do not extend the simulation domain beyond 90% of the total stellar radius for numerical stability. We have included the spectrum at this radius to be compared with the spectrum at the surface (r = 0.98). For all the quantities shown in the figure, the frequency slopes at r = 0.98 and r = 0.90 are similar. These frequency slopes are negative close to the stellar surface, with the values being $-0.43/-2.23$ (low frequency/high frequency regime)[6] for radial velocities, $-1.53/-3.29$ for tangential velocities and $-1.35/-3.07$ for temperature perturbations. Linear theory shows that the frequency slope for the radial velocities is related to the frequency slope of the tangential velocities by approximately a factor of ω^{-1} through the following relation:

$$\frac{v_\theta}{v_r} = \left(\frac{N_{mod}^2}{\omega^2} - 1\right)^{\frac{1}{2}} \tag{3.29}$$

$$\approx \frac{N_{mod}}{\omega}, \tag{3.30}$$

where the approximation in the second line is true for frequencies much smaller than the Brunt–Väisälä frequency. From the ratio of the exponents, we can see that this relation is approximately satisfied in both the high and low-frequency regimes in our simulation

[5] We only consider waves with frequencies more than 10 µHz because to resolve waves down to 1 µHz with four grid points, we need at least 12000 grid points in the radial direction, which is approximately 10 times the current resolution.

[6] The high frequency regime is defined from 50 µHz to 150 µHz and the low frequency regime is defined from 10 µHz to 50 µHz.

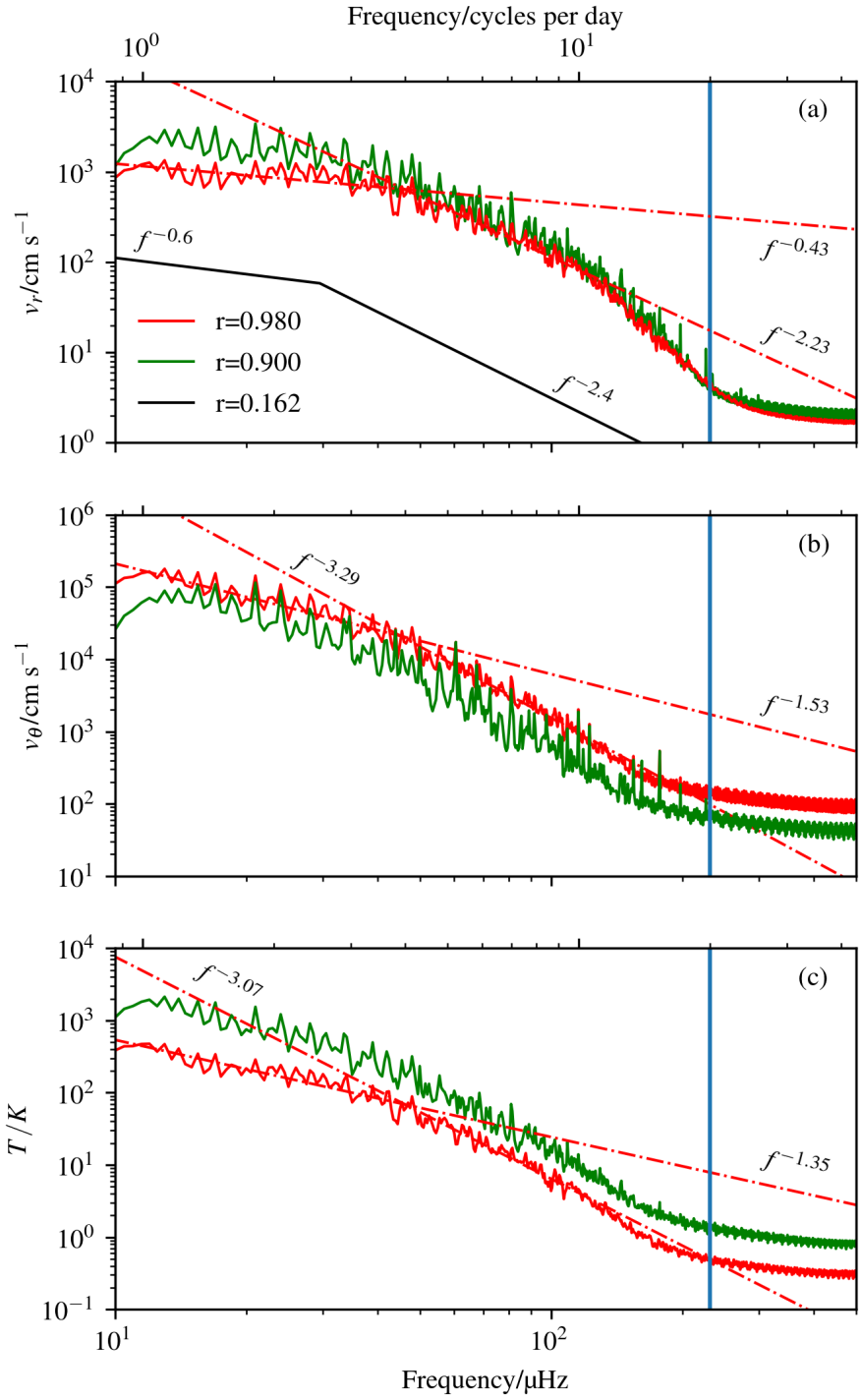

Figure 3.18: Temporal Fourier transforms of the (a) radial velocities, (b) tangential velocities and (c) temperature perturbations at the generation radius (black line), r = 0.90 (green line) and r = 0.98 (red line), for a 3 $M_\odot$ ZAMS star with no rotation. The red dotted-dash lines represent the fit done to the spectrum at r = 0.98 between 10 μHz and 50 μHz, and between 50 μHz and 150 μHz. The vertical blue lines represent the upper frequency limit in the observational data used in Aerts & Rogers (2015) to compare with numerical results.

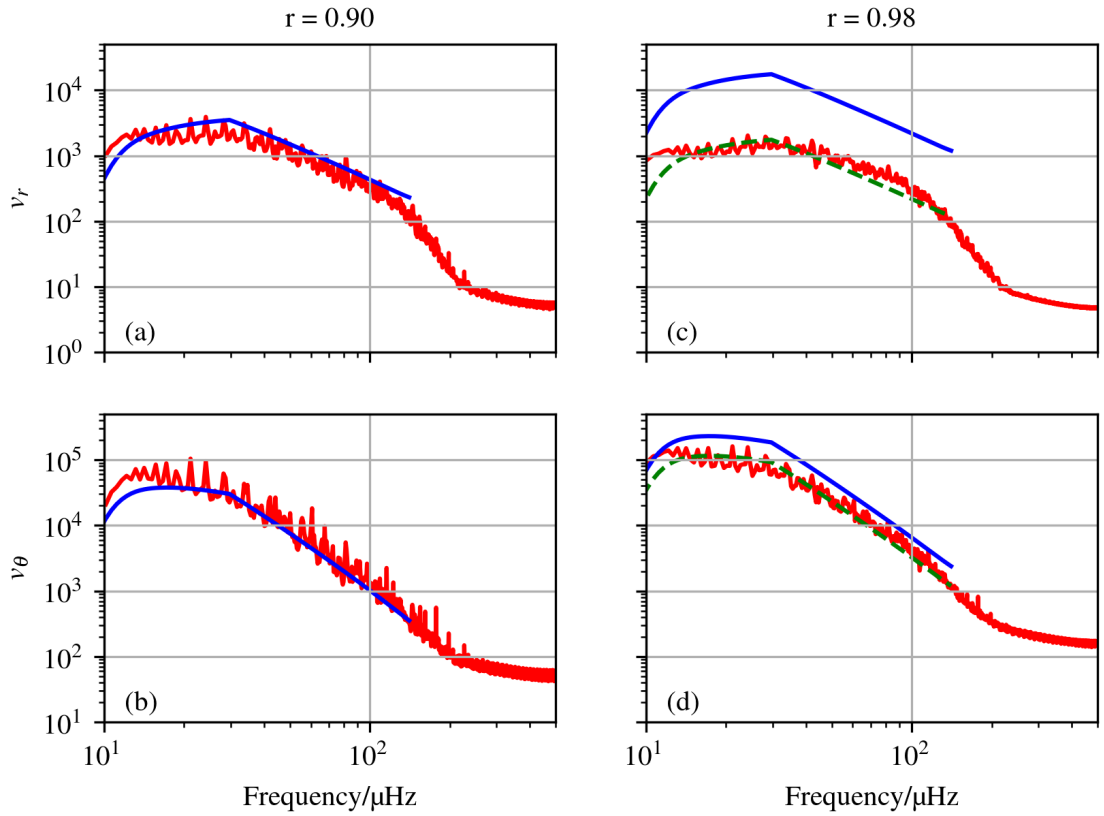

Figure 3.19: The radial and tangential velocity spectra at r = 0.9 (first column) and r = 0.98 (second column). The blue lines represent the spectra from linear theory and the green dashed lines represent the linear spectra multiplied by a constant factor to match the non-linear amplitudes.

results. Furthermore, comparing the slope of IGWs seen here with observational results from Bowman *et al.* (2019) which find the slopes from O- and B-type stars to be less than 3.5, we see that our tangential velocity slopes are within the observational prediction range. We have included the upper frequency limit (f = 231 μHz) of observational data from Aerts & Rogers (2015) as a reference point in our plots and we can see that our frequency slopes are for IGW frequencies below this observational limit. This limit has been increased to a larger frequency (f = 1160 μHz) in Bowman *et al.* (2019).

Contrary to the expected effect due to the density stratification, both the radial velocity amplitudes in panel (a) and the temperature perturbation amplitudes in panel (c) at r = 0.98 are lower than those at r = 0.90. This is likely an artefact of the impermeable upper boundary condition for these quantities. In panel (b), we see the tangential velocities to be higher at r = 0.98 compared to those at r = 0.90, exhibiting a trend that is opposite to those shown by the radial velocities and temperature perturbations. This is due to the top boundary condition for tangential velocities being stress-free.

Comparing these simulation results to those of linear calculations from Section 3.3.1, Fig. 3.19 shows the radial and tangential velocity spectra at two different radii from the non-linear simulation (red line) and linear model (blue line) At r = 0.90, the non-linear spectra for v_r and v_θ matches the linear spectra very well, in terms of the expected frequency slope, as seen in panel (a) and (b). At r = 0.98, there is a clear mismatch between the linear (blue lines) and non-linear (red lines) amplitudes for both the radial and tangential velocities. As discussed above, the IGW amplitudes near the surface are reduced due to the boundary conditions. However, we see that the slopes match remarkably well, from the green lines, which show the linear model predictions multiplied by a certain factor so that it overlays the numerical simulation results. The linear model has a cut-off at 140 µHz, which is the smallest Brunt–Väisälä frequency in the simulation domain. One of the key differences between the linear and non-linear models is that at the lowest frequencies, there is significantly more energy in the full non-linear simulation spectrum, which is likely due to local non-linear energy transfer (as seen in Fig. 3.5(a) and Fig. 3.6).

3.5.1 Rotation and Age Analysis

Convective processes are known to be affected by rotation. In the case of stellar convection, Rogers *et al.* (2013) showed that the spectrum of gravity waves due to core convection for a $3M_\odot$ star varies when rotation is introduced to the system. We ran non-linear simulations with two of the rotational velocities and their corresponding wave spectra from that paper to study the effect of rotation on gravity waves in the radiation zone. Note that we consider the tangential velocity to be the best proxy to compare with observational results (which mainly work with surface brightness variation) and not temperature, as the relationship between temperature variation and surface brightness variation is not well understood. Thus, we only show tangential velocity results from here on.

The stellar angular velocities, Ω, used here are 0.796 µHz and 12.73 µHz, referred to as models U3 and U8 in Rogers *et al.* (2013) (see Fig. (1.12)). Note that these refer to stars in solid-body rotation. The critical stellar angular velocity is 60 µHz, so our fastest rotating model is at 20% of the critical velocity or break-up velocity. For $\Omega = 0.796$ µHz, the generation spectrum has a frequency slope of $-1.43/-2.27$ and for Ω =12.73 µHz, the generation spectrum has a frequency slope of $-1.07/-2.36$. For zero rotation, the slope is $-1.55/-2.41$. Figure 3.20 shows the tangential velocity spectra at $r = 0.98$ for three different stellar angular velocities, which are $\Omega = 0.0$ µHz (red line), $\Omega = 0.796$ µHz (green line) and $\Omega = 12.73$ µHz (black line). In all cases, the surface spectra for the tangential velocities were found to have a steeper slope than those at generation. However, comparing the slopes at different stellar angular velocities, we found all slopes at both the low- and high-frequency ranges to be very similar.

The work done in Rogers *et al.* (2013) show that as IGW frequencies approach the

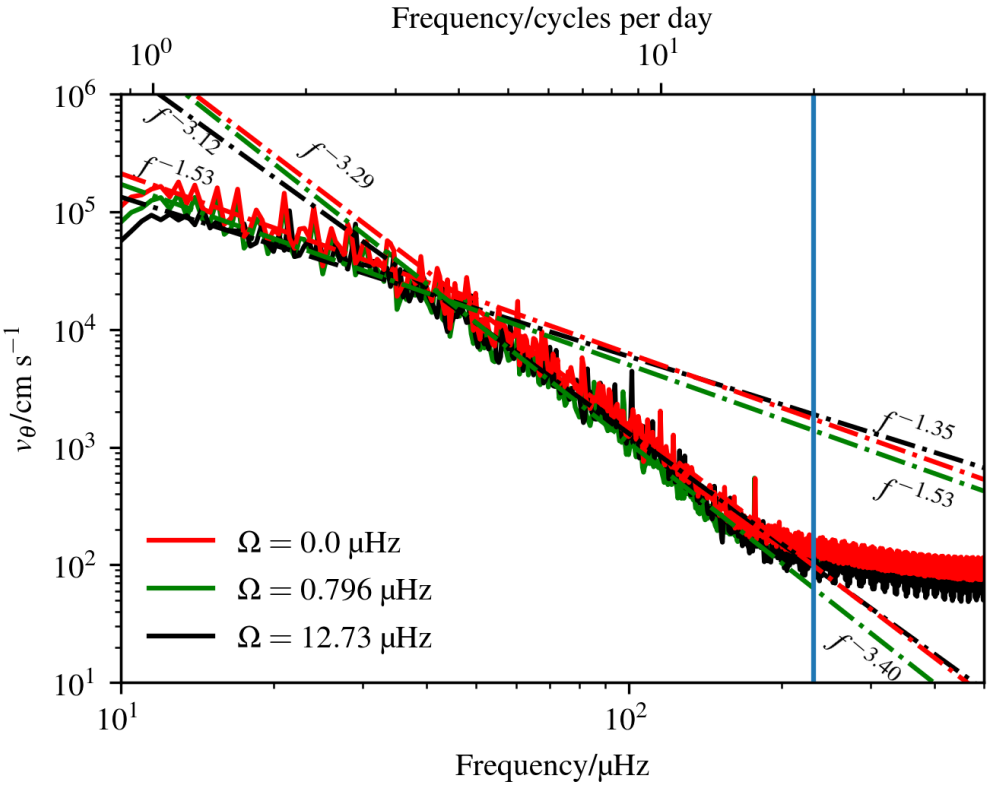

Figure 3.20: Temporal Fourier transforms of the tangential velocities close to the stellar surface (r = 0.98) for 3 $M_\odot$ ZAMS star with no rotation (red line), Ω = 0.796 μHz (green line) and Ω = 12.73 μHz (black line). The generation spectrum when Ω = 0.796 μHz has a slope of -0.5/-2.35 and when Ω = 12.73 μHz, the slope is -0.25/-1.95. For zero rotation, the slope is the same as R_{break}. The vertical blue line represents the upper frequency limit in the observational data used in Aerts & Rogers (2015) to compare with numerical results.

stellar rotational frequency, they start to become more and more affected by the rotation. In our simulations, where we tested waves in systems with rotational rates up to 12.74 μHz, we would expect only waves with frequencies up to this value to be affected. However, we were limited in our investigation by resolution. Furthermore, due to time constraints, we did not test the other rotational rate of 15 μHz, that was presented in Rogers *et al.* (2013), which showed steeper frequency and wavenumber slopes. All our simulations were also limited to solid-body rotation but it is known that generally, IGWs are Doppler shifted in a differentially rotating frame where the following equation holds true:

$$\omega(r) = \omega_{gen} + k_h[\Omega_{gen} - \Omega(r)], \tag{3.31}$$

where $\omega(r)$ radially-varying IGW frequency, ω_{gen} is the IGW frequency at generation, Ω_{gen} is the stellar rotational frequency at IGW generation and $\Omega(r)$ is the stellar rotational frequency at radius, r. This equation shows that for a differentially-rotating star, the

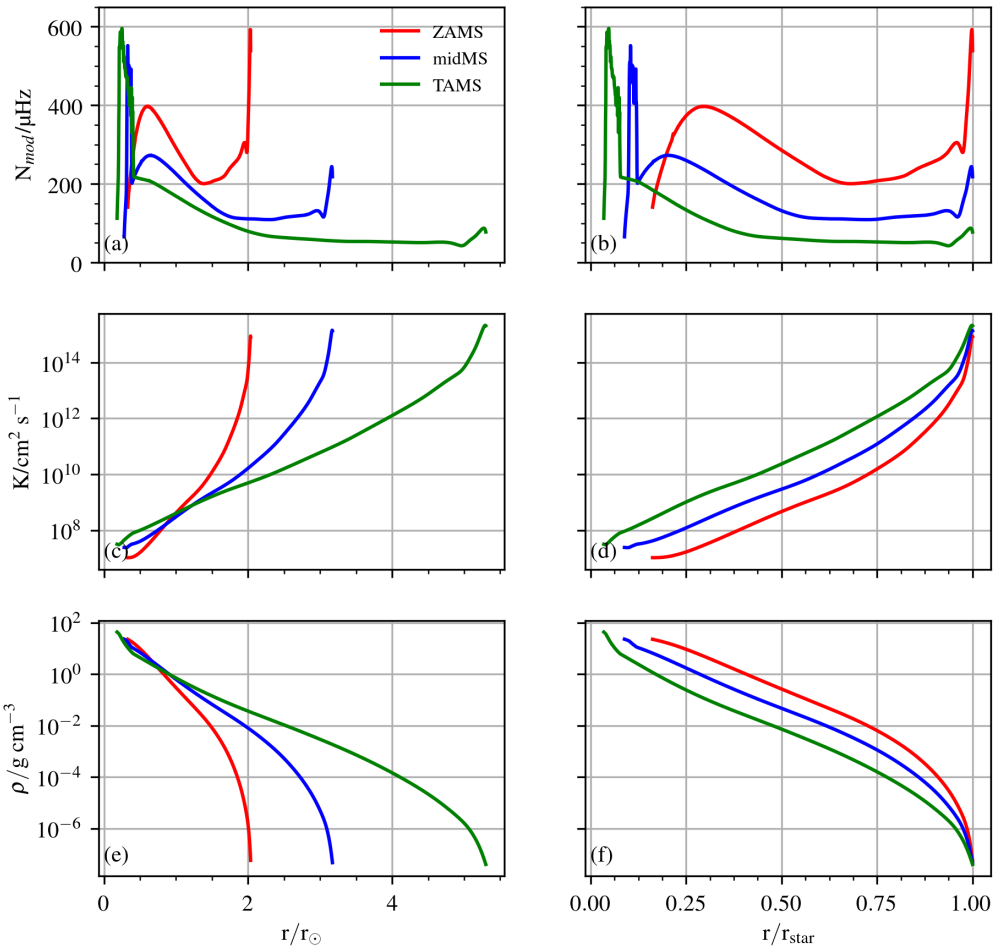

Figure 3.21: The Brunt–Väisälä frequency (top panel), thermal diffusivity (middle panel) and density (bottom panel) profiles as a function of stellar radius as a unit of total solar radius for stellar models of a 3 $M_\odot$ at ZAMS (red line), midMS (blue line) and TAMS (green line).

surface IGW frequency spectrum can be one that is very much shifted that at generation.

Next, we study the effect of stellar age on non-linear IGW propagation. Here, we have kept the generation spectrum constant for all three stellar models: 3 $M_\odot$ ZAMS, 3 $M_\odot$ midMS and 3 $M_\odot$ TAMS. This fixes the radial velocity spectrum at the inner boundary for all three models but not the tangential velocity spectrum. Locally, tangential velocities and radial velocities are related by Eq. 3.29. Thus, the tangential velocity generation spectrum varies between the different models by the same amount the Brunt–Väisälä frequency varies between the models at generation. However, in Fig. 3.21, which shows the Brunt–Väisälä frequency (N_{mod}), thermal diffusivity (K) and density (ρ) profiles of all three stellar models as functions radius in units of the solar radius ($r_\odot$) and in units of total stellar radius (r_{star}), panels (a) and (b) show that there is little difference between the Brunt–Väisälä frequencies at generation for the different stellar models, leading to the

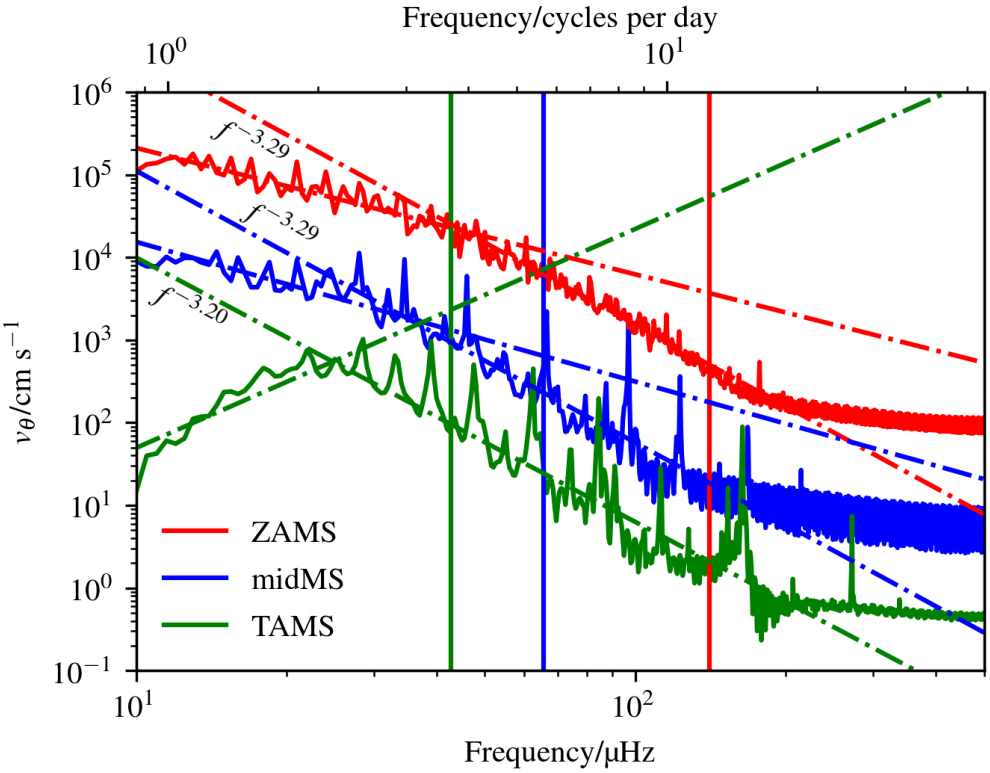

Figure 3.22: Temporal Fourier transforms of the tangential velocities close to the stellar surface (r = 0.98) for 3 $M_\odot$ ZAMS star (red line), 3 $M_\odot$ midMS star (blue line) and 3 $M_\odot$ TAMS star (green line). The solid vertical lines represent the minimum Brunt–Väisälä frequency of the respective models. The linear fits (dashed-dotted lines) show the general trend of the spectrum and were not done using a least-square fit method.

tangential velocity profiles at generation being similar too.

Figure 3.22 shows the surface tangential velocity spectra, defined at 98% of the total stellar radius, for the three different stellar ages. There are a few distinct features seen in this plot. The first feature is that the amplitudes of all waves at the surface decrease as the star ages. This occurs due to a few different factors. The first factor is that older stars are larger causing IGWs to travel farther from generation and reach the surface with lower amplitudes than those in younger stars. This spreading out of waves is expected to cause the IGW amplitudes to decrease as r^{-1} in 2D. Second, the Brunt–Väisälä spike that older stars (see top panels of Fig 3.21) develop causes IGWs to generally experience a stronger radiative damping (see Eq. (2.9)). The third factor is that all IGWs experience extra damping due to them losing their wave-like properties at the turning point (see Section 3.3.1) in the radiation zone. For older stars, the turning point is located at a lower fraction of their total radius. To understand this better, we look at the top panel of Fig. 3.23, which shows the ratio between the oscillatory terms(OT) and the density terms

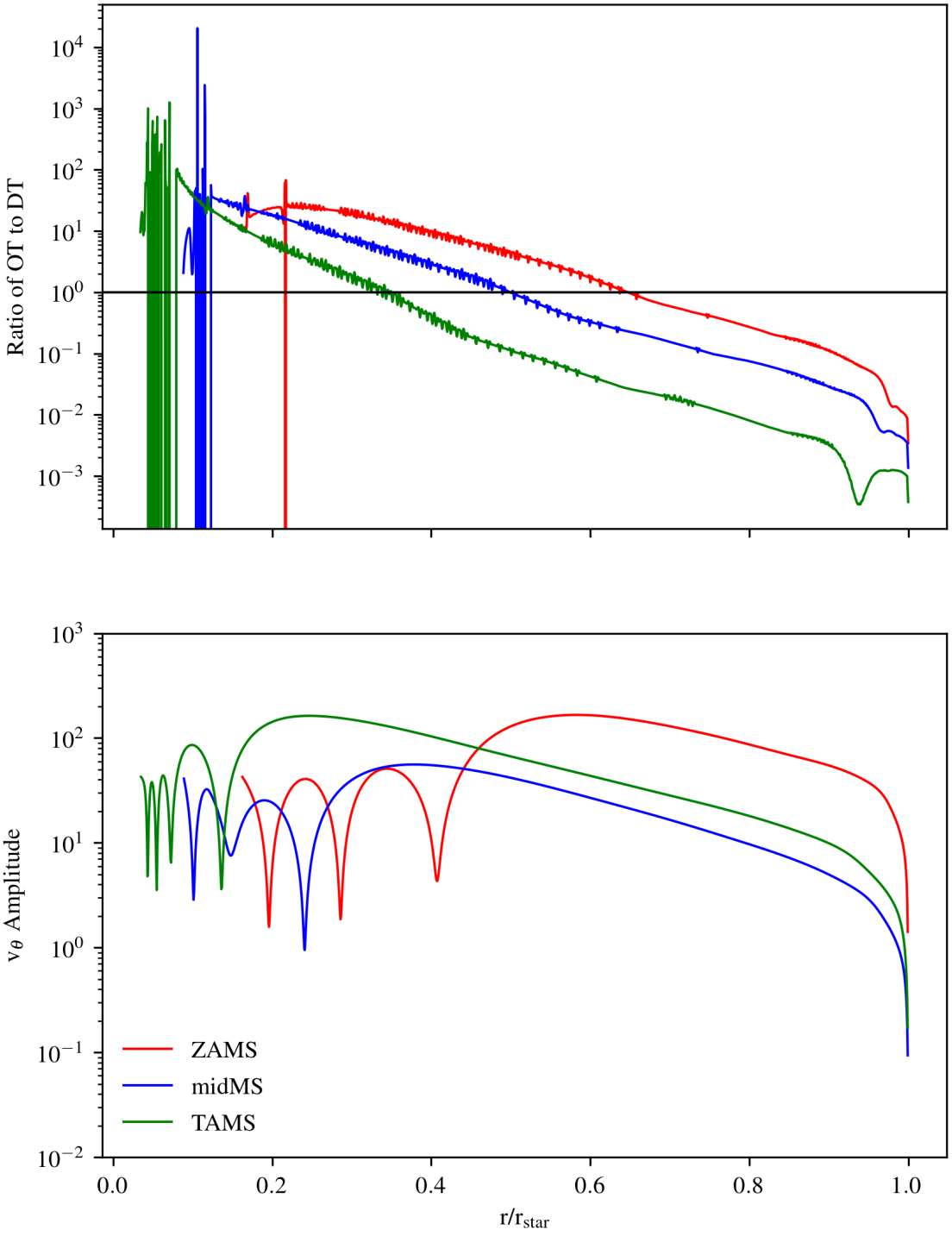

Figure 3.23: The ratio of the oscillatory term (OT) to the density term (DT) in Eq. (3.21) (top panel) and the v_θ amplitude as a function of radius in units of total stellar radius for a 40 μHz, m = 1 wave. The colors represent different stellar models as shown in the legend. The horizontal black line in the top panel represents a ratio of 1.

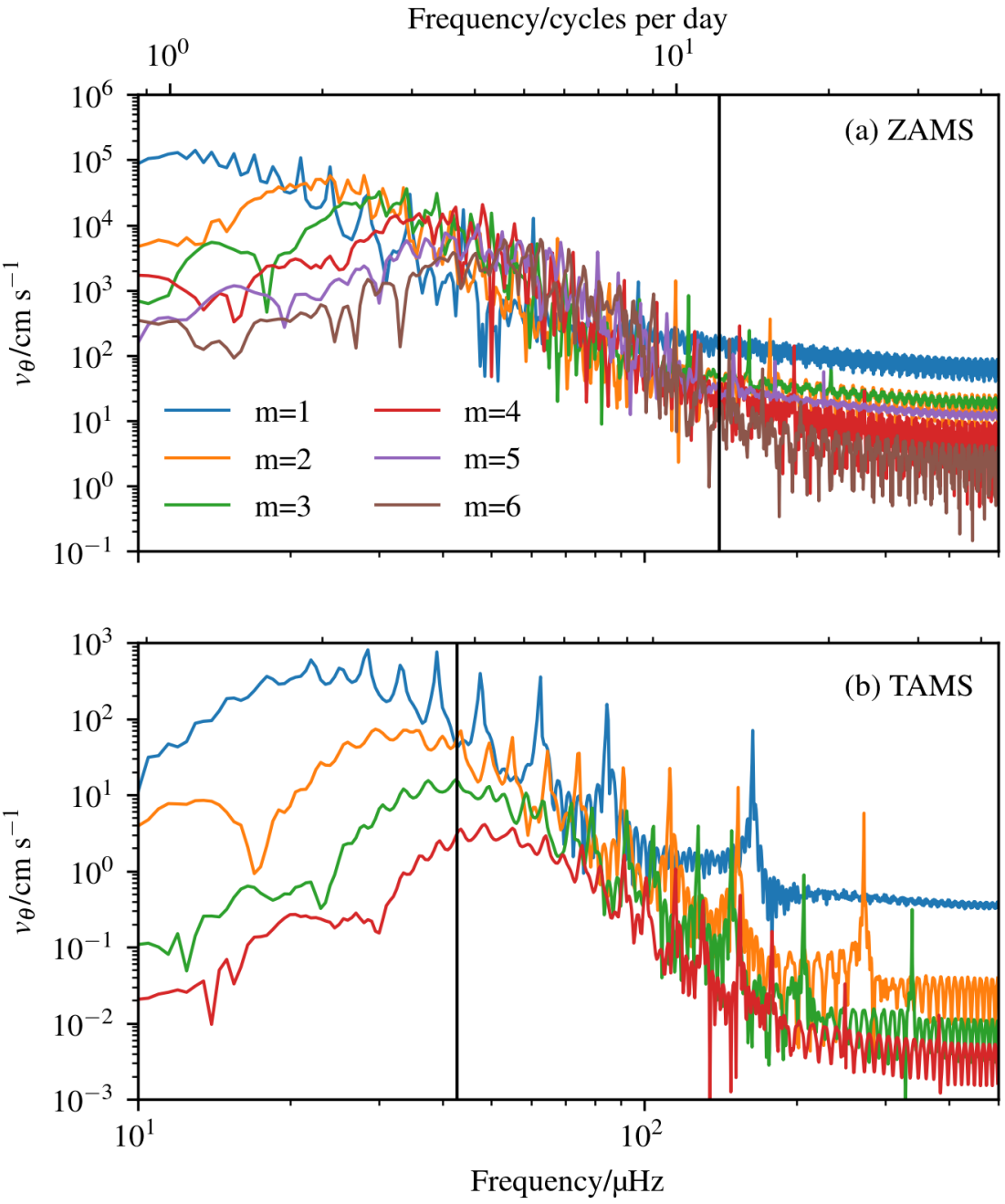

Figure 3.24: Tangential velocity amplitudes at different frequencies for horizontal wavenumbers up to 6. Panel (a) represents a ZAMS model whilst panel (b) represents a TAMS model. The vertical black lines represent the minimum Brunt–Väisälä frequencies in the respective model.

(DT) in Eq. (3.21) as a function of the stellar radius for a 40 µHz, $m = 1$ wave in different stellar models. The turning point location is indicated by the ratio equal to 1 (horizontal black line). We can observe that the wave maintains its oscillatory property (indicated by the ratio > 1) for a larger proportion of the radiation zone in younger stars. This can also be observed in the bottom panel of Fig. 3.23, which shows the horizontal velocity amplitude at 40 µHz, $m = 1$, for different stellar models, where the waves initially show an oscillatory behaviour followed by a decaying behaviour.

The second feature of Fig. 3.22 is the stationary mode peaks become more prominent for older stars. This effect is caused by the Brunt–Väisälä frequency spike that appears close to the convective core as the star ages, as seen in panels (a) and (b) of Fig. 3.21. As a result, the high-wavenumber waves in older stars undergo more rapid radiative damping compared to the high-wavenumber waves in younger stars causing only the low-wavenumber waves to reach the surface. This effect can be seen in Fig. 3.24, which shows the surface IGW spectra at different horizontal wavenumbers, for the (a) ZAMS model and the (b) TAMS model. Waves with horizontal wavenumbers up to $m = 6$ are still contributing to the total spectrum for a ZAMS star (panel (a)) whilst only waves up to $m = 3$ contribute to the total spectrum for TAMS star (panel (b)). In fact, this is also a contributing factor to the decreasing amplitudes of all waves in older stars, as discussed in the previous paragraph.

A third distinguishing feature appears at lower frequencies (12 µHz $\leqslant f \leqslant$ 20 µHz). The surface IGW spectrum for the TAMS model shows a positive slope whilst those for the ZAMS and midMS models show negative slopes. This is because low-frequency waves are damped more efficiently by the broad Brunt–Väisälä frequency spike near the interface, as seen in Fig. 3.21(a) for the TAMS model, similar to the effect discussed in the previous paragraph.

The final feature of Fig. 3.22 is that the frequency slopes at high frequencies (50 µHz to 150 µHz) are similar for all models close to the stellar surface. Note that the linear fits for these spectra were done manually, not using the standard least-square fitting because this would be are perturbed by the strong peaks, which in asteroseismology, are usually removed through methods such as pre-whitening. Thus, we find that our result is consistent with the most recent observational results (Bowman *et al.*, 2019, 2020), where the frequency exponent for a variety of high-mass stars was found to be $\leqslant 3.5$. For the list of all the frequency slopes for the stellar models in this thesis, please refer to Table 3.4.

3.5.2 Wave Spectrum Validation

As done in Section 3.3.3, we check whether the waves discussed in section discussed above have reached steady state, by selecting waves of specific frequencies and wavenumbers and studying their evolution with time. We selected stationary mode frequencies at $m = 1$ and $m = 2$ from a 3 $M_\odot$ ZAMS simulation and present them in Fig. 3.25. We choose these

Frequency Slopes	Low-Frequency	High-Frequency
ZAMS ($\Omega = 0.0$ µHz)		
Generation Spectra	-1.55	-2.4
Surface Spectra	-1.53	-3.29
ZAMS ($\Omega = 0.796$ µHz)		
Generation Spectra	-1.43	-2.27
Surface Spectra	-1.53	-3.40
ZAMS ($\Omega = 12.73$ µHz)		
Generation Spectra	-1.07	-2.41
Surface Spectra	-1.35	-3.12
midMS		
Generation Spectra	-1.55	-2.4
Surface Spectra	-1.69	-3.29
TAMS		
Generation Spectra	-1.55	-2.4
Surface Spectra	5.10	-3.20

Table 3.4: The table shows the frequency slopes of the tangential velocity amplitudes for all the models used in this work. The generation spectra are forced at the bottom boundary of the radiation zone and the surface spectra are defined at r = 0.98 $r_{\rm star}$.

large scale waves because they provide the dominant wave energy to the overall spectrum. We also overplotted the surface damping time (γ^{-1}, Eq. (2.10)) for these waves as vertical lines. In both cases (i.e. $m = 1$ and $m = 2$), we observe low-frequency waves undergoing a rapid increase in amplitude at the beginning followed by a steady-state evolution with some decrease at later times for the lower frequencies. High-frequency waves are in steady-state from early on. As shown in Section 3.3.3, comparing the damping timescales for these waves (vertical dotted lines) and the visible steady-state timescale, we can observe that the damping time calculated using Eq. (2.10) is not indicative of when a wave reaches steady-state.

We also check whether the modes seen our simulations satisfy the dispersion relation by comparing these modes to a stellar oscillation code, which solves the stellar pulsation equations (Saio, 1993), called GYRE (Townsend & Teitler, 2013). We used GYRE to calculate the radial structure of gravity modes, with the exact reference state models we used for our simulations and we present the results in Fig. 3.26. The top panel shows the radial structures of the horizontal velocity from GYRE (orange) and the simulations (blue) at 60.5 µHz and 44 µHz at $m = 1$ ($\ell = 1$, in the case of GYRE), for a radial order of 2, whilst the bottom panel shows the radial structures of the horizontal velocity at a radial order of 3. As seen in these figures, g-modes from the simulations match the shape of the g-modes calculated using GYRE, reasonably well. The discrepancies could arise due to a few reasons, such as geometry (2D cylindrical vs GYRE spherical), boundary conditions

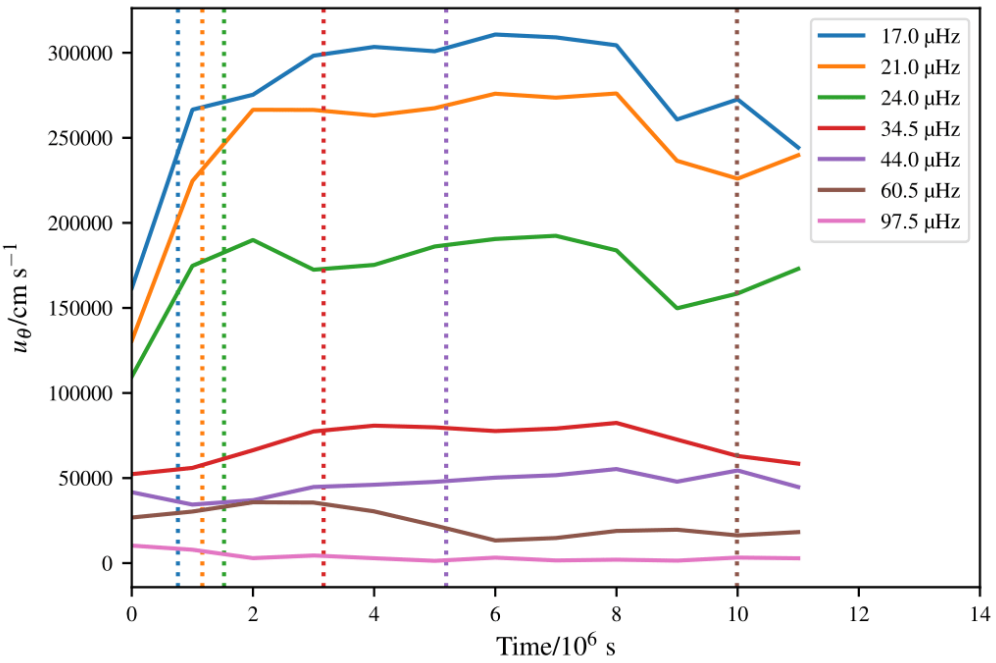

(a) $m = 1$

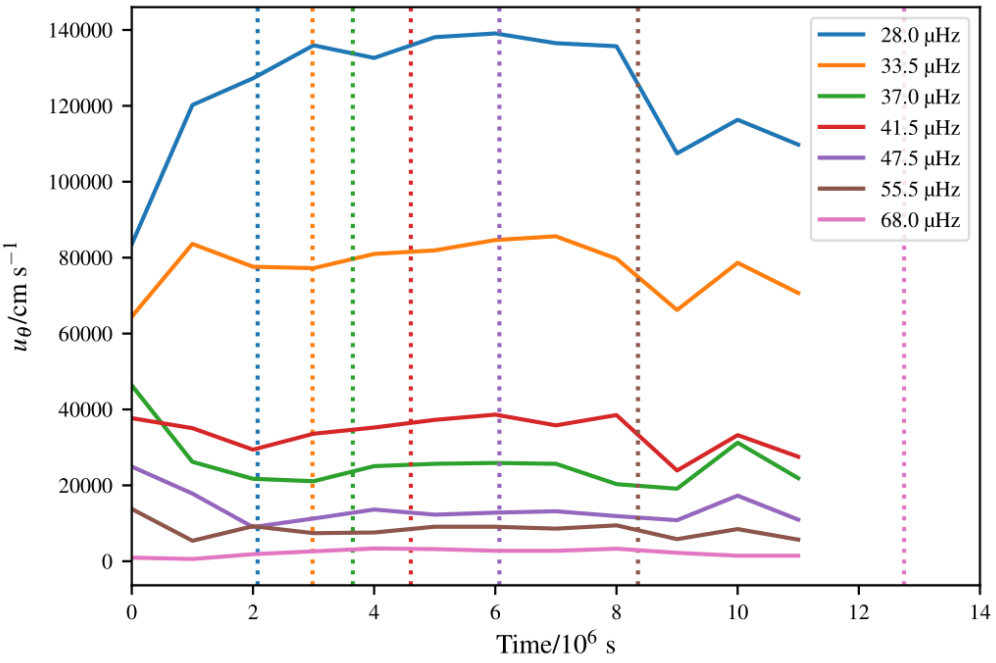

(b) $m = 2$

Figure 3.25: The amplitude evolution of stationary modes for (a) $m = 1$ and (b)$m = 2$ at the stellar surface, when a spectrum of waves is forced at the bottom boundary of a radiation zone. The vertical dotted lines represent the damping timescale (γ^{-1}) at the stellar surface.

and the treatment of the gravitational term.

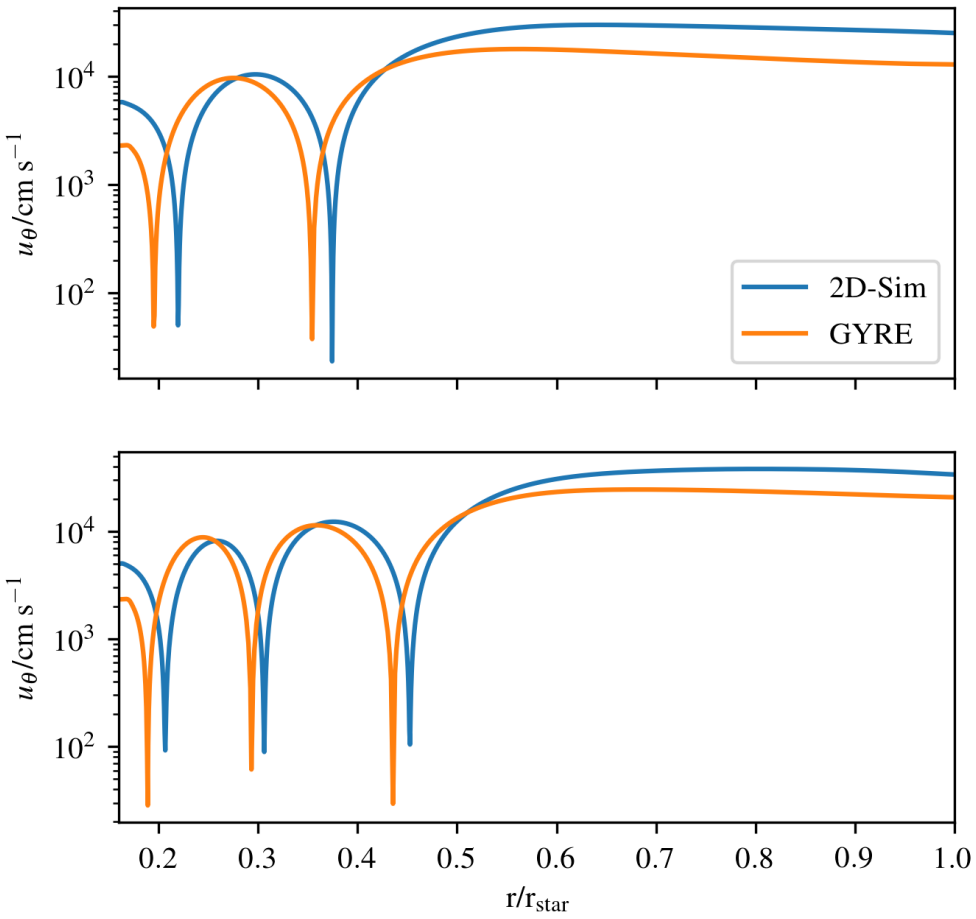

Figure 3.26: The radial structures of the horizontal velocity, u_θ from GYRE (orange) and our simulations (blue) for $m = 1$ at frequencies 60.5 µHz (top panel) and 44 µHz (bottom panel).

3.6 Summary and Discussion

We ran two-dimensional simulations of the evolution of stellar radiation zones, in which IGWs were forced at the bottom boundary. Since the convection zone was not included, we are able to simulate the radiation zone up to 99% of the stellar radius and implement realistic thermal diffusivities. We started the investigation with a series of validation tests by investigating monochromatic IGW forcing. We found that for different forced wave frequencies, the waves self-interact through triadic interactions and also resonate with

cavity modes if the forced wave frequency is close to a cavity mode frequency.

Our main conclusion is we find that the surface IGW frequency slopes broadly match those predicted by linear theory and reflect the generation spectrum. However, non-linear simulations show more energy at the lowest frequencies likely due to non-linear wave interactions at the surface. Furthermore, we find that up to 20% the critical velocity of a star, stellar rotation (in this case, solid body rotation) does not affect the surface IGW frequency slope. For these simulations, we took into account the effect of rotation on both the slope of the generation spectrum, using results from Rogers *et al.* (2013) and the rotation of the radiation zone.

Another result of our investigation is that the surface IGW frequency slopes are similar at different stellar age. However, we note that the same generation spectrum was used for three different stellar models (i.e. ZAMS, midMS and TAMS). We also find that for older stars, the IGW amplitudes are not only lower, but they also have more distinct peaks in their spectra.

Finally, our results show that the surface frequency slopes are consistent with the 2D hydrodynamical simulations of stellar interiors (Rogers *et al.*, 2013) and observational results to-date (Aerts & Rogers, 2015; Ramiaramanantsoa *et al.*, 2018; Bowman *et al.*, 2019). We find the most recent observational work, Bowman *et al.* (2019), which found that the frequency slope magnitudes of IGW signatures from a variety of blue supergiants (BSGs) are less than 3.5, to be the most compelling comparison to our results. This is due to the large number and variety of stars (i.e. O– and B– type stars), and their argument that the variability of the surface IGW spectrum does not have any dependence on metallicity. However, we note that BSGs can be fundamentally different than the stars that we tested. BSGs can be larger, more massive, more evolved, hotter and denser, which crucially affects convection in the stellar core and the subsequent IGW generation spectrum, which thus leads to the fact that our treatment of using the same generation spectrum for all three stellar ages may not be correct (see next chapter).

Chapter 4

Self-consistent Simulations across Stellar Mass and Age

In intermediate-mass stars, core convection is thought to be the major source for stochastically generated IGWs. So far, we have studied IGW propagation through the radiation zone using different numerical and theoretical prescriptions for IGW generation through stellar convection. In these studies, it was clear that the generation spectrum was of utmost importance. Now, we carry out a study on self-consistent simulations of stellar interiors, varying stellar age and mass, to investigate primarily the IGW generation spectrum from core convection. This parameter space study is one that is novel, but numerical studies on IGW generation from core convection are not new. One of the first works to do this consistently is Rogers *et al.* (2013), which investigated the IGW generation spectrum using 2D anelastic hydrodynamical simulations for a $3M_{\odot}$ ZAMS star. Another work, Edelmann *et al.* (2019) became the first work to study both IGW generation and propagation for an intermediate-mass star in a three-dimensional spherical geometry using the anelastic hydro code, SPIN. More recently, Horst *et al.* (2020) utilised a finite-volume method for solving the fully compressible Euler equations (using the Seven-League Hydro(SLH) code) to investigate the generation and propagation of both gravity and pressure waves in intermediate-mass stars. Our work is different from the examples given above by using a method similar to the work in Rogers *et al.* (2013) but cover a wider range of masses and age. We would like to stress that the results in this section are early.

4.1 Numerical Approach and Stellar Models

The numerical approach taken in this project is similar to that described in Chapter 3, Section 3.1 with some modifications. Primarily, instead of investigating just the radiation zone as done in the previous chapter, we now include the convective core in the simulations

domain as well. Some formal definitions of dimensionless quantities that play important roles when simulating convection zones are needed before we proceed further. First, the Reynolds number, Re, defined as

$$Re = \frac{uL}{\nu}, \tag{4.1}$$

where ν is the kinematic viscosity, u is the characteristic velocity in the convection zone and L is the characteristic lengthscale, usually defined as the radial extent of the convection zone. This quantity describes the ratio of the inertial forces to the viscous forces in the system. Low values signify laminar flow while high values show turbulent flow. Second, we define the Prandtl number (description given in Chapter 1,Section 1.3.2) as

$$Pr = \frac{\nu}{K}. \tag{4.2}$$

Finally, we define the Rayleigh number (description given in Chapter 1, Section 1.3.1), Ra as

$$Ra = \frac{gL^3}{K\nu}\frac{\Delta T}{T}, \tag{4.3}$$

where ΔT is the temperature difference between the top and bottom boundary of a smooth, continuously-decreasing temperature profile. These quantities will be addressed and used repeatedly in this chapter.

The stellar models used in this work are similar to those used in Chapter 2, so we investigate three stellar masses (i.e. 3 $M_\odot$, 7 $M_\odot$, and 20 $M_\odot$) and three stellar ages (i.e. ZAMS, midMS and TAMS). Note that we do not investigate the effects of rotation in this work, so rotation is set to zero for all the models. There are a few key differences between these models and the ones in previous chapters. First, the models in this work include the convection zone. We distinguish between the convection zone and the radiation zone by using the same method as in Section 2.4. The sign of the Brunt–Väisälä frequency squared profile from MESA was used to determine the exact location of the radiative-convective boundary.

The second difference is that the Brunt–Väisälä frequency and temperature profiles for the models here differ from those used in Chapter 2. Although we use the Brunt–Väisälä frequencies from MESA to determine the location of the convection and radiation zones, we use the modified Schwarzchild criterion, N_{mod}, (see Chapter 3, Section 3.1) to set the Brunt–Väisälä frequencies for our simulations. In the convection zone, we fix the "superadiabaticity" term (Rogers *et al.*, 2013) defined as

$$\text{superadiabaticity} = -\frac{d\overline{T}}{dr} + (\gamma - 1)h_\rho \overline{T}, \tag{4.4}$$

to a constant positive value (generally 10^{-6} K cm^{-1}). Referring back to Fig. 1.7, a positive

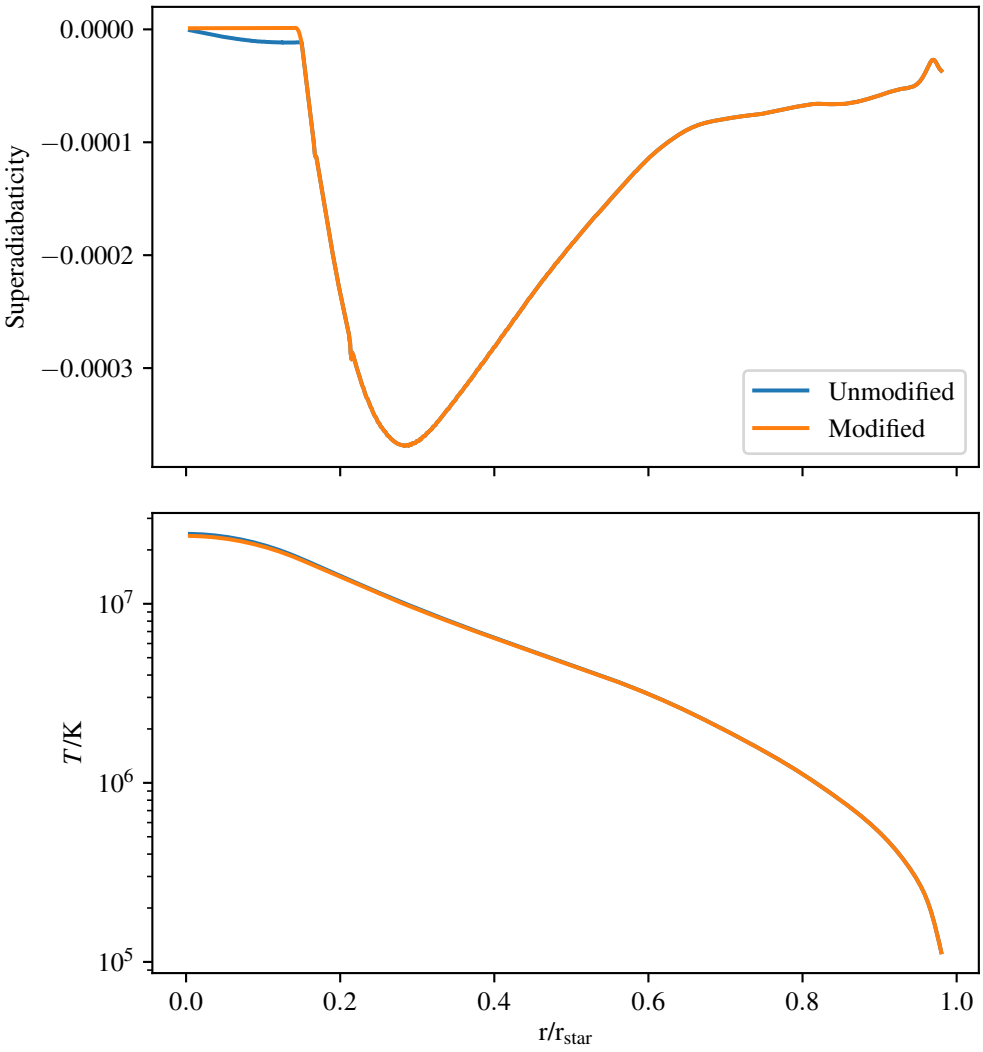

Figure 4.1: The superadiabaticity(see Eq. (4.4)) in the top panel and the reference state temperature in the bottom panel for a $3M_\odot$ ZAMS model. The unmodified version shows the parameters calculated without changes done to the superadiabaticity in the convection while the modified version shows the parameters with the superadiabaticity set to a positive constant value in the convection zone.

superadiabaticity results in the adiabatic temperature profile being less steep than the reference state temperature profile causing the onset of convection. To make sure that the temperature profile is consistent with our chosen superadiabaticity, we re-calculate the new temperature profile by numerically solving Eq. 4.4 as an initial-value problem from the surface of the star towards the centre. Figure 4.1 shows an example of the superadiabaticity and temperature profile for a $3M_\odot$ ZAMS stellar model from MESA (blue) and those calculated using the method mentioned above (orange). We find that the new temperature profile does not differ much from the temperature profile from MESA in the convection

Model	CZ Resolution/10^7 cm	RZ Resolution/10^7 cm	Radius of simulation domain/10^{11} cm	Radius of simulation domain/r_{star}	Radius of CZ/r_{star}
$3M_\odot$ ZAMS	4.146	10.71	1.284	0.9	0.142
$3M_\odot$ midMS	3.684	18.15	2.009	0.9	0.0827
$3M_\odot$ TAMS	2.195	32.55	3.378	0.9	0.0320
$7M_\odot$ ZAMS	8.975	15.69	2.027	0.9	0.192
$7M_\odot$ midMS	7.994	27.95	3.211	0.9	0.111
$7M_\odot$ TAMS	5.076	50.73	5.354	0.9	0.0455
$20M_\odot$ ZAMS	22.67	20.93	3.244	0.8	0.301
$20M_\odot$ midMS	21.35	41.14	5.210	0.8	0.179
$20M_\odot$ TAMS	14.41	106.5	11.44	0.8	0.0594

Table 4.1: The radial resolution used for all the models in the convection zone (CZ) and the radiation zone (RZ). We also include the total radius of the simulation domain in centimetres and in units of the total stellar radius, r_{star}.

zone and for all the stellar models we used, the re-calculated temperatures are within 10% of the MESA-generated temperatures at any given radius. Note that in Chapter 2, we did not include the $20M_\odot$ TAMS model as this model developed an intermediate convection zone, possibly related to composition-related convection. However, when we apply the modified Schwarzchild criterion to this profile, the Brunt–Väisälä frequency profile does not exhibit the presence of a convection zone. Thus, we include the $20M_\odot$ TAMS model in this investigation.

The third difference between the models for this work and those in Chapter 2 is the extent of the radiation zone. The radiation zones of the $3M_\odot$ and $7M_\odot$ models were cut off at 90% the total stellar radius whilst the radiation zones of the $20M_\odot$ models were cut off at 80% (for all three ages), instead of covering the whole stellar radius. This is done to maintain numerical stability. The remaining region was then split into 680 spectral modes in the horizontal direction and 1500 grid cells in the radial direction, with 500 grid cells for the convection zone and 1000 cells for the radiation zone. Table 4.1 shows the radial resolution for all the models used for this work. Since the resolution for the convection and radiation zone varies, to solve the RG equations in the radial direction, we use the non-uniform finite difference scheme, derived from the Taylor expansion of a function f and ignoring terms with order smaller than δr^3. In the horizontal direction, the spectral solution method is applied (see Chapter 3, Section 3.1).

The final difference is the values for thermal diffusivity, K. Whilst the work done in previous chapters considered realistic, varying K values, we fix the thermal diffusivities throughout the simulation domain to a constant value in this project for numerical stability. The viscosity is also set to a constant value. The exact values used will be discussed in the next section.

4.2 Simulations of the Stellar Interior

We can distinguish between the radiation zone and the convection zone in a simulation visually by observing the behaviour of fluid. For example, Fig. 4.2, Fig. 4.3 and Fig. 4.4 show time snapshots at $t = 9 \times 10^6$ s of the whole simulation domain (left column) and just

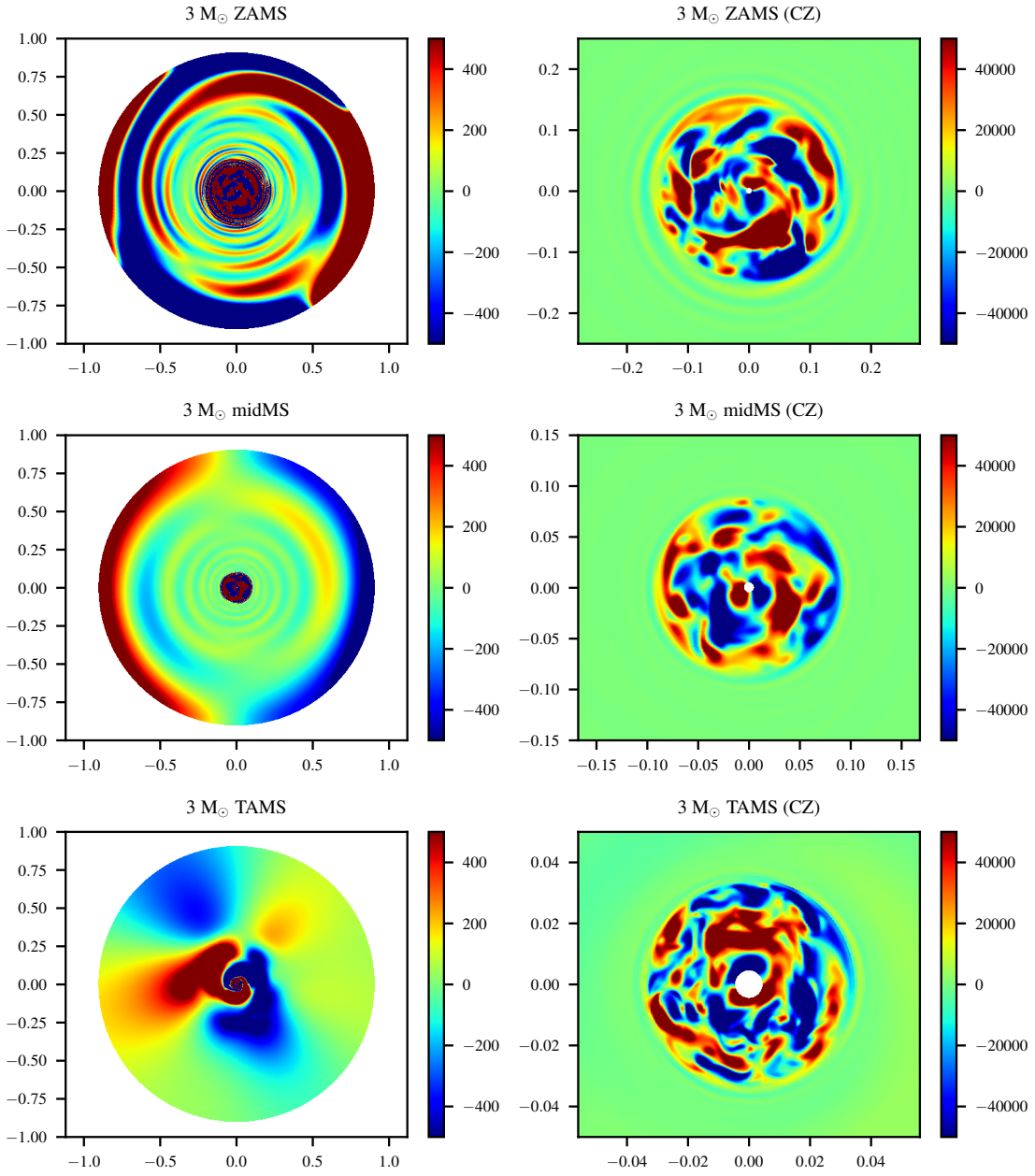

Figure 4.2: Time snapshot of the whole stellar interior (left panels) and just the convection zone/CZ (right panels) for the $3M_\odot$ ZAMS model (top panels), $3M_\odot$ midMS model (middle panels) and $3M_\odot$ TAMS model (bottom panels). The colour maps represent the tangential velocities in cm s^{-1}.

the convection zone (right column) for the masses and ages indicated above the panels. The colour map represents the tangential velocities minus the mean flow velocity (see Eq. 2.8). From all three figures, we can generally see that the fluid velocities in the convection zone have structures at both smaller and larger spatial scales, while the radiation zone is

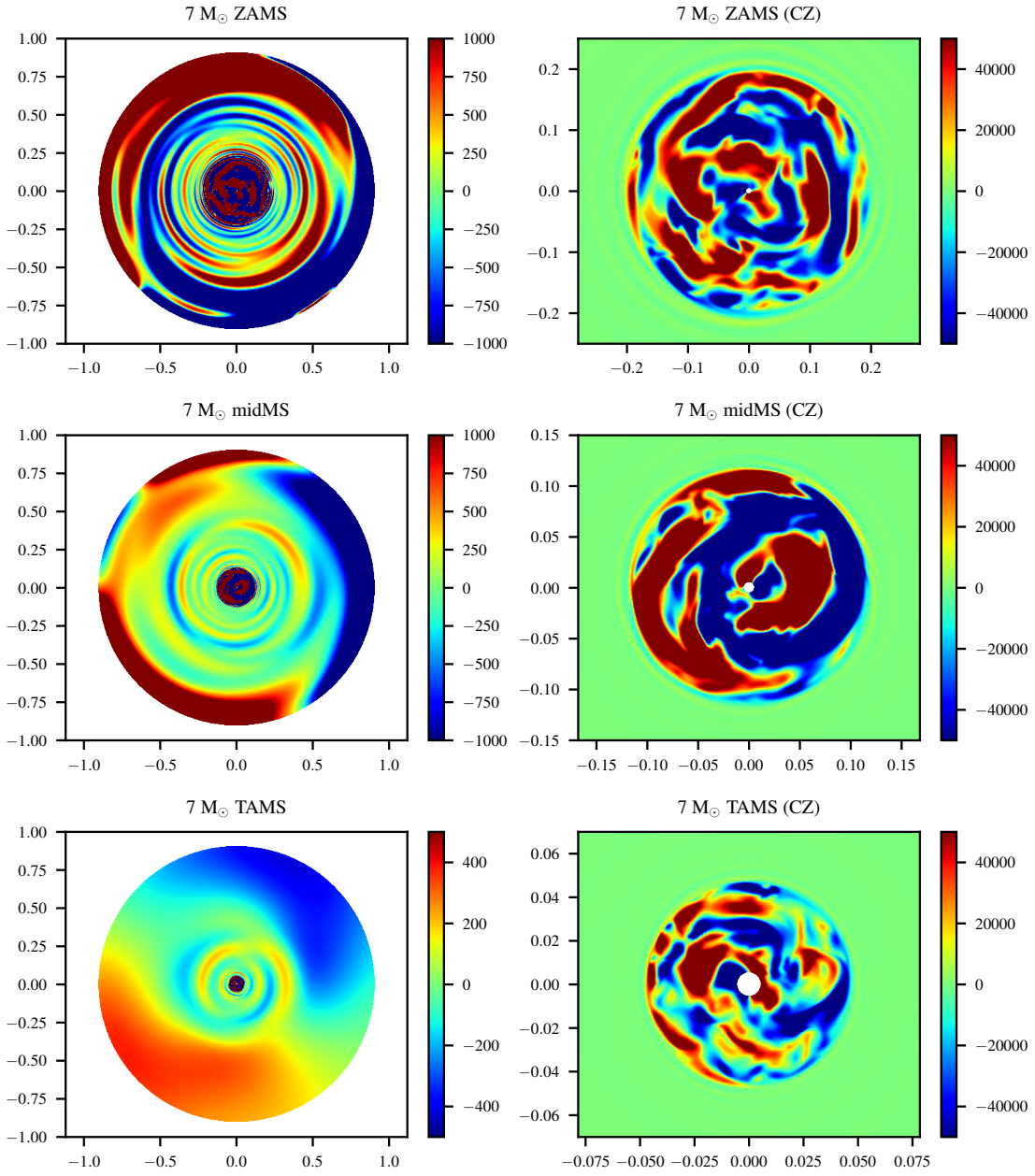

Figure 4.3: Time snapshot of the whole stellar interior (left panels) and just the convection zone/CZ (right panels) for the $7M_\odot$ ZAMS model (top panels), $7M_\odot$ midMS model (middle panels) and $7M_\odot$ TAMS model (bottom panels). The colour maps represent the tangential velocities in cm s^{-1}.

dominated by larger scale fluid motions. In fact, for older stars of a particular mass, we observe a decrease in the presence of smaller scale fluid motion in the radiation zone due to the larger damping experienced by waves, similar to that seen in Fig. 3.22 (Please refer to Sec 3.5.1).

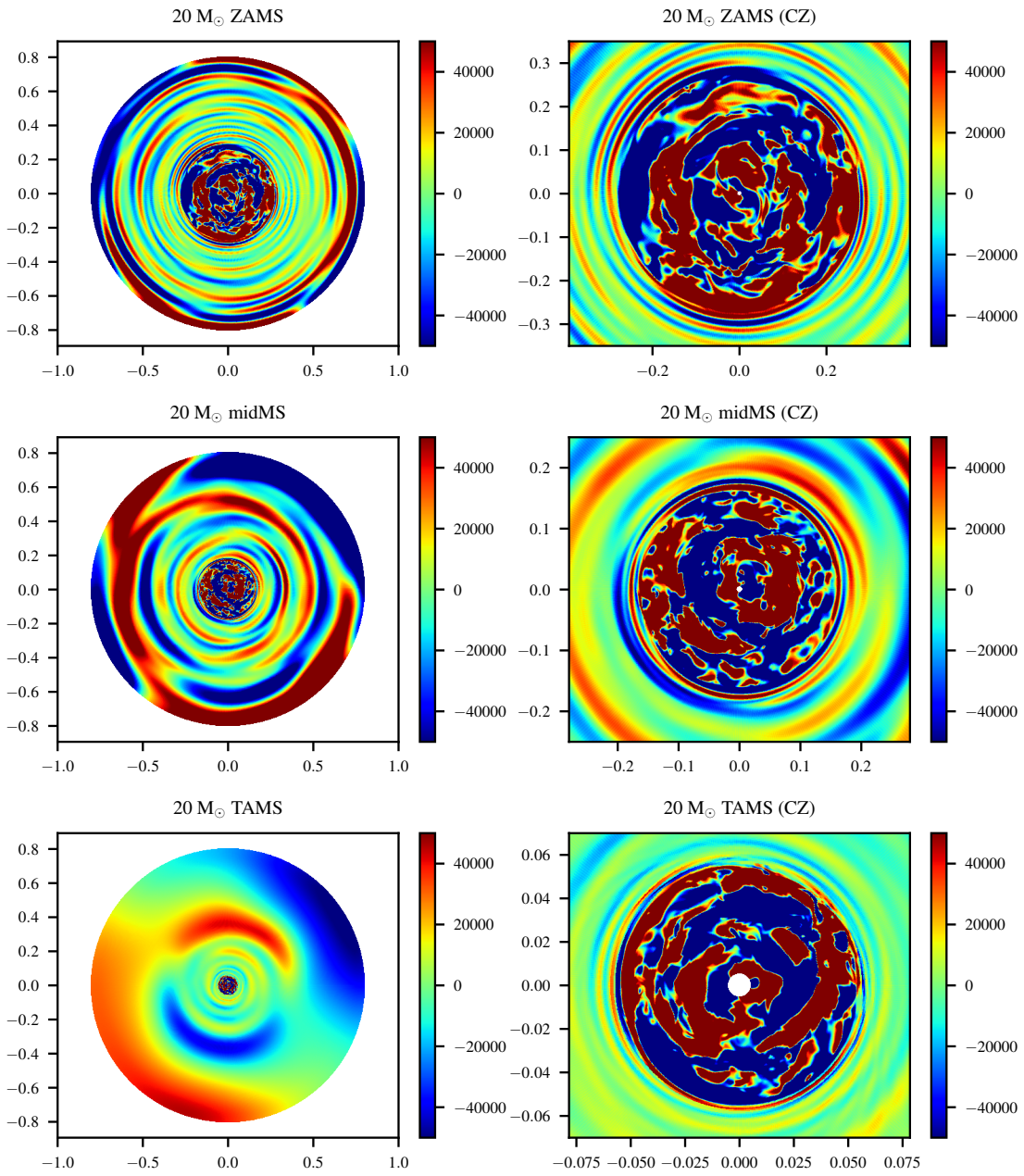

Figure 4.4: Time snapshot of the whole stellar interior (left panels) and just the convection zone/CZ (right panels) for the $20M_\odot$ ZAMS model (top panels), $20M_\odot$ midMS model (middle panels) and $20M_\odot$ TAMS model (bottom panels). The colour maps represent the tangential velocities in cm s^{-1}.

For all the models we used, the viscosity for the TAMS models has been set to a lower value than that for the ZAMS and midMS models for a given age. We do this to allow each model to achieve the highest possible *Re*, while still ensuring numerical stability. As a result, for the $3M_\odot$ models, we can clearly observe the TAMS model exhibiting more

Model	$\nu/10^{12}$ cm^2 s^{-1}	K$/10^{12}$ cm^2 s^{-1}	Re	Pr	$Ra/10^{11}$	average v_{rms}/cm s^{-1}	MLT velocity/cm s^{-1}
3M$_\odot$ ZAMS	5	5	281	1	0.13	65000	6500 ± 1500
3M$_\odot$ midMS	5	5	230	1	0.087	59000	8200 ± 1800
3M$_\odot$ TAMS	1	1	626	1	0.73	49000	9100 ± 1900
7M$_\odot$ ZAMS	5	5	921	1	1.12	100000	16000 ± 3700
7M$_\odot$ midMS	5	5	852	1	0.70	102000	21000 ± 4200
7M$_\odot$ TAMS	2.5	2.5	880	1	1.3	77000	24000 ± 4300
20M$_\odot$ ZAMS	8	8	3316	1	8.41	230000	39000 ± 9000
20M$_\odot$ midMS	8	8	3230	1	6.64	240000	50000 ± 10000
20M$_\odot$ TAMS	5	5	3453	1	11.26	220000	54000 ± 10000

Table 4.2: Stellar parameter for all the models used in this investigation. The average v_{rms} is the root-mean-square of the total velocity in the horizontal direction averaged over the radial extent of the convection zone and the time domain given in Fig. 4.6. The MLT velocity is the mixing-length theory velocity as given by MESA and plotted in Fig. 2.5.

small scale structures compared to the ZAMS and midMS models. This is not the case for the other two stellar masses. In fact, the Re (Eq. (4.1)) was found to be similar for all three ages for the 7M$_\odot$ and 20M$_\odot$ models but not for the 3M$_\odot$ model (see Table 4.2). The larger Re for the 3M$_\odot$ TAMS model explains the small scale structure that are observed. Comparing the convection zone for different stellar masses, as the mass increases, the fluid velocities increase and exhibit highly turbulent behaviour (more small-scale structures). Again, looking at Table 4.2, both the Re and Ra are larger for more massive stars, which indicates a more turbulent convection zone. Note that we chose to set Pr for all models to a constant value of 1. The general alternating pattern of positive and negative velocities in the radiation zone for all the models indicates IGWs.

One of the properties of turbulent convection is that it is expected to homogenise fluid velocities in the horizontal and vertical directions (Batchelor, 1960). To check this we calculate the ratio of the horizontal velocities to the vertical velocities of the models given in Table 4.2. Figure 4.5 shows this ratio for the three 3M$_\odot$ models (ZAMS, midMS and TAMS) at the mid-point of the convection zone. We find that for the three models mentioned above, the ratio lies between 0.4 and 2.0. This range is valid for the whole convection zone and all the other models we investigated as well. Ideally, a fully, homogenised turbulent convection zone is expected to have $u_r/u_\theta \sim 1$, so we believe that our range of ratios shows that the convection zones for the different models are fairly close to being fully homogenised.

4.2.1 Simulating the Convection Zone

In the last column of Table 4.2, we show the bulk convective velocity calculated with the mixing-length theory in MESA (also presented in Fig. 2.5). In general, the velocities in the convection zone from our simulations are between 4 to 10 times larger. Thus, to increase the comparability between stellar masses, we attempt to force the convective velocities for the different stellar models to match the ratio of bulk convective velocities from MESA.

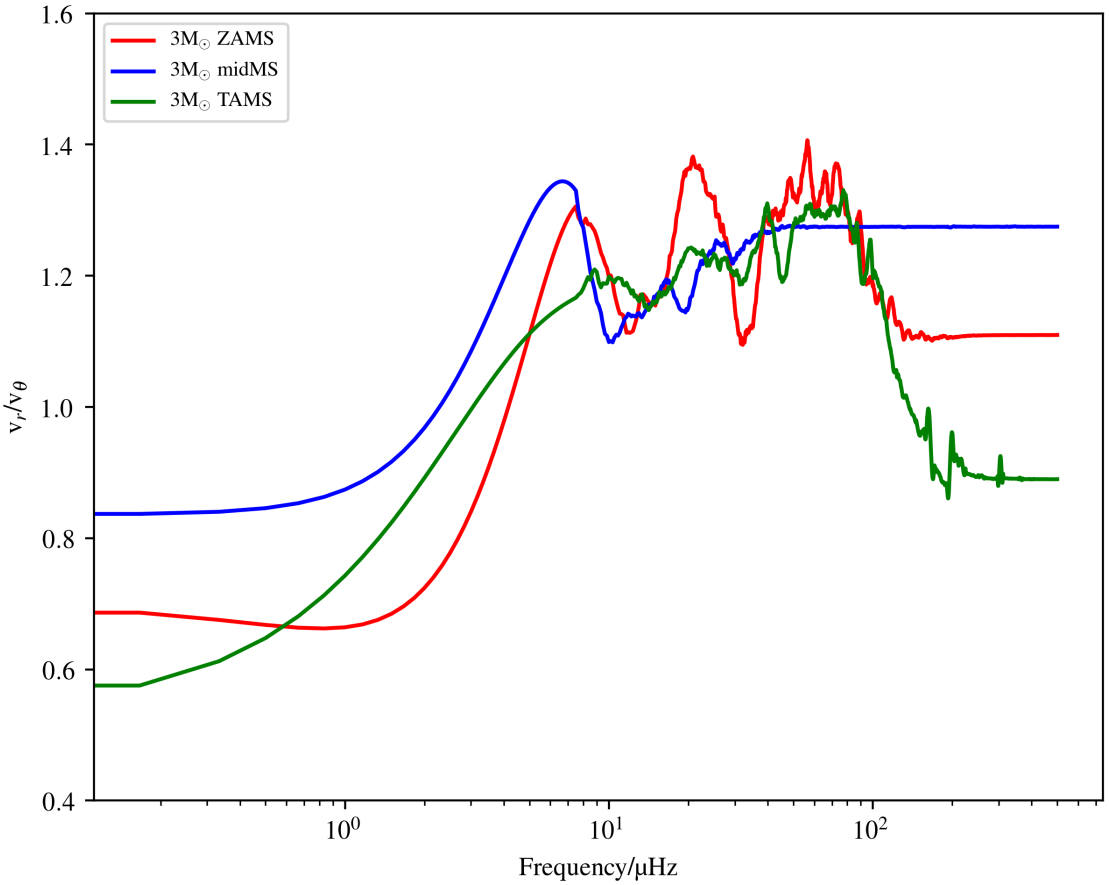

Figure 4.5: The ratio of the radial to tangential velocity as a function of frequency for $3M_\odot$ models in the middle of the convection zone. Generally, this ratio was found to be between 0.4 and 2 for all the stellar models investigated in this work.

As an example, the approximate convective velocity ratio between a $3M_\odot$ ZAMS model and $7M_\odot$ ZAMS model is 1:2, and that between a $3M_\odot$ ZAMS model and $20M_\odot$ ZAMS model is 1:4. Thus, we force convection for these models to produce fluid velocities that approximately match this ratio. This is done by manipulating the stellar parameters that govern the Rayleigh number, mainly the "superadiabaticity" (see Eq. (4.4)), thermal diffusivity, K, and viscosity, ν. One crucial point to mention here is that we try to match the ratio of velocities only for different stellar masses and not for different ages. We do this because we found that the uncertainties for the convective velocities given in MESA across age are large, for a given mass.

Once convection begins in our simulations, we track the root-mean-square velocity given as

$$\mathrm{v_{rms}}(r,t) = \left(\frac{1}{N} \sum_{n=1}^{N} v_{r,n}^2(r,t) + v_{\theta,n}(r,t)^2 \right)^{1/2}, \tag{4.5}$$

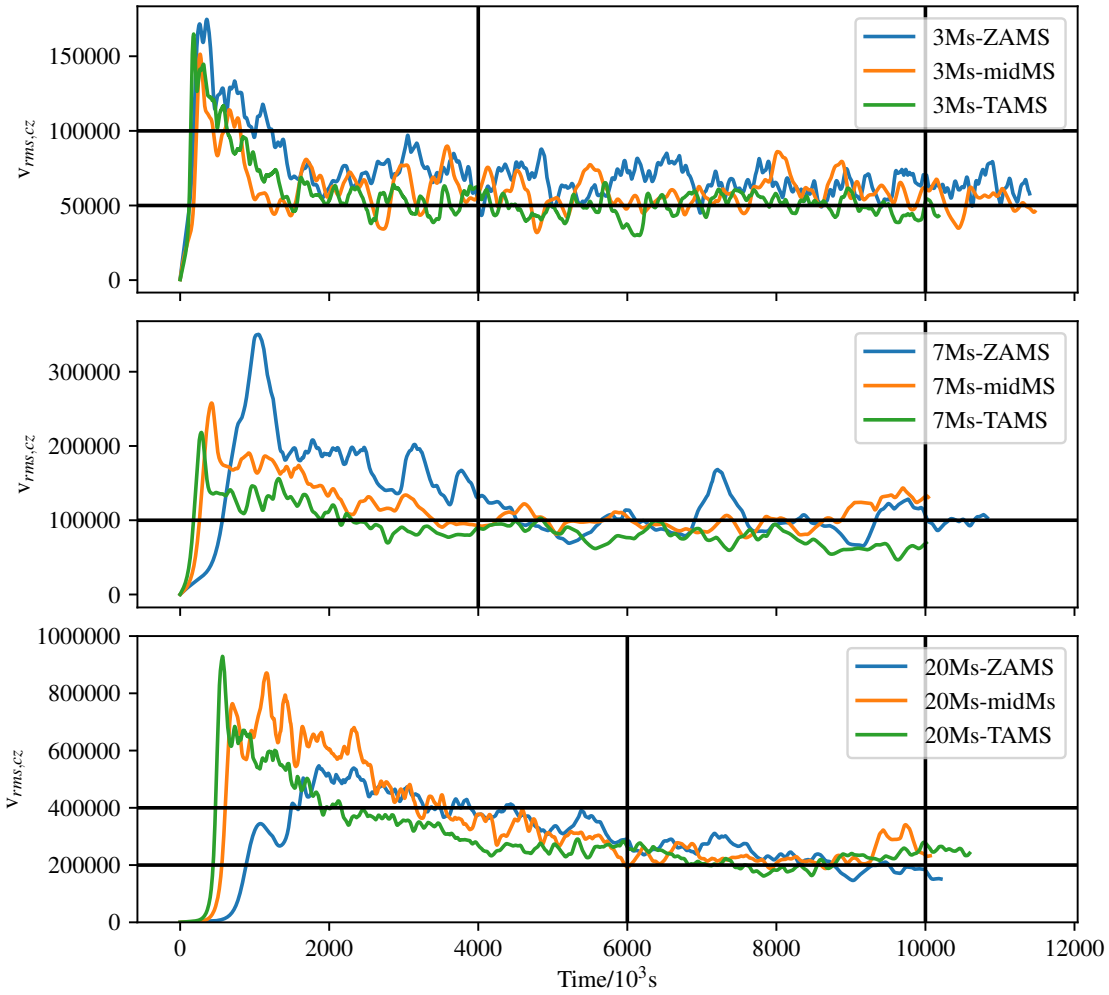

Figure 4.6: The root-mean-square velocity, $v_{\rm rms}$, calculated over the horizontal direction and averaged over the radial extent of the convection zone, as a function of time. The top panel shows the $v_{\rm rms}$ for the $3M_\odot$ models, the middle panel for the $7M_\odot$ models and the bottom panel for the $20M_\odot$ models. The solid, black, horizontal lines are plotted as guidance and the solid, black, vertical lines represent the time domain in which most of our analysis in this section was done.

where n is the horizontal grid index and N is the total number of horizontal grid cells, which is equal to 1024 in our case. Once the convective velocities reach a steady-state, $\mathrm{v_{rms}}(r,t)$ is then averaged over the radial extent of the convection zone and time. Figure 4.6 shows an example of the radially averaged $\mathrm{v_{rms}}$ evolution with time for the models used in this investigation. For the $3M_\odot$ and $7M_\odot$ models, we chose the time window between 4×10^6 s to 1×10^7 s (marked by vertical black lines), and calculated the time-averaged $\mathrm{v_{rms}}$. We chose a smaller time window, between 6×10^6 s to 1×10^7 s, for the $20M_\odot$ models. We use this $\mathrm{v_{rms}}$ (denoted as average $\mathrm{v_{rms}}$ in Table 4.2) to calculate Re, which we show in Table 4.2, along with other stellar parameters.

4.3 Frequency Spectra

As addressed in Chapter 1, Section 1.3.1, the IGW generation spectrum in intermediate-mass stars is a problem that has attracted the attention of theorists and observers alike. Published work on numerical studies on IGW generation in main-sequence intermediate-mass stars has so far been limited to stars with a specific stellar mass (i.e. $3M_{\odot}$ in Rogers *et al.* (2013), Edelmann *et al.* (2019) and Horst *et al.* (2020)) but as mentioned in Chapter 1, Section 1.4, there is more observational data available for high-mass stars (OB-type stars), so studying IGW generation for a range of masses and also ages, is critical at this point.

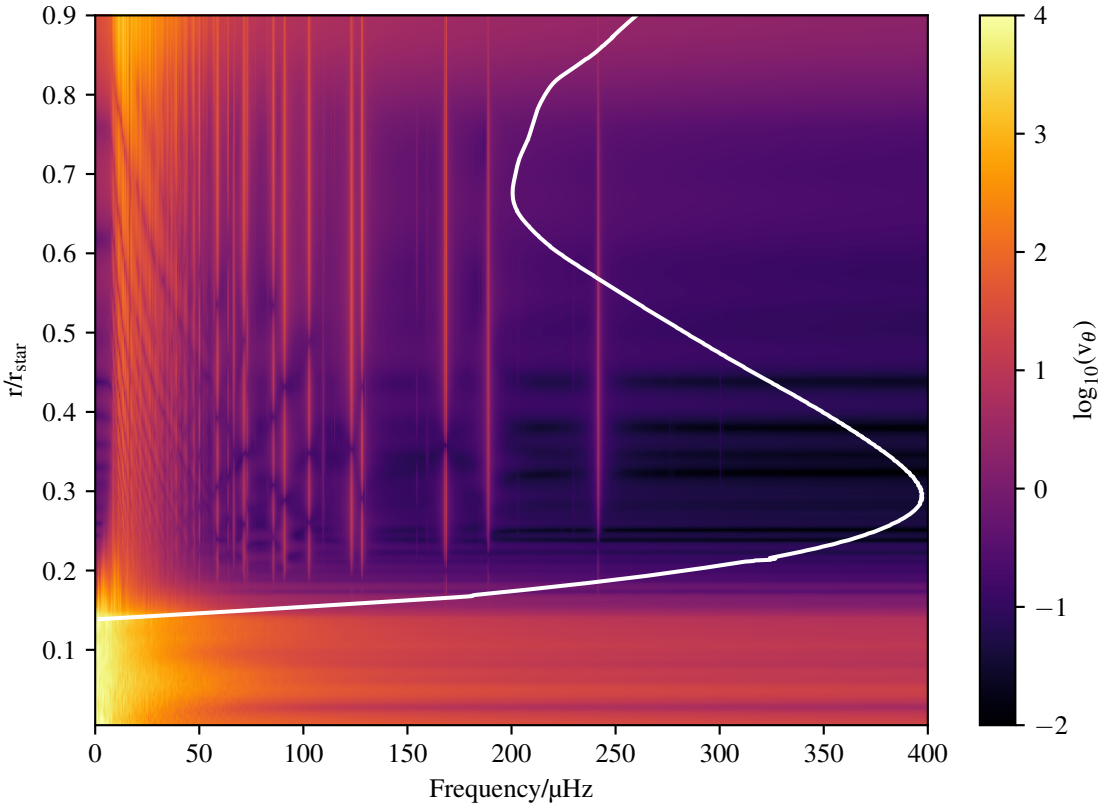

Figure 4.7: The tangential velocity amplitudes as functions of frequency and stellar radius for a $3M_{\odot}$ ZAMS star. The white line represents the Brunt–Väisälä frequency profile for this model.

4.3.1 Generation Spectra

Figure 4.7 shows the frequency spectrum of horizontal velocities in the whole stellar interior for a $3M_{\odot}$ ZAMS star, with colour representing velocity amplitude. One can see that velocities are significantly larger in the convection zone, which spans approximately 14% of the total stellar radius. Within the radiation zone, we can see strong stationary modes

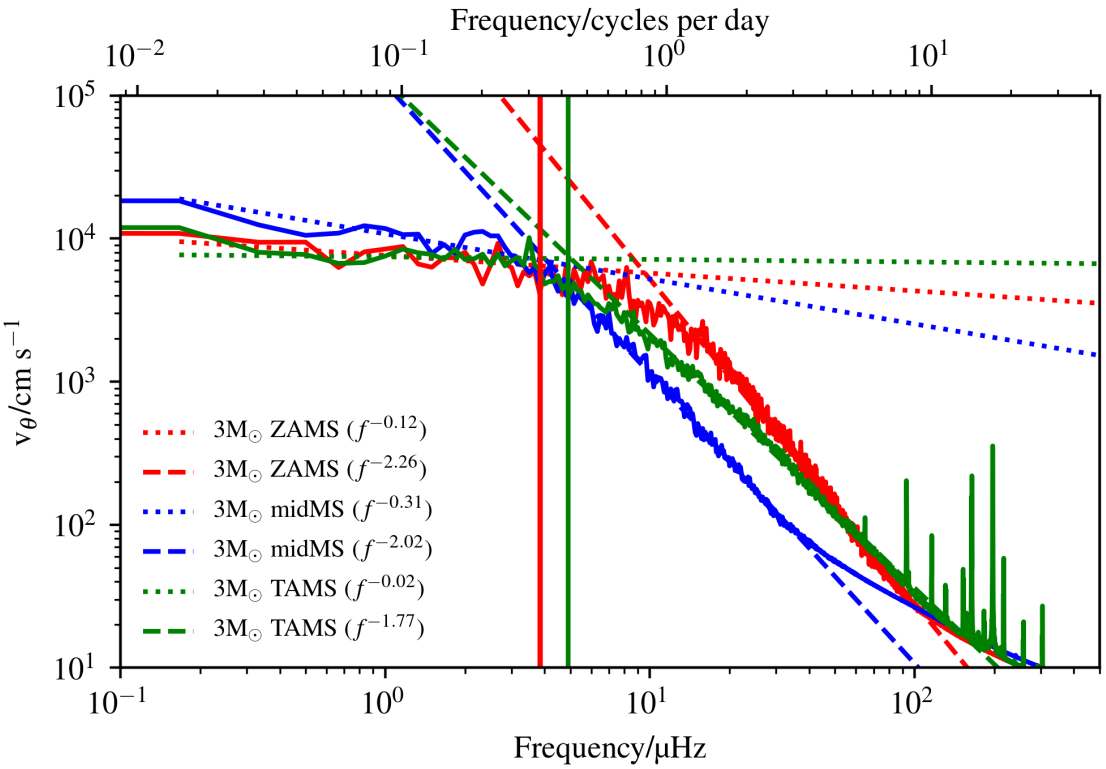

Figure 4.8: The tangential velocity at the top of the convection zone (see Table 4.1) of the 3M$_\odot$ models as a function of frequency. The vertical straight lines show the upper limit for the convective turnover frequencies (see Eq. (2.27)) for each model. The dashed lines show straight-line fits done using the least-squares fit method. We find a broken power-law for all these fits at 30 μHz.

and at lower frequencies, we see the effect of diffusion as waves damp rapidly as they move away from the convection zone.

The boundary layer between these the radiation zone and the convection zone is where IGWs are thought to be are generated. Theoretically, the exact transition between the two zones occurs at N = 0 μHz. We select the location where N = 0 and plot the tangential velocities as a function of frequency for three models, 3M$_\odot$ ZAMS, 3M$_\odot$ midMS and 3M$_\odot$ TAMS, at this boundary, as shown in Fig. 4.8. We overplot two straight-line fits in the log-log plot , done using the least-squares fit method, at a low-frequency regime and a high-frequency regime, which varies in range depending on the stellar model (see Table 4.3 for the exact frequency range). Generally, the frequency spectrum is flat at low frequencies and steeper at high frequencies, where the "turnoff" appears to depend on the model (still under investigation). It has been theorised (Lecoanet & Quataert, 2013) that this turnoff frequency is related to the convective turnover frequency (see Eq. (2.27)), which we plot as solid vertical lines for each model. The turnover frequencies here were calculated with the assumption that convective rolls span the whole convection zone. However, these

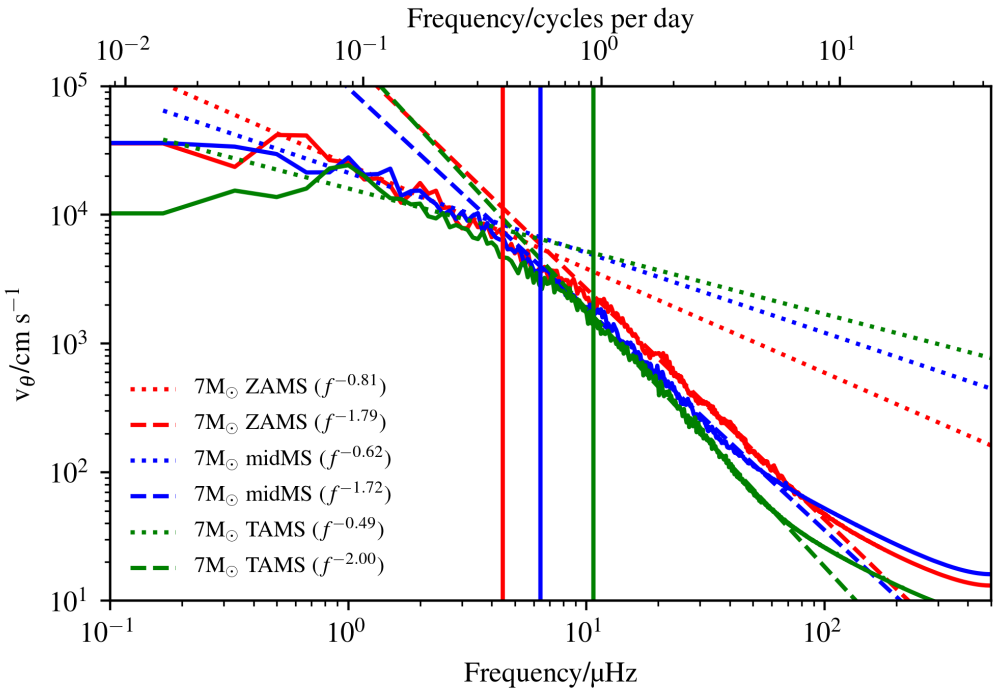

Figure 4.9: The tangential velocity at the top of the convection zone (see Table 4.1) of the 7M$_\odot$ models as a function of frequency. See Fig 4.8 for explanations for the vertical and dashed lines.

rolls exist at a much smaller scale too, and from Figures 4.2, 4.3 and 4.4, we estimate a minimum size of a convective roll to be 1/8th of the size of the convection zone. The convective turnover frequency (CTF) range is given in Table 4.3. We find that generally, the convective turnover frequencies are off by almost one order of magnitude compared to the "turnoff" frequency, when the size of convective rolls are approximated as the extent of the convection zone. The turnoff and turnover frequencies are closer, however, for smaller convective rolls. Also, note the broad agreement with a double power-law (Rogers *et al.*, 2013) with a shallow slope between 0 and -0.5 at lower frequencies and a steeper slope between -1.5 and -2.5 at higher frequencies. Comparing this with the work done in Chapter 3 where we analysed non-linear IGW propagation with the assumption that at different stellar ages, the generation spectrum does not change, we find that the assumption was not entirely incorrect.

An extra point to note for Fig. 4.8 are the peaks seen in the spectrum for the 3M$_\odot$ TAMS model at frequencies above 100 μHz. These peaks are stationary gravity modes which form within the Brunt–Väisälä frequency spikes just outside the convection zone in older stars, as shown in Fig 2.10. These peaks are effectively seen in the convection zone which indicates a tunnelling effect exhibited by gravity modes.

Next, we move on to the generation spectrum for the 7M$_\odot$ and 20M$_\odot$ models. We

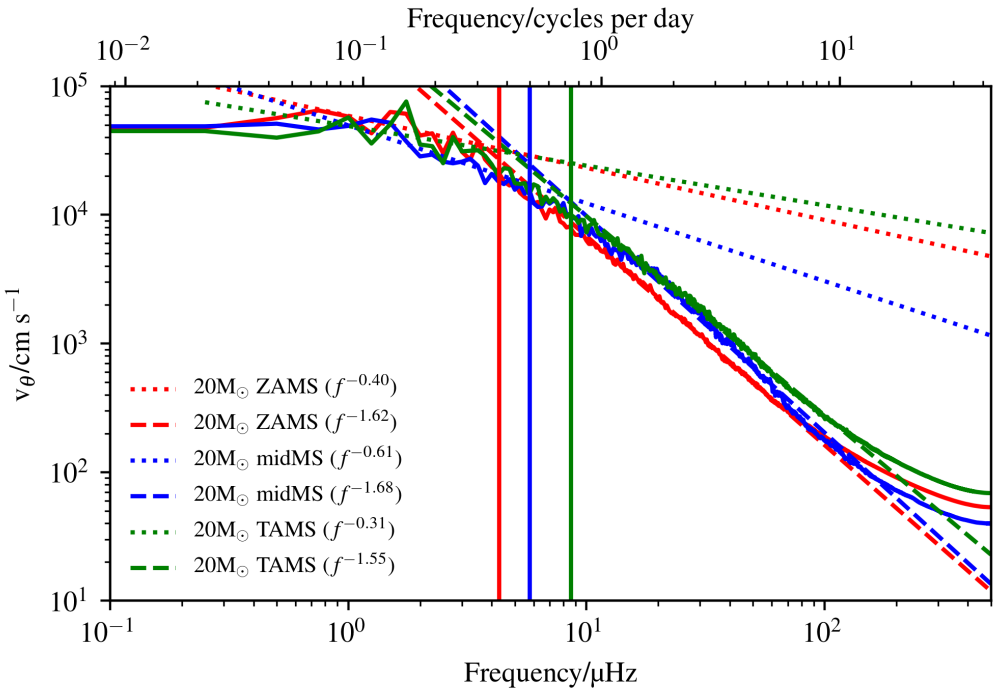

Figure 4.10: The tangential velocity at the top of the convection zone (see Table 4.1) of the 20M$_\odot$ models as a function of frequency. See Fig 4.8 for explanations for the vertical and dashed lines.

repeat the procedure done for the 3M$_\odot$ models and plot the results in Fig. 4.9 and Fig. 4.10 respectively. The frequency ranges for the fits and slopes are displayed in Table 4.3. We find the generation spectrum for these higher mass stars to exhibit the same trend: shallow slope at low frequencies and steeper slopes at higher frequencies. Also, we find the convective turnover frequencies are still quite far off from the "turnoff" frequency.

We find that for all the models, the frequency exponents for the tangential velocities lie between 0 and -1 at lower frequencies with the 3M$_\odot$ midMS model being an outlier, and between -1.5 and -3 at higher frequencies. Between the different stellar masses and ages, however, we do not find any discernible pattern in the IGW generation spectrum slopes.

4.3.2 Surface Spectra

Compared to the work done in chapter 3, Section 3.5.1, the study of the surface spectra for these simulation are less comparable to observational data due to one main factor: the use of different thermal diffusivities for different stellar models, which are kept constant throughout the simulation domain. However, they still provide an insight to the propagation mechanism for different stellar masses, which was not addressed before. Figure 4.11, Fig. 4.12 and Fig. 4.13 show the tangential velocities as a function of frequency

$3M_\odot$ ZAMS	Frequency Range	0.5 μHz $\leqslant f \leqslant$ 3 μHz	10 μHz $\leqslant f \leqslant$ 70 μHz
CTF Range	Frequency Slopes	-0.12	-2.26
(0.48 μHz – 3.86 μHz)			
$3M_\odot$ midMS	Frequency Range	0.5 μHz $\leqslant f \leqslant$ 3 μHz	3 μHz $\leqslant f \leqslant$ 30 μHz
CTF Range	Frequency Slopes	-0.31	-2.02
(0.48 μHz – 3.84 μHz)			
$3M_\odot$ TAMS	Frequency Range	0.5 μHz $\leqslant f \leqslant$ 3 μHz	7 μHz $\leqslant f \leqslant$ 70 μHz
CTF Range	Frequency Slopes	-0.01	-1.77
(0.62 μHz – 4.92 μHz)			
$7M_\odot$ ZAMS	Frequency Range	0.5 μHz $\leqslant f \leqslant$ 3 μHz	10 μHz $\leqslant f \leqslant$ 70 μHz
CTF Range	Frequency Slopes	-0.81	-1.79
(0.56 μHz – 4.44 μHz)			
$7M_\odot$ midMS	Frequency Range	0.5 μHz $\leqslant f \leqslant$ 3 μHz	10 μHz $\leqslant f \leqslant$ 70 μHz
CTF Range	Frequency Slopes	-0.62	-1.72
(0.80 μHz – 6.40 μHz)			
$7M_\odot$ TAMS	Frequency Range	0.5 μHz $\leqslant f \leqslant$ 3 μHz	10 μHz $\leqslant f \leqslant$ 70 μHz
CTF Range	Frequency Slopes	-0.49	-2.00
(1.34 μHz – 10.68 μHz)			
$20M_\odot$ ZAMS	Frequency Range	0.8 μHz $\leqslant f \leqslant$ 3 μHz	10 μHz $\leqslant f \leqslant$ 70 μHz
CTF Range	Frequency Slopes	-0.40	-1.62
(0.54 μHz – 4.30 μHz)			
$20M_\odot$ midMS	Frequency Range	0.8 μHz $\leqslant f \leqslant$ 3 μHz	10 μHz $\leqslant f \leqslant$ 70 μHz
CTF Range	Frequency Slopes	-0.61	-1.68
(0.72 μHz – 5.79 μHz)			
$20M_\odot$ TAMS	Frequency Range	0.8 μHz $\leqslant f \leqslant$ 3 μHz	10 μHz $\leqslant f \leqslant$ 70 μHz
CTF Range	Frequency Slopes	-0.31	-1.55
(1.08 μHz – 8.63 μHz)			

Table 4.3: The table shows the frequency slopes of the tangential velocity amplitudes at generation for all the models used in this work. The table also shows the convective turnover frequency (CTF) ranges for each model.

for $3M_\odot$, $7M_\odot$ and $20M_\odot$, close to the top boundary of the simulation domain, whilst Table 4.4 shows the frequency exponents from the fits for all the stellar models. Generally, the frequencies slopes at higher frequencies lie between -2 and -4, with the $7M_\odot$ ZAMS model being an outlier as this model did not have a clear broken power-law, whilst the slopes at lower frequencies lie between 0 and -2. As seen in the previous section, we find no discernible pattern between different stellar ages and masses. We also find that for more massive stars the amplitudes of waves flatten out more quickly at higher frequencies, which is due to the lower average Brunt–Väisälä frequencies in the simulation domain (see Fig. 2.10).

One important point to note here is that for older, more massive stars ($7M_\odot$ and $20M_\odot$), we do not see peaks that dominate the high-frequency spectrum as we see in the $3M_\odot$ TAMS case. This is likely due to the very low thermal diffusivity and viscosity (see Table 4.2) used for the $3M_\odot$ TAMS case, which allows waves formed in the Brunt–Väisälä

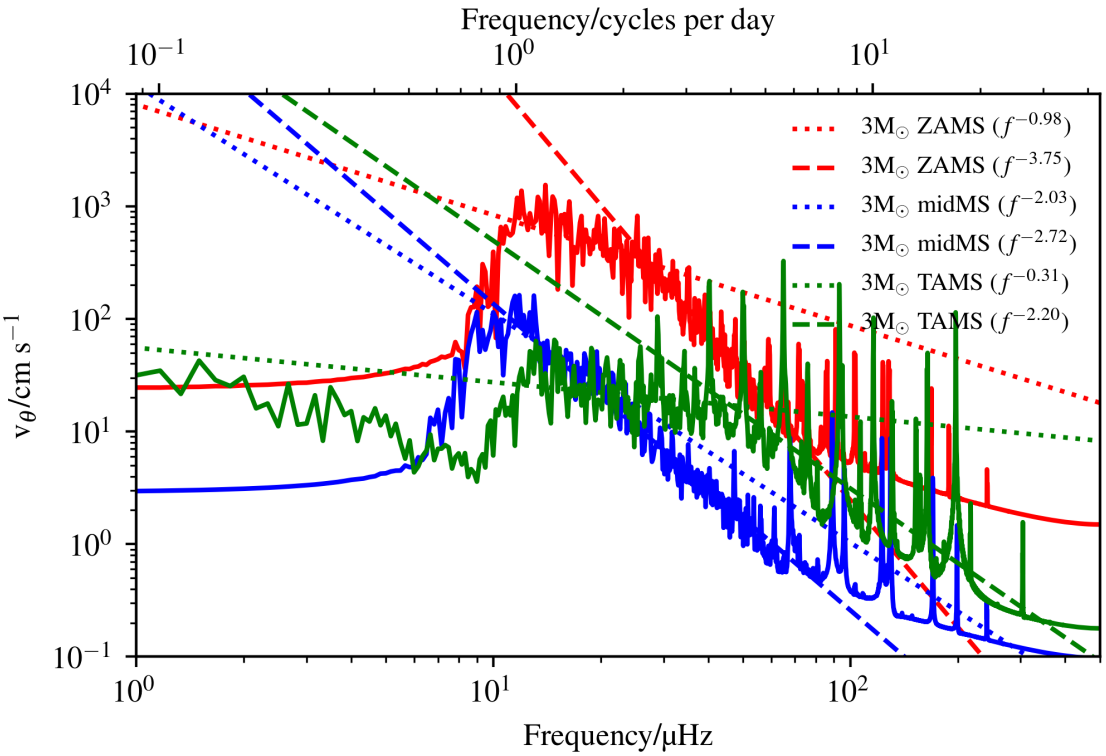

Figure 4.11: The tangential velocity of 3M$_\odot$ models as a function of frequency close to the top of the simulation domain.

spike to travel further into the radiation zone.

We also find that for the 3M$_\odot$ models and the 7M$_\odot$ models, there is a negative slope for frequencies below 10 μHz. This was found to be caused by a mean flow in the system. The dissipation of IGW amplitudes is expected to cause an acceleration of the background mean flow and we believe we are observing an artefact of this process here. One might argue that this mean flow develops form viscous interactions but using the viscosity values in Table 4.2 to calculate the rough timescales for viscous interaction shows that these timescales are larger than our simulation time. For example, taking the size of the radiation zone for a 3M$_\odot$ ZAMS model up to 90% of the stellar radius ($\sim 1.0 \times 10^1 1cm$) and the viscosity value of $5.0 \times 10^1 2$ cm^2 s^{-1}, we find a timescale of 2.0×10^9 s, which is 2 orders of magnitude larger than the simulation time for this model (see Fig. 4.6).

Comparing the frequency slopes at generation (Table 4.3) and the surface (Table 4.4) for all the models, we find the slopes at the surface to be generally steeper at the high-frequency range. We do not compare the low-frequency range as for all the stellar models, there is a steep drop in amplitude at low frequencies, where the drop-off frequency is dependent on the stellar age.

Returning to the point made at the beginning of this section on result comparability,

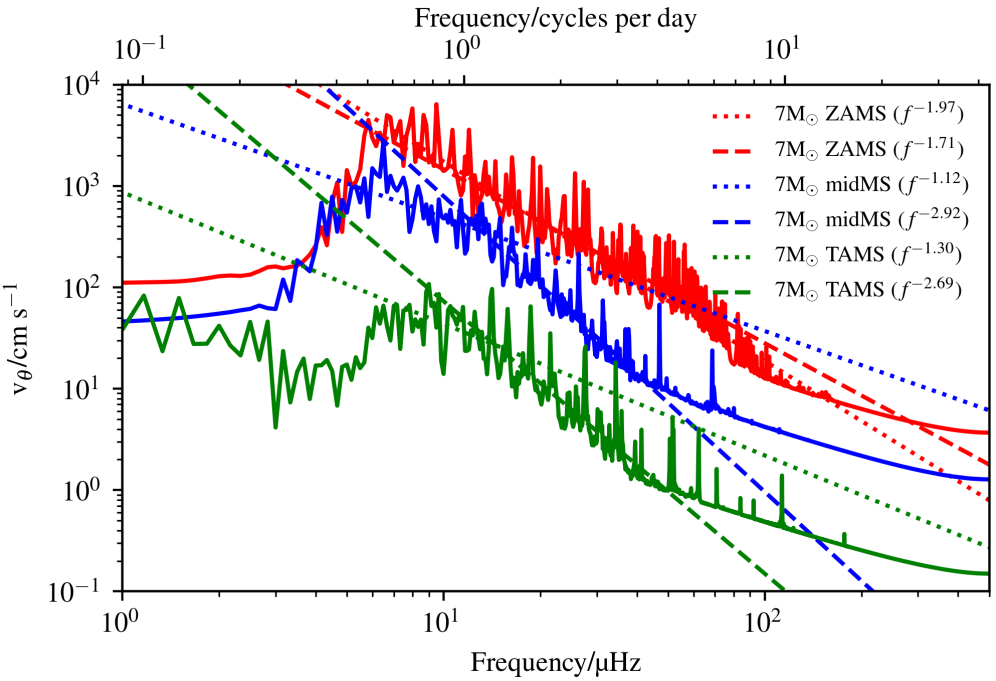

Figure 4.12: The tangential velocity of 7M$_\odot$ models as a function of frequency close to the top of the simulation domain.

a few improvements can be made to improve our work. One example would be to have a constant high thermal diffusivity and viscosity in the convection zone to maintain numerical stability and track the stellar thermal diffusivity out in the radiation zone. This will allow waves in the radiation zone to experience a more realistic effect from damping. We do a quick analysis, where we use linear theory to investigate the change in wave amplitudes as they propagate from a randomly chosen radius in the middle of the radiation zone for different thermal diffusivities (constant and real). The initial amplitudes were set to 1. Figure 4.14 shows the ratio of IGW amplitudes when we use stellar diffusivities to those when we use the constant diffusivities set in our simulations (Table 4.2). We find that at lower frequencies, the constant diffusivities overestimates damping. This causes loss of information from low-frequency waves, which might contribute significantly to the low-frequency slopes. We also find that for more massive and older stars, the effect of using a constant thermal diffusivity is seen at lower frequencies. This highlights the need to investigate the shortcomings of using constant thermal diffusivities and any other issues with our work in general, which will be discussed further in the next chapter.

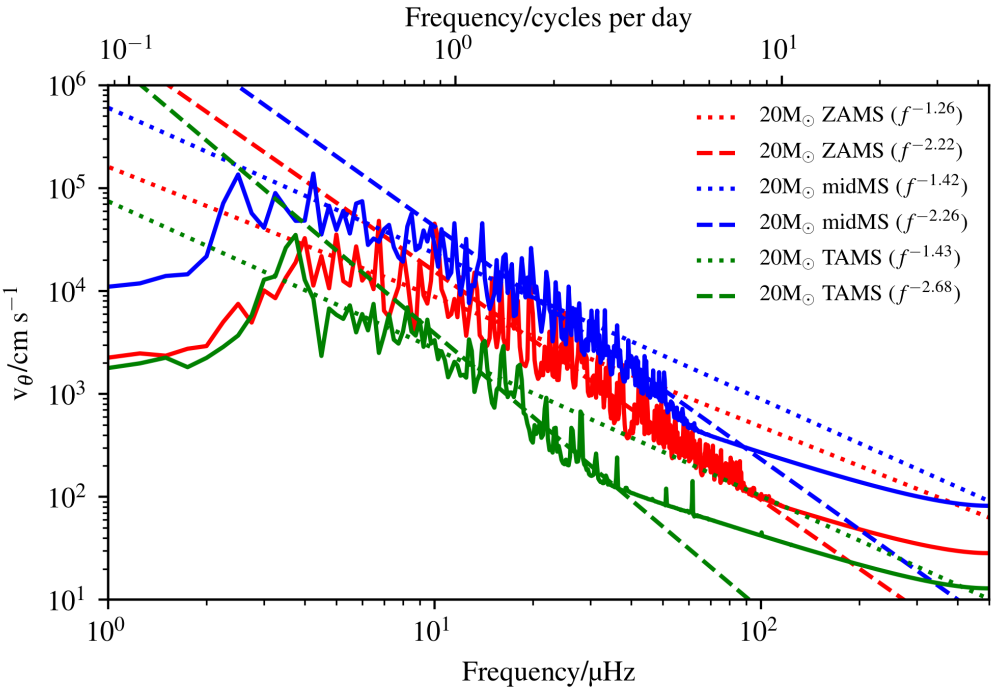

Figure 4.13: The tangential velocity of 20M$_\odot$ models as a function of frequency close to the top of the simulation domain.

3M$_\odot$ ZAMS	Frequency Range	10 μHz $\leqslant f \leqslant$ 30 μHz	30 μHz $\leqslant f \leqslant$ 70 μHz
	Frequency Slopes	-0.98	-3.75
3M$_\odot$ midMS	Frequency Range	10 μHz $\leqslant f \leqslant$ 20 μHz	20 μHz $\leqslant f \leqslant$ 70 μHz
	Frequency Slopes	-2.03	-2.72
3M$_\odot$ TAMS	Frequency Range	10 μHz $\leqslant f \leqslant$ 40 μHz	40 μHz $\leqslant f \leqslant$ 100 μHz
	Frequency Slopes	-0.31	-2.20
7M$_\odot$ ZAMS	Frequency Range	10 μHz $\leqslant f \leqslant$ 15 μHz	15 μHz $\leqslant f \leqslant$ 40 μHz
	Frequency Slopes	-1.97	-1.71
7M$_\odot$ midMS	Frequency Range	10 μHz $\leqslant f \leqslant$ 15 μHz	15 μHz $\leqslant f \leqslant$ 40 μHz
	Frequency Slopes	-1.12	-2.92
7M$_\odot$ TAMS	Frequency Range	10 μHz $\leqslant f \leqslant$ 15 μHz	15 μHz $\leqslant f \leqslant$ 40 μHz
	Frequency Slopes	-1.30	-2.69
20M$_\odot$ ZAMS	Frequency Range	6 μHz $\leqslant f \leqslant$ 15 μHz	15 μHz $\leqslant f \leqslant$ 40 μHz
	Frequency Slopes	-1.26	-2.22
20M$_\odot$ midMS	Frequency Range	6 μHz $\leqslant f \leqslant$ 15 μHz	15 μHz $\leqslant f \leqslant$ 40 μHz
	Frequency Slopes	-1.42	-2.26
20M$_\odot$ TAMS	Frequency Range	6 μHz $\leqslant f \leqslant$ 15 μHz	15 μHz $\leqslant f \leqslant$ 40 μHz
	Frequency Slopes	-1.43	-2.68

Table 4.4: The table shows the frequency slopes of the tangential velocity amplitudes close to the stellar surface.

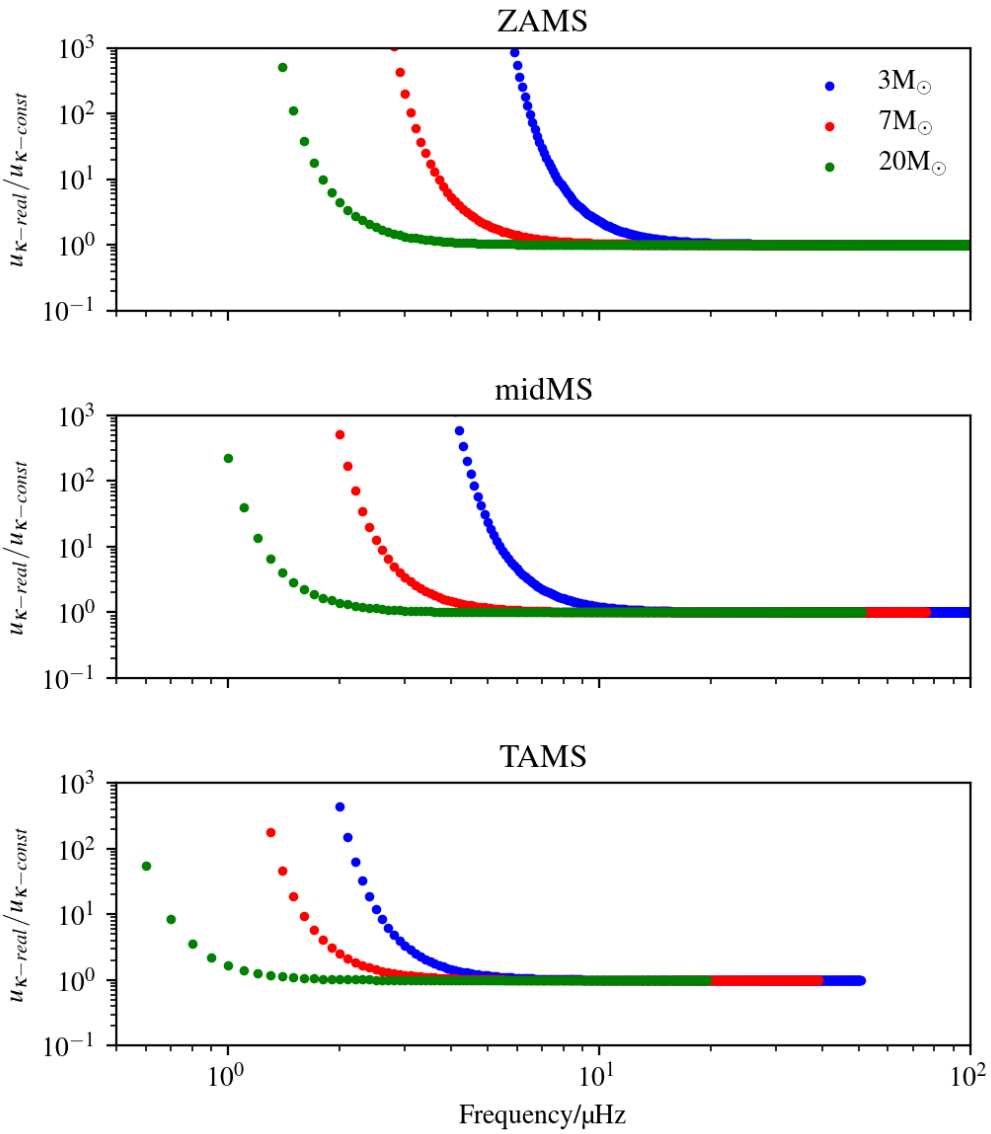

Figure 4.14: The ratio of linear IGW amplitudes as a function of frequency for stellar thermal diffusivities (see Fig. 2.1) to those for the constant thermal diffusivities used in our simulations (see Table 4.2 close to the top of the radiation zone for models of different stellar ages and masses. The wavenumber for these waves is 1. The initial radius for these IGWs was chosen at random from the middle of the radiation zone and the initial amplitude was set to unity.)

Chapter 5

Conclusion and Outlook

5.1 Conclusion

In this work, we have presented results on three projects involving internal gravity waves (IGWs) in intermediate-mass stars (with convective cores and radiative envelopes): Linear IGW propagation, Non-linear IGW Propagation and IGW generation through core convection in stars of different masses and ages. In the first project, we used a formulation developed to study IGW propagation in the linear regime and investigated the amplitude evolution of IGWs in the radiation zones of stars with masses from $3M_\odot$ to $20M_\odot$ and ages from Zero-Age-Main-Sequence (ZAMS) to Terminal-Age-Main-Sequence (TAMS). We find that more waves become non-linear when the dependence of the generation spectrum on frequency and wavenumber is less steep. We also find that higher convective velocities lead to more waves becoming non-linear. The effect of stellar metallicity and age on wave nonlinearity is found to be sensitive to the generation spectrum. Finally, with increasing stellar mass, there is an increasing trend in the amount of energy in non-linear waves. We find that for the generation spectrum given in Rogers *et al.* (2013) (which is likely to be the closest to real stars), the percentage of total energy in non-linear waves is at least 20% for almost all the models tested. This clearly underlines the necessity to study these with non-linear methods.

In the second project, we study the propagation of IGWs in the radiation zone using non-linear simulations. We find that even with low nonlinearity parameters, forced monochromatic IGWs still exhibit non-linear behaviour. We then move on to forcing a spectrum of waves at the base of the radiation zone of a $3M_\odot$ ZAMS model and find that the frequency slope of the tangential velocity amplitudes at the surface lies within the range of slopes given in multiple observational works. We also find that slopes match the prediction made based on linear theory alone, except at very low frequencies. We proceeded to investigate the changes in the surface frequency spectrum for the same stel-

lar model but with different rotation rate (which also causes the generation spectrum to change slightly) and find that no significant changes are observed. Finally, we investigate the effect of stellar age on the surface frequency spectrum with the same generation spectrum and find that the slopes are very similar. However, stars at different age and even mass, are expected to have different generation spectrum which was our next point of study.

Currently, we are investigating how IGW generation varies with stellar ages and masses. We use the same hydrodynamical code used in the previous project, but include the convection zone in the simulations as well. Our main criterion for comparing the generation spectra for the different models was to match the ratio of convective velocities from mixing-length theory (as given in MESA) between models of different stellar masses to those from the simulations. Unlike the previous project, the thermal diffusivities had to be set to constant values to ensure numerical stability and the radiation zones were limited to 90% (80% for the $20M_{\odot}$ models) of the total stellar radius. So far, we find that generally, the frequency exponents for the tangential velocities lie between 0 and -1 at lower frequencies, and between -1.5 and -3 at higher frequencies at generation for all the stellar models. The frequency exponents for the tangential velocities close to the stellar surface lie between -2 and -4, whilst the slopes at lower frequencies lie between 0 and -2.

5.2 Future Work

Most of the work done by me and my team here has been driven by the fact that there is observational data to compare our results with. Our collaborations with observational teams have provided the means to motivate our investigation and work towards complementing each other's investigations. This has been a key factor in all the projects that I have worked on, especially my second and current project. Thus, we believe that any improvements done to the work in these two projects will have the most impact on the wider stellar community. For example, at the end of Chapter 4, we discussed how the use of a constant thermal diffusivity in the radiation zone of our models has reduced comparability with observation data. A workaround for this (subject to future investigation) is to use the IGW generation spectra that we obtained for different stellar masses and ages to run simulations of non-linear simulations of IGW in the radiation zone only, as we did in Chapter 3. This could provide the most accurate representation of the IGW surface spectrum as we could use realistic thermal diffusivities and set the simulation domain up to the stellar surface, instead of limiting the radiation zone for numerical stability.

Another example is repeating all, or a subset, of the numerical work that has been done in this thesis with a three-dimensional solver will provide a better insight into more realistic IGW generation and propagation. The reason why 2D simulations were done

rather than 3D simulations for all of our work is simply a time factor. Doing a parameter space study over many stellar models is more time-consuming in 3D than 2D, so we chose two-dimensional simulations instead. However, selecting a subset of the work we have done and repeating these simulations in 3D will be very efficient. Furthermore, in terms of IGW propagation, we can investigate whether amplitudes of IGWs do indeed differ from each other by a factor of $r^{1/2}$ as discussed in Section 3.3.1 between 2D and 3D simulations. If this turns out to be true, we can reduce the use of computational resources by investigating IGW propagation in 2D. Indeed, this is just a simple example, that does not take into account non-linear effects in 3D.

In addition, as discussed in the introduction, most observational data have provided information on massive O- and B-type stars which are massive and sometimes more evolved stars. These stars almost certainly will possess surface/intermediate convection zones, which can also be the source of IGW generation. Currently, we have neither a good grasp on the IGW generation spectrum from these surface/intermediate convection zones nor do we know how waves generated in the core are modified as they pass through these convection zones. We have observed some tunnelling effects of g-modes through the convective core in our simulations (Chapter 4), but we do not clearly know how they interact with intermediate/surface convection zones, which is currently paramount in the study of surface IGWs. Thus, an investigation on surface/intermediate convection zones and their interaction with IGWs is very much required currently.

Another major characteristic of O- and B-type stars is that they are known to have an angular velocity that varies with radius, azimuthal and polar angles. Thus, the next natural step after studying the effect of stellar age and mass on IGW generation, as we did in Chapter 4 is to study the effect of rotation on IGWs in stars. Going back to the work done in Chapter 3, we saw that up to 20% of the critical velocity, there are no changes in the surface IGW frequency spectrum. First, investigating the surface spectrum at larger stellar rotation rate would be crucial, mainly to find whether there is a limit before the surface spectrum starts to show significant difference. Second, in reality, stars are more likely to develop differential rotation, which is a rotation rate that varies with r, θ and ϕ. In Chapter 3, Eq. (3.31) shows how the frequency spectrum of IGWs can be shifted due to differential rotation. As the stellar rotational velocity becomes larger, we expect the frequency shift to be larger as well, which in the long run, could be used to determine internal rotation rates of stars from observation alone (with some assumptions). This is only from a radially-varying rotation rate, which can be investigated using 2D simulations.

Moving to 3D, stellar internal rotation rate will start to vary with polar and azimuthal angles and these will most certainly, affect IGW propagation. In fact, Prat *et al.* (2018) showed that for rapidly rotating stars, the change in stellar shape to a more flattened sphere due to centrifugal force causes the propagation of gravity waves to be limited to certain θ

and ϕ. Besides that, stellar rotation in 3D gives rise to meridional circulation(Zahn, 1992), which can interact with IGWs. For example, Talon & Charbonnel (2004) showed that the transport of angular momentum due to IGWs can reduce the magnitude of meridional circulation in lower mass stars, which could explain the shape of the lithium dip (Schramm *et al.*, 1990) seen in the spectroscopic data of many stars.

Studies on the propagation of IGWs through a radial differential rotation have already been done on one stellar mass but repeating this for more masses and ages is crucial as we do not expect the rotation profile to be the same for all stellar masses and ages. This study on differential rotation will also greatly help us understand the transport of angular momentum and chemical composition. These are two of the fundamental problems in stellar evolution, which are still poorly understood.

One of the major processes an IGW goes through in the radiation zone is wave breaking. We discussed this process in Chapter 1, 2 and 3 and we observed energy transfer from higher scales/frequencies to smaller scales/frequencies in our simulations. However, we were limited by the resolution of our simulations. All the numerical simulations of stellar interiors described in this thesis were done using a pseudospectral solver that solves the Navier-Stokes equations in the anelastic approximation for a two-dimensional cross-section of a star in the equatorial plane. The radial number of grid cells set for all the models that we used was 1500, which was limited to this value due to two factors: shorter simulation time and solver limitations. As a long-term goal, one major improvement that could be done here is to improve this solver so that the models have better radial resolution and thus be able to resolve smaller IGW frequencies and wavelengths. This will prove very useful in studying highly non-linear waves, which are expected to be produced in more massive stars.

Appendix A

Wave Dispersion from the Linear RG Equations

The following equations show the full RG Navier-Stokes Equations:

$$\nabla \cdot \overline{\rho}\vec{v} = 0, \tag{A.1}$$

$$\begin{aligned}\frac{\partial \vec{v}}{\partial t} &= -(\vec{v}\cdot\nabla)\vec{v} - \nabla\left(\frac{P}{\overline{\rho}}\right) - C\overline{g}\vec{\hat{r}} + 2(\vec{v}\times\vec{\hat{z}}\Omega) \\ &\quad + \overline{\nu}\left(\nabla^2\vec{v} + \frac{1}{3}\nabla(\nabla\cdot\vec{v})\right),\end{aligned} \tag{A.2}$$

$$\begin{aligned}\frac{\partial T}{\partial t} &= -(\vec{v}\cdot\nabla)T + (\gamma-1)Th_\rho v_r \\ &\quad - v_r\left(\frac{\partial \overline{T}}{\partial r} - (\gamma-1)\overline{T}h_\rho\right) \\ &\quad + \frac{1}{c_v\overline{\rho}}\nabla\cdot(c_p\overline{\kappa}\overline{\rho}\nabla T) + \frac{1}{c_v\overline{\rho}}\nabla\cdot(c_p\overline{\kappa}\overline{\rho}\nabla\overline{T}).\end{aligned} \tag{A.3}$$

where ρ, T and P are the perturbation density, temperature and pressure respectively whereas the same quantities with an over-line represent reference state quantities which vary only with radius. The negative inverse density scale height is represented by h_ρ. The rotational angular velocity and viscosity are represented by Ω and $\overline{\nu}$. The specific heat capacity at constant volume, specific heat capacity at constant pressure and thermal diffusivity are represented by c_v, c_p and $\overline{\kappa}$ respectively. The reference state gravity is represented by $\overline{g}$. The co-density, C, is

$$C = -\frac{1}{\overline{T}}\left(T + \frac{1}{\overline{g\rho}}\frac{\partial \overline{T}}{\partial r}P\right). \tag{A.4}$$

I start by first, considering the two-dimensional linearisation of these equations. I consider only the linear terms, write the spatial derivatives in cylindrical coordinates and set the z-derivatives to 0. I do not consider the effects of viscosity, thermal diffusion or rotation for this derivation. Thus, Eq. (A.1) becomes

$$\begin{aligned} 0 &= \nabla \cdot \overline{\rho}\vec{v} \\ &= \overline{\rho}\left(\nabla \cdot \vec{v}\right) + \vec{v} \cdot \nabla\overline{\rho}, \end{aligned}$$

and since, the over-line here refers to values varying in the radial direction only,

$$0 = \overline{\rho}\left(\frac{1}{r}\partial_r\left(rv_r\right) + \frac{1}{r}\partial_\theta v_\theta\right) + v_r\partial_r\overline{\rho},$$

where ∂_r and ∂_θ refer to $\partial/\partial r$ and $\partial/\partial\theta$ respectively. Rearranging this gives

$$\partial_\theta v_\theta = -\partial_r\left(rv_r\right) - h_\rho r v_r. \tag{A.5}$$

where, I replace $\partial_r\overline{\rho}/\overline{\rho}$ with h_ρ. Next, Eq. A.2 can be split into two components: the radial component and the horizontal component. In the radial direction, Eq. (A.2) becomes

$$\partial_t v_r = -\partial_r\left(\frac{P}{\overline{\rho}}\right) - C\overline{g}, \tag{A.6}$$

and in the horizontal direction,

$$\partial_t v_\theta = -\frac{1}{r}\partial_\theta\left(\frac{P}{\overline{\rho}}\right). \tag{A.7}$$

Finally, the temperature equation, Eq. (A.3), becomes

$$\partial_t T = -v_r\left(\frac{\partial\overline{T}}{\partial r} - (\gamma-1)\overline{T}h_\rho\right). \tag{A.8}$$

Using the modified definition for the Brunt–Väisälä frequency (see Chapter 3, Section 3.1),

$$N_{mod}(r)^2 = \frac{\overline{g}}{\overline{T}}\left(\frac{\partial\overline{T}}{\partial r} - (\gamma-1)\overline{T}h_\rho\right),$$

Eq. (A.8) becomes

$$\partial_t T = -\frac{\overline{T}N_{mod}^2 v_r}{\overline{g}}. \tag{A.9}$$

Now that we have the required linear equations (Eq. (A.5), Eq. (A.6), Eq. (A.7) and Eq. (A.9)), I introduce a wave ansatz of the following form: $f(r,\theta,t) = f(r)e^{-im\theta}e^{-i\omega t}$,

where f can be any quantity, P, T, v_r or v_θ. Since each quantity is made up of separable functions for r, θ and t, their derivatives commute. Thus, taking the horizontal derivative of Eq. (A.7) gives

$$\partial_t \left(\partial_\theta v_\theta\right) = -\frac{1}{r\overline{\rho}}\partial_{\theta\theta} P.$$

Substituting Eq. (A.5) into the equation above gives

$$\partial_{\theta\theta} P = r\overline{\rho}\partial_t \left(\partial_r \left(r v_r\right) + h_\rho r v_r\right). \tag{A.10}$$

Taking the time derivative of Eq. (A.6) next, gives

$$\partial_{tt} v_r = -\partial_t \partial_r \left(\frac{P}{\overline{\rho}}\right) + \overline{g}\partial_t C$$

There are arguments as to the second term in the codensity equation (Eq. (A.4)) should be considered or not, with one of the arguments being ignoring this term improves energy conservation (Brown *et al.*, 2012). In this derivation, I ignore the second term, which results in the codensity equation becoming $C = -T/\overline{T}$. Substituting this into the previous equation gives

$$\partial_{tt} v_r = -\partial_t \partial_r \left(\frac{P}{\overline{\rho}}\right) + \frac{\overline{g}}{\overline{T}}\partial_t T.$$

Substituting in Eq. (A.9) gives

$$\partial_{tt} v_r = -\partial_t \partial_r \left(\frac{P}{\overline{\rho}}\right) - N_{mod}^2 v_r.$$

Taking the double horizontal derivative the above equation then, gives

$$\partial_{\theta\theta}\partial_{tt} v_r = -\partial_t \partial_r \left(\frac{\partial_{\theta\theta} P}{\overline{\rho}}\right) - N_{mod}^2 \partial_{\theta\theta} v_r,$$

and substituting Eq. (A.10) into the equation above gives

$$\partial_{\theta\theta}\partial_{tt} v_r = -\partial_r \partial_{tt} \left(r\partial_r \left(r v_r\right) + h_\rho r^2 v_r\right) - N_{mod}^2 \partial_{\theta\theta} v_r.$$

I introduce a substitution factor here, $v_r = \alpha\overline{\rho}^{-1/2} r^{-3/2}$, so the equation above becomes

$$\begin{aligned}
&\partial_{\theta\theta}\partial_{tt}\left(\alpha\overline{\rho}^{-1/2} r^{-3/2}\right) \\
&= -\partial_r \partial_{tt}\left[r\partial_r\left[r\left(\alpha\overline{\rho}^{-1/2} r^{-3/2}\right)\right] + h_\rho r^2\left(\alpha\overline{\rho}^{-1/2} r^{-3/2}\right)\right]
\end{aligned}$$

$$
\begin{aligned}
&\quad - N_{mod}^2 \partial_{\theta\theta} \left(\alpha \overline{\rho}^{-1/2} r^{-3/2} \right) \\
&\partial_{\theta\theta} \partial_{tt} \alpha \\
&= -\overline{\rho}^{1/2} r^{3/2} \partial_r \partial_{tt} \left[r \partial_r \left(\alpha \overline{\rho}^{-1/2} r^{-1/2} \right) + h_\rho \alpha \overline{\rho}^{-1/2} r^{1/2} \right] \\
&\quad - N_{mod}^2 \partial_{\theta\theta} \alpha \\
&= -\overline{\rho}^{1/2} r^{3/2} \partial_{tt} \left[\partial_r \left(\alpha \overline{\rho}^{-1/2} r^{-1/2} \right) + r \partial_{rr} \left(\alpha \overline{\rho}^{-1/2} r^{-1/2} \right) + \partial_r \left(h_\rho \alpha \overline{\rho}^{-1/2} r^{1/2} \right) \right] \\
&\quad - N_{mod}^2 \partial_{\theta\theta} \alpha.
\end{aligned}
$$

The first term in the square brackets can be expanded out as follows:

$$
\partial_r \left(\alpha \overline{\rho}^{-1/2} r^{-1/2} \right) = \left(\partial_r \alpha \right) \overline{\rho}^{-1/2} r^{-1/2} - \frac{\alpha}{2} \overline{\rho}^{-1/2} h_\rho r^{-1/2} - \frac{\alpha}{2} \overline{\rho}^{-1/2} r^{-3/2},
$$

while the second term can be expanded out as follows:

$$
\begin{aligned}
&r \partial_{rr} \left(\alpha \overline{\rho}^{-1/2} r^{-1/2} \right) \\
&= r \left[\left(\partial_{rr} \alpha \right) \overline{\rho}^{-1/2} r^{-1/2} - \frac{\left(\partial_r \alpha \right)}{2} \overline{\rho}^{-1/2} h_\rho r^{-1/2} - \frac{\left(\partial_r \alpha \right)}{2} \overline{\rho}^{-1/2} r^{-3/2} \right] \\
&\quad + r \left[-\frac{\left(\partial_r \alpha \right)}{2} \overline{\rho}^{-1/2} h_\rho r^{-1/2} + \frac{\alpha}{4} \overline{\rho}^{-1/2} h_\rho^2 r^{-1/2} - \frac{\alpha}{2} \overline{\rho}^{-1/2} \left(\partial_r h_\rho \right) r^{-1/2} + \frac{\alpha}{4} \overline{\rho}^{-1/2} h_\rho r^{-3/2} \right] \\
&\quad + r \left[-\frac{\left(\partial_r \alpha \right)}{2} \overline{\rho}^{-1/2} r^{-3/2} + \frac{\alpha}{4} \overline{\rho}^{-1/2} h_\rho r^{-3/2} + \frac{3\alpha}{4} \overline{\rho}^{-1/2} r^{-5/2} \right] \\
&= \left[\left(\partial_{rr} \alpha \right) \overline{\rho}^{-1/2} r^{1/2} - \frac{\left(\partial_r \alpha \right)}{2} \overline{\rho}^{-1/2} h_\rho r^{1/2} - \frac{\left(\partial_r \alpha \right)}{2} \overline{\rho}^{-1/2} r^{-1/2} \right] \\
&\quad + \left[-\frac{\left(\partial_r \alpha \right)}{2} \overline{\rho}^{-1/2} h_\rho r^{1/2} + \frac{\alpha}{4} \overline{\rho}^{-1/2} h_\rho^2 r^{1/2} - \frac{\alpha}{2} \overline{\rho}^{-1/2} \left(\partial_r h_\rho \right) r^{1/2} + \frac{\alpha}{4} \overline{\rho}^{-1/2} h_\rho r^{-1/2} \right] \\
&\quad + \left[-\frac{\left(\partial_r \alpha \right)}{2} \overline{\rho}^{-1/2} r^{-1/2} + \frac{\alpha}{4} \overline{\rho}^{-1/2} h_\rho r^{-1/2} + \frac{3\alpha}{4} \overline{\rho}^{-1/2} r^{-3/2} \right],
\end{aligned}
$$

and the last term can be expanded out as follows:

$$
\begin{aligned}
&\partial_r \left(h_\rho \alpha \overline{\rho}^{-1/2} r^{1/2} \right) \\
&= \left(\partial_r h_\rho \right) \alpha \overline{\rho}^{-1/2} r^{1/2} + h_\rho \left(\partial_r \alpha \right) \overline{\rho}^{-1/2} r^{1/2} - \frac{\alpha}{2} \overline{\rho}^{-1/2} h_\rho^2 r^{1/2} + \frac{\alpha}{2} h_\rho \overline{\rho}^{-1/2} r^{-1/2}.
\end{aligned}
$$

Putting them altogether gives

$$
\begin{aligned}
&\partial_{\theta\theta} \partial_{tt} \alpha \\
&= -\overline{\rho}^{1/2} r^{3/2} \partial_{tt} \left[\left(\partial_r \alpha \right) \overline{\rho}^{-1/2} r^{-1/2} - \frac{\alpha}{2} \overline{\rho}^{-1/2} h_\rho r^{-1/2} - \frac{\alpha}{2} \overline{\rho}^{-1/2} r^{-3/2} \right]
\end{aligned}
$$

$$
\begin{aligned}
&- \overline{\rho}^{1/2} r^{3/2} \partial_{tt} \left[\left(\partial_r \alpha \right) \overline{\rho}^{-1/2} r^{1/2} - \frac{\left(\partial_r \alpha \right)}{2} \overline{\rho}^{-1/2} h_\rho r^{1/2} - \frac{\left(\partial_r \alpha \right)}{2} \overline{\rho}^{-1/2} r^{-1/2} \right] \\
&- \overline{\rho}^{1/2} r^{3/2} \partial_{tt} \left[- \frac{\left(\partial_r \alpha \right)}{2} \overline{\rho}^{-1/2} h_\rho r^{1/2} + \frac{\alpha}{4} \overline{\rho}^{-1/2} h_\rho^2 r^{1/2} - \frac{\alpha}{2} \overline{\rho}^{-1/2} \left(\partial_r h_\rho \right) r^{1/2} + \frac{\alpha}{4} \overline{\rho}^{-1/2} h_\rho r^{-1/2} \right] \\
&- \overline{\rho}^{1/2} r^{3/2} \partial_{tt} \left[- \frac{\left(\partial_r \alpha \right)}{2} \overline{\rho}^{-1/2} r^{-1/2} + \frac{\alpha}{4} \overline{\rho}^{-1/2} h_\rho r^{-1/2} + \frac{3\alpha}{4} \overline{\rho}^{-1/2} r^{-3/2} \right] \\
&- \overline{\rho}^{1/2} r^{3/2} \partial_{tt} \left[\left(\partial_r h_\rho \right) \alpha \overline{\rho}^{-1/2} r^{1/2} + h_\rho \left(\partial_r \alpha \right) \overline{\rho}^{-1/2} r^{1/2} - \frac{\alpha}{2} \overline{\rho}^{-1/2} h_\rho^2 r^{1/2} + \frac{\alpha}{2} h_\rho \overline{\rho}^{-1/2} r^{-1/2} \right] \\
&- N^2 \partial_{\theta\theta} \alpha \\
= &- \overline{\rho}^{1/2} r^{3/2} \partial_{tt} \left[\left(\partial_{rr} \alpha \right) \overline{\rho}^{-1/2} r^{1/2} \right] \\
&- \overline{\rho}^{1/2} r^{3/2} \partial_{tt} \left[\frac{\alpha}{2} \left(\partial_r h_\rho \right) \overline{\rho}^{-1/2} r^{1/2} - \frac{\alpha}{2} \overline{\rho}^{-1/2} h_\rho^2 r^{1/2} + \frac{\alpha}{2} h_\rho \overline{\rho}^{-1/2} r^{-1/2} \right] \\
&- \overline{\rho}^{1/2} r^{3/2} \partial_{tt} \left[\frac{\alpha}{4} \overline{\rho}^{-1/2} r^{-3/2} \right] \\
&- N_{mod}^2 \partial_{\theta\theta} \alpha \\
= &\, \partial_{tt} \left[- \left(\partial_{rr} \alpha \right) r^2 \right] \\
&+ \partial_{tt} \left[- \frac{\alpha}{2} \left(\partial_r h_\rho \right) r^2 + \frac{\alpha}{2} h_\rho^2 r^2 - \frac{\alpha}{2} h_\rho r \right] \\
&+ \partial_{tt} \left[- \frac{\alpha}{4} \right] \\
&- N_{mod}^2 \partial_{\theta\theta} \alpha .
\end{aligned}
$$

Rearranging this equation gives

$$
\begin{aligned}
0 = &\, r^2 \partial_{tt} \partial_{rr} \alpha + N_{mod}^2 \partial_{\theta\theta} \alpha + \partial_{\theta\theta} \partial_{tt} \alpha \\
&+ \partial_{tt} \left[\frac{\alpha}{2} \left(\partial_r h_\rho \right) r^2 - \frac{\alpha}{2} h_\rho^2 r^2 + \frac{\alpha}{2} h_\rho r \right] \\
&+ \partial_{tt} \left[\frac{\alpha}{4} \right] .
\end{aligned}
$$

Substituting the wave ansatz $\alpha(r, \theta, t) = \alpha(r) e^{-im\theta} e^{-i\omega t}$ here gives

$$
\begin{aligned}
0 = &- \omega^2 r^2 \partial_{rr} \alpha - N_{mod}^2 m^2 \alpha + m^2 \omega^2 \alpha \\
&- \omega^2 \left[\frac{\alpha}{2} \left(\partial_r h_\rho \right) r^2 - \frac{\alpha}{2} h_\rho^2 r^2 + \frac{\alpha}{2} h_\rho r \right] \\
&- \omega^2 \left[\frac{\alpha}{4} \right] .
\end{aligned}
$$

Dividing through by $-\omega^2 r^2$ gives

$$
0 = \partial_{rr} \alpha + \frac{m^2}{r^2} \left(\frac{N_{mod}^2}{\omega^2} - 1 \right) \alpha
$$

$$+\left[\frac{1}{2}\left(\partial_r h_\rho\right)-\frac{1}{2}h_\rho^2+\frac{1}{2r}h_\rho\right]\alpha$$
$$+\frac{1}{4r^2}\alpha. \tag{A.11}$$

The terms in the first line of Eq. A.11 represent the gravity wave equation, and the dispersion relation for the gravity wave in the RG equations can then be derived. The term m/r is the horizontal IGW wavenumber, k_h and

$$k_r=\sqrt{\frac{m^2}{r^2}\left(\frac{N^2}{\omega^2}-1\right)} \tag{A.12}$$

where, k_r is the radial IGW wavenumber. The terms in the second line are collectively referred to as the density term (DT) and the term in the last line is referred to as geometric term (GT) in this thesis. The inverse density scale height, H_ρ is defined as $-1/h_\rho$. In the case where $k_r >> 1/H_\rho$, DT can be neglected since the terms in DT are of the order $1/H_\rho$. Furthermore, waves propagate only in regions where $\omega < N$, so for the lowest value of $m(=1)$, k_r will always be bigger than GT. Thus, we can write the following differential equation:

$$\partial_{rr}\alpha+\frac{m^2}{r^2}\left(\frac{N_{mod}^2}{\omega^2}-1\right)\alpha=0. \tag{A.13}$$

With the assumption that k_r varies slowly with radius, we can apply the WKB approximation here to get

$$\begin{aligned}
\alpha &\propto k_r^{-1/2}\exp\left[i\int k_r dr\right]\\
v_r\rho^{1/2}r^{3/2} &\propto m^{-1/2}r^{1/2}\left(\frac{N_{mod}^2}{\omega^2}-1\right)^{-1/4}\exp\left[i\int k_r dr\right]\\
v_r &\propto r^{-1}\rho^{-1/2}\left(\frac{N_{mod}^2}{\omega^2}-1\right)^{-1/4}\exp\left[i\int k_r dr\right]\\
v_r &\propto r^{-1}\rho^{-1/2}\left(N_{mod}^2-\omega^2\right)^{-1/4}
\end{aligned}$$

Repeating the derivation above with the second term in the co-density term included will give the following proportionality:

$$v_r \propto r^{-1}\rho^{-1/2}\left(N_{mod}^2-\omega^2\right)^{-1/4}T^{-1/2}.$$

Bibliography

Aerts, C., Bowman, D. M., Símon-Díaz, S., Buysschaert, B., Johnston, C., Moravveji, E., Beck, P. G., De Cat, P., Triana, S., Aigrain, S., Castro, N., Huber, D. & White, T. 2018 K2 photometry and HERMES spectroscopy of the blue supergiant ρ Leo: rotational wind modulation and low-frequency waves. MNRAS **476**, 1234–1241.

Aerts, C., Christensen-Dalsgaard, J. & Kurtz, D. 2010 *Asteroseismology*. Springer Netherlands.

Aerts, C. & Rogers, T. M. 2015 Observational Signatures of Convectively Driven Waves in Massive Stars. ApJ **806**, L33.

Aerts, C., Símon-Díaz, S., Bloemen, S., Debosscher, J., Pápics, P. I., Bryson, S., Still, M., Moravveji, E., Williamson, M. H., Grundahl, F., Fredslund Andersen, M., Antoci, V., Pallé, P. L., Christensen-Dalsgaard, J. & Rogers, T. M. 2017 Kepler sheds new and unprecedented light on the variability of a blue supergiant: Gravity waves in the O9.5Iab star HD 188209. A&A **602**, A32.

Alvan, L., Brun, A. S. & Mathis, S. 2014 Theoretical seismology in 3D: nonlinear simulations of internal gravity waves in solar-like stars. A&A **565**, A42.

Alvan, L., Mathis, S. & Decressin, T. 2013 Coupling between internal waves and shear-induced turbulence in stellar radiation zones: the critical layers. A&A **553**, A86.

Alvan, L., Strugarek, A., Brun, A. S., Mathis, S. & Garcia, R. A. 2015 Characterizing the propagation of gravity waves in 3D nonlinear simulations of solar-like stars. A&A **581**, A112.

Ansong, J. K. & Sutherland, B. R. 2010 Internal gravity waves generated by convective plumes. *Journal of Fluid Mechanics* **648**, 405–434.

Baraffe, Isabelle & Chabrier, Gilles 2018 A closer look at the transition between fully convective and partly radiative low-mass stars. A&A **619**, A177.

Barker, A. J. & Ogilvie, G. I. 2010 On internal wave breaking and tidal dissipation near the centre of a solar-type star. MNRAS **404**, 1849–1868.

Batchelor, G. 1960 *The theory of homogeneous turbulence*. University Press.

Beck, P. G., Montalban, J., Kallinger, T., De Ridder, J., Aerts, C., García, R. A., Hekker, S., Dupret, M.-A., Mosser, B., Eggenberger, P., Stello, D., Elsworth, Y., Frandsen, S., Carrier, F., Hillen, M., Gruberbauer, M., Christensen-Dalsgaard, J., Miglio, A., Valentini, M., Bedding, T. R., Kjeldsen, H., Girouard, F. R., Hall, J. R. & Ibrahim, K. A. 2012 Fast core rotation in red-giant stars as revealed by gravity-dominated mixed modes. Nature **481**, 55–57.

Biermann, L. 1951 Kometenschweife und solare Korpuskularstrahlung. ZAp **29**, 274.

Böhm-Vitense, E. 1958 Über die Wasserstoffkonvektionszone in Sternen verschiedener Effektivtemperaturen und Leuchtkräfte. Mit 5 Textabbildungen. ZAp **46**, 108.

Bowman, D. M., Burssens, S., Pedersen, M., Johnston, C., Aerts, C., Buysschaert, B., Michielsen, M., Tkachenko, A., Rogers, T., Edelmann, P., Ratnasingam, R., Simón-Díaz, S., Castro, N., Moravveji, E., Pope, B., White, T. & Cat, P. 2019 Low-frequency gravity waves in blue supergiants revealed by high-precision space photometry. *Nature Astronomy* **3**.

Bowman, D. M., Burssens, S., Simón-Díaz, S., Edelmann, P. V. F., Rogers, T. M., Horst, L., Röpke, F. K. & Aerts, C. 2020 Photometric detection of internal gravity waves in upper main-sequence stars - ii. combined tess photometry and high-resolution spectroscopy. A&A **640**, A36.

Brassard, P., Fontaine, G., Wesemael, F., Kawaler, S. D. & Tassoul, M. 1991 Adiabatic Properties of Pulsating DA White Dwarfs. I. The Treatment of the Brunt-Vaeisaelae Frequency and the Region of Period Formation. ApJ **367**, 601.

Brown, B. P., Vasil, G. M. & Zweibel, E. G. 2012 Energy Conservation and Gravity Waves in Sound-Proof Treatments of Stellar Interiors. Part i. Anelastic Approximations. ApJ **756** (2), 109.

Brummell, N. H., Clune, T. L. & Toomre, J. 2002 Penetration and Overshooting in Turbulent Compressible Convection. ApJ **570**, 825–854.

Brun, A. S., Miesch, M. S. & Toomre, J. 2011 Modeling the Dynamical Coupling of Solar Convection with the Radiative Interior. ApJ **742**, 79.

Couston, L.-A., Lecoanet, D., Favier, B. & Le Bars, M. 2018 The energy flux spectrum of internal waves generated by turbulent convection. *Journal of fluid mechanics* **854**.

Crowther, P. & Evans, C. 2009 A feros spectroscopic study of the extreme o supergiant he 3–759. A&A **503** (3), 985–990.

Degroote, P., Briquet, M., Auvergne, M., Simón-Díaz, S., Aerts, C., Noels, A., Rainer, M., Hareter, M., Poretti, E., Mahy, L., Oreiro, R., Vuckovi´c, M., Smolders, K., Baglin, A., Baudin, F., Catala, C., Michel, E. & Samadi, R. 2010 Detection of frequency spacings in the young o-type binary hd49 from corot photometry. A&A **519**, A38.

Deheuvels, S., Garcia, R. A., Chaplin, W. J., Basu, S., Antia, H. M., Appourchaux, T., Benomar, O., Davies, G. R., Elsworth, Y., Gizon, L., Goupil, M. J., Reese, D. R., Regulo, C., Schou, J., Stahn, T., Casagrande, L., Christensen-Dalsgaard, J., Fischer, D., Hekker, S., Kjeldsen, H., Mathur, S., Mosser, B., Pinsonneault, M., Valenti, J., Christiansen, J. L., Kinemuchi, K. & Mullally, F. 2012 Seismic evidence for a rapidly rotating core in a lower-giant-branch star observed with kepler. ApJ **756** (1), 19.

Dziembowski, W. A., Pamiatnykh, A. A. & Sienkiewicz, R. . 1991 Helium content in the solar convective envelope from helioseismology. MNRAS **249**, 602–605.

Edelmann, P., Ratnasingam, R., Pedersen, M., Bowman, D., Prat, V. & Rogers, T. 2019 Three-dimensional simulations of massive stars. i. wave generation and propagation. ApJ **876**, 4.

Fuller, J., Lecoanet, D., Cantiello, M. & Brown, B. 2014 Angular Momentum Transport via Internal Gravity Waves in Evolving Stars. ApJ **796**, 17.

Garaud, P., Medrano, M., Brown, J. M., Mankovich, C. & Moore, K. 2015 Excitation of Gravity Waves by Fingering Convection, and The Formation of Compositional Staircases in Stellar Interiors. ApJ **808** (1), 89.

Garcia Lopez, R. J. & Spruit, H. C. 1991 Li depletion in F stars by internal gravity waves. ApJ **377**, 268–277.

Georgy, C., Granada, A., Ekström, S., Meynet, G., Anderson, R. I., Wyttenbach, A., Eggenberger, P. & Maeder, A. 2014 Populations of rotating stars. III. SYCLIST, the new Geneva population synthesis code. A&A **566**, A21.

Goldreich, P. & Kumar, P. 1990 Wave generation by turbulent convection. ApJ **363**, 694–704.

Goldreich, P., Murray, N. & Kumar, P. 1994 Excitation of solar p-modes. ApJ **424**, 466–479.

Grossmann, C., Roos, H.-G. & Stynes, M. 2007 *Numerical treatment of partial differential equations*, , vol. 154. Springer.

Horst, L., Edelmann, P. V. F., Andrássy, R., Röpke, F. K., Bowman, D. M., Aerts, C. & Ratnasingam, R. P. 2020 Fully compressible simulations of waves and core convection in main-sequence stars. A&A **641**, A18.

Hurlburt, N. E., Toomre, J. & Massaguer, J. M. 1986 Nonlinear compressible convection penetrating into stable layers and producing internal gravity waves. ApJ **311**, 563–577.

Jieun, C., Dotter, A., Conroy, C., Cantiello, M., Paxton, B. & Johnson, B. 2016 Mesa isochrones and stellar tracks (mist). i. solar-scaled models. ApJ **823**.

Kippenhahn, R., Weigert, A. & Weiss, A. 2012 *Stellar Structure and Evolution*.

Kiraga, M., Jahn, K., Stepien, K. & Zahn, J.-P. 2003 Direct numerisimulations of penetrative convection and generation of internal gravity waves. *Acta Astronomica* **53**, 321–339.

Kumar, P., Talon, S. & Zahn, J.-P. 1999 Angular Momentum Redistribution by Waves in the Sun. ApJ **520**, 859–870.

Lecoanet, D. & Quataert, E. 2013 Internal gravity wave excitation by turbulent convection. MNRAS **430**, 2363–2376.

Lighthill, M. 1978 *Waves in Fluids*. Cambridge University Press.

Martins, F., Schaerer, D. & Hillier, D. J. 2005 A new calibration of stellar parameters of galactic o stars. A&A **436** (3), 1049–1065.

Montalbán, J. & Schatzman, E. 2000 Mixing by internal waves. III. Li and Be abundance dependence on spectral type, age and rotation. A&A **354**, 943–959.

Müller, P., Holloway, G., Henyey, F. & Pomphrey, N. 1986 Nonlinear Interactions Among Internal Gravity Waves (Paper 6R0117). *Reviews of Geophysics* **24**, 493.

Paxton, B., Bildsten, L., Dotter, A., Herwig, F., Lesaffre, P. & Timmes, F. 2011 Modules for Experiments in Stellar Astrophysics (MESA). ApJS **192** (1), 3.

Paxton, B., Cantiello, M., Arras, P., Bildsten, L., Brown, E. F., Dotter, A., Mankovich, C., Montgomery, M. H., Stello, D., Timmes, F. X. & Townsend,

R. 2013 Modules for Experiments in Stellar Astrophysics (MESA): Planets, Oscillations, Rotation, and Massive Stars. ApJS **208** (1), 4.

Paxton, B., Marchant, P., Schwab, J., Bauer, E. B., Bildsten, L., Cantiello, M., Dessart, L., Farmer, R., Hu, H., Langer, N., Townsend, R. H. D., Townsley, D. M. & Timmes, F. X. 2015 Modules for Experiments in Stellar Astrophysics (MESA): Binaries, Pulsations, and Explosions. ApJS **220** (1), 15.

Paxton, B., Schwab, J., Bauer, E. B., Bildsten, L., Blinnikov, S., Duffell, P., Farmer, R., Goldberg, J. A., Marchant, P., Sorokina, E., Thoul, A., Townsend, R. H. D. & Timmes, F. X. 2018 Modules for Experiments in Stellar Astrophysics (MESA): Convective Boundaries, Element Diffusion, and Massive Star Explosions. ApJS **234** (2), 34.

Paxton, B., Smolec, R., Schwab, J., Gautschy, A., Bildsten, L., Cantiello, M., Dotter, A., Farmer, R., Goldberg, J. A., Jermyn, A. S., Kanbur, S. M., Marchant, P., Thoul, A., Townsend, R. H. D., Wolf, W. M., Zhang, M. & Timmes, F. X. 2019 Modules for Experiments in Stellar Astrophysics (MESA): Pulsating Variable Stars, Rotation, Convective Boundaries, and Energy Conservation. ApJS **243** (1), 10.

Pedersen, M. G., Aerts, C., Pápics, P. I. & Rogers, T. M. 2018 The shape of convective core overshooting from gravity-mode period spacings. A&A **614**, A128.

Phillips, O. 1966 *The Dynamics of the Upper Ocean*. Cambridge U.P.

Phillips, O. 1980 *The Dynamics of the Upper Ocean*. Cambridge University Press.

Phillips, O. M. 1960 On the dynamics of unsteady gravity waves of finite amplitude part 1. the elementary interactions. *Journal of Fluid Mechanics* **9** (2), 193–217.

Phillips, O. M. 1961 On the dynamics of unsteady gravity waves of finite amplitude part 2. local properties of a random wave field. *Journal of Fluid Mechanics* **11** (1), 143–155.

Pinçon, C., Belkacem, K. & Goupil, M. J. 2016 Generation of internal gravity waves by penetrative convection. A&A **588**, A122.

Prat, V., Mathis, S., Augustson, K., Lignières, F., Ballot, J., Alvan, L. & Brun, A. S. 2018 Impact of general differential rotation on gravity waves in rapidly rotating stars. In *What physics can we learn from oscillating stars*. Banyuls, France, 4 pages, 5 figures, to appear in the proceedings of the PHOST conference in honour of Pr. Shibahashi.

Press, W. H. 1981 Radiative and other effects from internal waves in solar and stellar interiors. ApJ **245**, 286–303.

Ramiaramanantsoa, T., Ratnasingam, R., Shenar, T., Moffat, A. F. J., Rogers, T. M., Popowicz, A., Kuschnig, R., Pigulski, A., Handler, G., Wade, G. A., Zwintz, K. & Weiss, W. W. 2018 A BRITE view on the massive O-type supergiant V973 Scorpii: hints towards internal gravity waves or sub-surface convection zones. MNRAS **480**, 972–986.

Ratnasingam, R. P., Edelmann, P. V. F. & Rogers, T. M. 2019 Onset of non-linear internal gravity waves in intermediate-mass stars. MNRAS **482** (4), 5500–5512.

Ratnasingam, R. P., Edelmann, P. V. F. & Rogers, T. M. 2020 Two-dimensional simulations of internal gravity waves in the radiation zones of intermediate-mass stars. MNRAS **497** (4), 4231–4245.

Renzo, M., Ott, C. D., Shore, S. N. & de Mink, S. E. 2017 Systematic survey of the effects of wind mass loss algorithms on the evolution of single massive stars. A&A **603**, A118.

Rieutord, M. & Zahn, J.-P. 1995 Turbulent plumes in stellar convective envelopes. A&A **296**, 127.

Rogers, T. M. & Glatzmaier, G. A. 2005 Gravity waves in the Sun. MNRAS **364**, 1135–1146.

Rogers, T. M., Lin, D. N. C. & Lau, H. H. B. 2012 Internal Gravity Waves Modulate the Apparent Misalignment of Exoplanets around Hot Stars. ApJ **758**, L6.

Rogers, T. M., Lin, D. N. C., McElwaine, J. N. & Lau, H. H. B. 2013 Internal Gravity Waves in Massive Stars: Angular Momentum Transport. ApJ **772**, 21.

Rogers, T. M., MacGregor, K. B. & Glatzmaier, G. A. 2008 Non-linear dynamics of gravity wave driven flows in the solar radiative interior. MNRAS **387** (2), 616–630.

Saio, H. 1993 An Overview of Stellar Pulsation Theory. Ap&SS **210** (1-2), 61–72.

Schmitz, D. 1990 *Spherical harmonic analysis*, pp. 1217–1221. Boston, MA: Springer US.

Schramm, D. N., Steigman, G. & Dearborn, D. S. P. 1990 Main-Sequence Mass Loss and the Lithium Dip. ApJ **359**, L55.

Shiode, J. H., Quataert, E., Cantiello, M. & Bildsten, L. 2013 The observational signatures of convectively excited gravity modes in main-sequence stars. MNRAS **430**, 1736–1745.

Su, Y., Lecoanet, D. & Lai, D. 2020 Physics of tidal dissipation in early-type stars and white dwarfs: hydrodynamical simulations of internal gravity wave breaking in stellar envelopes. MNRAS **495** (1), 1239–1251.

Talon, S. & Charbonnel, C. 2004 Angular momentum transport by internal gravity waves - ii. pop ii stars from the li plateau to the horizontal branch. A&A **418** (3), 1051–1060.

Tayar, J. & Pinsonneault, M. H. 2013 Implications of Rapid Core Rotation in Red Giants for Internal Angular Momentum Transport in Stars. ApJ **775**, L1.

Thomas, L. 1949 Elliptic problems in linear differential equations over a network: Watson scientific computing laboratory. *Columbia Univ., NY* .

Townsend, A. A. 1966 Internal waves produced by a convective layer. *Journal of Fluid Mechanics* **24**, 307–319.

Townsend, R. & Teitler, S. 2013 Gyre: An open-source stellar oscillation code based on a new magnus multiple shooting scheme. MNRAS **435**, 3406–3418.

Unno, W., Osaki, Y., Ando, H., Saio, H. & Shibahashi, H. 1989 *Nonradial oscillations of stars*.

van Loon, J. Th., L. Cioni, M.-R., Zijlstra, A. A. & Loup, C. 2005 An empirical formula for the mass-loss rates of dust-enshrouded red supergiants and oxygen-rich asymptotic giant branch stars. A&A **438** (1), 273–289.

Weaver, T. A., Zimmerman, G. B. & Woosley, S. E. 2017 KEPLER: General purpose 1D multizone hydrodynamics code.

Winters, K. B. & D'Asaro, E. A. 1989 Two-dimensional instability of finite amplitude internal gravity wave packets near a critical level. *Journal of Geophysical Research: Oceans* **94** (C9), 12709–12719.

Winters, K. B. & D'Asaro, E. A. 1994 Three-dimensional wave instability near a critical level. *Journal of Fluid Mechanics* **272**, 255–284.

Zahn, J. P. 1975 The dynamical tide in close binaries. A&A **41**, 329–344.

Zahn, J. P. 1992 Circulation and turbulence in rotating stars. A&A **265**, 115–132.

Zahn, J.-P., Talon, S. & Matias, J. 1997 Angular momentum transport by internal waves in the solar interior. A&A **322**, 320–328.